ON THE APPLICATION OF HIGH-T_c SUPERCONDUCTORS IN POWER COILS AND TRANSFORMERS

The research described in this thesis has been supported by the Technology Foundation STW, Applied Science Division of NWO and the Technology Programme of the Ministry of Economic Affairs. It has been performed in the Low Temperature Division and the Special Chair for Industrial Applications of Superconductors within the Faculty of Applied Physics at the University of Twente, P.O. Box 217, 7500 AE Enschede, The Netherlands.

CIP-GEGEVENS KONINKLIJKE BIBLIOTEEK, DEN HAAG

Chevtchenko O. A.

On the application of high-Tc superconductors in power coils and transformers

Proefschrift Universteit Twente, Enschede.
Met literatuuropgave – Met samenvatting in het Nederlands.
ISBN 90-365-1791-5
Keywords: superconductivity, AC power coil

Printed in the Netherlands

ON THE APPLICATION OF HIGH-T_c SUPERCONDUCTORS IN POWER COILS AND TRANSFORMERS

PROEFSCHRIFT

ter verkrijging van
de graad van doctor aan de Universiteit Twente,
op gezag van de rector magnificus,
prof. dr. F. A. van Vught,
volgens besluit van het College voor Promoties
in het openbaar te verdedigen
op donderdag 17 oktober 2002 om 15:00 uur

door

Oleg Alexandrovitch Chevtchenko

geboren op 1 juni 1954
te Riga, Letland

Dit proefschrift is goedgekeurd door:

Prof. dr. ir. H. H. J. ten Kate (promotor)

Contents

Chapter 1

INTRODUCTION

In this chapter an introduction to power application of superconductors is provided. The chapter starts with a brief history of superconductivity. When cooled below a critical temperature T_c, a superconductor is able to carry macroscopic electrical current with almost no resistance. The amount of current per unit area depends on the type of superconductivity exhibited by the material. Technical superconductors like NbTi, Nb_3Sn, Bi-2223 and YBCO are able to carry high currents in high magnetic field when operating temperature is low enough. Furthermore, the study is confined to high-T_c superconductors that have critical temperatures of 90 - 120 K at present; the data for low-T_c superconductors are used for illustration purposes only. The second and third sections deal with the practical applications. Though during its history challenged by the statement "apply or die", low-temperature superconductivity today has a good reputation in medicine, science and technology. More is expected from high-temperature superconductivity especially for power applications. In the last section the scope and the structure of the thesis are presented.

1.1 Brief history of superconductivity

Two essential phenomena characterize superconductivity in solids: (almost) zero electrical resistance and the Meißner effect. Zero resistance means zero voltage across a superconductor when a certain transport current passes through it. Meißner effect means that induced surface currents in the superconductor shield the interior to some degree from the external magnetic field. The superconductivity of a certain material exists in a range of parameters such as temperature, electric and magnetic field, density of electric current and strain that together form a multidimensional volume of the parameters. The outer surface of the volume usually taken at a certain value of the electric field is called the critical surface; it separates superconducting and non-superconducting states and links the critical parameters.

The Dutch scientist H. Kamerlingh Onnes discovered type-I superconductivity in 1911 when he found that mercury cooled below 4 kelvin lost electrical resistance [Onne11]. It appeared that type-I superconductivity later on found in many pure metals such as In, Sn and Pb and alloys vanishes in presence of magnetic field of about 0.1 T and at temperatures slightly above 7 K. By the end of 1950's type-II superconductivity was found in Nb-based allows such as NbTi, Nb_3Sn, Nb_3Ge, Nb_3Al, other intermetallic compounds such as V_3Ga and recently in MgB_2 [Naga01]. Type-II superconductivity is destroyed by the relatively high magnetic field of about 60, 40, 20 and 10 T or above the temperature of about 14, 23, 39 and 9 K respectively for $PbGd_{0.2}Mo_6S_8$, Nb_3Ge, MgB_2 and NbTi [Wils83], [Larb01]. By convention these are called low-temperature or low-T_c metallic type-II superconductors. The BCS theory (of Bardeen, Cooper and Schrieffer) provides a description of the microscopic behaviour of low-T_c superconductors and predicts that the pairing of superconducting electrons in these materials exhibits "s-wave symmetry".

Swiss physicists J. G. Bednorz and K. A. Müller discovered high-temperature cuprate type-II superconductivity in 1986 [Bedn86]. Since then many superconductors of this new type have been found. The most common high-temperature or high-T_c cuprates are: $Bi_2Sr_2Ca_2Cu_3O_x$ (Bi-2223), $YBa_2Cu_3O_x$ (Y-123 or YBCO) and $Bi_2Sr_2Ca_1Cu_2O_x$ (Bi-2212). These exhibit a superconducting behaviour at the temperature below 110, 92 and 85 K respectively and hence could be operated in liquid nitrogen. The magnetic field that destroys superconductivity at 4 K is estimated at 100 to 400 T for the cuprates [Oome00a]. Recent observations [Pan00] confirmed that the pairing of superconducting electrons in high-temperature cuprates (Bi-2212 in particular) displays "d-wave symmetry" in contrast to the "s-wave symmetry" for low-temperature superconductors. Hence, there seems to be more than just a quantitative difference between high-T_c and low-T_c superconductors. The highest reported and generally accepted critical temperature is about 150 K so far. The search for superconductivity at even higher temperatures continues, see for instance [Djur01]. However, other groups do not confirm such results yet.

1.2 Application of superconductors

Use and properties of technical low-T_c superconductors are explained in several textbooks [Wils93], [Iwas94] and [Seeb98]. Besides the micro-scale application such as various Josephson devices (in electronics, sensors and metrology), the generation of stationary magnetic fields from 2 to 20 T in considerable volumes up to about 10^4 m^3 [Kate01] has been the major application of superconductivity. Established areas of application are: medicine (Magnetic Resonance Imaging); science and high-energy physics in particular (NMR, ESR, accelerator and detector magnets); energy generation (confinement of the hot plasma in experiment nuclear fusion reactor); technology (separation of dia- or paramagnetic substances, non-interruptible power supply with magnetic energy storage units) and transport (levitation trains).

Use and properties of technical high-T_c superconductors are subjects of ongoing research. The up to date summary and forecast are given in [Shea94], [Wesc98], [Seeb98], [Shea01]. When compared to low-T_c superconductors, the basic advantages of high-T_c superconductors

are relatively high operating temperature and heat capacity and hence simple cooling and high stability against disturbances. When used at 4 K another advantage is the possibility to generate in fully superconducting magnets magnetic fields in the 22 – 30 T range. A major drawback is the substantially higher conductor cost. The price of a superconductor is usually expressed per meter length per ampere of critical current. Typical values for Bi-2223 at 77 K; NbTi and Nb_3Sn at 4 K and copper at 300 K are: 100; from 1 to 10 and 10 US $/kA/m respectively (excluding the cooling cost). At present mainly the cost factor limits the penetration of high-T_c superconductors in the established application areas occupied by cheaper low-T_c superconductors. However, with time the price of high-T_c superconductors will decrease. For instance, in the year 2004 the price of about 50 US $/kA/m for Bi-2223 is expected [Masu99] hence indicating room for further improvement. Likely micro-scale applications of high-T_c superconductors are Josephson devices and microwave filters for mobile telecommunications. Potential large-scale use of high-T_c superconductors is in various magnets for science (high-field coils and inserts); power sector (transmission cables, motors and transformers); technology (crystal growth, separation); and transport (transformers for trains and propulsion thrusters with superconducting motors for ships).

1.3 Alternating transport current and magnetic field

Some perhaps optimistic estimates are that in the year 2020 up to 80 % of new power transformers; 75 % of motors, 40 % of generators and 35 % of transmission cables will be using high-T_c superconductors instead of copper or aluminium [Shea01]. Hence the expectations are rather high in the power-engineering sector. Most of the existing power grid uses a sinusoidal voltage and operates at 50 or 60 Hz. Some other applications demand a frequency of about 20 Hz (transformers for trains) and of 400 Hz (aero-space). Higher frequencies are also in use [Klop93], but not considered here. Consequently, the electromagnetic behaviour of high-T_c superconductors carrying alternating transport current; exposed to alternating magnetic and electric fields and operated at a certain frequency and temperature (often between 64 and 77 K) must be well understood and described.

Recent effort and progress are summarised in [Clerc95], [Nibb99], [Oome00a], [Rabb01a] thus indicating that not all problems are solved. In principle, such description can be provided with analytical, numerical or empirical method or a combination. For single Bi-2223 tapes analytical models lag behind and offer an incomplete description [Rabb99a]. Empirical data and formulas [Magn01], [Rabb01] do provide a flexible solution, but are confined to the range of the experimental parameters involved. Hence, numerical results [Shev01] (validated by experiments on crucial issues) provide the best solution for the problem. For Bi-2223 coils the approach at present is purely empirical and there are no general methods known that allow calculating loss *V-I* curves. When the project was set up in 1997 in the Netherlands to address the problem, it was decided to focus the efforts around an air-core power coil operated in liquid nitrogen at the frequency of 50 - 60 Hz.

1.4 Scope and structure of the thesis

The present study is confined to high-temperature superconductors and power coils operated in liquid nitrogen and intended for large-scale applications. The focus is on Bi-2223/Ag tapes with non-twisted superconducting filaments as these are the only high-T_c superconductors at present available in sufficient length. The aim of the study is three-fold. The first aim is to explore the options and the potential of increasing the critical currents and reducing the alternating current losses of practical superconductors in power coils (hence aiming at improved performance). The second goal is to build a model that is sufficient to describe behaviour and to calculate voltage-current curves of advanced Bi-2223 superconductors and coils carrying alternating current and exposed to alternating magnetic field. The application target is to develop fundamentals of high-T_c superconducting power coils and as an example to study a

prototype 1-MVA resonator coil both experimentally and numerically and hence to demonstrate the feasibility and predictable behaviour of high-T_c superconducting power devices. The final objective is, using the knowledge and the experience gained in the study, to evaluate the viability of a power transformer with high-T_c superconducting coils.

In Chapter 2 an overview of practical high-T_c superconductors such as Bi-2223/Ag tapes is given. The accent is made on the direct voltage-current characteristics of superconductors carrying transport current and exposed to magnetic field. The influence of magnetic field direction and magnitude on the critical current is analysed. The scaling relation between the critical current, magnetic field and temperature is derived for Bi-2223/Ag tapes. Finally, a compact way of describing direct voltage-current characteristics of the superconductors is found and used to create input data files for the numerical model described in Chapter 3. A new method of electrical insulation of Bi-2223/Ag tapes is presented together with test results gathered for insulated tapes.

Chapter 3 lays out the basics of an electro-magnetic numerical model sufficient to calculate voltage-current curves of high-T_c superconductors and coils carrying alternating current and exposed to alternating magnetic field. Existing formulations of the classical eddy current problem are compared and a new *E-J* formulation leading to a more elegant and precise procedure of solving the governing equations is derived. It is shown that in the two-dimensional case under the same assumptions, a simple numerical network model (employing Kirchhoff's instead of Maxwell's equations) can be used with equally good result. Using the network model the total, magnetisation and transport currents and the losses are calculated and the corresponding loss electric fields are derived hence resulting in the voltage-current curves. The model is verified with the experimental data obtained for relevant Bi-2223 tapes. Using the network model an error is eliminated from the measured direct voltage-current curves due to so-called self-field effect on the critical current.

In Chapter 4 the essentials of superconducting power coils are presented using a 1-MVA resonator coil operated in liquid nitrogen as an example. Arrangement, techniques and manufacturing of the prototype coil (with considerable effort from the Dutch industry) are described. The optimisation of coil design has led to a circular coil that consists of four long and thin concentric solenoids with a large diameter. The radial component of the magnetic field (to which Bi-2223 tapes are most sensitive) is suppressed by small iron pieces applied around the coil edges. The effect is studied both analytically and numerically; the results contributed to the coil design and are validated experimentally. For several magnetic configurations of the coil the direct and alternating voltage-current curves are calculated numerically and measured. Finally numerical estimates, their experimental verification and the results for the 1-MVA coil operated at 64 and 77 K are presented and discussed.

In Chapter 5 conventional and high-T_c superconducting power transformers are compared and the viability of a superconducting transformer is dealt with from economical and technical points of view. For a power transformer, the technical and economical parameters are linked closely due to the fact that copper transformers have been produced for almost a century now and have reached physical and technological limits in many aspects. The crucial question for future applications: "at which cost-effective conditions can the overall efficiency of a high-T_c transformer be made higher than that of a conventional one?" is discussed and answered in the chapter. Total, energy and capital costs of a model superconducting and a copper transformer rated at 30-MVA are compared. The energy costs of a high-T_c transformer are lower than of conventional transformer. The other costs are driven mostly by the superconductor specific cost (usually expressed in US $/kA/m). For a 30-MVA high-T_c transformer competitive total and capital costs are expected at 50 and 25 US $/kA/m respectively. Other less important issues are briefly discussed.

The thesis is completed with the conclusions (Chapter 6) followed by the list of symbols, references, appendices, summary and acknowledgements.

Chapter 2

TECHNICAL SUPERCONDUCTORS

This chapter gives an overview of the basic properties of practical high-T_c superconductors - namely Bi-2223/Ag tapes. The accent is on the constitutive equation that links electric field and current density (Ohm's law). A method to present measured direct V-I curves of superconductors in a compact form is discussed and applied to compose the input files of the numerical model. The effect of magnetic field magnitude and direction on the critical current is studied. As a result, an accurate scaling relation is derived. Available superconductors are usually bare tapes without electric insulation. For application in power circuits heavy-duty electric insulation is required. A new method to insulate high-T_c tapes is described. The method is successfully applied to insulate the tapes for constructing a unique 1-MVA superconducting coil operated in liquid nitrogen.

2.1 Introduction

A representative composite high-T_c tape shown schematically and for real in Figures 2.1 and 2.2, respectively, consists of many non-twisted superconductor filaments embedded in an Ag-matrix forming the multifilamentary core. An Ag or Ag-alloy sheath surrounds the core. Thin stainless strips soldered to both wide faces on top of the Ag-sheath (or alternatively, the Ag-alloy sheath) improve the mechanical properties of a tape. When operated in a device, the tape usually carries a current and is exposed to magnetic field, which may have arbitrary direction with respect to the tape surface.

The mutual orientations of the tape, co-ordinate system, current through arbitrary line along the tape (indicated by the density J_z) and magnetic field are shown in Figure 2.1. The tape length l, thickness $2b$ and width $2a$ are in z, y and x –directions respectively. The subscripts c, t and i in the figure refer to the filamentary core, bare tape and insulation respectively. In this study a long tape is assumed and for this reason only the case of a current parallel to the z – axis (along the tape) and magnetic field perpendicular to the current ($B_z \equiv 0$) is considered. Hence, the electric fields and currents due to the magnetic field change or of the transport source are parallel to the z – axis and the entry effects (re-distribution of the current at the tape ends) are excluded.

For power devices such as AC coils a good electrical insulation of the bare tape is required. The cross-section of an insulated Bi-2223/Ag/Ag tape is displayed in Figures 2.2 and 2.3. Starting from the outside, the film insulation, the Ag-sheath reinforced with stainless strips and the Bi-2223/Ag multi-filamentary core can be recognised.

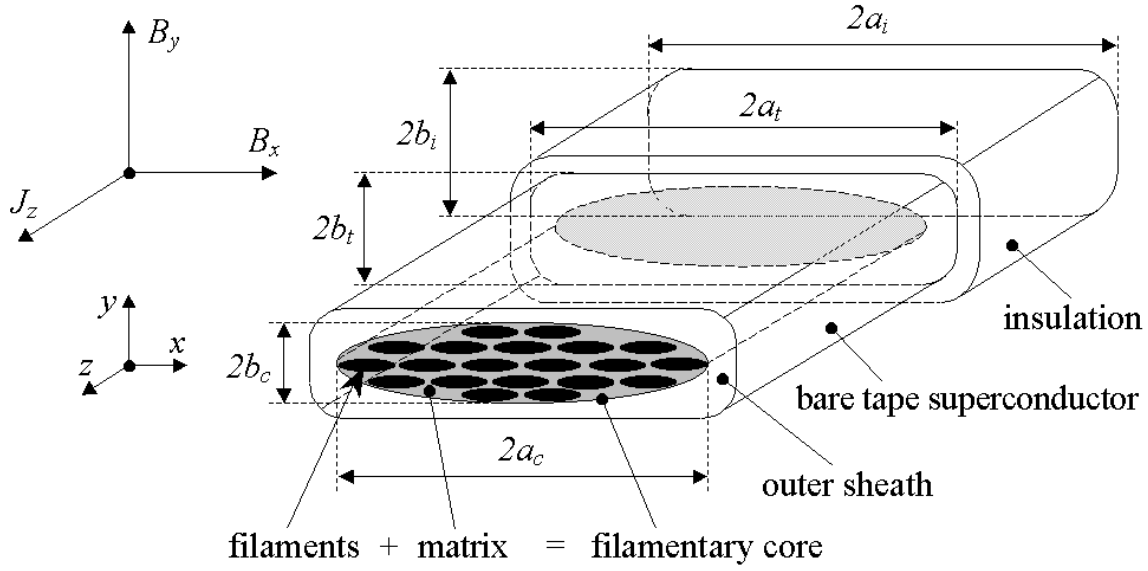

Figure 2.1 Layout of a composite Bi-2223/Ag/AgX tape superconductor comprising filaments, matrix, outer sheath and insulation.

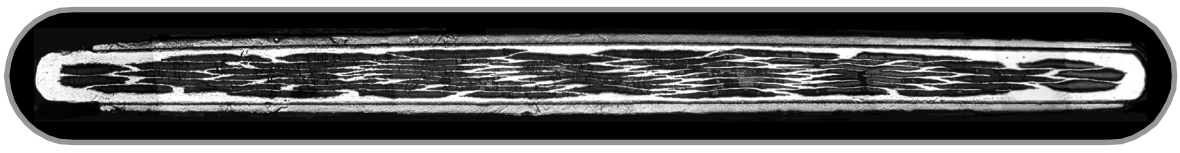

Figure 2.2 Cross-section of an insulated Bi-2223/Ag/Ag tape with well-aligned filaments.

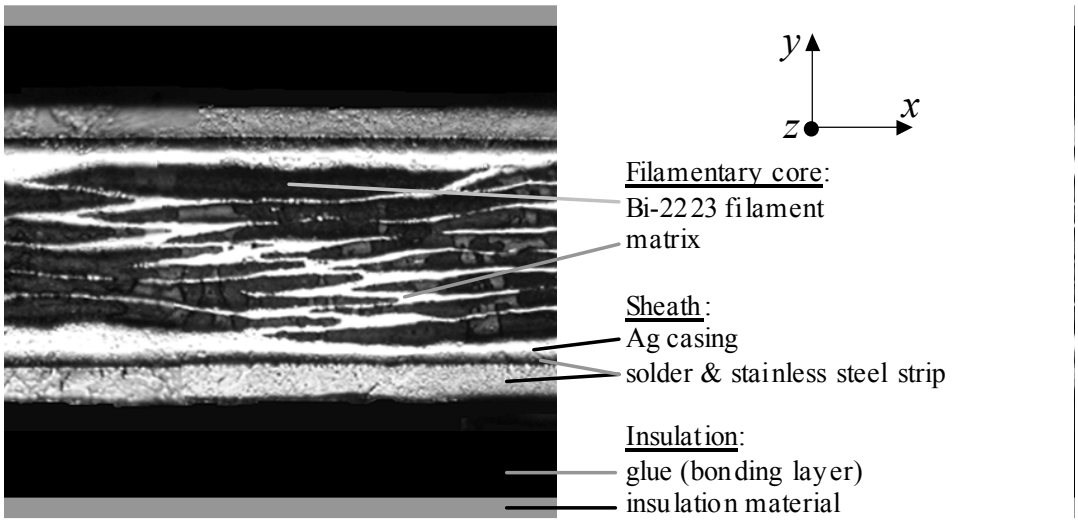

Figure 2.3 Zoom in the cross-section of an insulated Bi-2223/Ag/Ag tape (fragment).

A comprehensive overview of high-T_c tapes is given in [Vase00]. High-T_c tapes are commonly made using the powder-in-tube technique (PIT). Companies like American Superconductor Corporation [Amer01] and Intermagnetics General Corporation [Inte01] in USA, Sumitomo Electric Industries in Japan [Kane99], Vacuumschmeltze [Vacu01] and Nordic Superconductor Technologies [Nord01] in Europe are involved in the manufacturing of practical superconductors of sufficient quality and quantity.

At a glance, the manufacturing includes the following steps. A Bi-2212 powder (of precursor grains) is put in a silver tube, mechanically deformed and heat-treated in oxygen atmosphere until a round multifilamentary $(Bi, Pb)_2Sr_2Ca_2Cu_3O_x$/Ag wire is obtained. The wire is rolled into a flat tape in order to texture the grains and to enable bending of the brittle composite conductor over smaller radius. Further thermo-mechanical cycles form the right superconducting phase (Bi-2223), heal cracks, increase the compaction and improve connectivity between individual grains. Typical dimensions of Bi-2223 flake-like grains in a polycrystalline filament are $10\ \mu m \times 10\ \mu m \times 1\ \mu m$ [Paas98a], [Tan01]. Silver matrix is chosen for chemical reasons as silver does not react with the filament material and allows penetration of the oxygen during the heat treatment procedure, which is essential for controlling the conduction properties.

2.2 Essential properties of Bi-2223 tape

Typical specifications of past, present and future Bi-2223 tapes are summarised in Table 2.1, the numbers are based on [Vase00] and personal assessment of the author. The spread in bare tape outer dimensions and critical current along the tape length is kept now within a few percent and the surface quality is improving. Gas bubbles (blisters) in tapes due to the heat treatment have become history during the last few years. However, the microstructure of a tape such as shape, dimensions and alignment of Bi-2223 filaments and grains along the tape length are still to be improved. Photographs of tape transverse and longitudinal sections show that often the filaments wobble [Vase00], brake or merge [Oome00a] i.e. see Figures 2.3 and 2.6. A relative variation in thickness of the filaments along the tape length (called sausaging) is frequently observed (~ 10 %) and it possibly affects the filling factor, see Equation 2.3. The effective grain misalignment angle (with respect to the tape wide face) estimated from transport measurements and x-ray diffraction measurements is between 5 and 10º. Connectivity of the grains could also be improved by their better alignment and control of the grain boundaries.

Table 2.1 Typical specifications of Bi-2223/Ag/AgX tapes.

Parameter \ Year	1999 (past)	2002 (present)	2005 (future)
Geometry:			
Width, [mm] (std. dev, %)	2.5 to 3.5 (10)	2.5 to 4.5 (2)	2.5 to 4.5 (< 2)
Thickness, [mm] (std. dev, %)	0.15 to 0.3 (10)	0.15 to 0.3 (5)	0.15 to 0.5 (2)
Unit length, [m]	1 to 50	200 to 1000	200 to 1000
Surface quality	insufficient	fair	good
Distance between two blisters, [m]	1 to 10	100 to 300	200 to 1000
Sc/total filling factor γ_{st}	0.15 to 0.26	0.2 to 0.4	0.25 to 0.5
Superconductor properties:			
Material	Bi-2223	Bi-2223	Bi-2223
I_c, [A] at 77 K, self-field	10 to 35	35 to 130	50 to 150
n at 77 K, self-field	12 to 15	15 to 20	20 to 25
Std. dev. of I_{c0}, [%] within batch	3 to 5	2 to 3	1 to 3
Std. dev. of I_{c0}, [%] batch to batch	-	6	5
Misalignment angle α_0, [°]	8 to 15	7 to 10	5 to 8
Critical temperature T_c, [K]	110	110	110
Matrix/Sheath properties:			
Material	Ag/Ag	Ag/Ag or Ag/Ag-alloy	Ag/Ag or Ag/Ag-alloy
Resistivity ρ_{md}, [nΩm] at 77 K	2.8 to 4.5	2.8 or 40	2.8 or 40
Composite properties:			
Critical stress, [MPa]	30 to 40	30 to 270	30 to 300
Critical strain, [%]	0.15 to 0.20	0.15 to 0.40	0.15 to 0.40
AC loss voltage*, [mV_{rms}/m]	same as copper	Table 5.4	Table 5.4
Filament twist pitch, [mm]	non-twisted	< 5	< 3
Turn-to-turn insulation available [kV]	no	yes (0.3 to 2)	yes (0.1 to 5)
Production length, [km/year]	5 to 50	500 to 1000	> 10^4
Price-performance at 77 K and self-field condition, [US \$ kA^{-1} m^{-1}]	> 1000	500 to 200	100 to 25

* including the cooling penalty, see section 5.1.5.

The strain at which intergrain cracking starts in the Bi-2223 filaments is around 0.2 %. For a multi-filamentary Bi-2223/Ag/Ag tape an axial tensile stress of 30 MPa or strain of 0.05 % may reduce the critical current by 5 % and so would a transversal compressive stress of 10 MPa [Vase00]. Bending a tape over the wide side with a radius of 35 mm or 110 mm respectively in the same or opposite direction (as on the delivery reel) will decrease the critical current by less than 20 %. Bending a tape over the narrow side with a radius of 500 mm will decrease the critical current by less than 30 % [Vacu01]. Proper reinforcement of the tapes can improve these figures. For example, in a Bi-2223/Ag/Ag tape reinforced with two 35-μm thick stainless steel strips (so-called 3-ply tape, see Figures 2.2 and 2.3) axial tensile stress of 265 MPa or strain of 0.4 % may reduce the critical current by 5 %. So does the transverse compressive stress of 20 MPa or bending the tape over the wide side on a radius of 35 mm in the same direction as on the delivery reel [Amer01]. Clearly, a Bi-2223 tape needs to be handled with care in order to avoid a reduction of the critical current.

A mismatch in the thermal contraction of a Bi-2223 tape and a holder can cause a thermo-mechanical stress and a reduction of the critical current after cool-down. The thermal contraction coefficient of a representative Bi-2223/Ag tape after 1-st (and successive) cool-down(s) from room temperature to 100 and to 50 K are respectively: -0.17 % (-0.25 %) and

Table 2.2 Specifications of multifilament Bi-2223/Ag tapes used in this study.

Parameter \ Sample label	A	V	Sm [Kane99]	Sh
Width × thickness, [mm^2]:				
- when insulated with polyimide	4.3 × 0.46	4.0 × 0.4	-	-
- outer Ag sheath	4.1 × 0.21	3.9 × 0.26	3.3× 0.22	2.9 × 0.2
- filamentary core	3.9 × 0.15	3.47 × 0.15	-	2.6 × 0.15
Number of sc. filaments	55	55	61	55
Sc/total filling factor γ_{st}	0.40	0.26	0.28	0.26
Sc/core filling factor γ_{sf}	0.57	0.52	-	0.39
I_c, [A] at 77 K, self-field	116 ± 15	55 ± 10	37	21 ± 1
n at 77 K, self-field	18.5 ± 0.5	17.5 ± 1.5	-	19.5 ± 1.5
Field dependence of I_c at 77 K	Figs. 2.13, 2.14	Figs. 2.11, 2.12	[Kane99]	[Shev98]
Temperature dependence of I_c	Figure 2.19	[Vacu01]	[Kane99]	-
Ag-sheath re-enforcement	yes	no	no	no

-0.20 % (-0.27 %) [Vacu01]. The stress due to cooling can be minimised by winding Bi-2223 tapes on a glass-fibre reinforced plastic (such as G-10) holder as G-10 in the warp direction of the fibres has matching values of the thermal contraction. At 60 to 80 K the thermal conductivity of composite Bi-2223/Ag/Ag tape, and insulation KAPTON are: about 500 [Vase00] and 0.2 [Yoko95] W $m^{-1}K^{-1}$; of the epoxy: filled (STYCAST-2850 FT) and unfilled about 10 [Muld88] and 0.2 [Iwas94] W $m^{-1}K^{-1}$; of the glass-fibre reinforced epoxy composite both parallel and perpendicular to the fibres: about 0.3 W $m^{-1}K^{-1}$ [Radc82] respectively.

The silver matrix defines the normal state resistivity of the composite tape, which is typically between 3 and 5 nΩm at 80 K and between 15 and 25 nΩm at 300 K [Naka96], [Vase00]. For Ag-(Au, Mg, Pd) alloys the resistivity is in the range of 6 to 65 nΩm at 80 K. The normal state resistivity of stainless steel is about 0.5 μΩm; of Bi-2223 at 120 K it is even higher, ranging from 1.5 to 8 μΩm [Vase00]. Mechanical (handling) parameters of tapes are usually given at room temperature. Most of the present long tapes have non-twisted filaments. Comparing past, present and future Bi-2223/Ag/AgX tapes as listed in Table 2.1 and displayed in Figure 5.3 one may conclude that various tape parameters are rapidly improving, while others still are to be improved. Specifications of four commercially available Bi-2223 tapes are shown in Table 2.2. Tapes A, V and Sh are used in this study as samples and for constructing coils, tape Sm is studied in [Kane99], [Funa01] and used here as a reference.

A schematic drawing of a sample is shown in Figure 2.4. A short piece of the conductor tape is mounted on a strip of glass-fibre reinforced epoxy (G-10 or G-11) with the glass fibres oriented along the tape in order to match the thermal contraction. Direct contact of liquid nitrogen and a bare high-T_c tape may cause a degradation of the critical current after few cool-downs and is not recommended by the tape vendors. The contact is prevented by covering most of the sample tape length (except the current contact areas) with epoxy or with clear shrink tube (the latter case is shown in the figure). Both covers effectively prevent the contact between liquid nitrogen and the tape and show comparable effect on the critical current (both the absolute value of the current and reproducibility after successive cool-downs). The distance between the voltage contacts l_v of 50 to 100 mm leaves sufficient length for the entry zone and for the current contacts of every sample (about 30 and 10 mm respectively on each side of the sample).

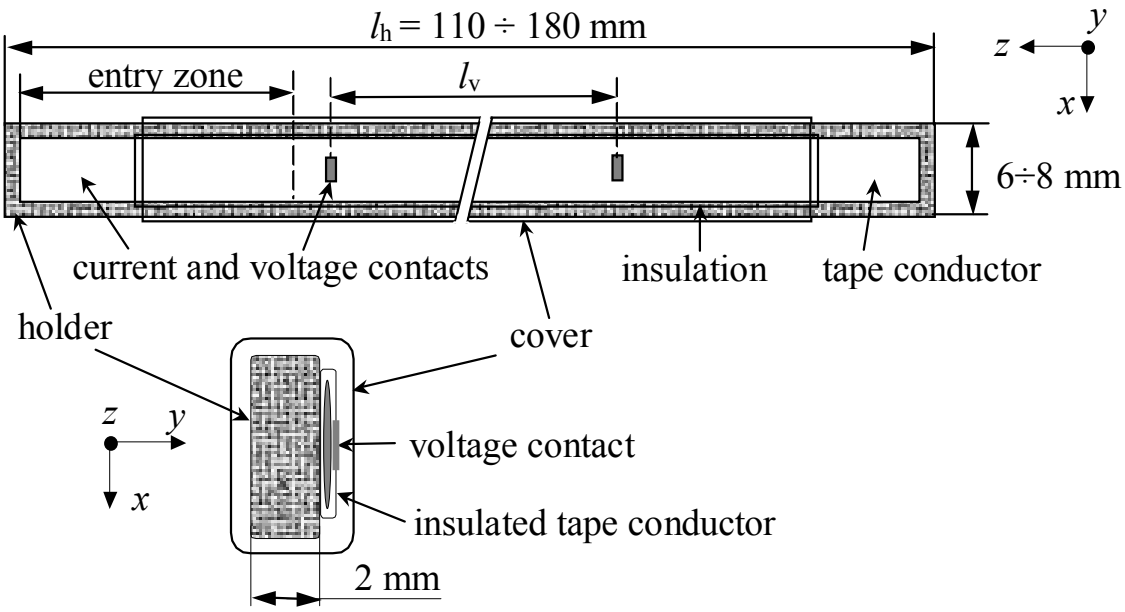

Figure 2.4 Layout of a sample high-T_c tape equipped with current and voltage contacts (the cross-section is also shown).

2.3 Constitutive equations

The relation between magnetic field strength H and induction B is:

$$\boldsymbol{B} = \mu \cdot \boldsymbol{H}\,, \qquad \textit{Eq. 2.1}$$

where $\mu = \mu_r \mu_0$ and μ_r are the absolute and relative permeability of the medium respectively, and $\mu_0 = 4\pi \cdot 10^{-7}$, [H/m] is the absolute permeability of vacuum. For high-T_c tapes (as well as for low-T_c superconductors) the assumption $\mu_r = 1$ is generally accepted for modelling, see for example [Bran96], [Amem98], [Paas98a], [Rhyn98], [Yaza98] and [Nibb99]. The same assumption is used in this study. The relation between direct electric field strength E_ρ and direct current density J is known as Ohm's law:

$$\boldsymbol{E}_\rho = \rho \cdot \boldsymbol{J}\,, \qquad \textit{Eq. 2.2}$$

where E_ρ is the resistive (drain) electric field and ρ the specific resistivity of a conductor. The resistivity ρ depends on current density, magnetic field, temperature, strain and conductor arrangement.

2.4 Resistivity and critical current of a Bi-2223 tape

A Bi-2223 tape is a composite of superconducting filaments embedded in a matrix of normal conducting metal as depicted in Figure 2.1. The volumetric content of a superconductor is usually defined by a filling factor γ, the ratio of the section of sc. filaments $S_s = \gamma \cdot S$ and the total cross-section of the bare tape defined by the outer dimensions $S = S_s + S_m$. Consequently the cross-section of the matrix is $S_m = (1-\gamma) \cdot S$. Assuming that the transport current I_{tr} is shared between the superconducting filaments and the matrix and zero contact resistance at the filament- matrix interface, the static longitudinal specific resistivity of such a tape is:

$$\rho = \frac{\rho_m \cdot \rho_s}{\gamma\rho_m + (1-\gamma)\rho_s}. \qquad \textit{Eq. 2.3}$$

The specific resistivity ρ_m of silver in a tape at 77 K is about 3 to 4 nΩm, while the effective resistivity of the superconductor itself ρ_s when being in the superconducting state is mush lower and in the normal metal state is much higher [Vase00]. The *E-I* relation and consequently the resistivity of a practical superconductor is usually described by the so-called Power Law:

$$E = E_c\left(\frac{I}{I_c}\right)^n \text{ or } \rho_s = \frac{E_c \cdot S_s}{I_c}\left(\frac{I}{I_c}\right)^{n-1}, \qquad \textit{Eq. 2.4}$$

where E_c is the electric field criterion (usually equal to 10^{-4} V/m), I_c is the critical current and n is the power index. At a glance, the critical current defines the transition between superconducting and normal metal states and the power index reflects the steepness of the transition. Both I_c and n are magnetic field, temperature and strain dependent.

The strain dependence is briefly discussed in section 2.2; the dependence on magnetic field and temperature is treated in sections 2.4.1 - 2.4.3. The current through a filament creates its own magnetic field (or self-field). The self-field adds to the external magnetic field when present and causes a change of resistivity of the neighbouring filaments, see Equation 2.4. Typical *E-I* curves of samples A and V in Table 2.2 calculated from Equations 2.2-2.4 at constant temperature and in self-field are depicted in Figure 2.5. The inset shows the low electric field region of the *E-I* curves indicated by the dashed box in the figure.

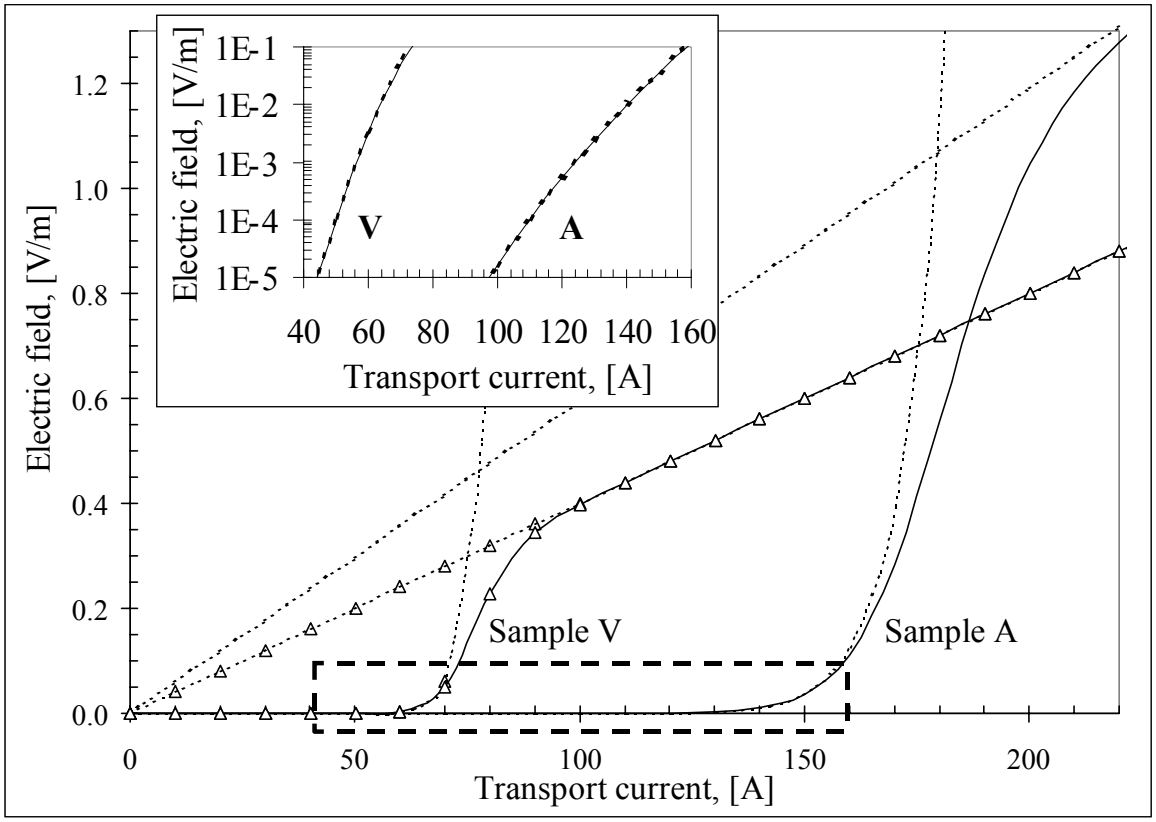

Figure 2.5 Direct E-I curves of Bi-2223/Ag tape samples V and A at 77K.

The dashed lines are representing the superconductor (Equation 2.4) and the matrix; the solid lines are for the Bi-2223/Ag composite, Equations 2.2 and 2.3. When an external magnetic field or a temperature increase is applied, both the critical current and the power index are reduced so that the *E-I* curve of the composite shifts to the left and becomes less steep, see Figure 2.5 and Equation 2.4. It is seen from the inset in the figure that for $E \leq 10^{-2}$ V/m the current through the matrix can be neglected, for this reason Equation 2.4 is often used instead of Equation 2.3. However, in coils the peak operating current may exceed the critical current and hence Equation 2.3 is used in the numerical model described in Chapter 3. When the electric field exceeds 0.1 V/m the condition of constant temperature is increasingly difficult to fulfil and the *E-I* curve starts to be affected by the cooling conditions.

Most of the available long tapes and all tapes of this study have non-twisted filaments which are well coupled magnetically. Instead of treating separately the filaments and the matrix, the uniform filamentary core with the equivalent dimensions and (anisotropic) resistivity given by Equation 2.3 is assumed further on. The anisotropy is explained in section 2.4.1. Hence the anisotropic continuum model [Paas98] is applied to the filamentary core. Thus the model composite tape has the uniform filamentary core covered by the normal metal sheath. Furthermore, contact resistances between the core and the sheath are neglected. An example cross-section of such a model tape with an elliptical filamentary core and rectangular sheath (with rounded corners with radius r_t of about 80 μm) is shown in Figure 2.6b, the details of the core interior arrangement (such as in Figure 2.6c) are neglected. In the following sections the influence of magnetic field and temperature on the resistivity of Bi-2223 tapes is considered.

The expected maximum of the magnetic field in the windings of a 1-MVA coil is about 0.3 T as it is explained in Chapter 4. In transformers the operating magnetic field is also limited due to the losses. The expected operating temperature range is from 64 to 77 K. At a lower or a higher temperature liquid nitrogen is more difficult to use and the complexity of the cooling system increases.

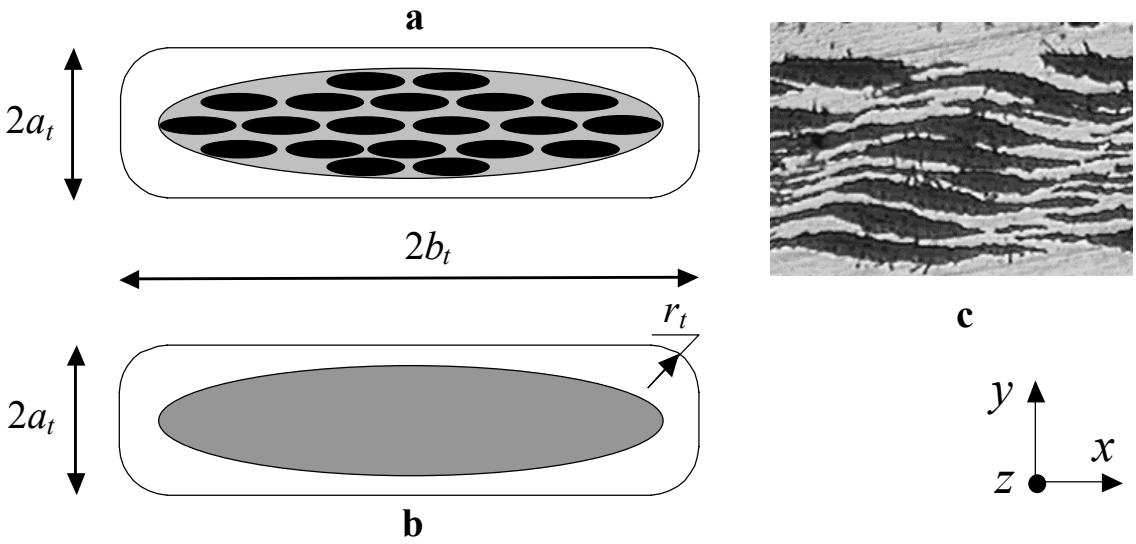

Figure 2.6 Equivalent multi- (a, c) and mono- (b) filamentary cores of bare high-T_c tape with non-twisted filaments.

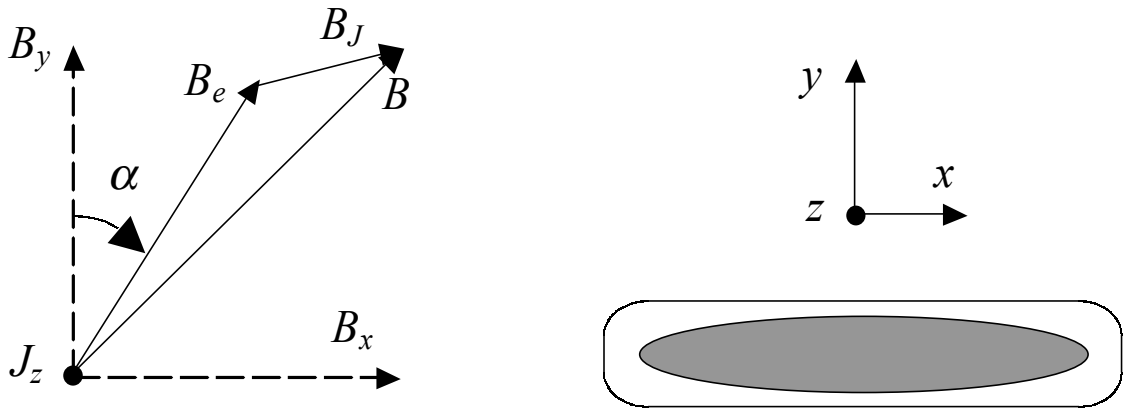

*Figure 2.7 Total, self- and external magnetic field (*B, B_J *and* B_e *respectively) inside a high-*T_c *tape.*

2.4.1 Influence of an external direct magnetic field

The mutual orientation of the tape, co-ordinate system, current through the tape (indicated by the density $\boldsymbol{J}_z$ at a point inside the cross-section) and magnetic field are shown in Figures 2.1 and 2.7. The *y*-axis is always normal to the tape wide face. At any point inside the tape cross-section the vector of magnetic field *B* is the sum of the external magnetic field B_e and of the self-field B_J, see Figure 2.7. The field B_e is due to the external currents (flowing outside the tape and coupled to the current in the tape). The field B_J is due to the internal currents (all line currents inside the tape coupled to the current flowing through the considered point) and it depends on the current distribution inside the tape. The angle $\alpha(\boldsymbol{B}_y, \boldsymbol{B}_e) = \text{atan}\,(B_{ex} / B_{ey})$ between the *y*-axis and the vector $\boldsymbol{B}_e$ is referred to as the direction angle of the external magnetic field.

The self-field adds to the external field and creates an uncertainty, as the current distribution inside the tape (and hence B_J) usually is not known during the *E-I* measurement. For instance, when the external field B_e is uniform, the field *B* depending on the current flowing through the tape can be substantially non-uniform. At constant temperature and strain both the value *B* and the direction of the magnetic field vector *B* affect the *E-I* curve. Furthermore, the self-field B_J affects the critical current and the power index [Garb89] and [Spre99]. Hence, the field B_J and the current distribution inside the tape are mutually dependent. The effect is treated in Chapter 3, as the treatment requires the numerical model.

Often the filaments (and therefore the grains) are not well aligned with respect to the *y*-axis, which creates an additional uncertainty. The photo in Figure 2.6c is a typical detail of the transversal cross-section of a tape displaying wobbled, broken and merged Bi-2223 filaments with the interfilament growth (the filaments are shown in black and the matrix in grey, the boundaries of the photo are parallel to the *x*- and *y*-axes). A similar (less expressed) picture can be seen in Figures 2.2 and 2.3. Characteristic *E-I* curves for sample V are displayed in Figures 2.8 and 2.9 for $\alpha = 0°$ and 90° respectively. The dots are measured and the lines are guide for the eye. In the figures the magnetic field amplitude is kept constant for each curve. It is seen that magnetic field of the same magnitude when applied perpendicular to the tape wide face ($\alpha = 0°$) causes a much larger reduction of the critical current as compared to the case when the field is parallel ($\alpha = 90°$).

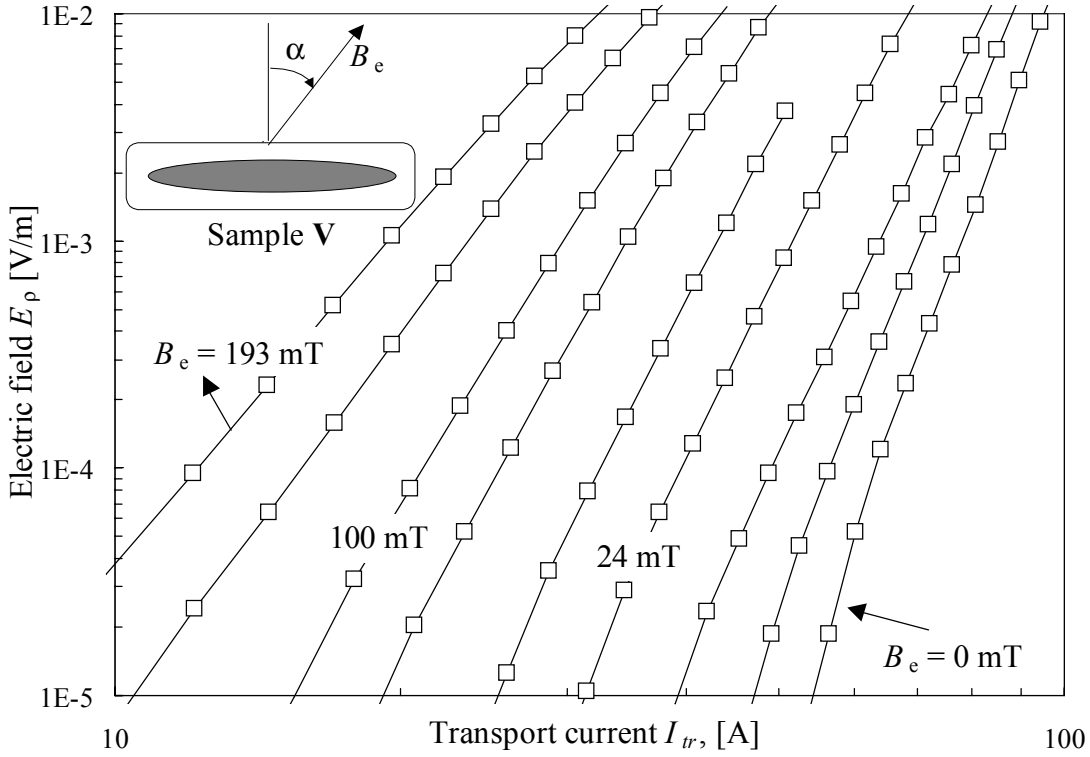

Figure 2.8 Direct E-I curves of the Bi-2223/Ag tape at 77 K, $\alpha = 0°$ and $B_e = 0$; 9; 14; 24; 39; 70; 100; 150 and 193 mT respectively.

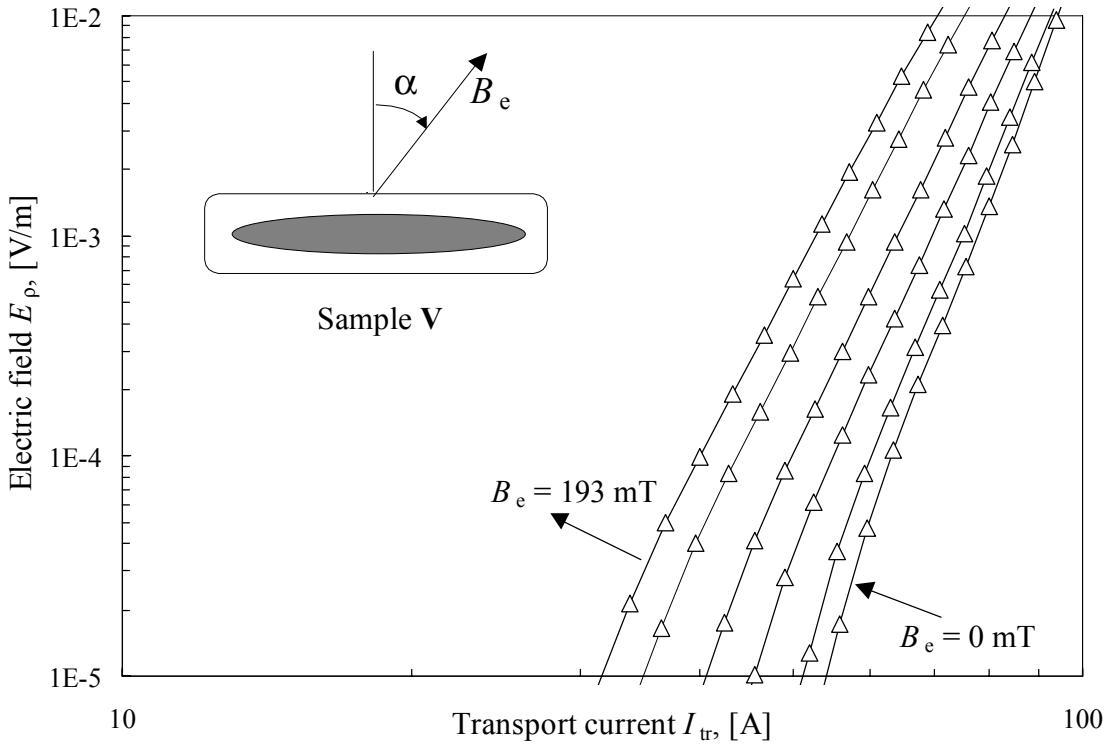

Figure 2.9 Direct E-I curves of the Bi-2223/Ag tape at 77 K, $\alpha = 90°$ and $B_e = 0$; 39; 70; 100; 150 and 193 mT respectively.

It is thus clear that both magnitude and direction of magnetic field affect the *E-I* curves of Bi-2223 tapes and a systematic study of the effect is required for a complete characterization. A similar effect is observed for all Bi-2223 tapes and in particular for those listed in Table 2.2. Using the power law expressed by Equation 2.4, one may analyse the influence of the direction and the magnitude of magnetic field on the critical current and the power index.

2.4.1.1 Effect of the field direction and magnitude

Due to different dimensions and internal filament arrangements of the tapes, the dependence of the critical current and the power index on magnetic field is somewhat different, though the qualitative behaviour is the same. For this reason each Bi-2223/Ag tape has a unique *E-I* curve. A typical dependence of the critical current on magnetic field (in presence of the self-filed) is shown in Figure 2.10. The boxes represent the measured points and the lines are calculated using Equation 2.5 as it is explained below. For each set of dots and the corresponding line, the field magnitude B_e is varied and the angle α is kept constant. At the same conditions, similar sets of dots and lines are obtained for the magnetic field dependence of the power index *n*.

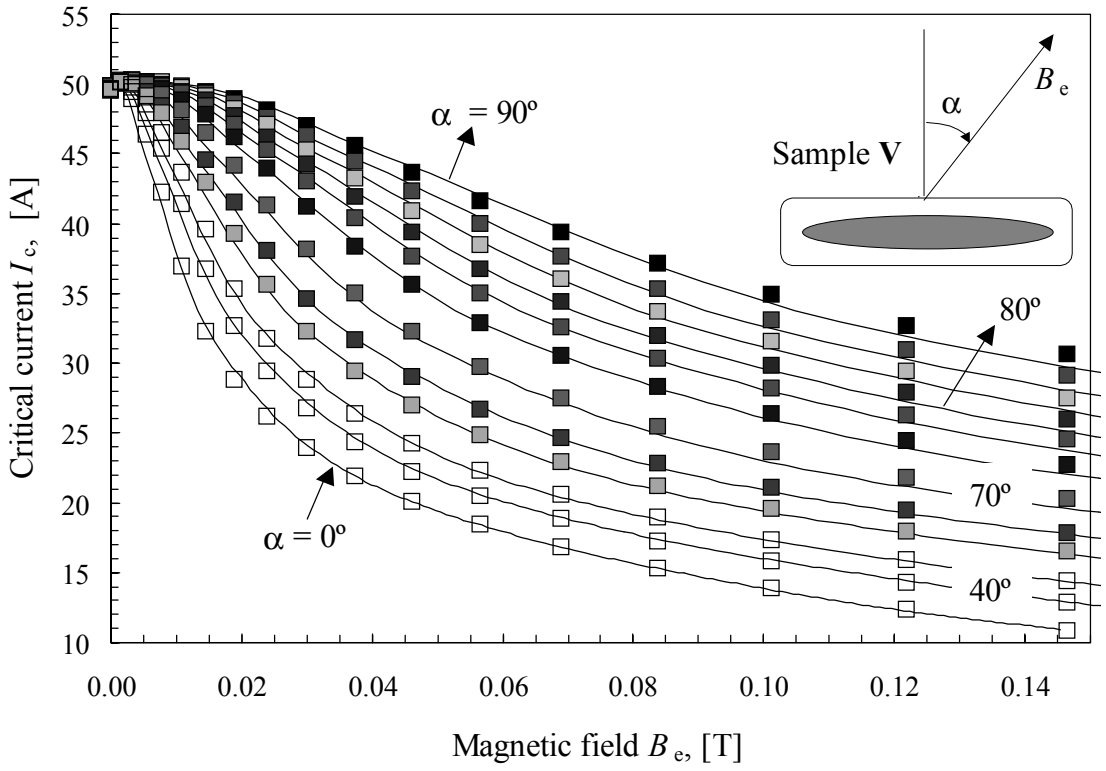

Figure 2.10 Critical current of the Bi-2223/Ag tape versus magnetic field amplitude B_e at 77 K for different angles α = 0°; 40; 50; 60; 65; 70; 75; 77.5; 80; 82.5; 85 and 90° respectively.

The angle dependence of both the critical current and the power index is accounted for by assuming that there is a field error due to misaligned grains inside a tape. Texturing of Bi-2223 is not perfect and with a certain distribution grains are misaligned with respect to the tape wide face [Vase00]. Thus the magnetic field seen locally by a grain has a different angle than α, the difference is referred to as the misalignment angle, see Table 2.1. The error due to the misalignment angle is accounted for by correcting the external magnetic field magnitude with an empirical factor f_α [Shev98] and [Shev99]:

$$B^* = B_e \cdot f_\alpha \,. \qquad \textit{Eq. 2.5}$$

The critical current and the power index as functions of the characteristic magnetic field B^* are shown in Figures 2.11 and 2.12 for the same sample. The inset in Figure 2.12 shows the dependence of the factor f_α on the angle α. Angle dependence of both the critical current and the exponent n can indeed be described by a single factor f_α, which depends on the direction of the magnetic field (angle α) and is independent from the field magnitude. The symbols represent the measured data and the three solid lines in the figures represent the data derived with a cubic spline interpolation, as explained in section 2.5. Using the data, the dependence of the critical current and the power index on magnetic field (B_e and α) is calculated back and compared with the experiment. As it is illustrated in Figure 2.10, the agreement between the experimental and calculated values represented by the dots and the lines respectively, is very good. The standard deviation and the maximum error are within 3 and 5 % respectively.

The measured data for samples A and Sh treated in the same way are presented in Figures 2.13, 2.14 and in [Shev98] respectively. The method offers a compact description for the influence of the magnitude and the direction of the magnetic field on the critical current and the power index at constant temperature. The latter are the key parameters of Equation 2.4. Thus the calculation of direct *E-I* curves (such as in Figures 2.8 and 2.9) and the specific resistivity of a superconductor are possible (by using only the three empirical curves as the source data) and consequently the specific resistivity for a composite tape is defined for an arbitrary magnitude and direction of the magnetic field at constant temperature, using Equation 2.3.

2.4.1.2 Effect of magnetic field and pinning force

Due to a change in transport current or magnetic field, flux lines move in a technical superconductor. The flux lines move in a direction perpendicular to the directions of both the current and magnetic field and cause a loss of energy. The electric field corresponding to the energy loss is parallel to the direction of the transport current. At the critical current, the pinning force is equal to the Lorentz force and the motion is just about to begin. Therefore, the Lorentz force defined at the critical current is a measure for the pinning force. Equation A1.7 contains a classical description of the pinning force (the dependence on both magnetic field and temperature) as proposed by Fietz and Webb for low-T_c superconductors (see for instance [Gode99]).

A practical advantage of considering magnetic field dependence of the pinning force in addition to the critical current is that the former changes less over the full range of magnetic field. A disadvantage is that the description is proven for a high-field region; while for power applications of Bi-2223 tapes often the low-field region is of importance. High- and low-field regions are defined here with respect to the field at which the maximum of the pinning force occurs. The dependencies of the pinning force and of the critical current on magnetic field B^* for sample A are illustrated in Figures 2.15 and 2.16 respectively. Here the same measured data (as plotted in Figure 2.13 with the solid line) are shown as boxes. The open and the filled triangles represent experimental data of [Spre99] for an almost identical sample measured over a wider range of magnetic field with the self-field effect present and suppressed respectively (see section 3.4.1 for further details).

The critical current of the sample (equal to 112 A at $B_e = 0$ and self-field effect present [Spre99]) is multiplied by the factor $126/112$ in order to enable comparison with sample A, see Figure 2.15. Indeed, both samples show then almost identical dependence of the pinning force on magnetic field amplitude when the self–field effect is present. However, two different curves can clearly be observed in the low field region in the cases when the self-field effect is present (solid line) or suppressed (dashed line). As it is expected from Equation A1.7, the pinning force has a maximum F_{mx} at a certain value of the magnetic field B_{mx}^*. In the low field region the presence of the self-field effect makes it more difficult to find a proper scaling factor for the pinning force. At the maximum of the pinning force the self-field effect on the critical current is less pronounced than in the low-field region (as the transport current is far lower). In the high-field region less experimental data are available and the irreversibility effect is more pronounced.

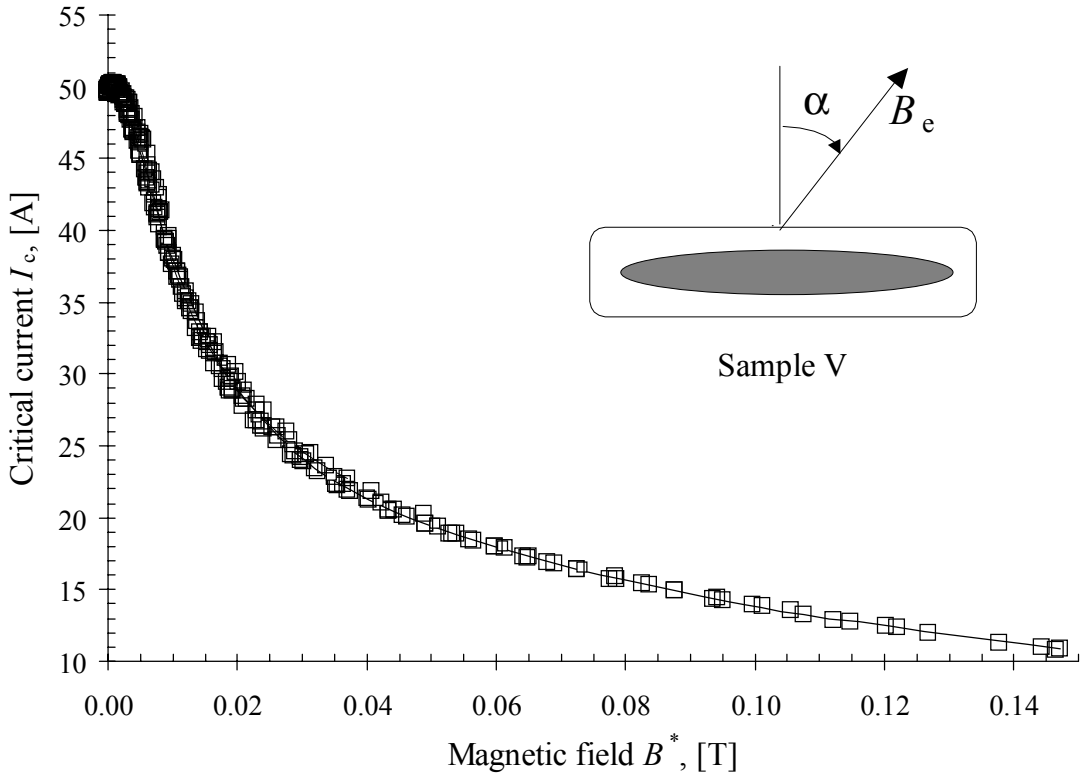

Figure 2.11 Critical current versus magnetic field B^* at 77 K and α = 0°; 40; 50; 60; 65; 70; 75; 77.5; 80; 82.5; 85 and 90°.

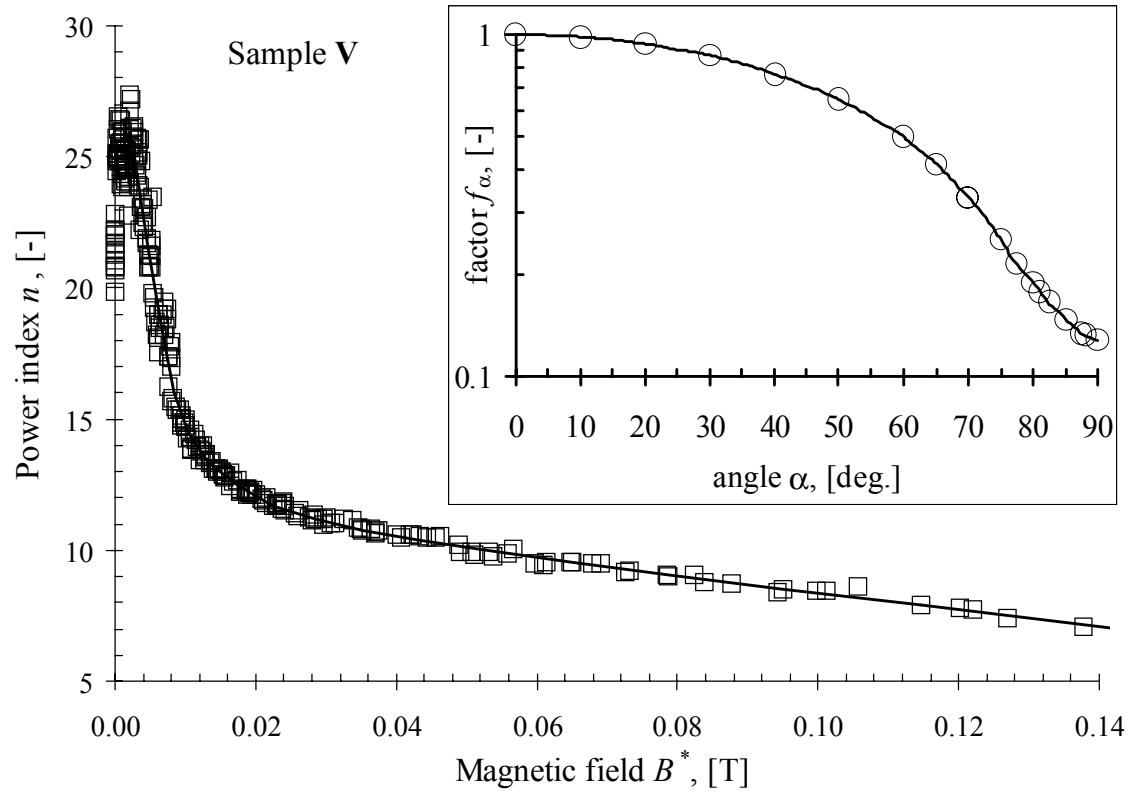

Figure 2.12 Power index versus magnetic field B^* at 77 K and α = 0°; 40; 50; 60; 65; 70; 75; 77.5; 80; 82.5; 85 and 90°.

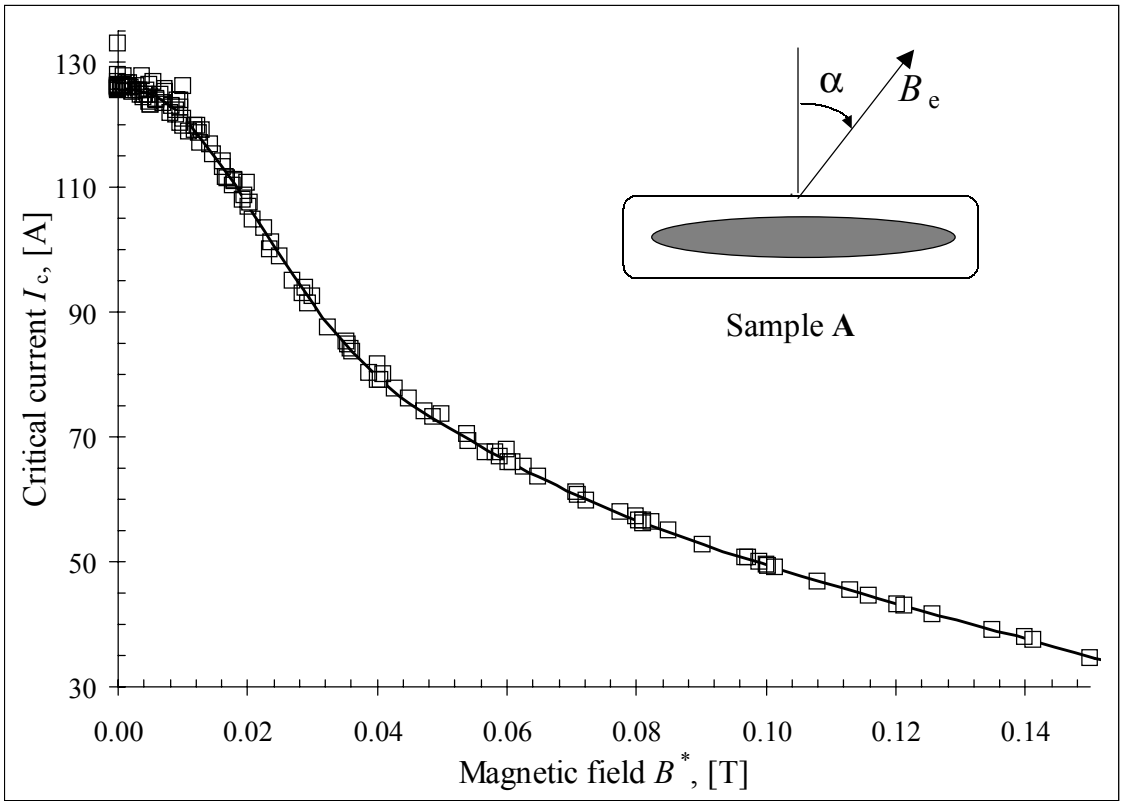

Figure 2.13 Critical current versus magnetic field B^* at 77 K and α = 0°; 9; 18; 27; 36; 45; 54; 63; 72; 77; 81; 85; 87.5 and 90°.

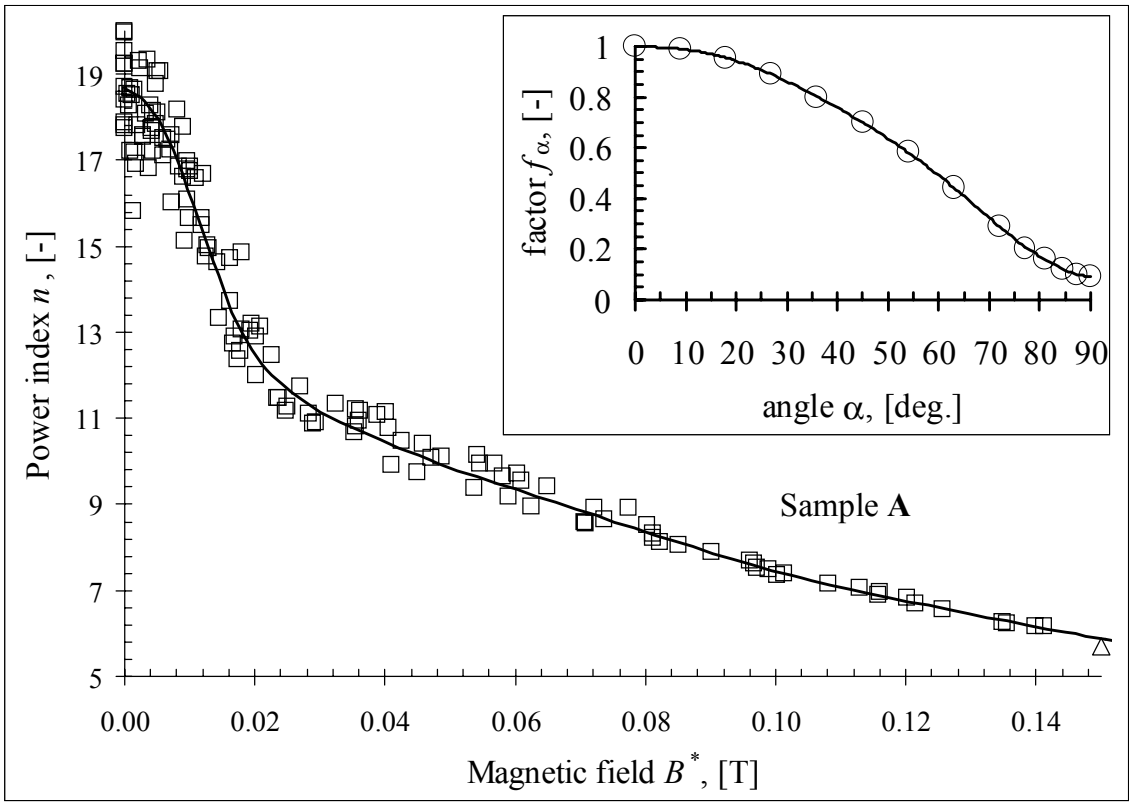

Figure 2.14 Power index versus magnetic field B^* at 77 K and α = 0°; 9; 18; 27; 36; 45; 54; 63; 72; 77; 81; 85; 87.5 and 90°.

For high-T_c superconductors the pinning description has to be modified by introducing the irreversibility field B_{ir} [Fuch95]. The irreversibility field accounts for the dependence of the upper critical magnetic field B_{c2} on the angle α. At the irreversibility field (and $0^\circ \le \alpha < 90^\circ$) the critical current becomes practically zero before the upper critical field B_{c2} (α = 90°) is reached. In order to account for the irreversibility effect on the critical current, Equation A1.7 (Appendix A) is modified by replacing B_{c2} and $b = B/B_{c2}(T)$ with B_{ir} and $b_{ir} = B/B_{ir}(T)$ respectively and the dependencies of the critical current and the pinning force on magnetic field and temperature are found:

$$I_{c,B,T} \cdot B^* = F_{mx} \frac{f_{bir}}{f_{bir,mx}}; \qquad \textit{Eq. 2.6}$$

$$f_{bir} = b_{ir}^p \cdot (1 - b_{ir})^q \text{ and} \qquad \textit{Eq. 2.7}$$

$$b_{ir} = b_{ir}(B^*; T) = \frac{B^*}{B_{ir}^*(T)}, \qquad \textit{Eq. 2.8}$$

where $I_{c,B,T}$ is the magnetic field and temperature dependent critical current; B^* is defined by Equation 2.5; $f_{bir}/f_{bir,mx}$ is the scaled pinning curve; p and q are empirical constants.

At the maximum of the pinning force $df_{bir}/db_{bir} = 0$ and Equation 2.7 leads to [Bott99]:

$$b_{ir} = b_{mx} = (1 + q/p)^{-1}; \qquad \textit{Eq. 2.9}$$

$$f_{bir,mx} = (1 + q/p)^{-p} \cdot (1 + p/q)^{-q}.$$

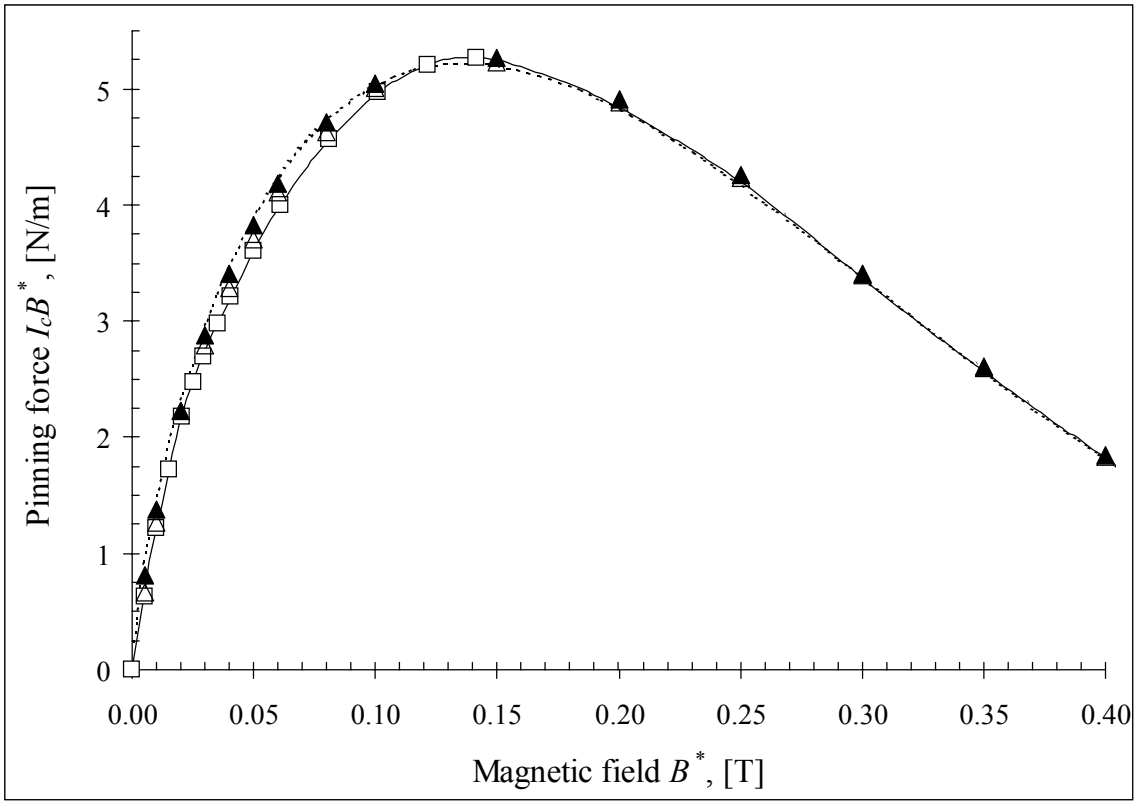

Figure 2.15 Pinning force in samples A versus magnetic field B^* at 77 K and arbitrary α (the symbols are explained in the text, the lines are calculated).

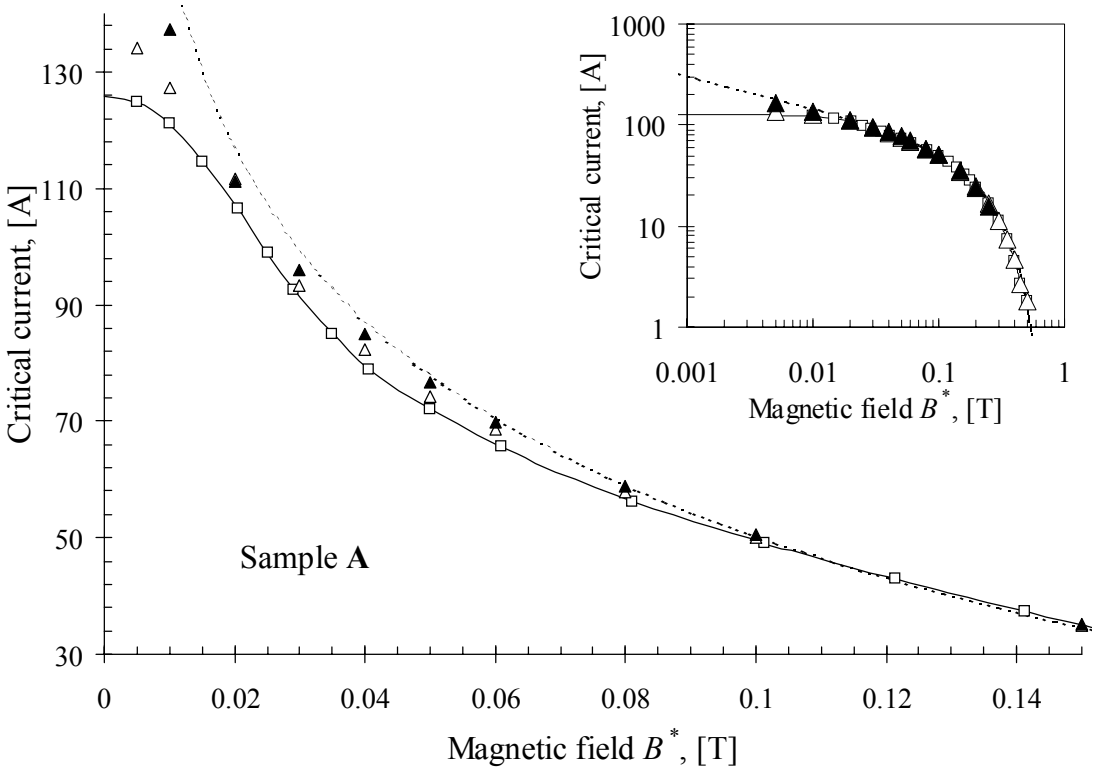

Figure 2.16 Critical current of the Bi-2223/Ag tape versus magnetic field B^* at 77 K and arbitrary α (the symbols are explained in the text, the lines are calculated).

The position of the maximum is given by B^*_{mx} and F_{mx} (or equally by $I_{c,mx}(T)$) that depend on temperature and are defined using Equations 2.6, 2.8 and 2.9:

$$B^*_{mx}(T) = b_{mx} \cdot B^*_{ir}(T) \text{ and} \qquad \textit{Eq. 2.10}$$

$$F_{mx} = F^*_{mx}(T) = I_{c,mx}(T) \cdot B^*_{mx}(T), \qquad \textit{Eq. 2.11}$$

where $I_{c,mx}(T)$ is the critical current at the maximum of the pinning force F_{mx}.

The dashed line in Figure 2.16 is calculated from Equations 2.6 - 2.9 for the case when the self-field is suppressed. The best fit of the line to the experimental data yields the values $p = 0.7$; $q = 2.9$; $B^*_{ir} = 0.7$ T and $I_{c,mx} = 38$ A. When the self-field is present, the pinning curve is too complex to be described by Equation 2.7 and the cubic spline interpolation for f_{bir} is used instead. The result is shown as the solid line in the figure. The calculated (lines) and the measured values (symbols) of the critical current are compared in order to ensure that the accuracy is not lost. The error is within a few percent hence justifying the modification of Equation A1.7. Therefore, the dependence of $I_{c,mx}(T)$ on α is in fact the angle dependence of the magnetic field as determined by Equation 2.5. The inset in Figure 2.16 shows the whole $I_c(B^*)$ curve measured up to 0.5 T.

2.4.2 Scaling relation between critical current and magnetic field

It is clear from Figure 2.16 that the self-field effect is stronger at a lower magnetic field B^* where the critical current is higher. The effect makes accurate scaling of the critical current difficult.

The reason is that the total magnetic field seen by a superconducting filament (or a grain), and hence the error due to the self-field depends on the critical current. The scaling relation between the critical current, magnetic field and temperature for Bi-2223 tapes follows from Equations 2.5 - 2.11:

$$I_{c,B,T} = i \cdot I_{c,mx}(T) \cdot b_{mx} / f_{bir,mx} , \qquad \textit{Eq. 2.12}$$

where $i = f_{bir}/b_{ir} = b_{ir}^{p-1} \cdot (1-b_{ir})^q$ scaled critical current, see Equation 2.7; $b_{mx}/f_{bir,mx}$ is a constant defined by Equations 2.9; $I_{c,mx}(T)$ is described by Equation 2.11, the corresponding values are given in Table 2.3. The available measured data for Bi-2223 tapes, for instance [Amer01] and [Vacu01] are influenced by self-field and possibly by strain (both thermo-mechanical and electro-magnetic), which is a complication when deriving general and accurate scaling relations.

In Figure 2.17 the lack of scaling at a low magnetic field is illustrated using the experimental data (with self-field present) for three samples (for sample A it can also be seen in Figure 2.16). Line 1 is calculated using Equation 2.12: $p = 0.7$; $q = 2.9$; $B_{ir}^* = 0.7$ T and $I_{c,mx} = 38$ A. Line 2 represents the data shown as filled triangles in Figure 2.16 (sample A with the self-field suppressed). The arrow indicates the location of the pinning force maximum. At $b_{ir} > 0.1$ the self-field effect is relatively small and the experimental data with the self-field present can be fitted to the line(s) with relatively small error for all samples.

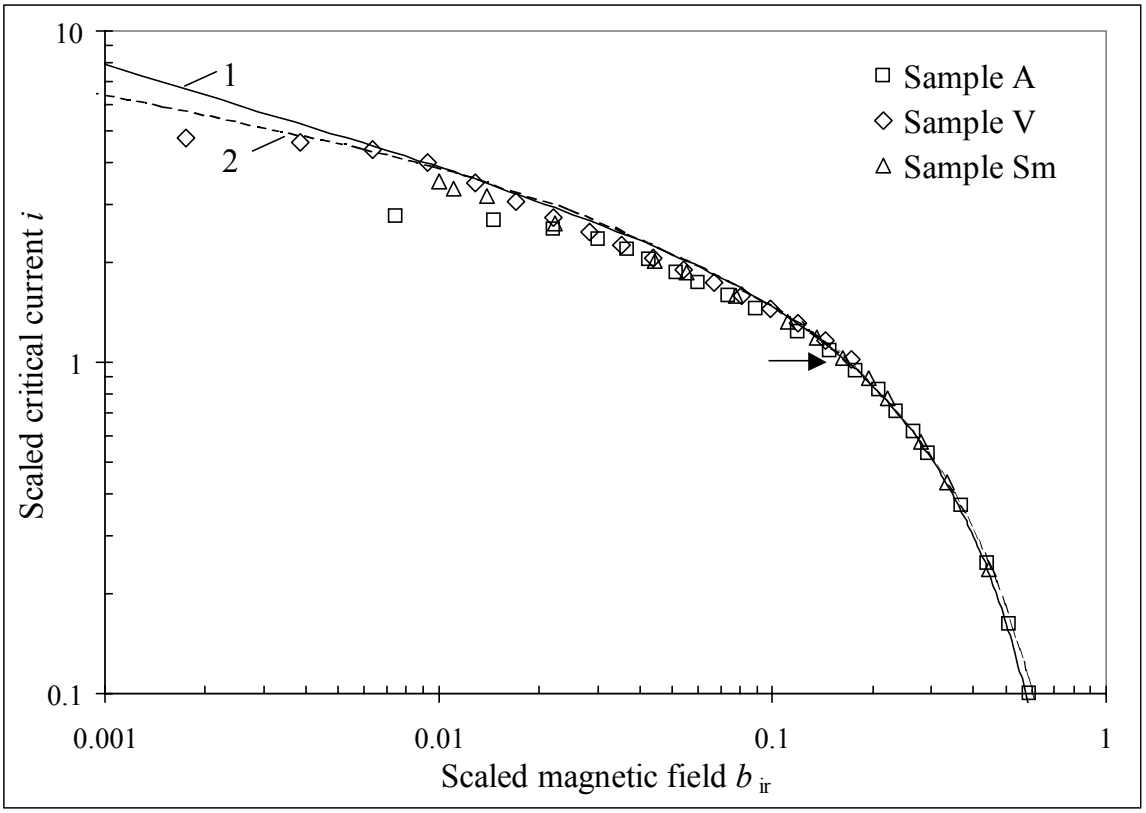

Figure 2.17 Scaled critical current $i = f_{bir}/b_{ir}$ of Bi-2223/Ag tapes versus magnetic field b_{ir} at 77 K, the arrow indicates location of the pinning force maximum, the symbols represent the measured data.

Table 2.3 Values of the scaling parameters for samples A, V and Sm (p= 0.7; q=2.9) at 77 K.

Parameter \ Sample	A_{off}	A_{on}	V	Sm
B_{ir}^{*}, [T]	0.7	0.7	0.9	0.9
$I_{c,mx}$, [A]	38	45	11	11

A_{off} - self-field suppressed; A_{on} self-field present

At $b_{ir} < 0.1$ when moving towards a lower external field the error increases. The critical current of sample A (at zero external field, see Table 2.2) is the highest of all three samples and hence the error due to the self-field is the largest. The scaling parameters for all three samples resulting from the best fit are shown in Table 2.3. For samples V and Sm the data with self-field suppressed are not available and the treatment (as shown in Figure 2.17 for sample A) is not possible. For this reason it is assumed in this study that when the self-field will be completely suppressed in sample V, the data will follow the solid line in Figure 2.17. For numerical modelling the data obtained when the self-field effect is suppressed are most valuable, see section 3.4.1.

In Figure 2.18 a comparison of Equation 2.12 to other models is made. Lines 1 and 2 are the same lines as in Figure 2.17. The agreement between the lines is fair everywhere except in the low-field region $b_{ir} \le 0.01$. Simulations performed in section 3.4.1 show that in the experiment of [Spre99] the perpendicular component of the magnetic field is not completely suppressed, but only partly from about 20 mT down to 3 mT at a transport current of 100 A. Hence the error due to the self field is present, but becomes visible at lower value of the external magnetic field. Line 3 represents the empirical equation, which is similar to the one proposed in [Kane99]:

$$i_1 = -1.05 \cdot \ln\left(\frac{b_{ir}}{2 \cdot b_{mx}}\right), \qquad \textit{Eq. 2.13}$$

where 1.05 and 2 are the fitting constants. The agreement between lines 2 and 3 is fair for the low-field region $10^{-3} \le b_{ir} \le 0.06$. At higher fields the agreement is insufficient and the equation underestimates the irreversibility field. A similar conclusion is drawn for the Kim relation used by several authors like [Magn01], [Oome00], [Nibb99] and [Nibb01]. Following [Oome00, p. 32] the equation describing sample A becomes:

$$i_2 = 4.18 \cdot (1 + 18.67 \cdot b_{ir})^{-1}, \qquad \textit{Eq. 2.14}$$

where 4.18 and 18.67 are the fitting constants. The fit using Equation 2.14 is shown as line 4 in the figure. Obviously, the agreement with the self-field free data is not satisfactory as the equation overestimates the irreversibility field. However, the equation gives a good result for the data when the self-field effect is present (at $b_{ir} \le 0.2$, see also Figure 2.17).

Therefore, Equation 2.12 at $p = 0.7$ and $q = 2.9$ provides an accurate self-field effect free scaling relation between the critical current and magnetic field for Bi-2223 tapes at 77 K over the whole range of magnetic field amplitudes and angles (up to the irreversibility field B_{ir}^{*} and except $b_{ir} \le 0.01$ where more data is required to draw a conclusion). Though empirical, Equation 2.12 is consistent with the data for Nb_3Sn and with theory, see Appendix A. Further measurements with the self-field suppressed (such as for instance [Spre99] and [Fles99]) and the strain controlled are required both at 77 K and at other temperatures.

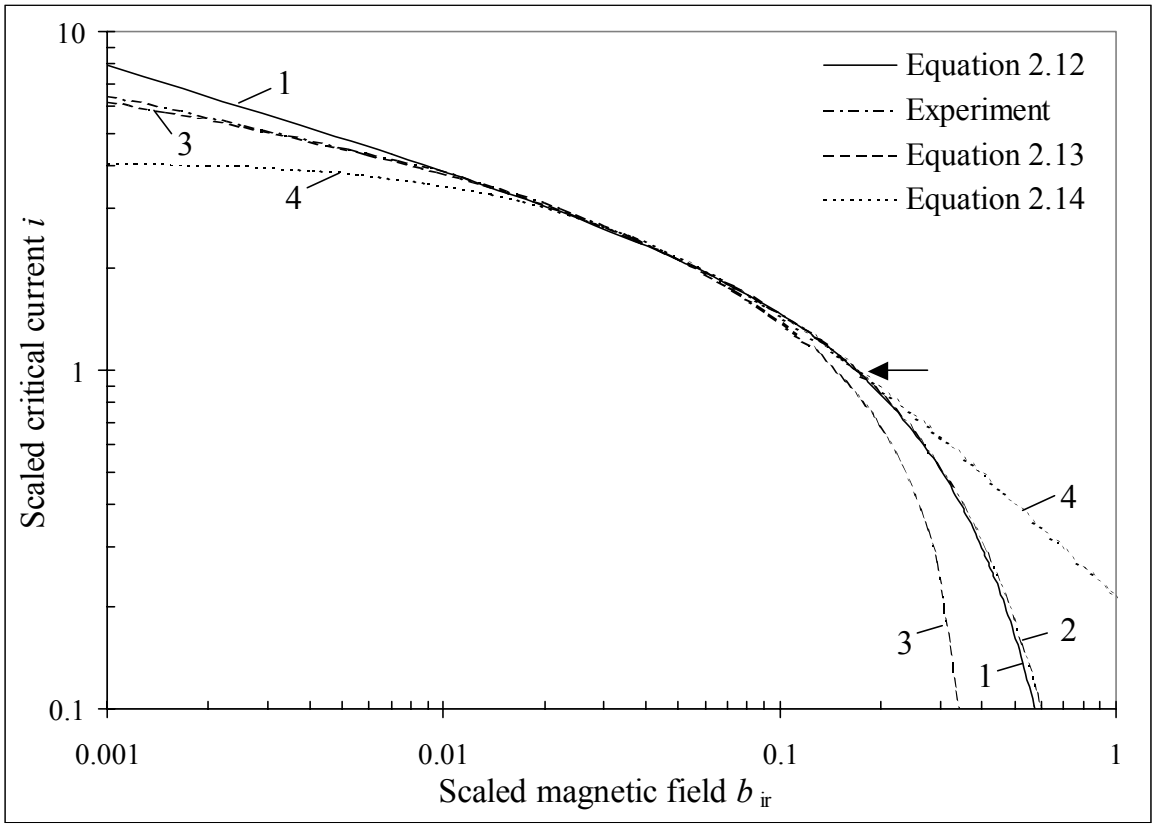

Figure 2.18 Scaled critical current $i = f_{bir}/b_{ir}$ versus the magnetic field b_{ir}, the arrow indicates location of the pinning force maximum.

2.4.3 Influence of temperature

Equation 2.12 now provides, using the data obtained at 77 K, a method to calculate the critical current with the self-field suppressed at a different temperature and for an arbitrary angle α. It is expected that temperature does not affect the values of p and q, though they could be slightly different from those derived at 77 K. The measured I_c - B_e data for at least two angles $\alpha = 0°$ and $\alpha = 90°$ in the temperature range of 64 to 77 K are available from the vendors [Amer01], [Vacu01]. Indeed, for sample A the values $p = 0.7$ and $q = 2.9$ are found in the temperature range from 64 to 77 K using the experimental data of [Amer01]. In terms of the pinning force, the change in temperature alters mainly the co-ordinates $B^*_{mx}(T)$ and $I_{c,mx}(T)$ of the pinning maximum (Equations 2.10 and 2.11). Hence for every temperature the values of $B^*_{mx}(T)$ and $I_{c,mx}(T)$ can be obtained from the $I_c - B^*$ data, see the example in Figure 2.15.

2.4.4 Critical current versus magnetic field and temperature

Using Equation 2.12, the dependence of the critical current on magnetic field B^* and temperature is calculated in a way consistent both with experiment and theory. An example is shown in Figure 2.19 for sample A (with the self-field suppressed: $p = 0.7$ and $q = 2.9$). The inset shows assumed dependencies on temperature of the maximum pinning force F_{mx} and of the irreversibility field B_{ir} used in the calculation. In order to assess the dependencies, the data from Figure 2.16 and from [Spre99], [Amer01] and [Fuch95] are used. Also for other samples one can attain the lines such as in Figure 2.19 by using Table 2.3 and Equation 2.12. Additional experiments are required in order to make such an extrapolation more accurate.

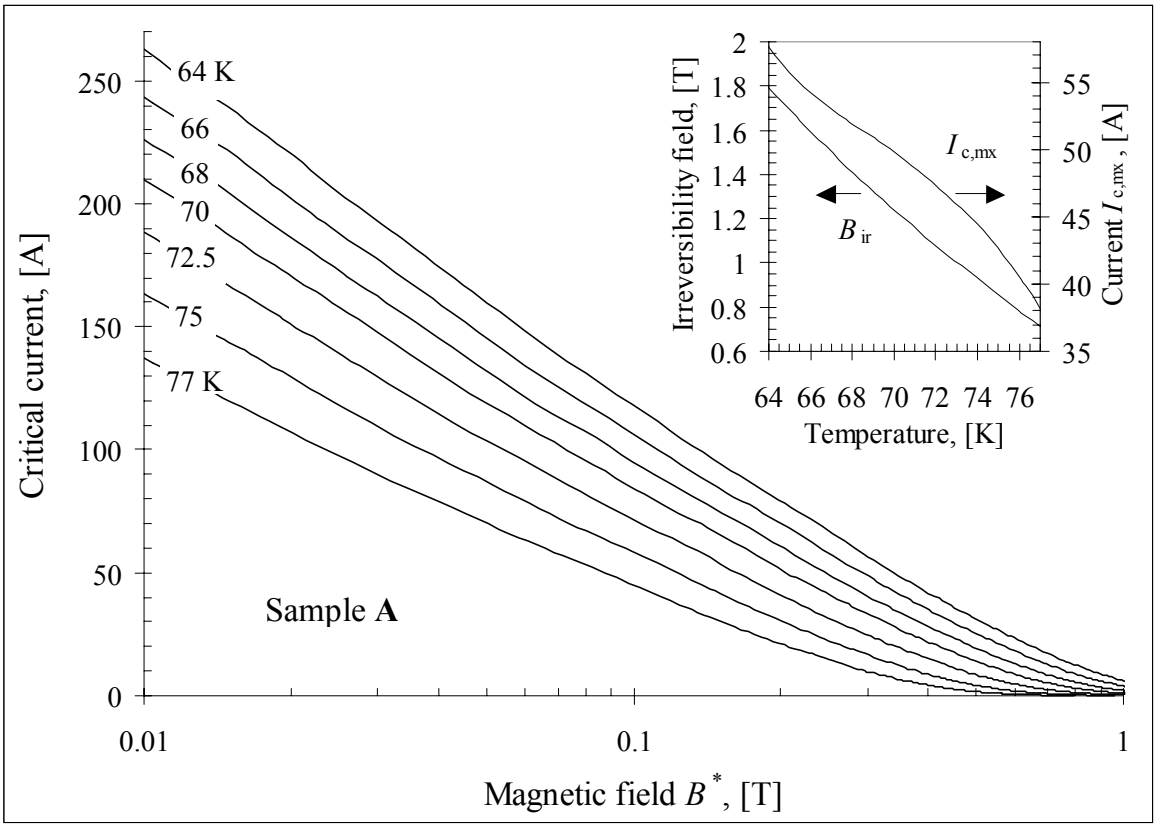

Figure 2.19 Calculated self-field free critical current of the Bi-2223/Ag tape versus magnetic field B^* and temperature (see Table 2.3).

2.5 Input to the numerical model

In the numerical model describing a sample at any temperature T between 64 and 77 K, the Equations 2.1, 2.3- 2.5 and the data from Table 2.2 and Figure 2.19 (for sample A) are used to fill in Equation 2.2. To calculate the corresponding $I_c(B^*,T)$ curve at a certain temperature T (such as shown in Figure 2.19 for sample A), Equation 2.12 is applied as it is explained in the previous section.

In the input files of the model each curve is represented by a compact array of node points. An example is shown in Tables 2.4 and 2.5. To calculate the values between the node points, cubic spline interpolation is used and the spline coefficients are given in the tables. At present insufficient information is available on the temperature dependence of the power index n and for this reason it is assumed independent on temperature in this study. The dependence of the index n on magnetic field B^* is accounted for; see Table 2.4, Figures 2.12 and 2.14 for samples V and A respectively.

2.6 Electrical insulation and power superconductor

Most commercially available Bi-2223 tapes are bare and have no electrical insulation at all. On the other hand, reliable insulation of the conductor is a must for power applications (such as cables, coils and transformers). The technical difficulties of using superconducting tapes in high-voltage power applications are highlighted in [Tana99]. Insulated Bi-2223 tape as shown in Figure 2.1 allows carrying both power and current flows at high density. However, it is not easy to insulate a high-T_c tape without causing a reduction of the critical current, as superconducting filaments are fragile (see section 2.2). Small radius r_t at the bare tape edges (see Figure 2.6) makes it difficult to apply any conventional varnish insulation (such as enamel

Table 2.4 Input data file of the numerical model for sample A at 77 K: critical current and power index vs. magnetic field.

Parameter	Scaled critical current [-]		Scaled n-index [-]	
magnetic field B^* [T]	node point	spline coeff.	node point	spline coeff.
0.00E+00	1.72E+00	-7.49E+01	2.00E+00	-1.40E+03
5.00E-04	1.68E+00	-9.02E+01	1.40E+00	-8.05E+02
1.00E-03	1.63E+00	-1.04E+02	1.20E+00	-1.81E+02
2.00E-03	1.53E+00	-9.46E+01	1.07E+00	-9.08E+01
3.00E-03	1.44E+00	-8.74E+01	1.00E+00	-5.53E+01
5.03E-03	1.28E+00	-6.30E+01	9.13E-01	-3.56E+01
7.26E-03	1.18E+00	-3.38E+01	8.50E-01	-2.68E+01
1.00E-02	1.10E+00	-2.49E+01	7.90E-01	-1.69E+01
1.27E-02	1.04E+00	-2.08E+01	7.46E-01	-1.46E+01
1.52E-02	9.90E-01	-1.84E+01	7.14E-01	-1.16E+01
2.00E-02	9.18E-01	-1.28E+01	6.64E-01	-9.06E+00
2.45E-02	8.63E-01	-1.20E+01	6.28E-01	-7.32E+00
2.85E-02	8.15E-01	-1.19E+01	5.99E-01	-6.35E+00
3.32E-02	7.60E-01	-1.14E+01	5.73E-01	-5.36E+00
4.03E-02	6.85E-01	-9.45E+00	5.38E-01	-4.47E+00
5.13E-02	6.00E-01	-6.45E+00	4.99E-01	-3.54E+00
6.88E-02	5.07E-01	-4.37E+00	4.42E-01	-2.63E+00
8.79E-02	4.36E-01	-3.25E+00	3.98E-01	-2.06E+00
1.07E-01	3.80E-01	-2.57E+00	3.62E-01	-1.71E+00
1.27E-01	3.33E-01	-2.32E+00	3.31E-01	-1.42E+00
1.46E-01	2.89E-01	-2.16E+00	3.06E-01	-1.22E+00
1.78E-01	2.30E-01	-1.74E+00	2.71E-01	-1.01E+00
2.03E-01	1.87E-01	-1.60E+00	2.47E-01	-9.03E-01
2.52E-01	1.26E-01	-9.94E-01	2.08E-01	-7.10E-01
3.01E-01	8.45E-02	-7.05E-01	1.76E-01	-6.03E-01
3.51E-01	5.52E-02	-4.88E-01	1.48E-01	-5.20E-01
4.01E-01	3.43E-02	-3.56E-01	1.24E-01	-4.39E-01
4.50E-01	2.02E-02	-2.04E-01	1.04E-01	-3.89E-01
5.00E-01	1.34E-02	-1.02E-01	8.48E-02	-3.81E-01

Table 2.5 Input data file of the numerical model for sample A: factor f_α vs. the angle α.

Parameter	Factor f_α **[-]**	
angle α [°]	node point	cubic spline coefficient
0.00E+00	1.00E+00	-5.56E-04
9.00E+00	9.90E-01	-2.22E-03
1.80E+01	9.55E-01	-5.56E-03
2.70E+01	8.90E-01	-8.87E-03
3.60E+01	8.00E-01	-1.06E-02
4.50E+01	7.00E-01	-1.19E-02
5.40E+01	5.82E-01	-1.43E-02
6.30E+01	4.43E-01	-1.65E-02
7.20E+01	2.90E-01	-1.69E-02
7.74E+01	2.05E-01	-1.37E-02
8.10E+01	1.60E-01	-1.20E-02
8.46E+01	1.20E-01	-9.12E-03
8.75E+01	1.00E-01	-4.96E-03
9.00E+01	9.00E-02	-3.52E-03

type coating) as capillary forces drag the insulation from the corners during the baking process [King96]. Besides, an insulation layer may change the properties of the surface of the tape, which might alter the adhesion of a tape in a winding and finally degrade the mechanical and thermal integrity of a coil. The surface sheath of a tape is a part of the interface between superconducting filaments and the coil former. It must provide electromagnetic, mechanical, thermal and manufacturing integrity of a coil.

Recently a new method to insulate a superconducting tape has been developed in the Netherlands as a joint effort between the University of Twente and Smit Draad, Nijmegen B.V. Insulation of a reacted high-T_c tape is achieved by folding around the bare tape a plastic film (polyimide, polyester) [Gode00a]. The insulation process is continuous and allows to insulate a tape unit length at once. The cross-section of a film insulated 3-ply high-T_c tape is illustrated in Figure 2.2 for a Bi-2223 tape, which is identical to sample A specified in Table 2.2. Starting from the outside, layers of the insulation, stainless steel strip, solder, few air voids, silver sheath and finally the filamentary core can be recognized in Figure 2.3.

The properties of the insulated tape are listed in Table 2.6. The critical current is the same prior and after the insulation process and the breakdown voltage is 2.5 - 6 kV. Multiple thermo-cycles between room and liquid nitrogen temperatures are allowed and a fair adhesion of the insulation to epoxy resin is provided. The thickness of the insulation layer is currently about 75 to 100 μm per side. A thinner insulation is possible but it requires a better surface quality of the bare tape. The surface quality of bare tapes is an important factor for a good insulation.

Several kilometres of various high-T_c tapes are already insulated and operated successfully in various coils. Commercial high-quality insulation of superconducting tapes has become available as a result of the development. The new insulation method is developed and applied in an industrial environment. It demonstrates that multi km-long fragile Bi-2223 tape superconductors can be professionally insulated and exhibit a favourable combination of properties that are required for high-voltage power applications such as coils, transformers, and current limiters.

Table 2.6 Typical properties of insulated Bi-2223/Ag tapes (measured).

Parameter		
Insulation material	polyimide	polyester
Increase of tape thickness / width, [mm/mm] after insulation	0.1 / 0.1	0.1 / 0.1
Mechanical properties		
Peel strength, [N/mm] at 300 K	0.3	0.3
Adhesion to common impregnation varnishes	reasonable	good
Dielectric properties		
Minimum breakdown voltage, [kV] at 300 K:		
- parallel	6	6
- straight with metal foil	4	4
Minimum breakdown voltage, [kV] at 77 K:		
- parallel	6	6
- straight with metal foil	4	2.5
Typical unit length, [m]	250	250
Handling precautions at 300 K, see section 2.2	unchanged	unchanged
Superconducting properties:		
after insulation	unchanged	unchanged
after multiple thermo-cycles between 300 and 77 K	unchanged	unchanged
after removing the insulation and soldering at 500 K	unchanged	unchanged

2.7 Conclusions

The essential properties of technical multifilament Bi-2223/Ag superconducting tapes are summarized. The spread along the length of outer dimensions and critical currents for Bi-2223/Ag tapes is kept within a few percent at present. The demonstrated constantly improving technical parameters of the tapes promise interesting opportunities for future scientific and technical applications.

The constitutive equations linking magnetic field strength and induction as well as electric field strength and current density for superconducting tape are introduced. The electric resistivity of Bi-2223/Ag tapes depends on the current density, magnetic field, temperature and conductor interior arrangement.

Measured direct Voltage-Current Curves of several tapes are analysed as function of the external magnetic field (magnitude and angle with respect to the tape surface) and temperature. The angle dependencies of the critical current and the power index are described using a single correction factor. The factor depends only on the direction of the magnetic field and is autonomous for the field magnitude. As a result, a compact description for the effect of the magnitude and the direction of magnetic field on the critical current and the power index at constant temperature is provided.

An empirical scaling relation known for Nb_3Sn wires and describing the dependence of the critical current on external magnetic field and temperature is applied for Bi-2223/Ag tapes. The relation is modified to account for the dependence of experimental *E-I* curves on magnetic field angle and for the irreversibility field. Using the novel relation, the dependence of the critical current on magnetic field and temperature is calculated and presented for one of the tapes.

The studied *E-I* curves provide the input to the numerical model presented in Chapter 3. A cubic spline interpolation technique is used to minimize the number of experimental data points required for smooth and accurate representation of the input curves for the numerical model.

A new method to insulate long reacted and fragile Bi-2223/Ag superconducting tapes is developed and successfully implemented in an industrial environment. The method enables industrial application of the tapes and development of commercial power superconductors. Here the insulated tapes are used in the 1-MVA high-T_c superconducting coil presented in Chapter 4.

Chapter 3

ELECTRO-MAGNETIC MODEL

In this chapter a numerical model is presented, which describes the electro-magnetic behaviour of high temperature superconductors. The accent is on physics, while the mathematics for solving the equations is kept to a minimum. A new E - J formulation for the eddy current problem is derived, leading to a more elegant and precise procedure for solving the equations. A relatively simple network model is proposed to simulate electro-magnetic behaviour of superconductors. The results of the model are verified against measurements and an excellent agreement is found. The total loss of a technical BSCCO-2223 tape with non-twisted filaments carrying a transport current and exposed to external magnetic field can be predicted using the accurately measured direct E-I curve of a tape sample as input for the network model. The importance of the self-field effect is underlined.

3.1 Introduction

The objective is to find a general method and a reasonably simple model to simulate the electro-magnetic behaviour of high-T_c tapes and coils. Such a model verified against the experimental data gathered for single tapes will then be applied to simulate voltage-current curves of coils as presented in Chapter 4. Considering the complexity of the case, the numerical approach seems to be the only realistic one. When computing a current distribution inside a superconductor, the classical eddy current problem has to be solved [Stee97]: a magnetic field changing in time will induce eddy currents in the conducting medium. The currents affect the performance of the conductor by increasing the losses. It is important to be able to compute the eddy currents in advance. In this section existing formulations for the eddy current problem and numerical models are compared.

Consider a long and single Bi-2223 tape with a transport current (parallel to the z-axis) in a uniform transverse magnetic field B_e as sketched in Figures 2.1 and 2.7. At present the only high-T_c tapes available in quantities sufficient for making coils are those with non-twisted filaments (for this reason the study below is confined namely to this case). A number of two-dimensional numerical models has been developed for high-T_c superconductors. Most of the existing models allow simulating a current distribution and losses in the electric cross-section of a single tape as shown in Figure 2.1. The models can be distinguished in several groups.

Group 1 uses the finite difference method and the Brandt model (solving Maxwell equations) extended to the case when both the magnetic field and the transport current are present [Yaza99], [Rhyn98] or a network model (solving Kirchhoff's equations) [Shev99a] and [Yang99]. The advantage is simplicity and besides spatial integration is confined to the conductor volume. The disadvantages are that calculations are rather time-consuming and the finite element method is difficult to apply.

The models of group 2 are based on classical formulations for the eddy current problem [Stee97]. The basic formulations are: A - φ [Hoff01], [Nibb99], [Nibb01], and θ - Ω [Amem98]. The advantage of the models is that the finite element method is applied to perform spatial integration. The disadvantage is that the method requires more (time to be invested in) programming. Also, the method requires computing of intermediate quantities such as magnetic vector-potential. The calculations are performed over the entire space inside and outside the conductor and in time.

In group 3 [Gure97] and [Masl97] the basic equations for a superconductor are derived from Maxwell's equations linking the current density and the electric field directly. To solve the equations, the finite difference method and integration over the entire space is used by [Masl97] and [Masl98].

The models in all three groups use the power law to describe the direct voltage-current characteristic of the superconductor and most of the results are obtained for a single tape. An arbitrary dependence of the transport current and external magnetic field on time is allowed. However, the integration over both time and space makes simulations rather time consuming. The analysis shows that the basic formulation of the eddy current problem can be further improved as it is shown in the next section.

Two methods to speed up the calculations have recently been proposed in [Hofm01] and [Sjös00], group 4. In [Hofm01] the harmonic analysis is applied by introducing an effective resistivity of the superconductor averaged over a period. This method causes a dramatic acceleration of the calculations because time as one of the variables is omitted. However, the method is only approximate and it is not clear if it is applicable in all relevant non-linear cases. With the losses known for harmonic currents and fields, the Preisach model (a phenomenological expression of hysteresis) is applied to predict the response of a superconductor to currents and fields varying arbitrarily in time [Sjös00].

Group 5 comprises semi-empirical models [Rabb00] and [Magn01] using measured loss data on a single tape and fitting formulas. Application of such models to coils is less evident. The loss of a single tape is increased by the self-field, while in coils the self-field is largely influenced by an array of adjacent turns. Hence in a coil the effect per tape is less pronounced inside the array of turns and more pronounced at the coil edges, see for example results of [Iwak01] for the transformer coils and of [Shev01] for a resonator coil.

3.2 Basic electro-magnetic theory

In this section a general formulation of the eddy current problem is derived. In order to keep the complexity of the problem acceptable, only quasi-static and static cases are considered. Unless stated otherwise, all the media are isotropic and uniform. The displacement currents are neglected. The external magnetic field B_e is transversal, uniform and has two components B_{ex} and B_{ey}, (Figure 2.7). Maxwell's equations relevant for a superconductor by which displacement currents are neglected, are:

$$\nabla \times \boldsymbol{E} = -\dot{\boldsymbol{B}}; \quad \nabla \times \boldsymbol{H} = \boldsymbol{J}; \qquad \textit{Eq. 3.1}$$

$$\nabla \cdot \boldsymbol{B} = 0; \qquad \nabla \cdot \boldsymbol{J} = 0, \qquad \textit{Eq. 3.2}$$

where E is the electric field strength, J is the current density; $\dot{B} = \partial B / \partial t$, t time, B and H are the magnetic induction and field strength respectively, the bold symbols indicate vectors and matrices. Equations 3.1 expresses Faraday's law of induction (left) and Ampere's law (right). The continuity Equations 3. 2 for the induction B (left) and for the current density J (right) imply *solenoidal* vector fields for both $\boldsymbol{B}$ and $\boldsymbol{J}$. In order to reduce the number of unknown variables in Equations 3.1 and 3.2, constitutive equations are required.

The constitutive equations describe the material properties by linking H and B, E and J and are discussed in section 2.3, see Equations 2.1 and 2.2. Here the $\boldsymbol{E}-\boldsymbol{J}$ relation is discussed in more detail. Since the sum of all local source and drain electric fields of a point is zero, the resulting (inductive drain) electric field strength $\boldsymbol{E} \equiv \boldsymbol{E}_{di}$ inside the conductor is described via the sources E_{sr} and resistive drains E_{dr} as follows:

$$\boldsymbol{E} = \boldsymbol{E}_{di} = \boldsymbol{E}_{sr} - \boldsymbol{E}_{dr}. \qquad \textit{Eq. 3.3}$$

The source electric field of a point inside the conductor reads:

$$\boldsymbol{E}_{sr} = \boldsymbol{E}_b + \boldsymbol{E}_{tr}, \qquad \textit{Eq. 3.4}$$

where $\boldsymbol{E}_b$ is the electric field due to the changing magnetic field B_e; $\boldsymbol{E}_{tr}$ is the electric field of the transport source. Ohm's law expressed by Equation 2.2 describes the (resistive) drain electric field of a superconductor: $E_{dr} = E_\rho$. When the resistivity of the superconductor is given, Equations 2.2, 3.3, and 3.4 allow to relate $\boldsymbol{E}$ and $\boldsymbol{J}$.

3.2.1 Basic equations of the superconductor model

In this section the $\boldsymbol{E}-\boldsymbol{J}$ formulation is derived for the eddy current problem. Assuming that μ is time-independent and by re-arranging Equations 3.1 and 2.1, one finds:

$$\dot{\boldsymbol{J}} = -\nabla \times \mu^{-1} \nabla \times \boldsymbol{E} \,. \qquad \textit{Eq. 3.5}$$

The continuity Equation 3.2 for arbitrary time reads:

$$\nabla \cdot \boldsymbol{J} = 0 \text{ or } \oint_s \boldsymbol{J}(\boldsymbol{r}) \mathrm{d}^2 r = 0 \,, \qquad \textit{Eq. 3.6}$$

where $\boldsymbol{r}(x, y, z)$ is the radius-vector; x, y and z are the co-ordinates of a point within the superconductor volume, S is the surface, see Figure 2.1.

Therefore under the assumptions made and for given μ, a set of Equations 3.5 and 3.6 together with corresponding initial and boundary conditions links the unknown variables $\boldsymbol{E}$ and $\boldsymbol{J}$ confined to the volume of superconductor in the 3-dimensional case. In order to solve for $\boldsymbol{J}(\boldsymbol{r}, t)$, Equations 3.3, 3.4 and 2.2 must be added (since $\boldsymbol{E}$ depends on $\boldsymbol{J}$).

3.2.2 Two - dimensional case

To simplify the problem, consider only a z - projection of the vectors $\boldsymbol{E}$ and $\boldsymbol{J}$ [Bran96]. The assumption means neglecting the entry effects (re-distribution of the currents at the conductor ends, see also section 2.2). This allows to consider an electric cross-section of a conductor far from the ends instead of the whole volume and to also apply a 2-dimensional model instead of a 3-dimensional one. A useful vector equality for this case is:

$$\nabla \times \nabla \times \boldsymbol{E}_z \equiv \nabla(\nabla \cdot \boldsymbol{E}_z) - \Delta \boldsymbol{E}_z \equiv -\Delta \boldsymbol{E}_z \,, \qquad \textit{Eq. 3.7}$$

as only z - projections are considered and therefore the vector does not diverge. Here $\Delta = \nabla^2 = \partial^2/\partial x^2 + \partial^2/\partial y^2$ is the Laplacian operator. For a point (x, y) in a conductor cross-section a substitution of Equations 3.4 and 2.2 into Equation 3.3 results in z - projection of the $\boldsymbol{E} - \boldsymbol{J}$ relation that is set by the considered boundary conditions and Ohm's law, see Figure 2.7:

$$\boldsymbol{E}_z = -x \cdot \dot{\boldsymbol{B}}_{ey} + y \cdot \dot{\boldsymbol{B}}_{ex} + \boldsymbol{E}_{tr} - \rho_z \cdot \boldsymbol{J}_z \,. \qquad \textit{Eq. 3.8}$$

When μ is constant (both time and space-independent, for instance $\mu = \mu_0$) from Equations 3.5 and 3.7 Poisson's equation is found for the 2-dimensional case [Gure97]:

$$\dot{\boldsymbol{J}}_z = \mu^{-1} \Delta \boldsymbol{E}_z \,. \qquad \textit{Eq. 3.9}$$

Note that Equation 3.9 is valid only for constant μ, so it is a particular case of the more general Equation 3.5. The latter allows for instance the permeability to depend on magnetic field so that non-linear ferro-magnetic components could be included into the model (such as for instance iron pieces used for shaping magnetic field around coil edges as it is explained in Chapter 4). Equations 3.5 and 3.6 are the governing equations of the $\boldsymbol{E} - \boldsymbol{J}$ formulation for the eddy current problem in a 3-dimensional case. Substituting Equation 3.8 into Equation 3.5 together with Equation 3.6 gives the required set of 2-dimensional equations written in differential form:

$$\begin{cases} \dot{\boldsymbol{J}}_z = \nabla \times \mu^{-1} \nabla \times \left(x \cdot \dot{\boldsymbol{B}}_{ey} - y \cdot \dot{\boldsymbol{B}}_{ex} - \boldsymbol{E}_{tr} + \rho_z \cdot \boldsymbol{J}_z \right) ; \\ \nabla \cdot \boldsymbol{J}_z = 0 \,. \end{cases} \qquad \textit{Eq. 3.10}$$

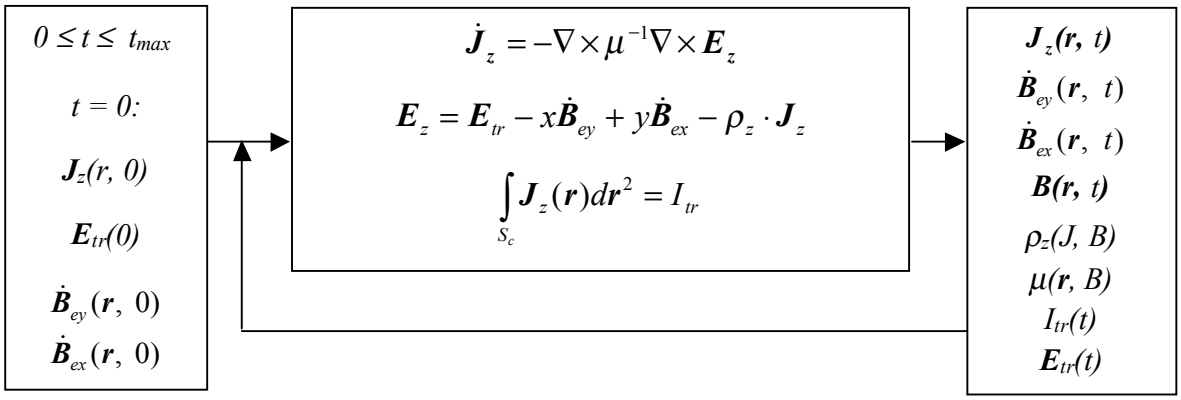

*Figure 3.1 Solving the basic equations of the **E** - **J** formulation in the 2-dimensional case.*

The set of Equations 3.10 [Shev01] forms the basis of the 2-dimensional electromagnetic model used here. The block-diagram illustrating how to solve the equations is shown in Figure 3.1. For a constant μ the upper Equation 3.10 becomes:

$$\dot{\boldsymbol{J}}_z = \mu^{-1} \Delta \left(\boldsymbol{E}_{tr} - x \cdot \dot{\boldsymbol{B}}_{ey} + y \cdot \dot{\boldsymbol{B}}_{ex} - \rho_z \cdot \boldsymbol{J}_z \right) \quad . \qquad \textit{Eq. 3.11}$$

Using proper start and boundary conditions, the set of Equations 3.10 can be solved numerically in one of the ways summarised for instance in [Stee97], [Hofm01], [Nibb99] or [Amem98]. The set has the following advantages when compared to the other formulations:

- ✓ The problem domain is confined to the electric cross-section (volume) of the conductor and therefore the calculation area is minimized;
- ✓ A finite element method is directly applicable;
- ✓ Only relevant quantities are computed, there are no intermediate quantities involved;
- ✓ Non-linear components such as ferro-magnetics are allowed.

The characteristic boundary and the initial conditions are briefly summarised below, see [Seeb98, p. 232] for more details. The electric field of the transport source is the electromotive force (e. m. f.) per unit length and for this reason it is a space-independent variable: $E_{tr}(r, t) \equiv E_{tr}(t)$. The e. m. f. is the driving voltage generated by the source in free space (with the conductor removed). Usually the transport source is either a current source or a voltage source. In the case of a current source the transport current $I_{tr}(t)$ is a given function of time and the unknown variables of the Equations 3.10 are: $J_z(r, t)$ and $E_{tr}(t)$.

In the case of a voltage source the transport electric field is a given function of time $E_{tr} = E_{tr}(t)$ and the unknown variables of the Equations 3.10 are: $J_z(r, t)$ and $I_{tr}(t)$. For the magnetic field source the case of a transversal magnetic field $B_e(t)$ uniform in space is considered. Note that the total magnetic field *B(t)* includes the self-field component B_J, see Figure 2.7. Both external magnetic field and the transport current (or e. m. f.) can be arbitrary functions of time. At the starting point $t = 0$, a uniform distribution of the current density over the electric cross-section of the tape is assumed: $J_z(r, 0) = 0$. Furthermore, a condition: $E_{tr}(t = 0)$ or $I_{tr}(t = 0)$ is applied.

In conclusion, for the 2-dimensional case a set of Equations 3.10 is derived. It allows to find a distribution of the current density inside the superconductor $\boldsymbol{J}_z(\boldsymbol{r}, t)$ and therefore to solve the eddy current problem.

3.2.3 Example of solving the basic equations

One way to solve Equations 3.10 in a 2-dimensional case is illustrated below as the solution is in close relation to that of the network model described in section 3.3. It remains to be seen if the method is advantageous in solving Equations 3.10 as compared to a finite element method. The general solution [Korn68] of Equation 3.9 (confined to conductor cross-section S_c) is:

$$\int_{S_c} d^2r' M_\infty(\boldsymbol{r},\boldsymbol{r}')\dot{\boldsymbol{J}}_z(\boldsymbol{r}',t) = \boldsymbol{E}_z(\boldsymbol{r},t). \qquad \textit{Eq. 3.12}$$

Here

$$M(\boldsymbol{r},\boldsymbol{r}') = -\frac{\mu}{2\pi}\cdot\ln|\boldsymbol{r}-\boldsymbol{r}'| = \overline{M}_G \qquad \textit{Eq. 3.13}$$

is Green's function (multiplied by μ), $\boldsymbol{r}\equiv(x,y)$ and $\boldsymbol{r}'\equiv(x',y')$ are radii-vectors of two arbitrary "source" and "field" points respectively [Stee97] within the conductor cross-section S_c and $E_z(\boldsymbol{r},t)$ is specified by Equation 3.8. In the case when $I_{tr}(t)$ is a given function, Equation 3.6 for an arbitrary moment of time reads:

$$\int_{S_c} \boldsymbol{J}_z(\boldsymbol{r},t)\mathrm{d}^2 r = I_{tr}(t). \qquad \textit{Eq. 3.14}$$

The set of Equations 3.12 and 3.14 can be solved numerically for the unknown variables $\boldsymbol{J}_z(\boldsymbol{r},\ t)$ and $\boldsymbol{E}_{tr}(t)$. Splitting the conductor cross-section into m rectangular cells with finite dimensions $\Delta x\times\Delta y$ as shown in Figure 3.2 and replacing each i - rectangular cell (with a current $\Delta I_{zi} = \boldsymbol{J}_{zi}\Delta x\Delta y$) by an equivalent line cell (with the same current flowing through the centre of rectangular cell) one may write discrete (in space) Equation 3.12 in matrix form:

$$\dot{\mathbf{J}}_\mathbf{z}\cdot\Delta x\Delta y = \overline{\mathbf{M}}_G^{-1}\cdot\mathbf{E}_\mathbf{z}, \qquad \textit{Eq. 3.15}$$

where $\dot{\mathbf{J}}_\mathbf{z} = [\dot{J}_{zi}]$ and $\mathbf{E}_\mathbf{z} = [E_{zi}]$ are column matrices, $\overline{\mathbf{M}}_G^{-1}$ is the inverse of matrix $\overline{\mathbf{M}}_\mathbf{G} = [\overline{M}_{G,ik}]$, $i = 1,\ 2..m$ and $k = 1,\ 2..m$ are integer counters and m is total number of the cells.

Since by definition $\dot{J}_{zi}\Delta t = J_{zi}(t+\Delta t) - J_{zi}(t)$, starting at $t = 0$ with $J_{zi} = 0$ the evolution of the current density in time can be calculated with discrete (in time and space) equation:

$$\mathbf{J}_\mathbf{z}(t+\Delta t) = \mathbf{J}_\mathbf{z}(t) + \frac{\Delta t}{\Delta x\Delta y}\overline{\mathbf{M}}_G^{-1}\cdot\mathbf{E}_\mathbf{z}(t), \qquad \textit{Eq. 3.16}$$

where $\dot{\mathbf{J}}_\mathbf{z}(t) = [\dot{J}_{zi}(t)]$, $\dot{\mathbf{J}}_\mathbf{z}(t+\Delta t) = [\dot{J}_{zi}(t+\Delta t)]$ and $\mathbf{E}_\mathbf{z}(t) = [E_{zi}(t)]$. The corresponding discrete continuity Equation 3.14 at any moment of time reads:

$$\sum_i^m J_{zi}(t)\Delta x\Delta y = I_{tr}(t). \qquad \textit{Eq. 3.17}$$

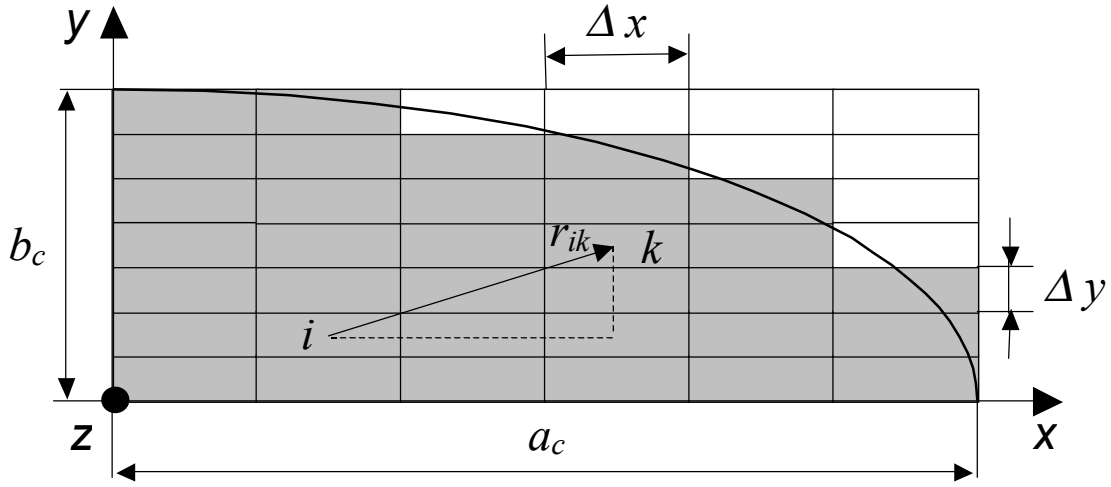

Figure 3.2 Elliptical cross-section of the model superconductor filamentary core replaced with a grid of equal rectangular cells (only ¼ of the actual cross-section is displayed).

In Figure 3.2 the conductor has an elliptical cross-section (of which ¼ is limited by the curve and by the axes). The approximating grid cells with and without cell currents are shown in grey and white respectively. For symmetry reasons only one quarter of the conductor actual cross-section is shown, while in general when both the transport current and external magnetic field of arbitrary direction are present, the calculation is performed over the whole cross-section of the conductor. For each moment of time the x, y - components of the total magnetic field for cell i are calculated using superposition and Biot-Savart's law for an infinite straight line conductor, see also Figure 2.7:

$$B_{xi} = B_{ex} + \sum_{k}^{m-1} X_{ik} J_k, \quad X_{ik} = \frac{\mu \cdot \sin \xi_{ik}}{2\pi \cdot |r_{ik}|} \Delta x \Delta y \text{ and} \qquad \textit{Eq. 3.18}$$

$$B_{yi} = B_{ey} + \sum_{k}^{m-1} Y_{ik} J_k, \quad Y_{ik} = \frac{\mu \cdot \cos \xi_{ik}}{2\pi \cdot |r_{ik}|} \Delta x \Delta y, \qquad \textit{Eq. 3.19}$$

where ξ_{ik} is the angle between the vector $\boldsymbol{r_{ik}} = \boldsymbol{r_i} - \boldsymbol{r_k}$ and the positive direction of x-axis, see Figure 3.2 and $i \neq k$. The components B_{xi} and B_{yi} are used to obtain the direction angle $\alpha_i(B_y, B_i) = \arctan(B_{xi}/B_{yi})$ and hence $B_i^* = B_i \cdot f(\alpha_i)$, see Equation 2.5. The dependencies of the critical current and the power index on magnetic field B_i^* and $f(\alpha_i)$ shown in Figures 2.11-2.14 are used to calculate the resistivity ρ_i, see Equations 2.3 and 2.4.

The matrices $\overline{\mathbf{M}}_G^{-1}$, $\mathbf{X} = [X_{ik}]$, and $\mathbf{Y} = [Y_{ik}]$ contain only geometrical information and have to be calculated once prior to the time integration process. Strictly saying Equations 3.13 and 3.16 - 3.19 are accurate for a (infinitely long and straight) line current $dI_z = J_z dx dy$ within the conductor. A cross-section of such line current is a point. When the conductor cross-section split into m cells with finite dimensions $\Delta x \times \Delta y$, see Figure 3.2, the errors made in matrices $\overline{\mathbf{M}}_G^{-1}$, $\mathbf{X}$, and $\mathbf{Y}$ when using Equations 3.13 and 3.18 - 3.19 depend on cell shape and dimensions and can be substantial (the physical reason is that the equations are valid for line cells only). When the step between a line cell and a cell with finite dimensions is made, see Equations 3.15 and 3.16, the error occurs due to ignoring relevant space integration.

Smaller dimensions $\Delta x \times \Delta y$ of the rectangular cell might reduce the errors, but would increase calculation time when solving Equations 3.16 - 3.19. For tapes the rectangular cell usually has a high aspect ratio given by tape typical dimensions, see Table 2.2. A correct way to reduce the errors in $\overline{\mathbf{M}}_G^{-1}$ is described rather in [Yang99] than in [Bran96] or [Rabb01]. The same idea as in [Yang99] is used here to accurately calculate the coefficients of the matrices $\overline{\mathbf{M}}_G^{-1}$, $\mathbf{X}$, and $\mathbf{Y}$. At a glance, the idea of the refinement is to divide additionally each (rectangular) cell with the dimensions $\Delta x \times \Delta y$ by a sufficient number of square sub-cells and to accurately calculate the coefficients of the matrices using Equations 3.13, 3.18 and 3.19. The fine mesh of the sub-cells is used only for this purpose. Since the matrices are calculated only once prior to solving Equations 3.16 - 3.17, the increase of the total calculation time is negligible. Hence a new and more accurate set of Equations 3.16 –3.19 (as compared to [Bran96], [Rabb01] and [Yang99]) is derived from Equations 3.10. Note that the error made in calculating magnetic field of a cell with finite width and thickness using Equations 3.18 and 3.19 remains after the refinement, accurate formulas will be derived in section 3.3.

In this section, the model expressed by Equations 3.10 is detailed to the level when a numerical method can be applied and a solution can be found. However, the described way of solving Equations 3.10 results in errors caused by replacing a line cell with a cell that has finite dimensions. The errors will be eliminated in sections 3.3.2 and 3.3.3.

3.2.4 Time-harmonic source fields

Consider the important case for practical applications when all the source fields are harmonic functions of time and oscillate with the same frequency and phase. For instance, during normal operation of transformers and power coils the e. m. f. of the transport source and the external magnetic field indeed vary harmonically with time at the same angle frequency ω. When the medium has linear properties, the eddy current problem is a steady-state problem [Stee97] and a complex representation of the fields makes sense. Equations 3.5 and 3.6 in a complex form read in this case:

$$j\omega\hat{J} = -\nabla \times \mu^{-1} \nabla \times \hat{E}\,, \qquad \textit{Eq. 3.20}$$

$$\int_S \hat{J}(r) d^2 r = \hat{I}_{tr}\,. \qquad \textit{Eq. 3.21}$$

Here $j^2 = -1$, $\hat{J}$ and $\hat{E}$ are the amplitudes of J and E respectively, S is the superconductor surface, Figure 2.1. With the medium properties given, the set of complex Equations 3.20 and 3.21 is solved numerically. The computation effort reduces drastically when the variable time is omitted.

In the case when the medium is non-linear, a method to avoid time-dependent computations was recently proposed [Hofm01]. The applicability of the method is less evident in this case. Time-dependent analysis shows that locally inside a superconductor in the time dependency of both the current density and the electric field the harmonics of the higher order than 1 are present. However, the loss per cycle contains effectively only the first harmonic, while the contribution of the higher order harmonics can be neglected with an acceptable error. This is supported by many measurements usually performed with a lock-in amplifier where a measured first harmonic of the voltage together with the (transport) current and external magnetic field provides sufficient information about the losses [Rabb01, pp. 94 and 103]. Equation 3.8 in complex form reads:

$$\hat{E}_z = j\omega\left(x\cdot\hat{B}_y - y\cdot\hat{B}_x\right) - \hat{E}_{tr} + \rho_{ef}\cdot\hat{J}_z\,. \qquad \textit{Eq. 3.22}$$

The complex form of Equations 3.10 for the two dimensional case follows from Equations 3.20 and 3.21.

The mean (averaged over a period) resistivity ρ_{ef} of a composite conductor with non-twisted superconducting filaments embedded into a homogenous matrix is:

$$\frac{1}{\rho_{ef}} = \frac{\gamma}{\rho_{sef}} + \frac{1-\gamma}{\rho_{mef}}\,, \qquad \textit{Eq. 3.23}$$

where γ is the superconductor-to-total filling factor. The mean resistivity of a (pure silver) matrix ρ_{mef} is:

$$\rho_{mef} = \frac{\rho_{md}}{1+\frac{4}{3}\left(\frac{\hat{E}_b}{\hat{E}_{tr}}\right)^2}\,, \qquad \textit{Eq. 3.24}$$

where ρ_{md} is the longitudinal resisitivity of the matrix for a direct current (zero frequency), $\hat{E}_{tr}$ and $\hat{E}_b$ are e.m.f. amplitudes of the transport source and of the eddy current source respectively. The eddy currents are induced by changing magnetic field with an amplitude $\hat{B}$, see Figure 2.7: $\hat{E}_b = \omega\hat{B}\cdot a_{tb}$. Here a_{tb} is the characteristic dimension of the matrix perpendicular to the direction of magnetic field. One may account for the presence of the filamentary region in the matrix and rounded corners of the outer sheath as depicted in Figure 2.1 by superimposing the losses of a rectangular bar, an ellipse and a circle, the corresponding formulas can be found for instance in [Namj88].

Consider a superconductor with a direct *E-I* curve described by the power law, Equation 2.4:

$$\frac{J}{J_c} = \left(\frac{E_\rho}{E_c}\right)^{n_1}\,, \qquad \textit{Eq. 3.25}$$

where J_c is the critical current density, E_c is the electric field and $n_1=n^{-1}$ is the exponent.

For a harmonic transport source with e. m. f. amplitude $\hat{\boldsymbol{E}}_{\boldsymbol{tr}}$ connected to a superconductor, the mean resistivity of the superconductor ρ_{sef} is [Hofm01]:

$$\frac{1}{\rho_{sef}} = 2\frac{J_c}{\hat{E}_{tr}}\left(\frac{\hat{E}_{tr}}{E_c}\right)^{n_1}\cdot\phi(n_1)\,. \qquad \textit{Eq. 3.26}$$

Here t is the time, $\phi(n_1) = \frac{1}{2\pi}\int_0^{2\pi}\left|\sin(\omega t)\right|^{1+n_1} d(\omega t)$ and it can be calculated accurately using the Gamma function. Note that by doing so an analytical expression is found for the mean resistivity of the superconductor. With the resistivity known, the loss can be calculated. In practice, the

constraint $0 < n_1 \leq 1$ holds for any superconductor and within this range the approximation: $\phi(n_1) \approx 4 - 1.16 \cdot n_1 + 0.3 \cdot n_1^2$ is valid with the relative error below 0.2 %. For a typical Bi-2223/Ag tape in most cases: $0.01 < n_1 \leq 0.3$. The exact (boxes) and the approximate (line) solutions are compared in Figure 3.3. As mentioned, the method itself [Hofm01] is approximate and more effort is required to validate it in all cases typical for (non-linear) superconductors.

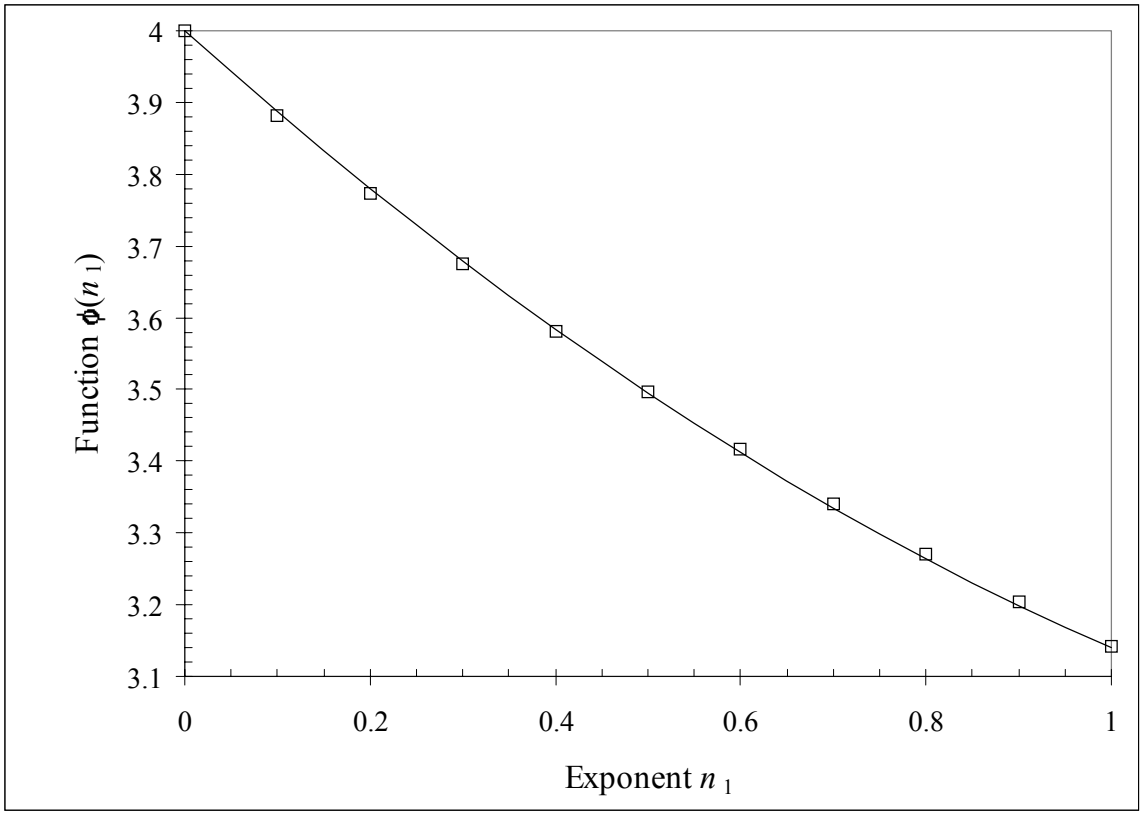

Figure 3.3 Function ϕ versus the exponent n_1, see Equation 3.26.

3.3 Network model

A reliable model is preferred above a new model that may be faster but less trustworthy. For reasons of clarity and transparency for understanding, a relatively simple 2-dimensional network model is applied to simulate the electro-magnetic behaviour of the (HTS tape) superconductor. The network model is often used for low-T_c superconductors [Verw95], [Akhm98] and [Seeb98], however mostly for modelling a cable and not a wire.

3.3.1 Assumptions

The assumptions of the network model are as follows. All currents within a tape are considered parallel to each other. The actual current distribution inside the superconductor can be approximated by a bundle of cell currents confined to the same cross-section, forming a 2-dimensional grid of cells and directed along the tape. Since all cell currents are assumed parallel, they behave as they are electrically *insulated* from each other along the tape length and electrically connected to each other at the conductor ends (the entry zones, which are outside the considered area, see Figure 2.4). Furthermore, the displacement currents are neglected (see section 3.2). Hence the path for every cell current in the 2-dimensional approximation is defined.

Consequently, by avoiding most of the formalism of the previous sections, one may directly write Kirchhoff's equations for a set of cell currents within a tape conductor as it is explained in more detail in the following section. Under these assumptions a cell current obeys Kirchhoff's equations and this justifies the network model approach [Shev99]. Recently it has been discussed [Yang99] that with a certain refinement the model proposed by [Bran96] (and therefore by [Yaza99] and [Rhyn98]) is in fact identical to the network model.

On one hand, this is not surprising as obviously Kirchhoff's equations are a particular integral form of Maxwell's equations. Under the assumptions made here (a constant μ, zero displacement currents, disregarded edge effect and insulated cell current representation) Kirchhoff's equations follow from Equations 3.10 and 3.11 directly. Indeed, Equations 3.2 imply *solenoidal* vector fields for both $\boldsymbol{B}$ and $\boldsymbol{J}$. The current in a superconductor in this case can be replaced by a bundle of the non-crossing cell currents that behave as though they are insulated from each other. Therefore Kirchhoff's equations can be used instead of Maxwell's equations, which lead to a simple network model [Shev99] and [Shev99a].

On the other hand, Equation 3.13 describes the mutual inductance of two parallel, straight infinitely long lines. The network model uses instead accurate formulas for self- and mutual inductances of two parallel straight (rectangular) cells of finite dimensions [Grov46]. The network model also requires the constitutive Equations 2.1 and 2.2, the boundary conditions expressed by Equation 3.8, Biot-Savart's law, Equations similar to 3.18 and 3.19 and equations for self- and mutual inductances of two parallel straight rectangular cells of finite length. In the case of time-harmonic source fields similar considerations as in section 3.2.4 are obviously applicable within the network model.

3.3.2 Basic and governing equations

The 2-dimensional network model applied to a superconductor as displayed in Figures 2.1 and 2.7 states the following. For a set of *m* cell currents (each flowing through a rectangular cell with finite dimensions, see Figure 3.2) avoiding space integration of Maxwell equations by using the assumptions mentioned in the previous section one may directly write the following basic set of Kirchhoff's equations per unit length in space-integral form:

$$\Delta I_{z1} + \ \dots \ + \Delta I_{zi} + \ \dots \ + \Delta I_{zm} = I_{tr}(t) \ \text{ and} \qquad \textit{Eq. 3.27}$$

$$\begin{cases} M_{11}\Delta \dot{I}_{z1} + \ \dots \ + M_{1k}\Delta \dot{I}_{zk} \ \ \dots \ + M_{1m}\Delta \dot{I}_{zm} = E_{z1} \\ \dots \ \ \dots \ \ \dots \ \ \dots \ \dots \ \ \dots \ \ \dots \ \ \dots \ \dots \ \ \dots \\ M_{i1}\Delta \dot{I}_{z1} + \ \dots \ + M_{ik}\Delta \dot{I}_{zk} \ \dots \ + M_{im}\Delta \dot{I}_{zm} = E_{zi} \\ \dots \ \ \dots \ \ \dots \ \ \dots \ \dots \ \ \dots \ \ \dots \ \ \dots \ \dots \ \ \dots \\ M_{m1}\Delta \dot{I}_{z1} + \ \dots \ + M_{mk}\Delta \dot{I}_{zk} \ \dots \ + M_{mm}\Delta \dot{I}_{zm} = E_{zm} \end{cases} . \qquad \textit{Eq. 3.28}$$

Equally, one may write:

$$\sum_{i=1}^{m} \Delta I_{zi} = I_{tr}(t) \ \text{ and} \qquad \textit{Eq. 3.27a}$$

$$\sum_{k=1}^{m} M_{ik}\Delta \dot{I}_{zk} = E_{zi} \ , \qquad \textit{Eq. 3.28a}$$

where $\Delta I_{zk} = J_{zk}\Delta x\Delta y$ and $\Delta I_{zi} = J_{zi}\Delta x\Delta y$ are the *k*- and *i*- cell currents respectively, the current density is assumed constant within each cell; $k = 1,2,...m$; $i = 1,2,...m$; M_{ik} is mutual inductance per unit length of the *k*- and *i*- cells; E_{zi} is the local electric field of the cell *i*, see Equation 3.8 and *m* is total number of the cells, see Figure 3.2.

In matrix form the set 3.28 can be written as follows:

$$\dot{\mathbf{J}}_{\mathbf{z}} \cdot \Delta x\Delta y = \mathbf{M}^{-1} \cdot \mathbf{E}_{\mathbf{z}}, \qquad \textit{Eq. 3.29}$$

where $\dot{\mathbf{J}}_{\mathbf{z}} = [\dot{J}_{zi}]$ and $\mathbf{E}_{\mathbf{z}} = [E_{zi}]$ are the column matrices, $\mathbf{M}^{-1}$ is an inverse of matrix $\mathbf{M}=[M_{ik}]$, $i = 1, 2..m$ and $k = 1, 2..m$. Note that a method of solving a set of linear equations using inverse matrix is known in both mathematics and physics for a long time. Since by definition $\dot{J}_{zi}\Delta t = J_{zi}(t+\Delta t) - J_{zi}(t)$, starting at $t = 0$ with $J_{zi} = 0$ the evolution in time of the current density can be calculated with discrete (in time and space) governing equation:

$$\mathbf{J}_{\mathbf{z}}(t+\Delta t) = \mathbf{J}_{\mathbf{z}}(t) + \frac{\Delta t}{\Delta x\Delta y}\mathbf{M}^{-1} \cdot \mathbf{E}_{\mathbf{z}}(t), \qquad \textit{Eq. 3.30}$$

where $\dot{\mathbf{J}}_{\mathbf{z}}(t) = [\dot{J}_{zi}(t)]$, $\dot{\mathbf{J}}_{\mathbf{z}}(t+\Delta t) = [\dot{J}_{zi}(t+\Delta t)]$ and $\mathbf{E}_{\mathbf{z}}(t) = [E_{zi}(t)]$. The discrete continuity Equation 3.27a is the same as Equation 3.17.

For each moment of time the *x*, *y* - components of the total magnetic field for cell *i* are calculated using superposition of external magnetic field and the field of *m* - 1 rectangular cells (each with the final dimensions $\Delta x \times \Delta y$, see Figure 3.2):

$$B_{xi} = B_{ex} + \sum_{k}^{m-1} X_{ik}^{\Diamond} J_k \quad \text{and} \qquad \textit{Eq. 3.31}$$

$$B_{yi} = B_{ey} + \sum_{k}^{m-1} Y_{ik}^{\Diamond} J_k, \qquad \textit{Eq. 3.32}$$

where $i \neq k$ and the field constants $X_{ik}^{\Diamond}$ are $Y_{ik}^{\Diamond}$ are given by Equations B3.12 and B3.13, see Appendix B. The components B_{xi} and B_{yi} are used to obtain the field direction angle $\alpha_i(B_y, B_i) = \arctan(B_{xi}/B_{yi})$ and hence $B_i^* = B_i \cdot f(\alpha_i)$, see Equation 2.5. Note that by introducing in the model Equations 3.31 and 3.32 (instead of Equations 3.18 and 3.19) errors in calculating magnetic field are eliminated.

The dependencies of the critical current and power index on magnetic field B_i^* and $f(\alpha_i)$ shown in Figures 2.11 - 2.14 are used to calculate the resistivity ρ_i, see Equations 2.3 - 2.4. The matrices $\overline{\mathbf{M}}^{-1}$, $\mathbf{X}^{\Diamond} = [X_{ik}^{\Diamond}]$, and $\mathbf{Y}^{\Diamond} = [Y_{ik}^{\Diamond}]$ contain only geometrical information and have to be calculated once prior to the time integration process.

3.3.3 Mutual and self inductances of cells

In order to calculate matrix [M_{ik}], accurate formulas for mutual and self-inductances of the cells are needed. The inductance per unit length M_{ik} depends on the distance, shape and

dimensions (length in particular) of the grid cells ΔS_i and ΔS_k. The general formulas and algorithms to calculate the mutual inductances of two parallel straight filaments of equal finite length can be found for instance in [Grov46], see also Appendix B. Accurate formulas employ self- and mutual mean geometric, arithmetic and quadratic distances of cross-sections of the filaments. An approximate formula for the mutual inductance (per unit length, at low-frequency and $i \neq k$) of two long and straight parallel cells of arbitrary cross-section constant along the length and of equal and finite length ℓ_v, is:

$$M_{ik} = \frac{\mu}{2\pi}\left(\ln\frac{2\ell_v}{g_{ik}} - 1\right). \qquad \textit{Eq. 3.33}$$

Here g_{ik} is the mutual mean geometrical distance of two cells cross-section areas and μ is the constant magnetic permeability inside and outside the cells, see Appendix B.

The self-inductance (per unit length, at low-frequency and $i = k$) of a long straight cell of finite length ℓ_v and arbitrary cross-section constant along the cell length is approximately:

$$L = M_{kk} = \frac{\mu}{2\pi}\left(\ln\frac{2\ell_v}{g_k} - 1\right), \qquad \textit{Eq. 3.34}$$

where g_k is the mean geometric distance of the cell cross-section from itself. For a cell with rectangular cross-section of finite dimensions $\Delta x \times \Delta y$ one finds: $g_k \approx 0.2236(\Delta x + \Delta y)$, see Appendix B.

A finite length of the conductor affects the inductance. Length $l_v \approx 100$ mm of a straight sample as shown in Figure 2.4 is in practice often limited by the size of the magnet that provides external magnetic field. A typical width of a Bi-2223/Ag tape is about 4 mm. One may see that according to Equation 3.33 mutual inductance per unit length depends on the ratio of sample length to the distance between the cells. In first instance, the distance between the cell centres varies from Δy to about $2a_c$, see Figure 3.2.

Let us assume that values $l_v = 0.1$ m, $\Delta x = 0.2$ mm, $\Delta y = 7.7$ μm and the distance between two cell centres ranging from $\Delta y = 7.7$ μm to $2a_t = 4$ mm are representative for numerical simulation of straight sample tapes; see Table 2.2 and Figure 2.4. In this case l_v/g_k is a constant and l_v/g_{ik} changes over the range: $25 < l_v/g_{ik} < 1.3 \cdot 10^4$. From more accurate Equations 3.33 and 3.34 one finds: $2.97 < 2\pi M/\mu < 7.32$ and $2\pi L/\mu = 7.37$ correspondingly. For the same range $25 < l_v/(r_i - r_k) < 1.3 \cdot 10^4$ from the less accurate Equation 3.13 it follows $5.55 < 2\pi\overline{M}_G/\mu < 11.8$ and from the less accurate Equation B3.11 it follows: $2\pi M_{G,kk}/\mu = 13.9$.

Hence, Equations 3.13 and B3.11 provide incorrect values of the inductances within the range important for simulating electro-magnetic behaviour of tapes with the relative error that can be as high as 87 % for mutual and self-inductances. Such error is unacceptable for numerical modelling. To abolish the errors instead of Equation 3.13 for $i \neq k$ Equation 3.33 and instead of Equation B3.11 for $i = k$ Equation 3.34 should be used in the model. Note that this step makes Equations 3.16 and 3.30 identical. An error made when using Equations 3.33 and 3.34 is less than 1 % as compared to the existing more accurate, but also more complex formulas for mutual and self-inductances of rectangular cells [Grov46]. Therefore the network model allows to eliminate serious errors in calculating mutual and self- inductances and hence the current density, see Equation 3.29.

In the general case the basic Equations 3.30 and 3.17 represent a set of $m + 1$ equations which are readily accessible with matrix algebra and easy to solve using the finite difference method.

The solution depends on the boundary conditions. When I_{tr} and E_{bz} are given functions of time, the $m + 1$ unknown variables are $\Delta I_{zi}(\boldsymbol{r}, t)$ and $E_{tr}(t)$. The electric field $E_{tr}(t)$ is space-independent as stated in section 3.2.2 and it represents only one unknown. When E_{tr} and E_{bz} are given functions of time, the $m + 1$ unknowns are: $\Delta I_{zi}(\boldsymbol{r}, t)$ and $I_{tr}(t)$.

The input files of the numerical model include: the dimensions of the sample tape and relevant information about the grid (see for example Figure 3.2); magnetic field and temperature dependent direct *E-J* curves of the sample tape; amplitude, direction, frequency and phase of the external magnetic field; amplitude, frequency and phase of the transport current; the operating temperature and the initial conditions. The output files provide information about the time-space evolution of the cell currents and relevant source and drain electric fields, the transport and the total currents (see section 3.5) and the losses calculated over a period (see section 3.4).

The quasi-elliptical cross-section formed by the grid cells approximates the filamentary region of a sample tape (see Figure 3.2). A smaller size of the grid cell on one hand reduces the calculation error and on the other hand increases the calculation time, as the size of the matrix $[M_{ik}]$ is proportional to m^2 due to the mutual inductances involved. About 120 to 250 grid cells provide a reasonable accuracy at an acceptable calculation speed.

The duration of the time step is adapted following the Fehlberg method [DeVr92] to keep the time integration error adequate. For every time step and every point in space the new value for each cell current is established, the magnetic field is calculated using Biot-Savart's law (see Equations 3.31 and 3.32), the field and current dependent resistivity is corrected and new values of the electric field $E_{zi}(t)$ are defined (see Equations 2.3 and 2.4), which allows performing the next step in time. The matrices of the mutual and self-inductances of the cells (Equations 3.33 and 3.34) and of the field constants (Equations B3.12 and B3.13) are calculated once prior to the time integration. The algorithm for solving the governing equations of the network model is illustrated in Figure 3.4.

Therefore, the network model allows a simple and clear derivation of the governing equations for the numerical model. Moreover, the errors in calculating magnetic fields, mutual and self-inductances and hence the current density are eliminated.

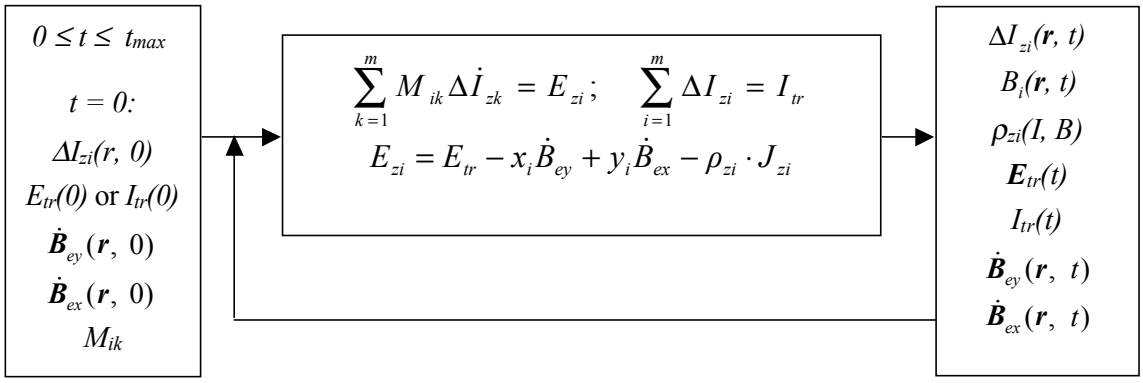

Figure 3.4 Solving the governing equations of the network model.

3.3.4 An example

For a simple case of $m = 2$ the circuit representation of Equations 3.27 and 3.28 using the lumped components is shown in Figure 3.5. Here the voltage sources V_{b1}, V_{b2} and V_{tr} represent the electric fields E_{b1}, E_{b2} due to the changing magnetic field and the transport (current or voltage) source E_{tr} respectively, according to Equations 3.8 and 3.28. The drain electric field $E_{\rho i} = \rho_i J_i$ is represented by the voltage drop across the non-linear resistors $R_1 = \rho_1 l/\Delta S$ and $R_2 = \rho_2 l/\Delta S$, where l is tape length and ρ is given by Equation 2.3. The cell currents

ΔI_{z1} and ΔI_{z2} and the transport current I_{tr} are also displayed. The inductances M_{ik} correspond to the self- and mutual inductances: $M_{11} = M_{22}$ and $M_{12} = M_{21}$.

Equation 3.29 applied to the case reads:

$$\begin{bmatrix} \dot{J}_{z1} \\ \dot{J}_{z2} \end{bmatrix} \cdot \Delta x \Delta y = \begin{bmatrix} M_{11} & M_{12} \\ M_{21} & M_{22} \end{bmatrix}^{-1} \cdot \begin{bmatrix} E_{z1} \\ E_{z2} \end{bmatrix} = \begin{bmatrix} \dfrac{M_{22} \cdot E_{z1} - M_{12} \cdot E_{z2}}{M_{11} \cdot M_{22} - M_{12} \cdot M_{21}} \\ \dfrac{-M_{21} \cdot E_{z1} + M_{11} \cdot E_{z2}}{M_{11} \cdot M_{22} - M_{12} \cdot M_{21}} \end{bmatrix}. \qquad \textit{Eq. 3.35}$$

It is clear from Equation 3.35 that when both the self- and mutual inductances are overestimated by a factor of about 1.8 (for instance due to using Equations 3.13 and B3.13 instead of Equations 3.33 and 3.34) every time step the time derivative of the current density is underestimated by a factor of about 1/1.8, hence resulting in a substantial systematic error in calculated change of the current density in time.

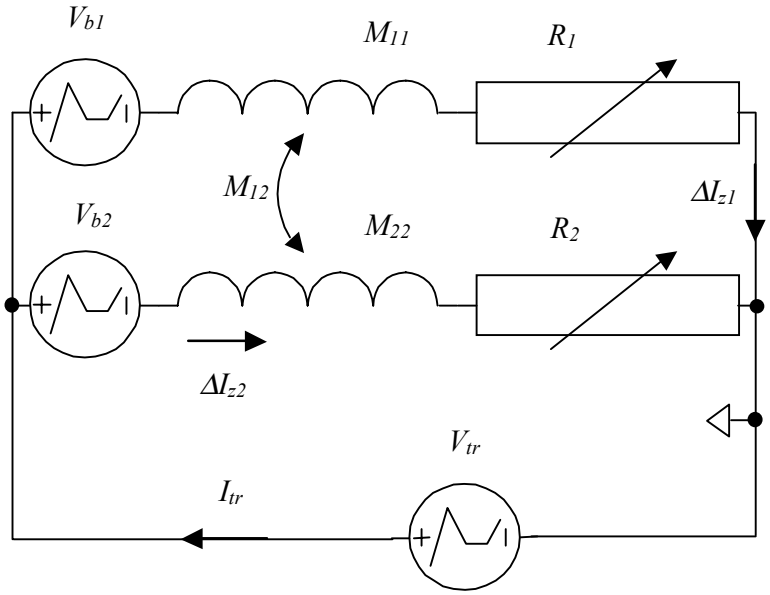

Figure 3.5 Electric circuit representation of Equations 3.27 and 3.28 in the case of $m = 2$.

3.3.5 Macroscopic currents

The numerical model allows to access quantities that are difficult to measure such as the local distribution of the current inside a superconductor. However, it is not less important to introduce macroscopic quantities that can be measured. Hence, to enable a verification of the network model, the outcome of the model must be converted into measurable quantities. Equation 3.36 states that at any moment of time the transport current through a tape is the algebraic sum of the cell currents, see also Equation 3.27:

$$I_{tr} = \int_{S_c} J(r) dS = \sum_{i=1}^{m} J_i(r) \cdot \Delta S_i \,. \qquad \textit{Eq. 3.36}$$

The total current I_{tt} through a tape is the sum of modules of cell currents:

$$I_{tt} = \int_{S_c} |J(r)| dS = \sum_{i=1}^{m} |J_i(r)| \cdot \Delta S_i \ . \qquad \textit{Eq. 3.37}$$

Therefore, the total induced (screening or magnetization) current I_{id} in a superconductor is defined as:

$$I_{id} = I_{tt} - |I_{tr}| . \qquad \textit{Eq. 3.38}$$

Note that a known relation between the modulus of a sum $|I_{tr}|$ and the sum of modules I_{tt} states that $I_{tt} \geq |I_{tr}|$.

The current I_{id} is confined to the tape volume and for this reason difficult to measure in the same way as for instance a transport current in the electrical circuit. Indirectly it can be evaluated by measuring the magnetic moment with pick-up coils, see for instance [Rabb01]. Obviously, in an ideal superconductor with many fine twisted and decoupled filaments the condition $|I_{id}| << |I_{tr}|$ should be fulfilled. At present in practical high-T_c superconductors, the filaments are not twisted and fully coupled and therefore rather the condition $|I_{id}| \sim |I_{tr}|$ might be expected.

When the self-field effect is negligible, the external magnetic field is constant and the transport source provides a constant e. m. f. of $E_{tr} = E_c = 10^{-4}$ V/m and after the transients have decayed out then both the transport and the total currents are equal to the critical current, hence $I_{id} = 0$ and $I_c = |I_{tr}| = I_{tt}$. At this condition the critical current of a tape can be calculated using Equation 3.37:

$$I_{c1} = |I_{tr1}(E_c)| = \sum_{i=1}^{m} |J_{1i}(r)| \cdot \Delta S_i \ . \qquad \textit{Eq. 3.39}$$

The effect of self-field on the critical current is discussed in section 3.4.1.

3.3.6 Cyclic losses

The loss of a Bi-2223/Ag tape superconductor depends on many parameters. The total and the transport losses of a superconductor per unit length per cycle of duration τ_0 are respectively:

$$Q_{tot} = \int_{\tau_0} \int_{S_c} E_\rho \boldsymbol{J} d\boldsymbol{S} dt \quad \text{and} \quad Q_{tr} = \int_{\tau_0} E_{tr} I_{tr} dt \ , \qquad \textit{Eq. 3.40}$$

where E_ρ is given by Equation 2.2. The magnetisation loss Q_m is calculated by:

$$Q_m = Q_{tot} - Q_{tr} \ . \qquad \textit{Eq. 3.41}$$

For the case when $I_{id} \equiv 0$ the transport current is uniformly distributed over the cross-section of the superconductor and the total loss given by Equation 3.40 reads:

$$Q_{ts} = \int_{\tau_0} E_\rho I_{tr} dt \ . \qquad \textit{Eq. 3.42}$$

The cyclic loss depends on the time derivative of the transport current. For sinusoidal transport current it changes linear with frequency. The mean power loss depends on the current amplitude but not on the frequency and for this reason this part of the loss is called static further on.

3.4 Verification of the network model

In this section calculated losses of superconducting tapes are discussed and compared to the relevant measurements. The goal is to verify the network model prior to calculating *V-I* curves and losses of AC coils. Geometry and properties of the studied sample tapes are summarised in Chapter 2. A tape is placed in an external uniform, transversal, and unidirectional magnetic field, which is a given function of time. The tape is connected to a transport current (or voltage) source. The temperature is kept at 77 K unless stated otherwise.

The model allows to calculate the current distribution inside a superconductor for an arbitrary combination of transport current, transverse magnetic field and temperature. However, the current distribution inside a tape is rather difficult to obtain experimentally. It is therefore more convenient to verify the model by comparing for instance the simulated and measured losses under the same conditions. For power coils the case when harmonic transport current and harmonic magnetic field are simultaneously present is of most importance.

The input data characterising the tape (model sample A**)** are taken from Table 2.2. In addition the following parameters are used: $I_{c0} = 126$ A, $n_0 = 19$ (at 77 K, self-field and $E_c = 10^{-4}$ V/m) and $\rho_m = 2.5$ nΩm; the outer dimensions of the elliptical filamentary core are $a_c = 3.9$ mm and $b_c = 0.17$ mm, the rectangular grid cells are sized $\Delta x = 217$ μm and $\Delta y = 21.3$ μm and the length between the voltage taps is $\ell_v = 48.2$ mm (Figures 2.4 and 3.2).

3.4.1 Both direct transport current and magnetic field present

In order to illustrate the interplay of total, transport and induced currents (as defined by Equations 3.36 - 3.38) in a BSCCO-2223/Ag tape the following numerical experiment is performed and the result is shown in Figure 3.6. The uniform and transversal magnetic field is ramped during 1.5 s with a constant derivative up from zero to the value of $B_e = 45$ mT and then kept constant. The field is directed perpendicular to the tape broad face meaning $\alpha = 0^\circ$ (see Figure 2.7).

The changing magnetic field induces the current I_{id} reaching 90 A in this case. Since the critical current density depends on the magnetic field, the change in current is non-linear with time. During the period when the magnetic field is constant, relaxation of the current to a steady value (flux creep) obviously takes more than 10 s. During this period of time the transport current I_{tr} is zero and for this reason $I_{tt} = I_{id}$.

The e.m.f. of the transport voltage source connected to the sample is kept zero until the moment of time t_2 (equal to 12 s in Figure 3.6) and then within 0.2 s it increases so that the electric field across the sample $E_{tr}(t > 12.2\ \text{s}) = E_c = 10^{-4}$ V/m. The value of the electric field across the sample is kept constant until the end of the simulation (to match the scale of the right vertical axis, the value of E_{tr} is multiplied by 100 in the figure).

The transport current increases and reaches a stable value at the end of the transient process that takes a few seconds. During the transient process the current I_{id} decays to zero so that at the end of the process $I_{tt} = I_{tr}$. As $E_{tr} = E_c$, by definition the later value is the critical current of the

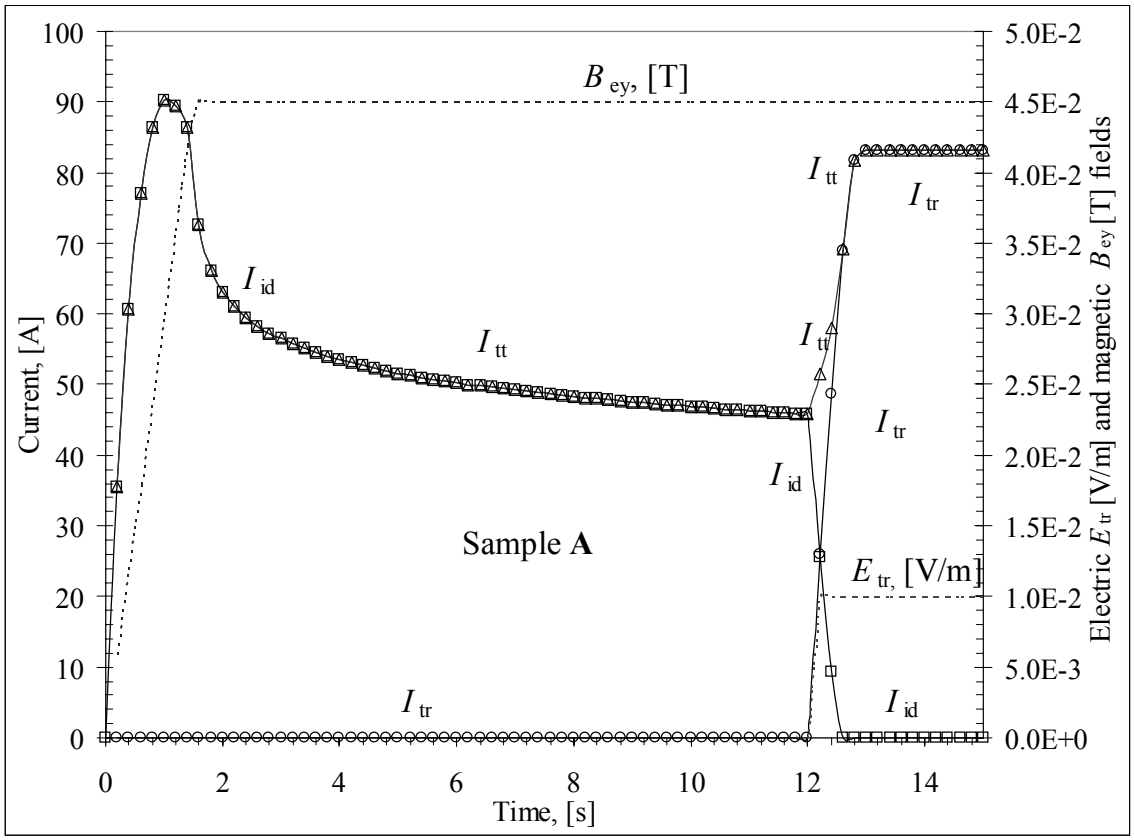

Figure 3.6 Calculated total, induced and transport currents versus time at 77 K for sample A (as the response to a field sweep, the markers are used to distinguish the crossing lines).

sample: $I_{tt} = I_{tr} = I_c(B_e)$ equal to 83.1 A in this example. The result is independent on the value of t_2 that is varied from 1 to 100 s during the simulation. From the view of application at 50-60 Hz it is evident that modern commercial high-T_c superconductor responds slowly to changing magnetic and electric fields (typical response time of 1 to 100 s as compared to a typical change of the fields within 5 ms at 50 Hz).

Choosing a value of E_{tr} and repeating the calculation, the whole $E_\rho(I_{tr})$ curve can be calculated and then compared to measured curves (such as displayed in Figure 2.8 for sample V). Such a comparison shows that when the measured $E_\rho(I_{tr})$ characteristic is not corrected for the self-field effect (see section 2.4.1) and is used as input for the numerical model, the model is and is not self-consistent at a magnetic field above and below about 0.1 T (for $\alpha = 0^\circ$) respectively.

Consider a tape placed in a direct uniform external magnetic field and carrying a direct transport current. The transport current through the tape produces an additional magnetic field that makes the resulting magnetic field non-uniform and affects the critical current of the tape itself. For high-T_c tapes that are able to carry higher currents the effect is more pronounced.

Due to the intrinsic anisotropy of the Bi-2223 superconductor, tapes are especially sensitive to the component of magnetic field that is perpendicular to the tape broad face (Chapter 2, Figures 2.1 and 2.7). A simple calculation shows that a transport current of 100 A through tape A produces a perpendicular magnetic field of 10 to 20 mT at the sample surface, so the effect may be significant, see Figure 2.13. An experimental attempt to compensate the self-field with two additional superconducting tapes sandwiching a sample is described in [Fles99] and [Spre99]. A 50-60 % increase of the critical current is demonstrated with the self-field largely suppressed leading to a considerably different E - I curve. For modelling it is important to employ the critical current as close as possible to the intrinsic one. An E - I curve

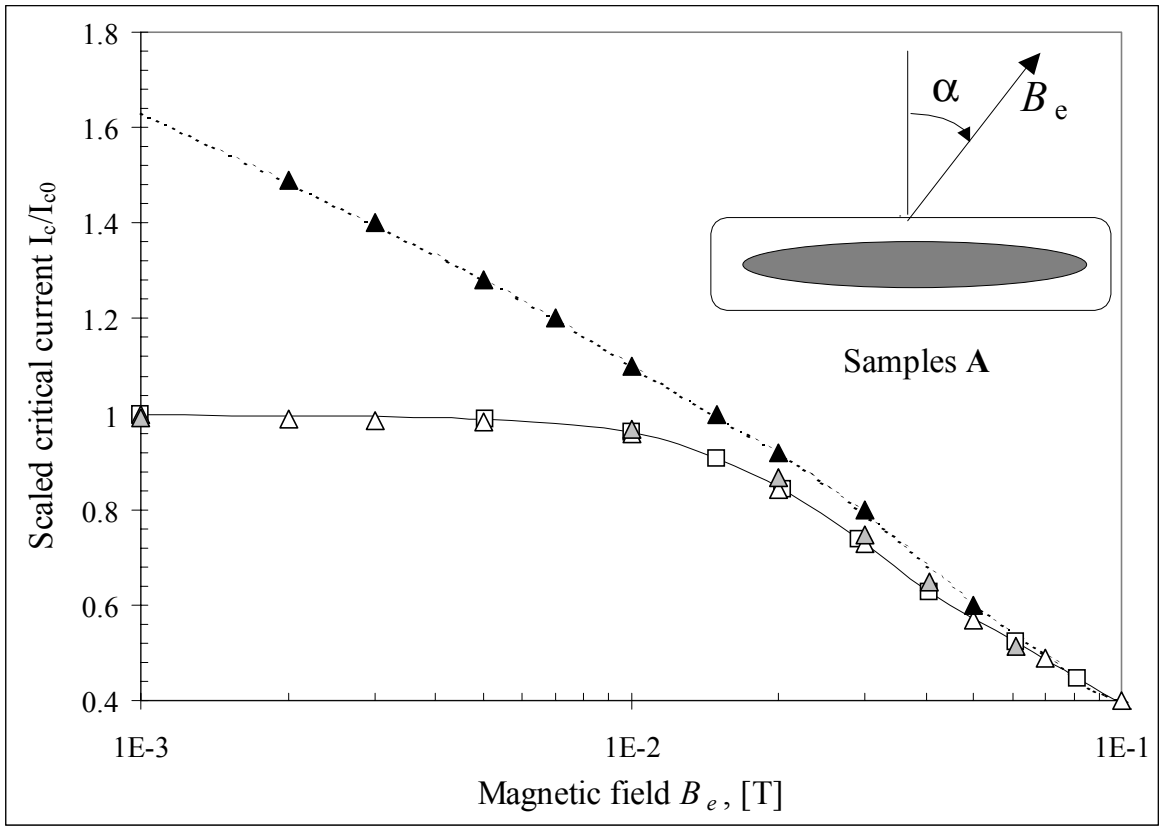

Figure 3.7 Scaled critical current versus external magnetic field with and without correction for self-field at 77 K and α = 0° for tape A, the lines are calculated, the symbols represent the measured data.

measured in presence of the self-field effect could not be used as an input of the model – in this case the self-field effect would be double accounted for (1-st time with the measurement and 2-nd time during the simulation) which would lead to an error. It is rather difficult to measure self-field inside the tape and for this reason the experimental critical currents are usually presented as a function of the external magnetic field. Therefore, the self-field is often ignored.

In order to determine the intrinsic J_c - B^* curve the following calculation is performed. All critical currents are gathered at bath temperature 77 K and electric field criterion $E_c = 10^{-4}$ V/m and the external magnetic field is perpendicular to the tape broad face. All I_c - B curves are scaled by the critical current I_{c0} measured without self-field correction (and equal to 126 and 112 A respectively for samples A and A6). The scaled I_c - B curves with self-field ignored are compared in Figure 3.7 (open boxes with the line – sample A, open triangles – sample A6). It is shown in the figure that both samples have practically the same magnetic field retention of the scaled critical current when the self- field is ignored despite different values of the critical current at zero external magnetic field. Outer dimensions of sample A6 (about 4×0.2 mm) are comparable to those of sample A, Table 3.1. Therefore the samples are comparable in terms of dimensions and performance.

The scaled measured I_c - B curve of sample A6 after self-field effect correction [Spre99] is shown by the filled triangles in Figure 3.7. An assumption is made that the scaled intrinsic J_c – B^* curve of sample A is the dashed line in Figure 3.7. Using the network model, the critical current of the sample without the self-field correction is calculated. The model uses the dashed line as the local J_c - B^* curve (assumed to be the same for any cell) and based on this it calculates the local values of the cell currents in a tape, Equations 3.30 and 3.17; then it calculates the magnetic field for the current pattern at every time step,

Equations 3.31 - 3.32 and finally it returns the value of the critical current for each value of the external magnetic field, Equation 3.37.

The calculated critical current without self-field correction is displayed by the grey triangles in Figure 3.7. The intrinsic (self-field free) scaled J_c - B curve for sample A is found rather close to the one measured by [Spre99] shown by black triangles in Figure 3.7. In this experiment the self-field was partly compensated by using two additional tapes fed with current. The intrinsic curve is used as input data for the calculation of E-I curves and losses of tapes and coils described further on. It is confirmed by numerical modelling that self-field considerably affects the critical current (of sample A) mostly via the perpendicular component of self-magnetic field.

When the self-field is compensated, the intrinsic I_{c1} - B curve can be obtained from a transport current measurement, where I_{c1} follows Equation 3.39. When the self-field effect is not negligible, a curve I_{c2} - B is obtained during transport measurement and Equations 3.36 - 3.38 are valid. In this case for each value of the external magnetic field the induced current is simply $I_{2id} = I_{c1} - I_{c2}$, see Figure 3.7.

In principle, the self-field effect on the critical current of an oxide superconductor tape can be reduced by transposition of the filaments. In practice however this is difficult to achieve without damaging the filaments (and hence reducing the critical current). For this reason commercial tapes with transposed filaments do not exist. Therefore, the numerical model completes the experiments and provides a valuable insight on the interplay between total, transport, induced and critical currents in high-T_c tapes.

3.4.2 Both time-harmonic transport current and magnetic field present

In this section a single tape carrying a transport current and simultaneously exposed to uniform external magnetic field is considered. The input data characterising tape A are taken from Table 2.2. The additional assumptions for the simulation are: $I_{c0} = 126$ A, $n_0 = 19$ (at 77 K, self-field and $E_c = 10^{-4}$ V/m) and $\rho_m = 2.5$ nΩm; the outer dimensions of the elliptical filamentary core $a_c = 3.9$ mm and $b_c = 0.17$ mm, the sizes of the rectangular grid cells are $\Delta x = 217$ μm and $\Delta y = 21.3$ μm and the length between the voltage taps is $\ell_v = 48.2$ mm (Figure 2.4). The dependencies of the critical current, n-value on magnetic field (both amplitude and direction) and $f_\alpha(\alpha)$ are listed in Tables 2.4 and 2.5. Note that the intrinsic dependence (self-field free, see Figure 3.7) is used for the critical current.

The purpose here is to verify the numerical model when using measured data for single tapes operating under model conditions that are typical for AC coils. For this reason measured and calculated total losses in tapes are only compared here without presenting all the details. The details of the measurements are described in [Rabb01] as well as the relevant components of the total losses (such as magnetisation and transport current) in [Rabb01], [Oome00] and [Clerc95]. The amplitude of the external magnetic field during the measurements was kept below 80 mT. In a 1-MVA coil operated at 77 K the amplitude of the magnetic field may exceed $B_{e0} = 80$ mT. For this reason the data calculated at $B_{e0} = 100$ and 150 mT are also shown in Figures 3.8-3.11.

Both transport current and magnetic field oscillate harmonically in time. The amplitudes of the transport current and magnetic field are varied independently in order to match most of the current and field combinations typical for coils. Note that the transport current loss consists of self-field and static loss components. A sinusoidal transport current through a high-T_c tape is assumed: $I_{tr} = I_{tr0} \sin \omega t$ with ω circular frequency and I_{tr0} amplitude of the current. The oscillating transport current causes self-magnetic field (see Figure 3.7), which oscillates harmonically with the same frequency and in phase with the transport current. The continuous changing self-field affects the critical current and causes screening currents. The combination of a changing transport current and self-field causes a self-field loss. The tape is also exposed to

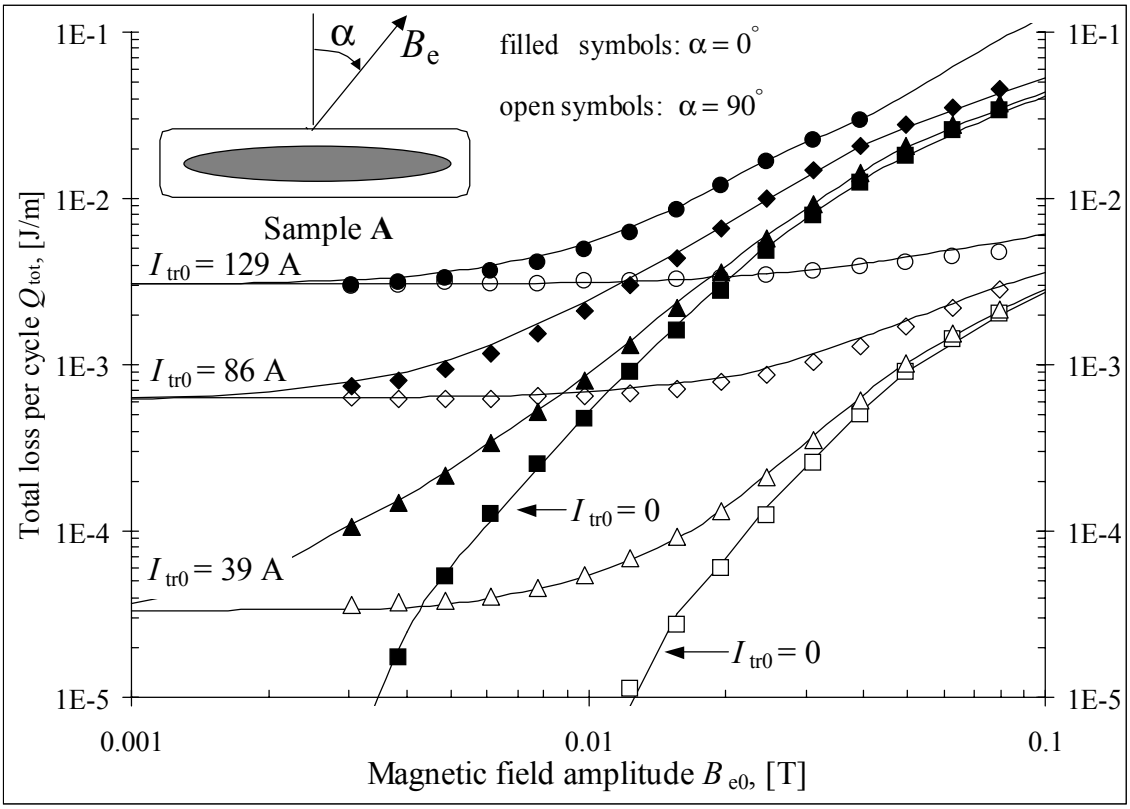

Figure 3.8 Total loss per cycle versus external magnetic field amplitude at 77 K and 48 Hz (the lines are calculated, the symbols represent the measured data).

external magnetic field that varies with the same frequency and in phase with the transport current: $B_e = B_{e0} \sin \omega t$, where B_{e0} is the amplitude.

A changing magnetic field induces an electric field inside a superconductor in agreement with Equation 3.8: $E_{bz} = \omega(-xB_{ey0} + yB_{ex0}) \cos \omega t$. The simulations and experiments described here are performed with tape A at the frequency 48 Hz and temperature 77 K. The amplitude and direction of magnetic field with respect to the tape, Figure 2.7 are varied independently from the transport current amplitude.

The losses are calculated using Equations 3.40. The results of the simulations (lines) and of the measurements (symbols) are compared in Figure 3.8 for $\alpha = 0^\circ$ and $\alpha = 90^\circ$ (filled and open symbols respectively). In the limit $I_{tr0} = 0$, the total loss is equal to the magnetisation loss, see Equations 3.40 and 3.41 (the measured loss is shown by the boxes in the Figure). The loss depends strongly on the magnetic field amplitude B_{e0} and angle α. For instance, at $\alpha = 0^\circ$ and 3 mT< B_{e0} < 100 mT, the loss changes by more than three orders of magnitude (from about 0.01 mJ/m to 40 mJ/m). The ratio of magnetisation loss for $\alpha = 0^\circ$ and for $\alpha = 90^\circ$ ranges from about 80 to about 15 at B_{e0} equal to 12 mT and 100 mT respectively, see also Figure 3.10. The calculated and measured magnetisation losses (for $I_{tr0} = 0$) agree well. The maximum relative error is less than 16 % and the average error is below 8 % over the whole range of parameters displayed in Figure 3.8.

In the limit of $B_{e0} = 0$ the total loss is equal to the transport loss, see Equations 3.40 and 3.41. For B_{e0} < 2 mT and I_{tr0} > 60 A the total loss is mostly the transport current loss and namely the self-field loss. Since the effect of external magnetic field on the losses is small in this range,

the dependence on the field angle vanishes and the loss curves for $\alpha = 0^\circ$ and for $\alpha = 90^\circ$ come together. For $I_{tr0} \leq 60$ A the same effect is observed outside the area displayed in the Figure at $B_{e0} < 1$ mT. Since there are no experimental data available in this range, in order to compare simulations and experiments we consider an expanded area $B_{e0} < 10$ mT. At a constant value of I_{tr0} for $\alpha = 90^\circ$ (since magnetisation loss is far lower) the total loss becomes independent of the amplitude of external magnetic field at higher values of B_{e0} than for $\alpha = 0^\circ$. Hence, for $I_{tr0} = 39$ A this allows to estimate the transport current loss (equal to 33 μJ/m) even before the total loss curves for $\alpha = 0^\circ$ and for $\alpha = 90^\circ$ come together. The calculated and measured total losses in this area agree well and predict the same values of the transport losses (for $I_{tr0} = 39$; 86 and 129 A). The maximum relative error is less than 13 % and the average error is below 5 % over the whole range of the parameters discussed.

The overall agreement between the measured and calculated total losses is very good. The average deviation is below 6 % over the whole range shown in Figure 3.8. To compare with, the estimated uncertainty of the loss measurement itself is about 15 % [Rabb01, p. 194]. The uncertainty in the calculated loss among other contributions (such as the assumptions of the model, dimensions of a sample, etc.) includes the uncertainty of the used direct *E-J* curve (see Equation 2.2). The uncertainty in the resistivity of the composite conductor is determined by the uncertainty in the filling factor, the resistivity of the matrix and of the superconductor (Equation 2.3). In turn, the uncertainty in resistivity of a superconductor depends on the uncertainty in the critical current and *n*-value. For instance, when the *n* -value ranges from 5 to 20 (Figure 2.14) an estimate using Equation 2.4 shows that the uncertainty of 1 % in critical current

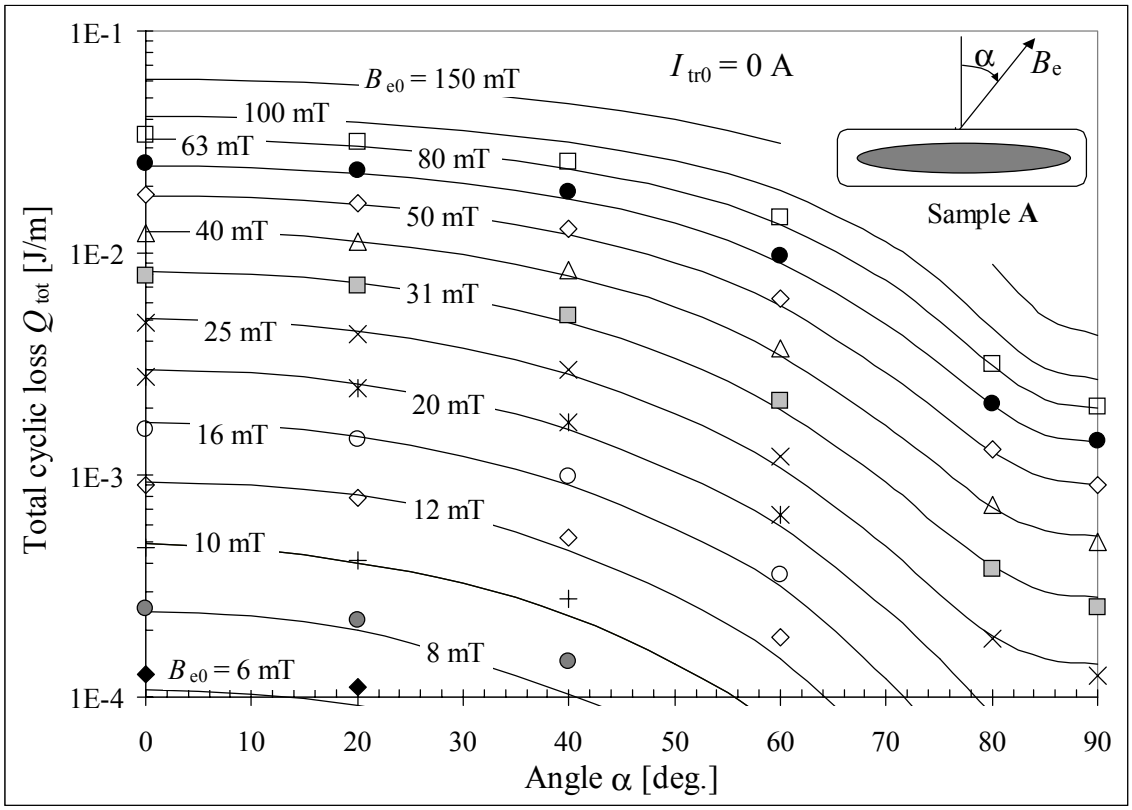

Figure 3.9 Total cyclic loss versus the angle between external magnetic field and the normal to the tape surface at I_{tr0} = 0 A, 77 K and 48 Hz (the lines are calculated, the symbols represent the measured data).

(Figure 2.13) causes an uncertainty in ρ_s ranging from 4 to 21 % respectively. This is the reason why a direct E - J curve used as an input for simulations must be accurately measured and described, see Chapter 2.

In Figures 3.9 - 3.11 the calculated and measured total losses of the same sample are compared at I_{tr0} = 0; 39 and 86 A in more detail. The loss is displayed as a function of the angle $0^\circ \le \alpha \le 90^\circ$ between the external magnetic field and the normal on the tape surface with other conditions kept the same as in Figure 3.8.

In Figure 3.9 over the whole range of parameters displayed (I_{tr0} = 0 A; $0^\circ \le \alpha \le 90^\circ$ and 6 mT ≤ B_{e0} ≤ 150 mT) the total loss changes from 10 μJ/m to 61 mJ/m, which is more than three orders of magnitude. The calculated data are shown by the lines while the experimental data are shown by the symbols in the range 6 mT ≤ B_{e0} ≤ 80 mT and 0.1 mJ/m ≤ Q_{tot} ≤ 34 mJ/m. In this range (except a few points at B_{e0} < 10 mT) an overall agreement between the simulation and the measurement is good. The maximum relative error is less than ± 14 % and the average error is below 9 %. In the range B_{e0} < 10 mT and $\alpha > 20^\circ$ the discrepancy between the simulation and the measurement is somewhat larger. A finer grid in the model could reduce the error. This, however, requires more computing effort. From a practical point of view such effort is not justified, since the loss Q_{tot} ≤ 0.1 mJ/m constitutes a small fraction (a few percent) of the maximum loss expected in a coil. For instance, at B_{e0} = 150 mT and $\alpha = 90^\circ$ Q_{tot} = 4.3 mJ/m and the loss Q_{tot} = 0.1 mJ/m represents merely 2 % of this value. Hence a larger error (made when calculating the loss in the range B_{e0} < 10 mT and $\alpha > 20^\circ$) due to the relatively small weight will cause an acceptable increase of the overall uncertainty.

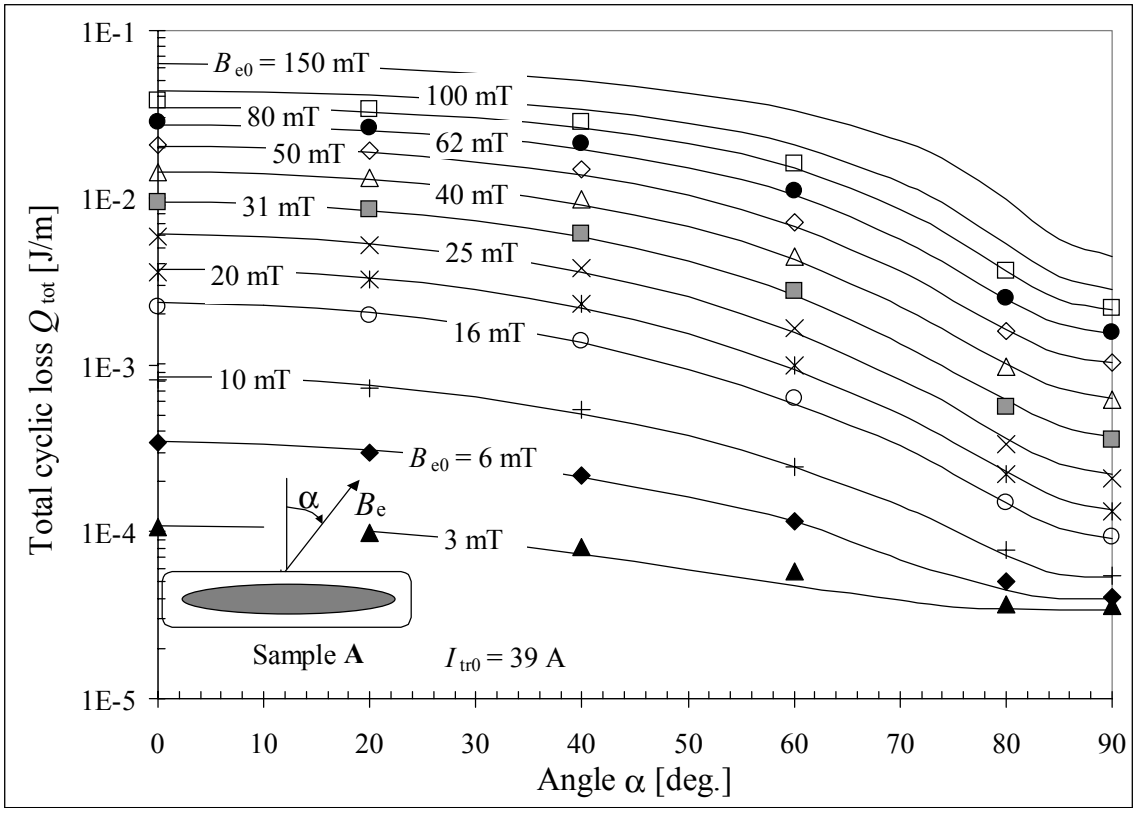

Figure 3.10 Total cyclic loss versus the angle between external magnetic field and the normal on the tape surface at I_{tr0} = 39 A, 77 K and 48 Hz (the lines are calculated, the symbols represent the measured data).

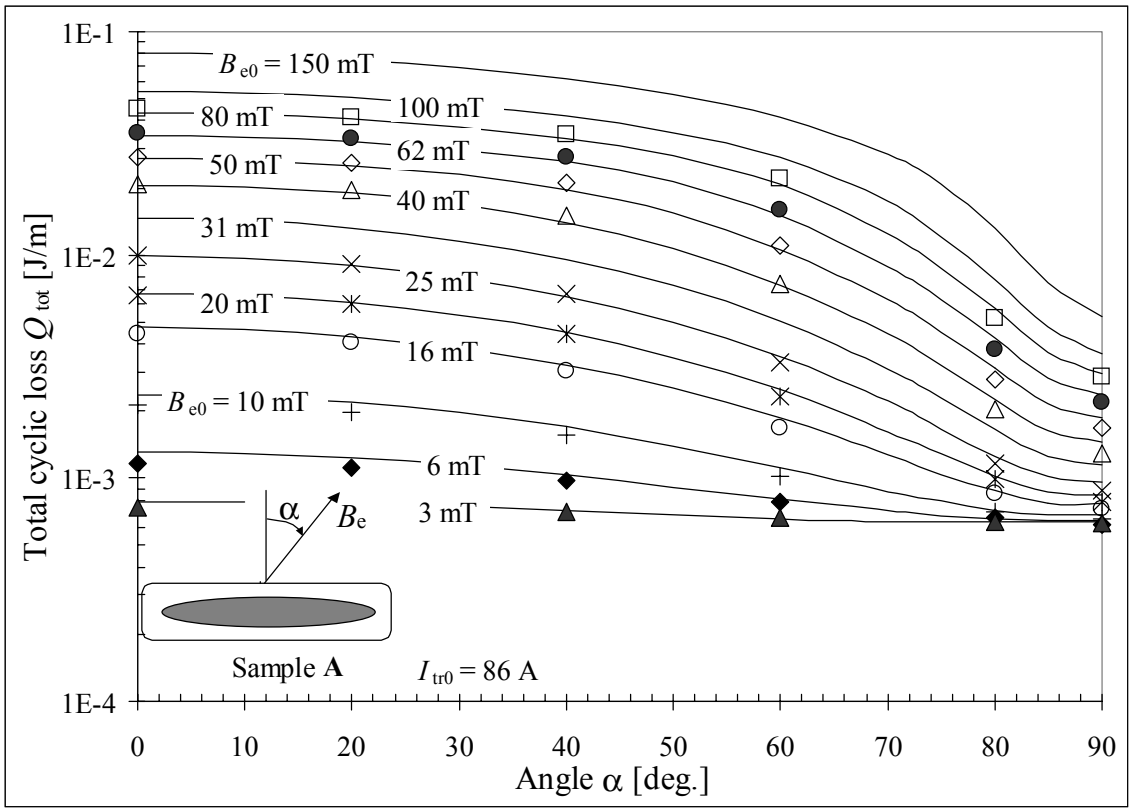

Figure 3.11 Total cyclic loss versus the angle between external magnetic field and the normal on the tape surface at I_{tr0} = 86 A, 77 K and 48 Hz (the lines are calculated, the symbols represent the measured data).

In Figure(s) 3.10 (and 3.11) the total loss changes from 40 μJ/m to 64 mJ/m (and from 620 μJ/m to 80 mJ/m), which is more than three (and two) orders of magnitude over the whole range of parameters displayed: $I_{tr0} = 39$ A (and $I_{tr0} = 86$ A); $0^\circ \le \alpha \le 90^\circ$ and $3\text{ mT} \le B_{e0} \le 150$ mT. The lines show the simulated data while the experimental data are shown by the symbols in the range $3\text{ mT} \le B_{e0} \le 80$ mT. Again, the agreement between simulation and measurement is very good. The maximum relative error is less than 12 % (and 13 %) and the average error is below 5 % (and 6 % respectively).

Summarising, the simulated and the measured total loss of sample tape A at 77 K and 48 Hz as function of the transport current amplitude I_{tr0} and external magnetic field amplitude B_{e0} and angle α are compared in Figures 3.8 - 3.11. The transport current and magnetic field are harmonic, present simultaneously, and oscillate in phase with each other. In this case I_{tr0}, B_{e0} and α are varied independently. The range of the parameters covered in the comparison is $0 \le I_{tr0} \le 129$ A; $3\text{ mT} \le B_{e0} \le 80$ mT and $0^\circ \le \alpha \le 90^\circ$. Within this range the total loss changes from less than 10 μJ/m ($I_{tr0} = 0$ A, $B_{e0} < 10$ mT and $\alpha > 10^\circ$) to more than 45 mJ/m ($I_{tr0} = 129$ A, $B_{e0} = 80$ mT and $\alpha = 0^\circ$) that is about four orders of magnitude. For practical reasons the comparison is confined to the range $10\text{ μJ/m} \le Q_{tot} \le 45$ mJ/m.

The total loss is computed using the 2-dimensional network model. The model uses as input direct magnetic field-dependent *E* - *J* curve of a sample together with the geometrical data of the cross-section. Within this range the calculated and the measured total loss agree with each other very well, the average relative uncertainty is below 7 %. Hence, the network model is verified against available experimental data, and it allows reliable calculation of the total losses when transport current and magnetic field are present simultaneously.

Similar conclusions are obtained by comparing simulated and measured total loss data at 77 K for sample tapes V and Sh (see Table 2.2). A detailed comparison is published in [Shev99]

(sample V) and in [Yaza00] (sample Sh). The somewhat larger discrepancy between the calculations and measurements (as compared to tape A) is due to a less advanced model used at the time, lower quality of sample tapes and a larger experimental uncertainty. Today further reduction of the error would be possible by comparing losses of the same tapes measured again in the advanced set up [Rabb01a] with calculated losses using the advanced network model as described in this chapter.

3.5 Numerical results outside the measured range

The total loss of a superconductor depends on many parameters. The external magnetic field may have different time dependence (can be harmonic or non-harmonic). A harmonic external magnetic field is represented by a number of independent variables, such as amplitude, angle, frequency, phase and spatial distribution (uniform, non-uniform). The transport source is characterised by amplitude, frequency, phase and time dependence and it can be a current or a voltage source. Temperature, strain, sample geometry and arrangement (internal, external, electromagnetic, thermal and mechanical) may as well affect the losses. Hence, assuming that for characterisation 10 data points per independent variable are required, one may estimate that a systematic study of even one sample tape would require an array of at least 10^{11} points, which obviously is a huge effort. In addition, the direct E - J relation may be affected by the tape manufacturing process, self-field, by handling the superconductor when preparing and when operating a sample or a coil, which further increases the size of such array. In order to keep the size of the parameter array at an acceptable level, the number of variables is drastically reduced in this study.

In the previous section both external magnetic field and transport current are assumed harmonic, oscillate at the same frequency and are in phase. The external magnetic field is uniform and the transport source is a current source. Any influence of strain on the direct E - J relation and losses is neglected. Only single straight tapes with non-twisted filaments are considered with the entry effects excluded. Hence, the independent variables so far are: amplitude and angle of harmonic external magnetic field and amplitude of the harmonic transport current at the frequency of 48 Hz and temperature of 77 K.

For calculating losses the network model uses magnetic field-dependent direct E - J curve of a sample together with the geometrical data. Hence, there are no other experimental (especially no AC) data used to come to the simulation results shown in Figures 3.8 - 3.11. Moreover, there are no assumptions or adjustments of the model made for calculating the loss specifically at 48 Hz. The good agreement achieved as presented in the previous section between simulation and experiment implies that at a different frequency around 50 Hz the simulation may be correct too. The calculated and measured losses are compared at 77 K so far. All the information required to compute the loss at this temperature is in the E - J curve. Hence, when the E - J curve is measured at a different temperature (see for instance Figure 2.19), it provides enough information for computing the loss at this temperature. This is an advantage of the numerical model as compared to empirical formulas [Rabb01] and [Magn01], where extrapolation outside the range covered by experiment usually lacks accuracy.

Furthermore, a good agreement of the calculated and measured loss data assures that other parameters computed simultaneously with the losses are also correct. The time dependence of the calculated current and electric field is presented in Figure 3.12 for the regime shown in Figure 3.8 by a single point. In Figure 3.12 the line with the circles shows the total current I_{tt}, the diamonds show the transport current I_{tr} and the boxes show the induced current I_{id} calculated from Equations 3.36 - 3.38 respectively, while the electric field of the transport current source is shown by the dashed line.

The calculation starts at the virgin state ($t = 0$, $B_e = 0$ and $I_{tt} = I_{tr} = I_{id} = 0$). The steady state (resulting in a current pattern repeating itself in time) is settled within less than 5 ms. Since this moment the modulus of total current changes from 86 to 165 A and the time dependence of the

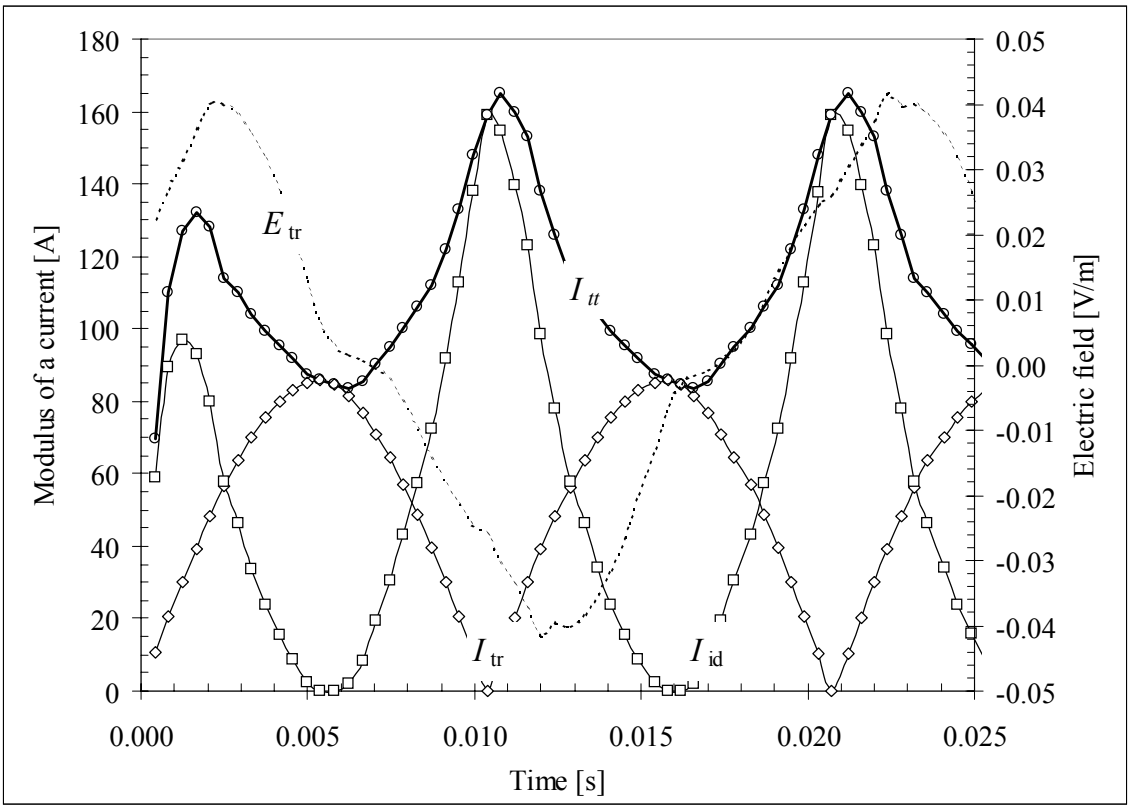

Figure 3.12 Calculated time dependence of the electric field of the transport current source E_{tr} and the modules of the total (I_{tt}), induced (I_{id}) and transport (I_{tr0}) currents and at B_{e0} =0.1 T, $\alpha = 0°$, 77 K and 48 Hz (the markers are used to distinguish between the crossing lines).

total current is rather complicated. Because the external magnetic field oscillates with the same frequency and in phase with the transport current, it is not shown in the figure. The phase of the induced electric field (caused by magnetic field change) is shifted 90° with respect to the phase of the transport current and has maxima when $I_{tr} = 0$. The induced current I_{id} follows almost instantly the induced electric field (the effective inductance of the loop is relatively small and the phase shift is not visible in the figure). It is seen that for this particular combination of parameters the modulus of the induced current is almost twice as large as of the transport current, which means that the superconducting tape is not used very efficiently.

The ratio of I_{tr} and I_{id} reflects the fact that the tape has non-twisted superconducting filaments. It is known that the twisting of the filaments in combination with resistive barriers around a filament or bundles of filaments would reduce I_{id}. In practice, however, it is difficult to realise without causing a reduction of the critical current and price-performance ratio. For this reason commercial tapes with twisted filaments do not exist yet.

Further analysis shows that a change of α (while other parameters are kept constant) has a relatively small effect on the peak value of the induced current. For instance, at $\alpha = 90°$, the peak value of $|I_{id}|$ is about 188 A (which is higher than at $\alpha = 0°$), though the total loss reduces 8 times as compared to the case when $\alpha = 0°$. At the same time, the phase shift between the induced electric field and I_{id} is well seen at $\alpha = 90°$ (not shown in the figure). Both electric field and current show a rather complicated spatial distribution. A precise analysis of the time-dependent signals is beyond the scope of this study.

So far it has been assumed that the total cyclic loss of a superconducting tape is independent from the operating frequency. The assumption is reflected in presenting the total

loss as energy per cycle per meter of tape. When the assumption holds, Q_{tot} can be defined at any frequency (for instance at 48 Hz as it was done for tape A, see Figures 3.8 to 3.12) and the power loss per meter tape at any other frequency f can be calculated in a convenient way as the product fQ_{tot}. To verify the assumption, a simulation is performed for tape A at 77 K, B_{e0} = 10 mT, $\alpha = 0°$, I_{tr0} = 71 A in the frequency range 1 Hz ≤ f ≤ 100 Hz.

The total, transport and magnetization losses are calculated using Equations 3.40 - 3.41. The result is shown in Figure 3.13. It is seen that transport, magnetisation and total energy losses depend on frequency. For this particular example the relative change (as compared to the loss at 50 Hz) of the total energy loss at 1 and 100 Hz is respectively 29 and 5.5 %. For the transport energy loss the change is even larger. For other combinations of the parameters the relative change in the total energy loss depends on the ratio between the transport and magnetisation energy loss. In this work the frequency dependence of the total loss for tapes was not studied experimentally. A comparison of the obtained numerical result with the measurements of [Stav98] performed (for a different tape) in the frequency range from 59 to 2500 Hz shows that the simulation and the measurement agree qualitatively. Hence, presenting the total loss as energy per cycle per meter of tape is only accurate when the frequency is specified at which the loss is measured.

So far I_{tr0}, B_{e0} and α were varied independently. For coils, however, there are certain specific cases. It will be shown (in Chapter 4) that for a tape wound in a power coil I_{tr0} and B_{e0} can be linked via the magnetic field constant k_m (which is time independent and space dependent). This assumption makes α time independent and space dependent since $\alpha = \arctan(B_{ex}/B_{ey})$, see Figure 2.7. When for every position inside the coil windings k_m and α are specified (in other words, k_m and α are averaged over the cross-section of the tape and specified along the tape length), then B_{e0} and α are known for every value of the amplitude I_{tr0} of the coil current. Hence, the local value of the total loss (per meter of the tape length, Equation 3.40) can be computed for every position along the tape in the coil.

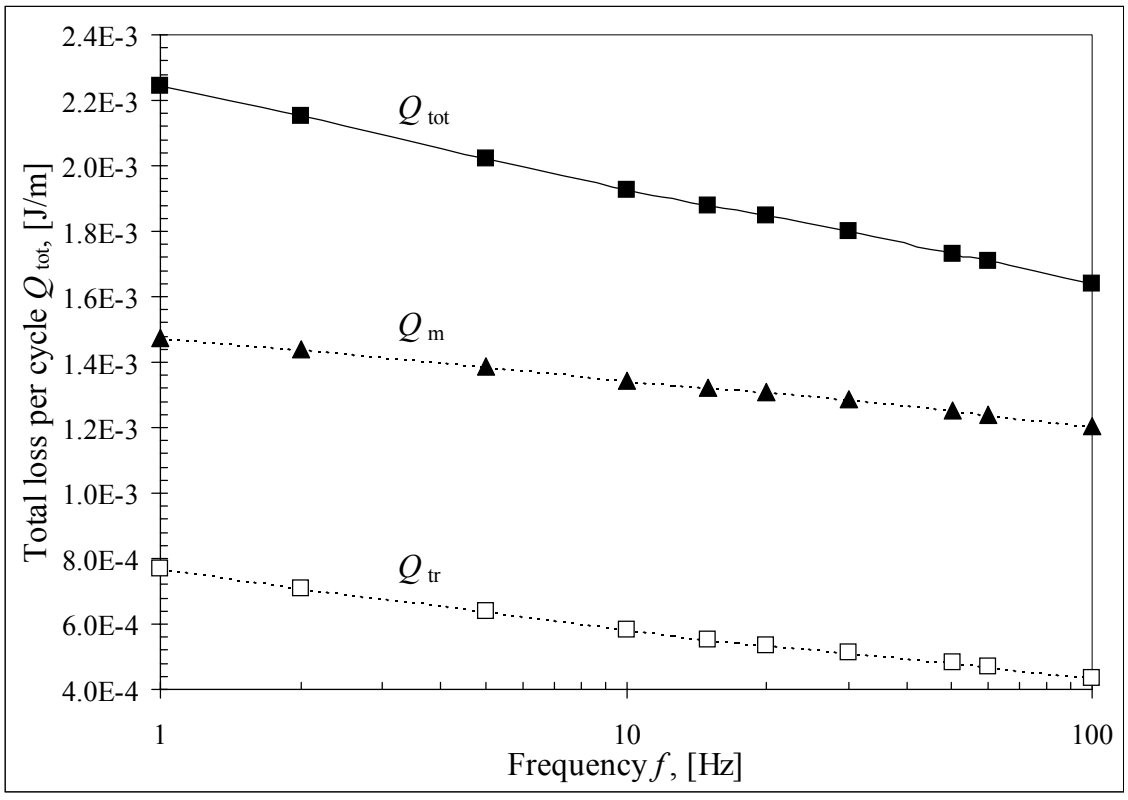

Figure 3.13 Calculated frequency dependence of the total (Q_{tot}), magnetisation (Q_m) and transport (Q_{tr}) losses per cycle for tape A at B_{e0} =10 mT, $\alpha = 0°$, I_{tr0} =71 A, T = 77 K (the lines are a guide to the eye).

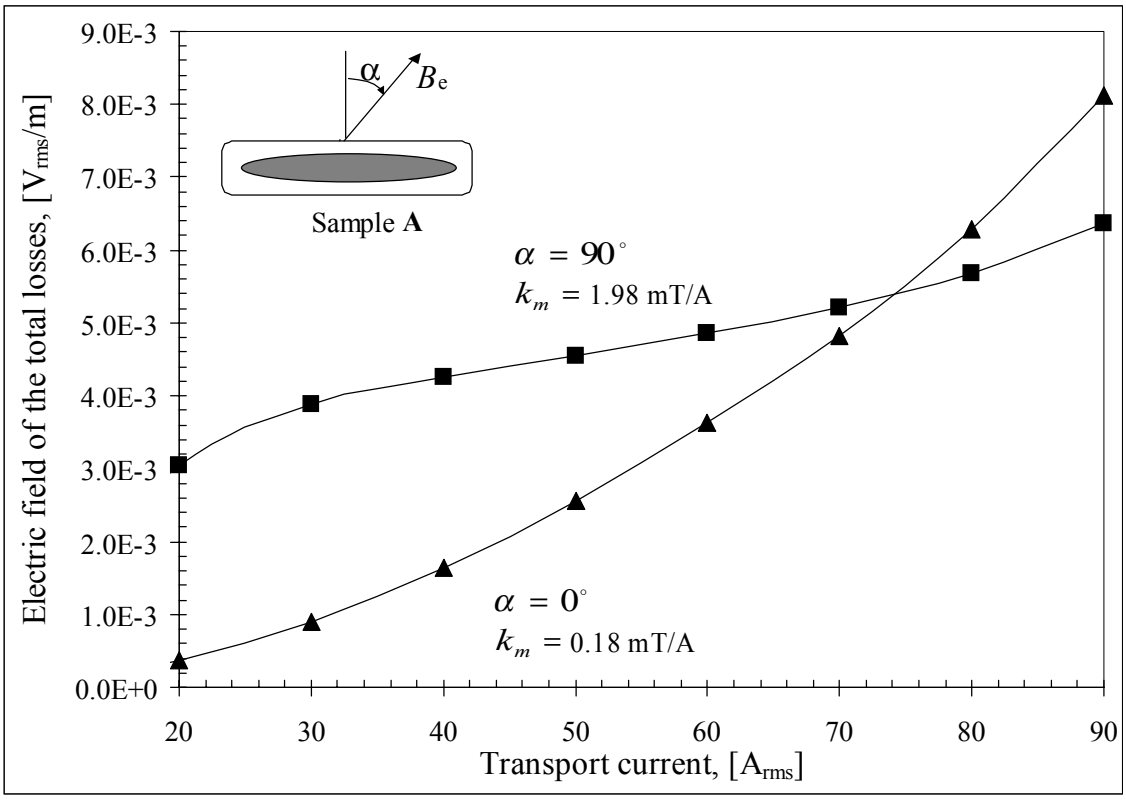

Figure 3.14 Calculated alternating loss $\hat{V}_\ell$ - $\hat{I}_{tr}$ curve for tape A at f = 50 Hz and T = 77 K: lines with the boxes and the triangles are for k_m = 1.98 mT/A, α =90° and k_m = 0.18 mT/A, α = 0° respectively, the lines are a guide to the eye.

Repeating the calculation for different values of the transport current, one will get the dependence of the total energy loss versus transport current. Instead of using the total energy loss, one may introduce the electric field of the loss voltage:

$$\hat{E}_{tot} = f \cdot Q_{tot} \,/\, \hat{I}_{tr} \,, \qquad \textit{Eq. 3.43}$$

where a cap above a symbol indicates the root mean square value. In the same way the electric field of the static loss voltage $\hat{E}_{ts} = f \cdot Q_{ts} \,/\, \hat{I}_{tr}$ can be introduced, see Equation 3.42.

In a coil both k_m and α are space dependent, for this reason $\hat{E}_{tot}$ varies along the tape length. For every value of $\hat{I}_{tr}$ one can find the loss voltages of the coil $\hat{V}_\ell$ and $\hat{V}_{\ell s}$ by integrating $\hat{E}_{tot}$ and $\hat{E}_{ts}$ over the length ℓ_1 of the tape wound in a coil:

$$\hat{V}_\ell = \int_0^{\ell_1} \hat{E}_{tot}\, d\ell \quad \text{and} \quad \hat{V}_{\ell s} = \int_0^{\ell_1} \hat{E}_{ts}\, d\ell \,. \qquad \textit{Eq. 3.44}$$

In the calculations the additional losses due to changing magnetic field along and across the superconductor (see for instance [Verv95, p. 102]) are neglected. Note that both $\hat{E}_{ts}$ and $\hat{V}_{\ell s}$ are independent from frequency. Hence for a coil instead of presenting the dependence of the total energy loss versus transport current at a certain frequency, one

may equally present an alternating loss $\hat{V}_\ell$ - $\hat{I}_{tr}$ curve. For coils this approach is advantageous, because both direct and alternating loss *V*-*I* curves can be treated in the same way as it will be explained in section 4.4.

An example of such a representation for sample tape A at f = 50 Hz and T = 77 K is shown in Figure 3.14 (magnetic field angle is constant for each $\hat{V}_\ell$ - $\hat{I}_{tr}$ curve shown in the figure). The curves shown are typical for optimised coil windings with k_m = 1.98 mT/A and α=90° (for instance, a centre of the innermost layer) and with k_m = 0.18 mT/A and α=0° (coil edge). Note that at $\hat{I}_{tr}$ = 74 A_{rms} the loss electric fields (α=90° and α=0°) are the same despite the fact that the corresponding magnetic field constants differ by a factor 11 (1.98 mT/A and 0.18 mT/A). In an air-core coil with a non-optimised magnetic field profile both magnetic field constants in the windings are usually about the same (as it will be shown in section 4.3) and for this reason the loss at the coil edges dominates. For instance at α = 0°, k_m = 1.98 mT/A and $\hat{I}_{tr}$ = 74 A_{rms} the calculated value of $\hat{E}_{tot} = 4.6 \cdot 10^{-2}$ V/m is found.

3.6 Conclusions

The existing physical and numerical models describing the electro-magnetic behaviour of high-T_c superconductors are reviewed. An advanced formulation for the classical eddy current problem is developed that links directly the current density and electrical field inside the superconductor and forms the basis of the presented electro-magnetic model. The formulation consists of the basic equations derived for the 3-dimensional quasi-static case of a high-T_c. tape with non-twisted superconducting filaments and also for the case of time-harmonic source fields.

For the 2-dimensional case the set of basic equations is also derived and allows to solve numerically the eddy current problem and find a distribution of the current density inside the superconductor and in time $\boldsymbol{J}_z(\boldsymbol{r}, t)$. However, the errors due to replacing a line cell with a cell of finite dimensions in the cross-section of the superconductor make the model inaccurate.

In contrast, the network model allows a simple and clear derivation of the governing equations for the numerical model in 2-dimensional case. Explicit formulas are found for calculating the inductances of the rectangular cells and the magnetic fields of the currents through the cells. The approach eliminates errors caused by replacing the cells of finite size with the line cells. Therefore, a new and more accurate numerical network model is developed.

The model is verified against available experimental data for high-T_c tapes (two cases: for both direct transport current and magnetic field present and for both time-harmonic transport current and magnetic field are included). In the former case, the calculated J_z-B_e characteristics with and without the self-field correction are found in agreement with the measured one's, thus confirming the consistency of the model. In the latter case, the calculated and the measured total cyclic losses for a tape agree with the average relative uncertainty below 7 % over the whole measurement range thus proving that the assumptions of the network model are correct and the total losses can be accurately calculated from the measured direct *E* - *J* curves.

Though the comparison is confined to the total cyclic loss alone and in rather specific conditions, the model allows to compute the current distribution and losses in many other cases as well as many other important characteristics of tapes. A number of selected examples (time dependence of the total, induced and transport currents at 48 Hz and frequency dependence of the total, magnetisation and transport current losses for tape A) are discussed. The purpose of the developed model is to serve as a tool for calculating the loss voltage-current curves of coils, since for various reasons the number of options to measure losses is very limited for coils.

Chapter 4

SUPERCONDUCTING POWER COILS

AC superconducting coils for high power applications are developed. As an example the development of a 1-MVA resonator coil is presented. The coil demonstrates the potential of Bi-2223/Ag superconductors for power applications. The characteristics of a full-scale demonstrator are as important for future applications as the properties of the tape itself, since not only the superconducting tapes, but devices based on them are essential. Anisotropy of the critical current of Bi-2223 tapes in external magnetic field affects the design of coils. An optimisation of the 1-MVA coil design has led to a circular coil system that consists of four long and thin concentric solenoids with a large diameter. The technology of winding superconducting coils is developed and applied in an industrial environment. Applying small iron pieces around the coil edges will reduce the radial component of the magnetic field i.e. the perpendicular field on the tape surface to which Bi-2223 tapes are most sensitive. As a result the critical current of a coil will increase and the loss will decrease. The effect is studied both analytically and numerically and the results contributed to the optimised design of the 1-MVA coil system. Details of magnetic field in the windings are calculated and voltage-current characteristics of the sub-coils are measured and analysed. The data are used to evaluate the coil loss voltage numerically. The measurement results confirm the estimates.

4.1 Introduction

High-T_c coils operating in liquid nitrogen may be applied in resonant circuits as shown in Figure 4.1. Such a circuit is often used for testing power cables and capacitors at full power. For the specifications given in the figure, the resonant frequency is 47 Hz. At a transport current of 110 A_{rms}, the voltage across both the capacitor and the inductor is 9.1 kV_{rms} and thus 1 MVA power is available for testing the capacitor.

The power delivered by the source PS depends on the quality factor of the circuit. The quality factor Q_L is the ratio of inductive power (or impedance) to the active power (or resistance) of the coil. When a copper coil is used as inductor, the power supply must deliver about 50 kW of active power (to compensate for the coil losses). At this rating the cost of the power supply is high. Cooling of power coil with liquid nitrogen is not a cost-effective option, since the resistivity of copper conductor decreases about 8 times (from $2 \cdot 10^{-8}$ Ω·m at room temperature [Wils83]), while the cooling penalty at 77 K ranges from 10 to 20, see Figure 5.5 and Equation 5.17.

When the copper coil is replaced by a high-T_c coil, the power supply has to deliver only a few kW. Thus the saving provided by a smaller power supply potentially may cover the extra investment in the inductor. Estimates show that a superconducting coil made with Bi-2223 tapes and operating in liquid nitrogen fits best this application. Obviously the coil requires a cryostat, a liquid nitrogen supply and a vacuum pump.

The power (voltage) source used in the experiments described below consists of a linear amplifier, a toroidal step-down copper transformer, a zero-flux meter to measure the transport current and a few voltmeters. The operating frequency of the power source must be adjustable. It has to be precisely tuned to the resonant frequency of the *LC* – circuit. The frequency may vary due to a spread in capacitance of the objects to be tested. In the case of a mobile unit, for future applications a car battery and an inverter may be used as a primary energy source [Jin97].

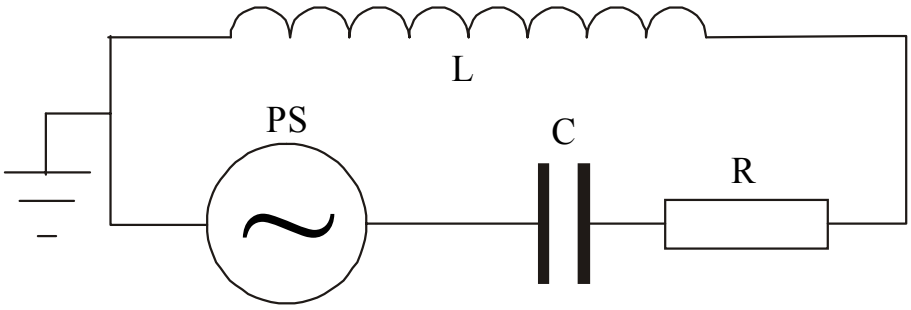

Figure 4.1 A resonant circuit for high voltage generation: power source PS, inductor L=0.28 H, resistor R = 80 mΩ and capacitor C = 40.9 μF.

4.2 Bi-2223/Ag resonator coil system

Bi-2223 are anisotropic as described in Chapters 2 and 3. At constant temperature the resistivity of Bi-2223/Ag tapes depend on several parameters, see Equations 2.3 and 2.4. The critical current and *n*-value as well as the total loss per cycle depend on magnitude B_e and direction angle α of magnetic field, see for instance Figures 2.10, 2.12, 3.8 and 3.9. The magnitude and direction of magnetic field may vary in the windings of a coil causing a variation of the critical current, *n*-value and of the total losses along the Bi-2223/Ag tape of which the coil is wound.

4.2.1 Impact of the critical current anisotropy on coil design

When a coil is made of the same superconducting tape, it would be best if the magnetic field everywhere in the coil is such that the critical current I_c and n –value are the same at any point along the tape. In this case the tape would be used in the most effective way [Shev97]. Equation 2.5 states that for each tape at a fixed temperature for any value of B_1^* there is one value of I_{c1} and one of n_1. Therefore, the condition to keep I_{c1} and n_1 the same everywhere in a coil is:

$$B_e = B_1^* / f_\alpha \,. \qquad \textit{Eq. 4.1}$$

Here B_e is average over the tape cross-section magnitude of magnetic field, since Equation 2.5 is derived for uniform external magnetic field and f_α depends only on the field angle α. For tape A at 77 K for instance in order to keep $I_{c1} = 117$ A and $n_1 = 15$ (which corresponds to $B_1^* = 13.5$ mT, see Figures 2.13 and 2.14) the values should be in the range from $B_{e0^\circ} = 13.5$ mT for $\alpha = 0^\circ$ to $B_{e90^0} = 150$ mT for $\alpha = 90^\circ$. In other words, Equation 4.1 can be written as:

$$\frac{B_{e0^\circ}}{B_{e90^\circ}} = f_{\alpha=90^\circ} \,. \qquad \textit{Eq. 4.2}$$

In a real coil the magnetic field may vary substantially along the tape and the condition expressed by Equation 4.1 is difficult to fulfil everywhere. It is known that in a circular solenoidal coil the maximum of axial magnetic field (which is parallel to the tape, $\alpha = 90^\circ$) usually occurs in the centre of the innermost conductor layer. The maximum of the coil radial magnetic field (directed perpendicular to the tape, $\alpha = 0^\circ$) usually occurs at the coil edge, see Figure 4.7. Therefore, in a well-designed coil made of Bi-2223 tape, Equation 4.2 relates the maxima values of the axial and radial magnetic fields although they may occur in different points along the conductor tape.

A similar condition that requires the losses to be the same everywhere along the tape in the coil is derived from Figures 3.10 and 3.11 (for the same tape at 77 K and 48 Hz). The condition contributes to a more uniform temperature of the coil winding. At the fixed amplitude of the transport current $I_{tro} =$ 86 A for the parallel magnetic field amplitude $B_{e90^0} = 150$ $\mathrm{mT_{peak}}$ ($\alpha = 90^\circ$) the total cyclic loss is equal to $5.3 \cdot 10^{-3}$ J/m. For $\alpha = 0^\circ$ the same value of the total loss is reached when the magnetic field amplitude is equal to $B_{e0^\circ} = 17$ $\mathrm{mT_{peak}}$.

Therefore, both conditions demand close values of the perpendicular component of magnetic field, though the condition expressed by Equation 4.2 and relevant to the critical current seems to be more stringent than the condition derived for the losses. For practical purposes, an approximate condition $B_{e0^\circ} / B_{e90^\circ} \approx 0.1$ can be adopted.

4.2.2 Design aspects

When the anisotropy of the conductor properties is not relevant, a Brooks (pancake type of) coil is more efficient than a long solenoid, as it requires less conductor and the edge cooling is almost perfect. However, more tape conductor (as compared to the thin solenoid) is located at the coil edge and thus exposed to the radial component of the magnetic field (which is perpendicular to the tape wide face). A reduction of the radial and average magnetic field in the windings combined with minimal costs implies a long, large diameter and thin solenoidal coil [Muld88]. A

toroidal type of coil would require 2-3 times more conductor than a solenoid [Muld88], which is in contradiction to the minimum cost requirements stringent for Bi-2223 tapes.
Figure 4.2 shows the overall design of the coil as it is mounted in a plastic cryostat with liquid nitrogen. The coil system is mechanically fixed to the top flange of the cryostat and it is electrically connected to the cryogenic feed throughs. The cryostat has a room temperature bore that allows using coils in an optional transformer mode (with the iron core operated at room temperature). However this option is not considered in the study.

An optimisation of the 1-MVA coil design has lead to a circular coil that consists of four long and thin concentric solenoids with a large diameter. The division of the coil into sub-coils reduces the risks associated with manufacturing and operation. It also provides the required cooling (since in order to keep the winding temperature within the defined limits, a cooling channel per each few layers is required) and enables a variety of electric configurations. An optional fifth sub-coil can be mounted as well. Each sub-coil is electrically connected to a pair of the cryogenic feed-throughs so that the electrical configuration of the coil can be changed from outside the cryostat without warming up the coil.

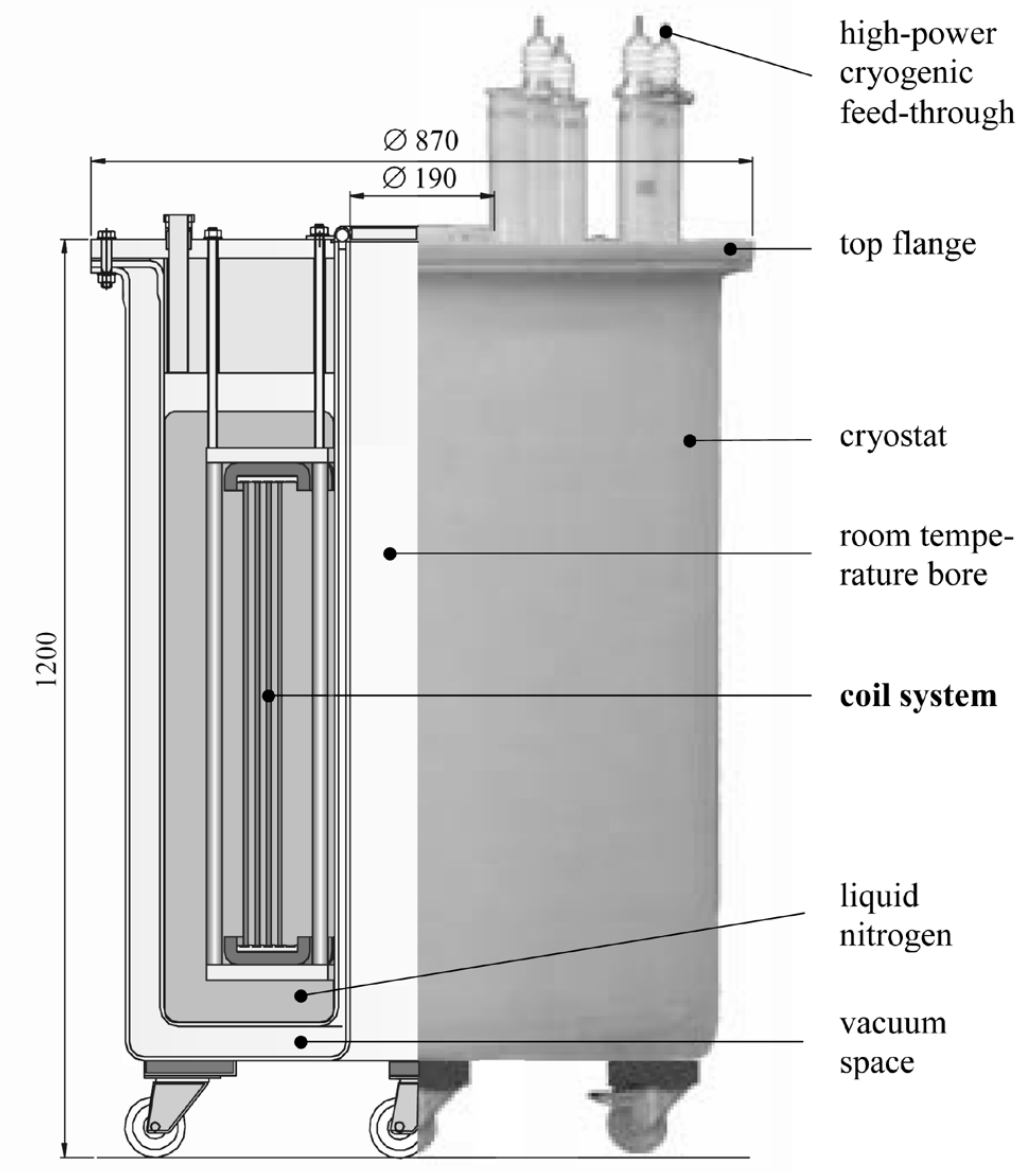

Figure 4.2 The 1-MVA resonator coil inside the plastic cryostat, the sizes are in mm.

4.2.3 Arrangement and manufacturing

The layout of the coil is shown in Figure 4.3. The coil consists of four sub-coils fixed between two flanges using 16 rods. The flanges, the rods, the spacers and the sub-coil formers are made of glass-fibre reinforced plastic (FRP). Laminated ferro-magnetic C-cups are fixed to the flanges and separated from the sub-coils by means of the radial spacers. The purpose and arrangement of the C-cups is discussed in section 4.3.1.

The four sub-coils are numbered from the outermost (1s) to the innermost (4s). The dimensions and other specifications of the sub-coils are given in Table 4.1. Each sub-coil is wound on a separate former of 5 mm wall thickness. Care is taken that the glass fibres are both parallel and perpendicular to the superconducting filaments of Bi-2223 tapes. In this case, the thermal contraction of the coil former and Bi-2223 filaments matches almost perfectly. Any other mutual direction would lead to a relatively larger contraction of the coil former and may damage fragile Bi-2223 filaments leading to irreversible reduction of the critical current [Gode00b].

Bare superconducting tapes from two vendors are used for the coil. Total length of the tapes is 1944 m. All tapes are insulated at Smit Draad Nijmegen B.V., The Netherlands using the method described in section 2.6. The winding technique is developed on pre-production model coils at the University of Twente in cooperation with Smit Transformatoren B.V., The Netherlands.

The resulting winding layout of the coil is illustrated in Figure 4.4. As an example, a circular solenoid of the outer diameter 2 R_e and the height $2\,x_{coil}$ is sketched in the figure. It consists of a 4-layer winding (dark grey) and G-10 former (light grey). For clarity the spacers, the end flanges, the sensors, the wiring, the impregnation material and the outer coil bandage are omitted. The top drawing shows an evolvent view of the coil (the tape conductor begins in the lower left corner). The bottom drawing represents a magnified cross-section of the insulated Bi-2223/Ag tape.

Figures CS_1, CS_2 and CS_3 show the coil cross-sections made along the horizontal lines CS_1, CS_2 and CS_3 respectively by the planes that are perpendicular to the figure plane.

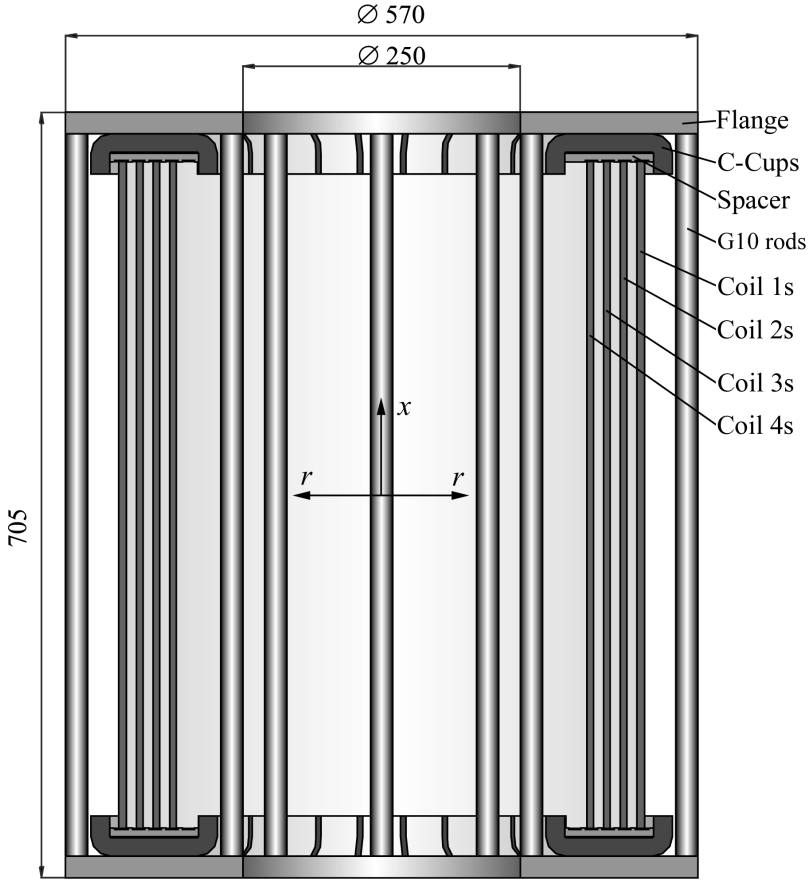

Figure 4.3 Layout of the 1-MVA resonator coil, the sizes are in mm.

Table 4.1 Specifications of the sub-coils.

Parameter \ Sub-coil number	1s	2s	3s	4s
Bi-2223/Ag tape used:				
manufacturer of the tape	V	A	A	A
total length, [m]	878	378	359	329
current I_c, [A] at 77 K; self-field; $E = 10^{-4}$V/m	54 ± 4	114 ± 13	123 ± 9	117 ± 7
n-value, [-] at 77 K; self-field; $E = 10^{-4}$V/m	19	18	18	20
Dimensions of the winding package:				
inner diameter, [mm]	470	440	410	380
outer diameter, [mm]	474	442	412	382
height, [mm]	614	614	614	614
size g of the air gap, [mm]	0.4	0.4	0.4	0.4
Other characteristics:				
number of tapes in parallel	2	1	1	1
number of conductor layers	4	2	2	2
number of conductor turns	296	273	278	277
self-inductance*, [mH]	24	18	15	13

* in magnetic configuration C1, see Table 4.2

When the number of turns per layer is integer, the conductor of the next layer is shifted exactly one conductor width. The bottom drawing shows also a zoomed cross-section of the insulated coil conductor (that consists in the example of a single tape).

The tapes are wet-wound on the coil formers using STYCAST 2850 FT and few layers of thin glass-cloth for the outer bandage. The coil winding technology was transferred to the factory and the company personnel manufactured all the sub-coils using industrial tooling. The winding process is illustrated in Figure 4.5 (left). The photo on the right shows zoom in the cross-section of 6-layer model coil. Note that in this case the number of turns per layer of the coil was not integer and as a result the tape of the next layer is shifted about ½ of the tape width.

The typical production unit length of the superconducting tapes is 200 m. Therefore resistive overlap joints are made between the layers of each sub-coil. The critical currents of the tapes are listed in Table 4.1. They are measured in tape samples cut from each tape unit. Each sub-coil is equipped with a set of thermometers to monitor the temperature of the windings along the height.

Sub-coil 1s is wound from tape delivered by Vacuumschmeltze GMBH, Germany [Vacu01]. Specifications of the tape are almost the same as listed in Table 2.2 for tape V. The sub-coil conductor comprises two insulated tapes wound in parallel, since a single tape is not able to carry the current of 110 A_{rms} alone. The tapes are laid next to each other and a transposition is not required in this case. The tapes are electrically connected in parallel at the coil ends. Sub-coils 2s – 4s, which are operating in successively higher magnetic field, are wound from a single tape delivered by American Superconductor Corporation, USA. The critical currents and n-values are listed in Table 4.1, other specifications of the tapes are the same as given in Table 2.2 for tape A.

In addition to Figure 4.3, the fragment view of the four sub-coils assembled in 1-MVA coil is shown in Figure 4.6 (left), the small c-cups are seen placed around the edge of the outer sub-coil 1s while the flange and the large C-cups are removed. Figure 4.6 (right) illustrates the arrangement of the upper coil edge with the FRP flange and large C-cups mounted.

To characterize (circular) sub-coils a cylindrical x, r - coordinate system is used, Figure 4.3. The x-axis is parallel to the coil axis and the r-axis is parallel to the coil radius. Cross-sections of Bi-2223/Ag tapes are characterized using Cartesian coordinate system x, y, see Figure 2.1. In the sub-coils the conductor tapes are laid so that, neglecting a small angle $\arctan(b_i/\pi R_e)$, see Figure 4.4, one may assume that the axes x of both coordinate systems are always parallel to each other and y-axis is always parallel to r-axis.

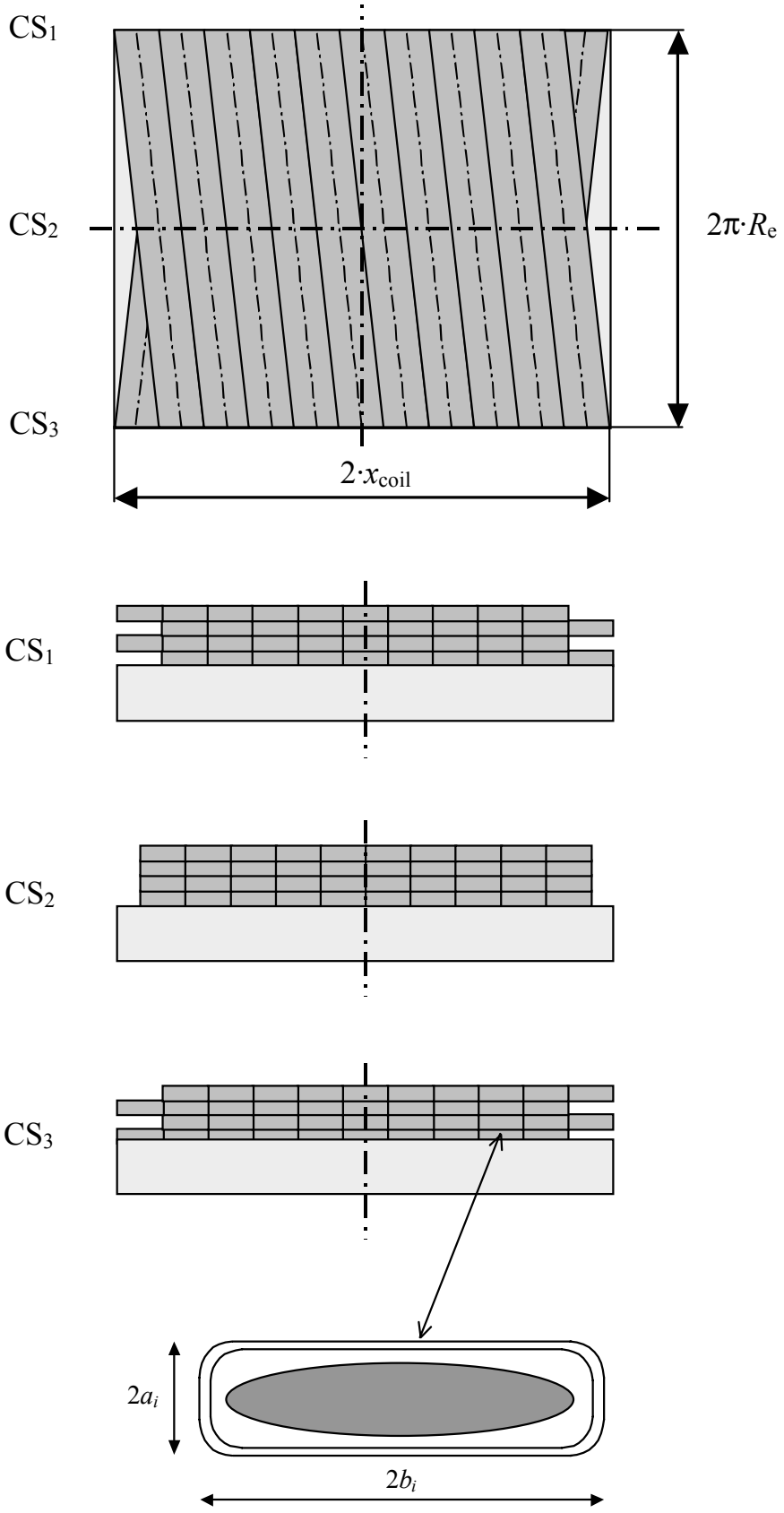

Figure 4.4 Windings layout in the 4-layer high-T_c coil.

4.2.4 Other components of the coil system

The coil is placed in a glass-fibre reinforced plastic cryostat as depicted in Figure 4.2. The cryostat is developed by DeMaCo Holland B.V., the Netherlands. The eddy current loss at 50 Hz in a stainless steel cryostat would prevent it from reaching a high quality factor of the coil. The cryostat has a room temperature bore of 190 mm, which enables the mounting of an iron core in the case one decides to run the set of coils in transformer mode. As the coil operates occasionally, the cooling is provided by liquid nitrogen from an external supply. The pressure inside the cryostat can be lowered by means of the vacuum pump SOGEVAC-65 [Leyb01] to reach and to maintain bath temperature as low as 64 K.

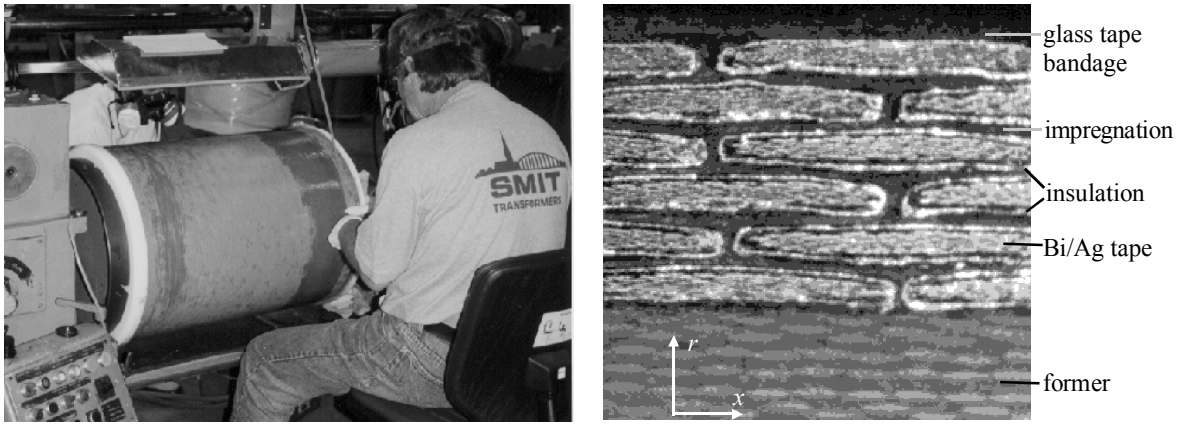

*Figure 4.5 Left: sub-coil **1s** during manufacturing at Smit Transformatoren B.V., right: zoom in the cross-section of 6-layer model coil.*

The inner vessel of the cryostat is gas-tight, which allows to measure the losses of the coil calorimetrically (by measuring the boil-off). The boil-off gas from the cryostat is heated up to about 300 K by means of a heat exchanger. The pressure inside the cryostat and the pump inlet pressure are measured with two Piezovac sensors [Leyb01].

A 10-kV_{rms} electrical drive circuit includes a number of cryogenic feed throughs made of copper that provides a connection to each sub-coil from the outside of the cryostat. Each feed through is designed to carry a current of 120 A continuously. It is connected to a copper-braid lead of a sub-coil inside the cryostat. The wiring is insulated using several layers of KAPTON and Teflon tapes and silicon tubes. The 120-A wiring on the upper flange of the 1-MVA coil is shown in Figure 4.6 (right). The insulation test is performed with the coil placed inside the cryostat filled with liquid nitrogen at 77 K. The test voltage up to 10 kV_{rms} is applied to the (floating) coil. The coil did not show any sign of the partial discharge.

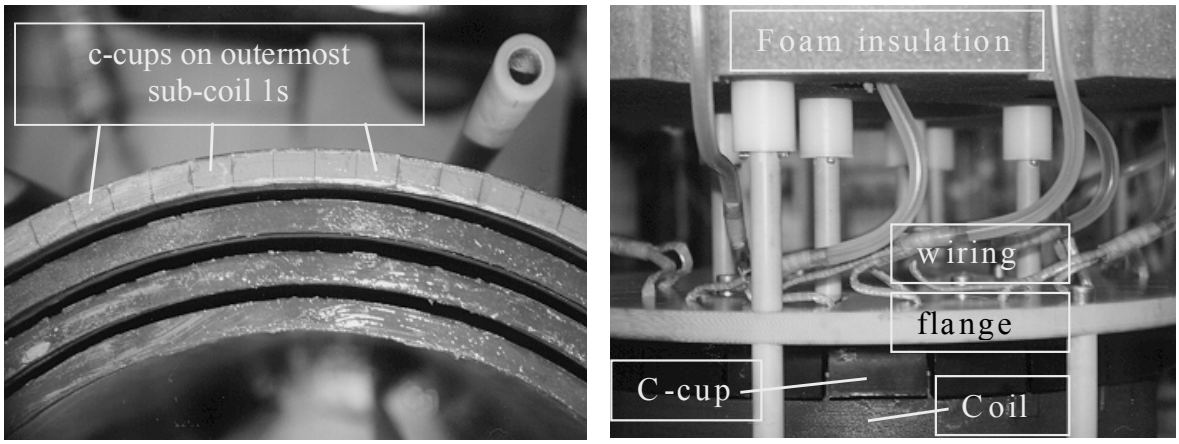

*Figure 4.6 Left: four sub-coils assembled in 1-MVA coil and showing small c-cups placed around the edge of the outer sub-coil **1s (**with the large C-cups removed. Right: arrangement of the 1-MVA coil upper edge (large C-cups, coil flange and the wiring are shown).*

4.3 Magnetic field in windings

The magnetic field of the same magnitude when applied perpendicular to the Bi-2223 tape wide surface causes a larger reduction of the critical current than when it is applied parallel to the tape wide surface, see Figure 2.10. The condition expressed by Equations 4.1 and 4.2 in fact requires the tape wide surface to be aligned almost parallel to the direction of magnetic field.

4.3.1 Air-core coil and iron C-cups

In a circular coil made with high-T_c tape, the radial component of the magnetic field is perpendicular to the tape wide surface. The radial magnetic field B_r reduces the critical current and causes part of the loss in air-core high-T_c coils. In a solenoid within the same layer the magnetic fields of the adjacent turns partly cancel out each other and B_r is reduced everywhere except at the coil edges. There a relatively small volume of superconducting tape is exposed to a relatively high B_r. In a coil, the maximum radial field $B_{r,mx}$ and the maximum axial field $B_{x,mx}$ usually occur in two different points of the coil cross-section, see Figure 4.7. The analysis below is confined to the case when a coil conductor in both points is made of the same tape(s).

As it follows from Equation 2.5, for any magnetic field angle $0^\circ \le \alpha \le 90^\circ$ the critical current is the same when the characteristic magnetic field B^* is the same. Thus in order to have an equal effect on the critical current of the tape, the ratio of maximum radial to maximum axial field in a coil must be kept at $B_{r,mx}/B_{x,mx} = f_\alpha(90^\circ)$, see Equation 4.2. From Figures 2.10-2.14 it is clear that for the tapes investigated one finds: $0.09 \le f_\alpha(90^\circ) \le 0.132$. In other words, at least the condition $\alpha > 82.5^\circ$ must be fulfilled as $tg\ \alpha = B_x/B_r$. Hence the magnetic field at the coil edges should be kept almost parallel to the tape wide surface.

In a typical air-core coil the ratio $B_{r,mx}/B_{x,mx}$ depends on the shape of the coil and is about 0.5 at best. In order to reduce the ratio, the edges of the coil are surrounded by 48 laminated ferromagnetic C-cups with a total weight of about 52 kilograms, see Figures 4.3 and 4.6. The purpose of the C-cups is to reduce locally the radial component of magnetic field at the coil edges [Shev97]. At glance the C-cups are iron pieces, which work as magnetic mirrors and mimic coaxial sub-coils of the same dimensions spaced by a gap 2*g* from the real sub-coils, see Figure 4.7. Using the model that considers a set of coaxial coils separated by an air gap 2*g*

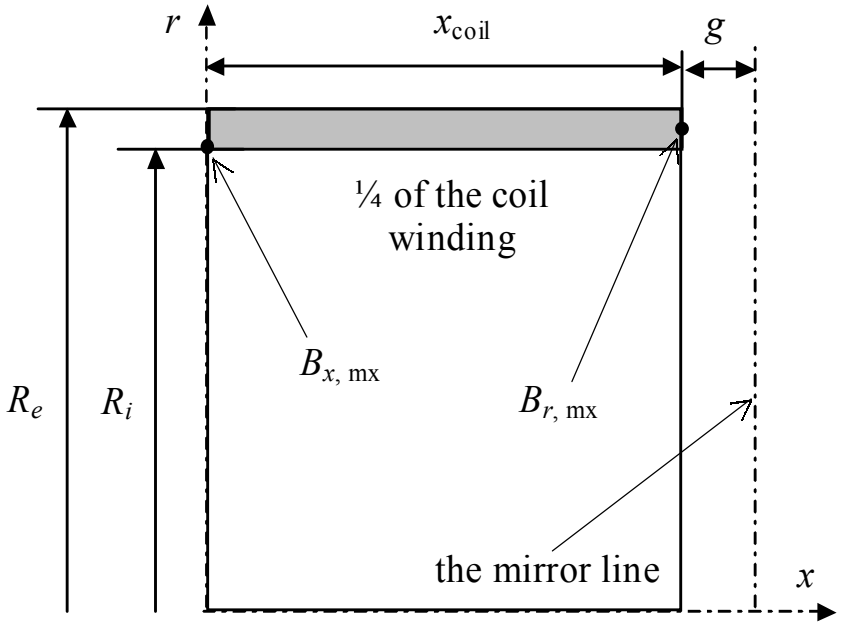

Figure 4.7 The solenoid (a quarter of the actual cross-section is depicted and the symmetry lines are shown as dash-dot). The arrows show the usual location of the maximum magnetic field in a solenoid; the mirror line indicates the position of the c-cups.

[Shev99a], one can estimate the gap size that provides the required ratio of $B_{r,mx}/B_{x,mx}$ for a circular coil of given shape. Calculations performed in [Shev99a] can be expressed in a dimensionless form using the radius $\sigma = R_e/R_i$; the height $\chi = x_{coil}/R_i$ and the air gap $\eta = g/R_i$. The results of such calculations are displayed in Figure 4.8. In general, for a fixed ratio $B_{r,mx}/B_{x,mx}$, longer and thinner coils would require a smaller air gap. For a fixed coil height a thinner coil would require a smaller air gap. For instance, approximating the results of the calculations for longer coils with $\chi - 1 \geq 6 \cdot (\sigma - 1)$ one finds $\eta \approx 0.18 \cdot (\sigma - 1)$ for $B_{r,mx}/B_{z,mx} = 0.14$ and $\eta \approx 0.12 \cdot (\sigma - 1)$ for $B_{r,mx}/B_{z,mx} = 0.1$. Note that here by definition: $\eta/(\sigma - 1) = g/(R_e - R_i)$ and $(\chi - 1)/(\sigma - 1) = (x_{coil} - R_i)/(R_e - R_i)$.

The C-cups are laminated using a conventional strip-wound cut C-cores technique [Vacu01]. The thickness of the ferro-magnetic strip made of cold rolled grain-oriented electro-technical steel is 0.3 mm. At 50 Hz operating frequency the skin depth of the eddy currents [Namij88] is estimated to be 30 mm for the strip at 77 K. Further lamination of the C-cups (primarily in the direction sensitive to the axial magnetic field of the coil, see Figure 4.3) would result in a further reduction of the eddy current loss (see Equation 3.18). However, this (rather trivial) option is beyond the scope of the study. The positive effect of the C-cups on the radial magnetic field of the coil is felt over the whole height of the coil, see Figures 4.10 - 4.12.

To refine the field at the very edge of the coil, in addition to the large C-cups, much smaller laminated ferro-magnetic c-cups are attached to the edges of each sub-coil, see Figures 4.6 (left) and 4.9. The c-cups act the same way as the large C-cups, but the effect is more local. It extends over a distance in the order of a few cm only. Hence, the c-cups reduce the radial magnetic field at the very edge of a sub-coil winding, where the large C-cups are less effective as they are further away. The total weight of the c-cups is about

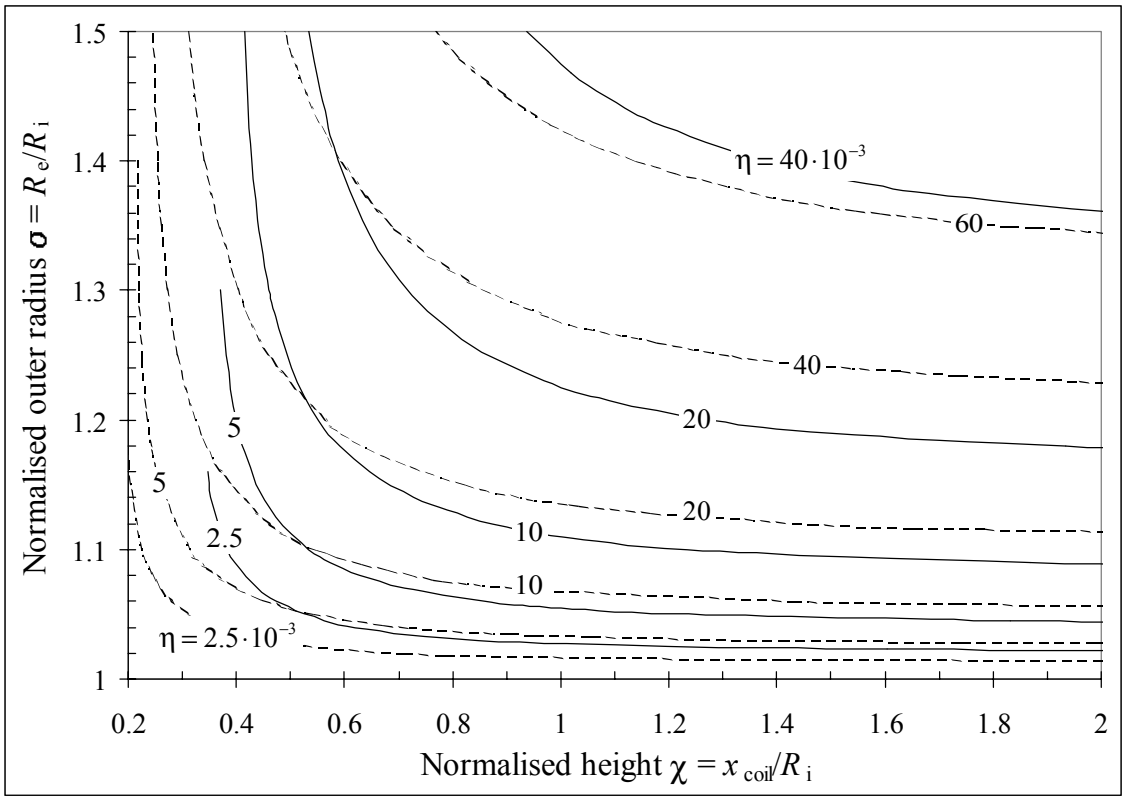

Figure 4.8 Calculated normalised dimensions of a solenoid that provides $B_{r,mx}/B_{x,mx} = 0.1$ (solid lines) and 0.14 (dashed lines) with the normalised air gap $\eta = g/R_i$.

Table 4.2 Magnetic configurations of the sub-coils.

Magnetic configuration	Label
a sub-coil alone without c- or C-cups	C1
a sub-coil alone with c- and C-cups	C2
in 1-MVA coil without c- or C-cups	C3
in 1-MVA coil with c- and C-cups	C4

4 kg and each of them is made of two layers of 0.27-mm thin electro-technical steel. The (large) C-cups are fixed to the FRP flanges as sketched in Figure 4.3 and shown in Figure 4.6 (right). The edges of the sub-coils are positioned inside the C-cups using the spacers. When mounted, the sub-coils are separated by at least 8-mm wide cooling gaps as it is displayed in Figures 4.3 and 4.6 (left). In total 16 tension rods connect the flanges. The rods are made of FRP and shown in Figures 4.3 and 4.6. The flanges and the rods are the components of the coil's mechanical structure.

The magnetic field of the coil is calculated using commercial software QuickField® [Quic01] and assuming a uniform distribution of the current over the cross-sections of the sub-coils. The code utilises a finite element method for modelling 2-dimensional fields. The model geometry of the coil edge is explained in Figure 4.9. Ferro-magnetic cups are modelled and their dimensions are optimised using realistic *B-H* curves for TRAFOPERM [Vacu01]. Four characteristic magnetic configurations of the sub-coils selected for the analysis are listed in Table 4.2. Note that this creates 16 cases in total (4 sub-coils times 4 magnetic configurations for each sub-coil). Therefore for obvious reasons not all, but the most important cases are presented here.

For a sub-coil alone an equivalent current layer represents each conductor layer. Thus the current in the layer is equal to a total current of the sub-coil divided by the number of layers. For the 1-MVA coil configurations, an equivalent current layer represents each sub-coil in order to keep an acceptable complexity of the model. Smaller details such as air-gaps between adjacent turns of superconducting tape are analysed separately.

In order to use the results of chapters 2 and 3, local magnetic fields in the coil windings are averaged over the transversal cross-sections of each tape. The distribution of magnetic field along the tape length for each magnetic configuration of a coil is calculated. Each calculated curve is compacted into an array of node points and cubic spline interpolation is used to calculate the field values for the intermediate points along the tape length. In all cases the magnetic field along the

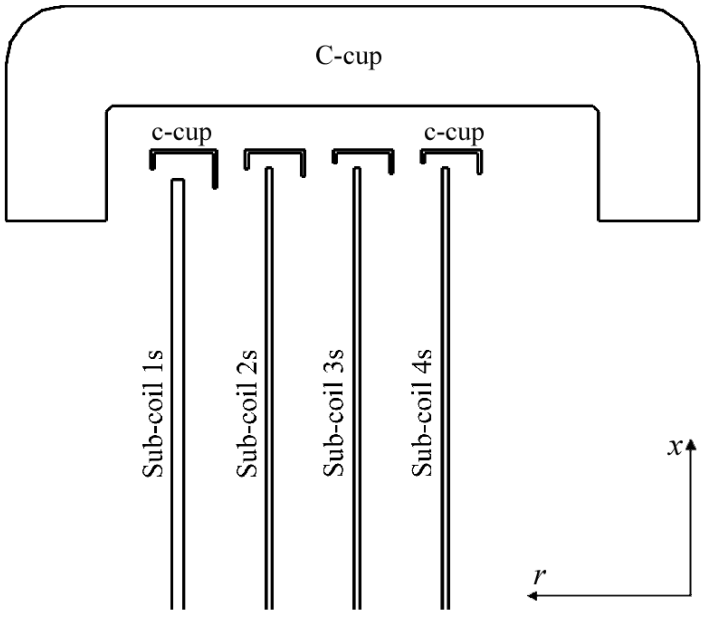

Figure 4.9 Model of the coil edge longitudinal section used to calculate magnetic fields.

*Table 4.3 Calculated radial magnetic field over the tape length of sub-coil **1s** at I_{tr}= 50 A.*

Case \ The magnetic field	$B_{r,mx}$, [mT] maximum value	$B_{r,av}$, [mT] average value
C1: the sub-coil alone without c- or C-cups	23	6
C2: the sub-coil alone with c- and C-cups	5	2
C3: in the 1-MVA coil without c- or C-cups	55	15
C4: in the 1-MVA coil with c- and C-cups	10	5

tape length varies with a certain periodicity. Here the coil analysed is a set of thin solenoids with a large diameter. The distribution of the radial magnetic field versus the tape length is practically the same for any layer of a sub-coil (small variations of the field from layer to layer at the very coil edge, see Figure 4.5, are averaged). For this reason it is depicted only once for each coil configuration.

4.3.2 Outer sub-coil 1s

The periodic patterns of the magnetic field are depicted in Figures 4.10 and 4.11 for ½ of the sub-coil (and for one of the two parallel tapes). As expected for an air-core coil, in case C1 (Table 4.3) within a layer the radial magnetic fields of the adjacent turns partly cancel out and B_r gradually increases towards the coil edge as shown in Figure 4.10. There a relatively small amount of the tape is exposed to a relatively high B_r. Namely this area limits the critical current of a coil. The axial field in the windings is shown in Figure 4.11 for each layer starting from the innermost.

In case C2 iron cups around the coil edges reduce the radial field B_r as it is depicted in Figure 4.10 and listed in Table 4.3. Axial magnetic field remains almost the same as in case C1, Figure 4.11. In case C3 the total current of the 1-MVA coil is higher and also the radial field of the sub-coil is higher, see Figure 4.10 and Table 4.3. The axial field in the windings is not shown

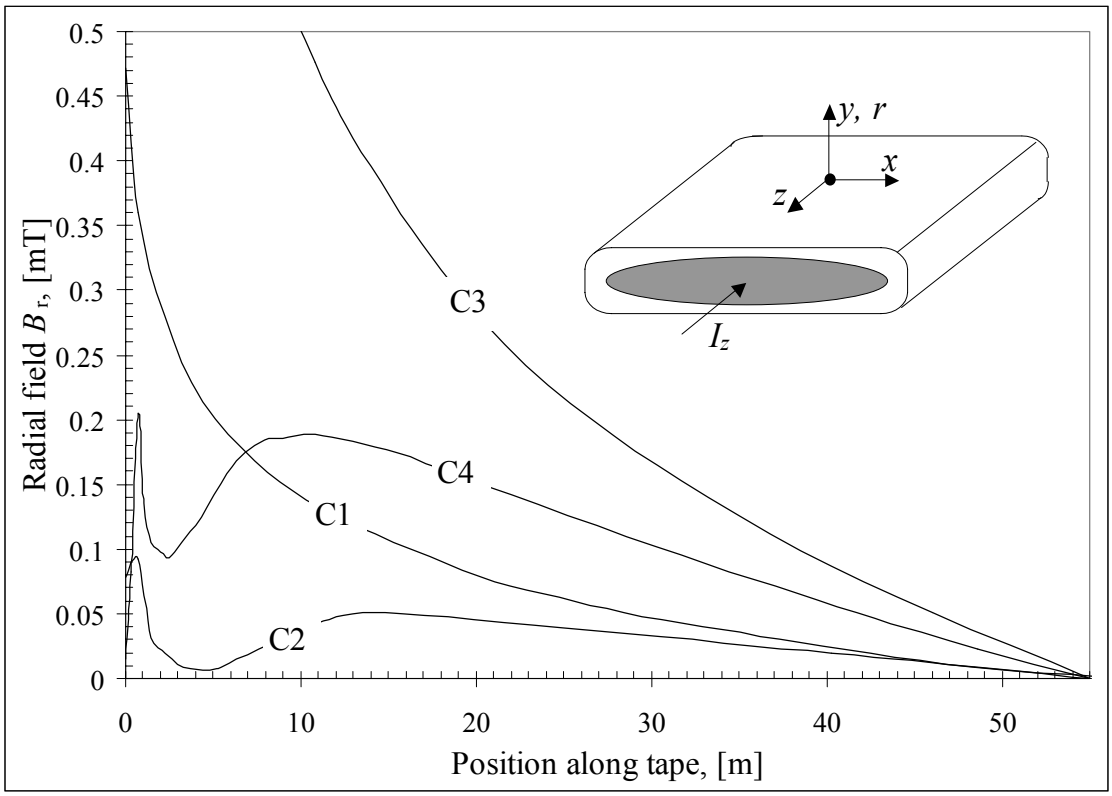

Figure 4.10 Calculated modulus of the coil radial magnetic field versus the position along the tape at a transport current of 1 A. The line labels indicate the configurations listed in Table 4.2; zero position in the tape is at the coil edge.

for this case. In case C4 iron cups reduce the radial field B_r as it is shown in Figure 4.10 and in Table 4.3. With the c-cups removed from the sub-coil edges, the radial field B_r at the very coil edge (practically in the first conductor turn) would rapidly increase. The axial field in case C4 is shown in Figure 4.11 by the dashed lines.

4.3.3 Sub-coils 2s, 3s and 4s

The sub-coils are made from the same tape and with the same technology and have similar cooling conditions. Hence, the differences between the sub-coils are mostly in dimensions, critical current and length of the tapes, see Table 4.1. The calculated periodic patterns of magnetic field are qualitatively similar to those shown in Figures 4.10 and 4.11 for sub-coil 1s**,** except of the axial field in 1-MVA configurations. When assembled in the 1-MVA coil, each inner sub-coil operates in successively higher magnetic field, which is an additional difference between the sub-coils. The periodic patterns of calculated axial and radial magnetic field for ¼ of sub-coils 2s - 4s in case C4 with 1 A transport current are depicted in Figure 4.12. Note that each of sub-coils 2s - 4s has 2 layers, while sub-coil 1s has 4 layers. Besides this, sub-coil 1s is the outermost and therefore it has different cooling conditions than other sub-coils.

In order to reduce the radial field B_r in the coil windings the linear analysis suggests to choose a proper shape of the coil and smaller air-gap size g, see Figure 4.8. More realistic numerical analysis allows also to optimise the dimensions and the position of the iron cups with respect to the coil edges; the result is displayed in Figure 4.9. For instance, for sub-coil 4s the values of $\chi = 1.615$ and $\sigma = 1.005$ are found using Table 4.1. The linear analysis for $B_{r,mx} / B_{z,mx} = 0.1$ suggests $\eta \approx 6 \cdot 10^{-4}$, which is rather unpractical: at $g \approx 0.1$ mm the insulation problems might be expected. The numerical analysis of the coil edge equipped with iron cups, see Figure 4.9 in case C4 returns $B_{r,mx} / B_{z,mx} = 0.08$ at $g \approx 0.4$ mm (hence $\eta \approx 0.002$).

In conclusion two stages of iron cups properly positioned around the coil edges provide a reduction of the radial component of the magnetic field to the desired level.

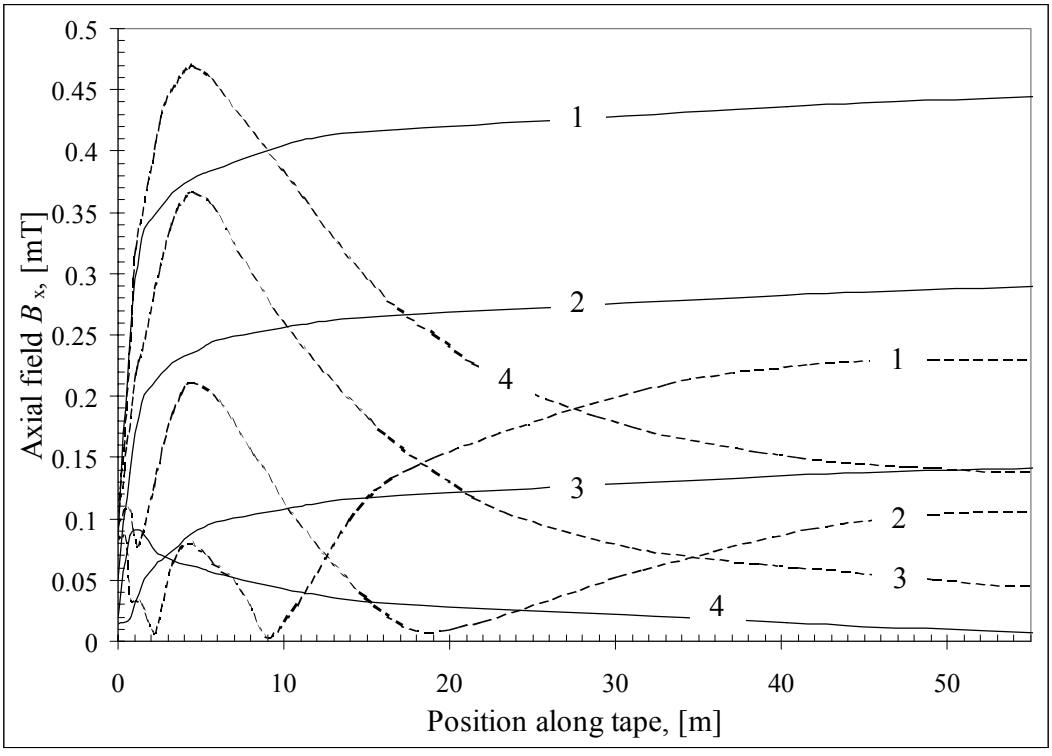

Figure 4.11 Calculated modulus of the coil axial magnetic field B_x at a transport current of 1 A versus the position along the tape: solid lines – cases C1 and C2, dashed lines – case C4; a number on the line indicates the layer, 1 = innermost, 4 = outermost.

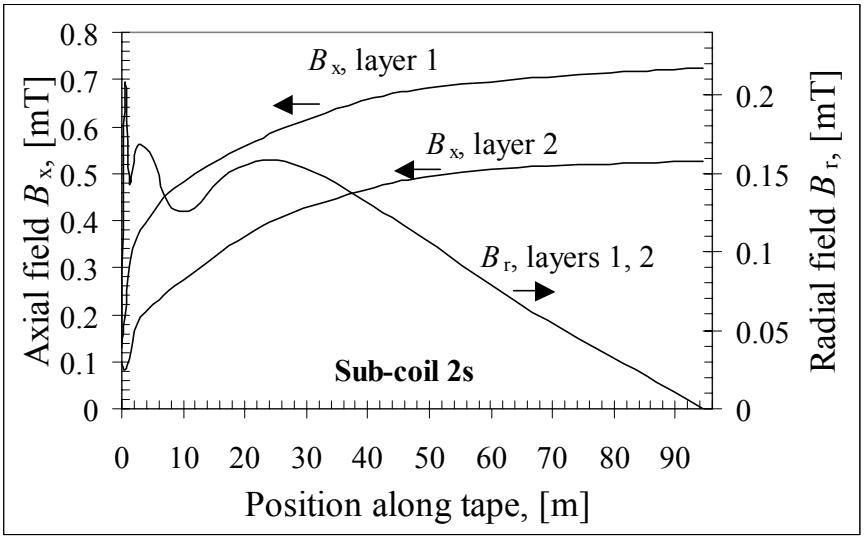

a

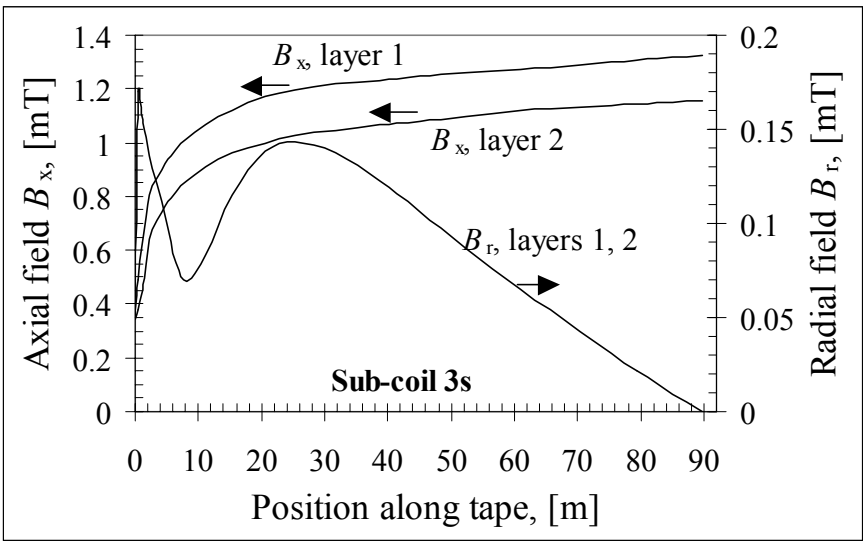

b

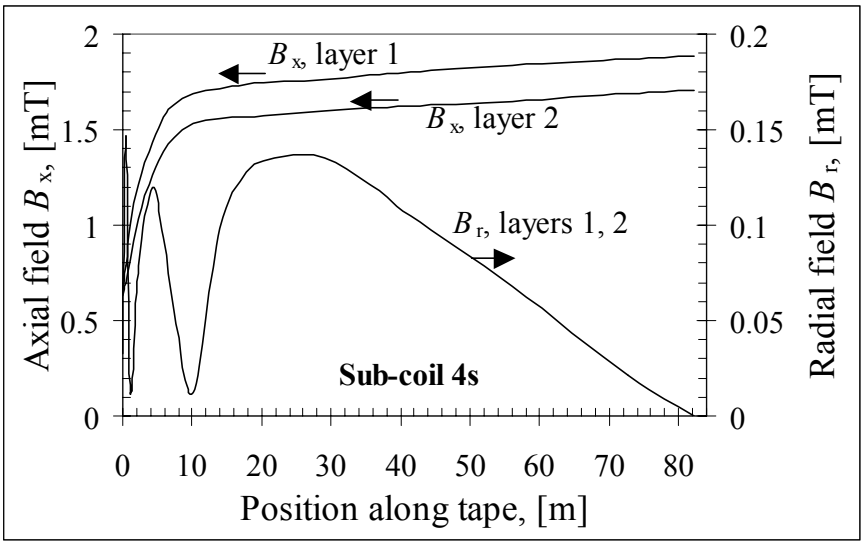

c

Figure 4.12 Calculated modulus of magnetic field components for sub-coils 2s - 4s versus the position along the tape in case C4; layer 1 = inner, layer 2 = outer.

4.4 Voltage-Current curves and losses

The 1-MVA coil is a complex object to analyse properly. The total voltage across the coil consists of the reactive and active parts. When a sinusoidal transport current flows through the coil, the inductance of the coil, the frequency and the amplitude of the current determine the reactive part of the voltage. The active part is determined by the coil loss. The AC loss has several contributions and hence it requires several methods to properly separate and understand them. Two methods are used for studying *V-I* curves of the coils: a numerical and an experimental. The latter includes thermal, calorimetric and electro-magnetic methods, which are complementary to each other as it is explained below. In all cases the transport current through a coil is measured with a zero-flux meter. All measurements and calculations described in this section are performed at (or scaled to) the bath temperature of 77 K.

To ensure the consistency of the numerical method, the analysis is performed in several steps. First, a single tape carrying a transport current and exposed to a transversal external uniform magnetic field varied independently from the transport current is studied as described in Chapters 2 and 3. Second, average (per tape cross-section) magnetic field profiles along the tapes wound in coils are calculated as explained in section 4.3. The network model developed and verified for a single tape (sections 3.3 and 3.4) is adopted to calculate *V-I* curves of coils by assuming the following. Both transport current and magnetic field of a coil oscillate harmonically with the same frequency and are in phase. At every point in the coil winding, the amplitude of the external magnetic field is coupled to the amplitude of the transport current via the magnetic field constant. As $tg\ \alpha = B_x / B_r$, it is clear that the direction of the magnetic field is space dependent and not time-dependent. For each value of the transport current, the loss voltage across the coil is calculated as follows:

$$V_{\rho t} = \int_0^{l_t} E_{\rho t} dl \,, \qquad \textit{Eq. 4.3}$$

where l and l_t are the position in and the total length of the tape, respectively. In the case of sinusoidal transport current through the coil, Equation 3.40 is used to find $E_{\rho t} = \frac{Q_{tot}}{\tau_0 \cdot I_{tr}}$. In the case of direct current through the coil, Equation 2.2 is used: $E_{\rho t} = \rho \cdot J_e$. Thus, the numerical method allows to evaluate the coil conductor loss *V-I* curves. Using Equation 3.24 and the local magnetic field calculated as described in section 4.3, one can calculate eddy-current loss in the iron cups. In order to test the theory for coils, the numerical method must be verified experimentally.

The conductor loss of sub-coils is measured with the thermal method using miniature silicon diodes as thermometers placed in thermal contact with the windings and insulated from the liquid nitrogen. The thermometers are calibrated during DC measurements using the coil itself as the heater ($I_{tr} > I_c$). For example in sub-coil 1s, a transport current flowing in opposite directions through the adjacent conductor tapes is used during the calibration [Gode00b]. The advantage of the thermal method is that it allows to estimate the conductor losses directly [Ashw00]. From the measured data the conductor loss *V-I* curves of the coils are derived.

The total losses inside the cryostat (of coil conductor, c- and C-cups, of current leads and of other metal parts) are measured with the calorimetric method. The significance of the method is that it allows measuring the loss subjected to the cooling penalty, Equation 5.5. The method is based on measuring the flow rate of boil-off nitrogen gas at standard conditions (room temperature and atmospheric pressure). An increase of the flow rate with a certain transport current through a coil (compared to the background flow rate at zero

current caused by the heat leak into the cryostat of 57 to 62 Watts) is related to the losses. The calibration at atmospheric pressure is performed using an additional heater (placed inside the cryostat) and a mechanical gas counter, see [Rabb01a] for further details.

To lower the bath temperature the vacuum pump is used, see section 4.5.3. In order to facilitate the method at lower bath temperatures, the pump was calibrated against the counter. It is found that at constant temperature T_2 the pressure P_2 (see Figure 4.21) is directly proportional to the gas flow rate measured by means of the counter with a reasonable error of few percent. The calibration curve is derived from the measurement and the reading of the pressure sensor P_2 is used to measure the flow rate of the boil-off nitrogen gas during the experiment. During measurements when possible a total dissipation inside the cryostat is kept constant by means of the heater in order to reduce the measurement time. Hence, the conductor losses derived with numerical and thermal methods can be separated from and compared to the losses of other coil components.

The total electro-magnetic losses during the coil operation are measured with an electro-magnetic method. The voltage across the sub-coils is measured using the voltage taps. The taps are soldered to each Bi-2223 tape individually and exclude the influence of the end joints. The inductive (out of phase) part of the voltage is compensated by subtracting an analogue signal directly proportional to the derivative of the transport current through the coil. The in-phase part of the remaining voltage represents the electro-magnetic losses of the coil and of the objects coupled to it. During the experiments the laboratory environment was moderately filled with ferro-magnetic objects (like structural iron in the floor). Consequently, the electro-magnetic losses appeared to be much higher than the calorimetric losses indicating that substantial part of the losses is in the coupled objects outside the cryostat.

4.4.1 Direct transport current

Voltage-current curves of the coils measured at 77 K in three of the four configurations are listed in Table 4.4 [Gode00]. The extracted from the measurements effective critical currents and *n*-values of the sub-coils as well as the data for the short samples used for reference are presented in the table. The gain in the critical current due to the application of the iron cups is clearly seen. For the stand-alone sub-coils in case C2 the gain is approximately 20-30 %, as compared to the case C1. The critical currents of sub-coils 3s and 4s alone even surpass those of the corresponding short samples. In the 1-MVA coil arrangement the critical current of the sub-coils is reduced due to the higher magnetic field. Remarkably, the same or slightly better values of the critical current and *n*-value are found in configuration C4 as compared to the configuration C1 for all sub-coils.

When the sub-coils are connected in series, the critical current of the 1-MVA coil is limited by sub-coil 1s. The *V-I* curves and thermal behaviour of sub-coil 1s at 77 K are presented in detail in [Gode00b] and [Shev01] and the summary is given in Figure 4.13 for the same cases as listed in Table 4.2. The points are measured and the lines are calculated using Equation 4.3, the magnetic field profiles and the short sample data from Table 4.1. In cases C1 and C2 the

Table 4.4 Short sample and coil critical currents and n-values of the sub-coils 1s-4s at 77 K and $E = 10^{-4}$ V/m.

Parameter or Magnetic arrangement	Sub-coil number							
Sub-coil number	1s		2s		3s		4s	
Critical current I_c and *n*-value	I_c	*n*	I_c	*n*	I_c	*n*	I_c	*n*
Unit	[A]	[-]	[A]	[-]	[A]	[-]	[A]	[-]
Short sample of tape in self-field	104[a]	19	114	18	123	18	117	20
C1: the sub-coil alone without c- or C-cups	67	13	92	15	102	16	104	16
C2: the sub-coil alone with c- and C-cups	86	10	112	18	126	18	128	18
C4: the 1-MVA coil with c- and C-cups	68	14	92	17	105	17	104	17

[a] this value is two times the current of a single tape

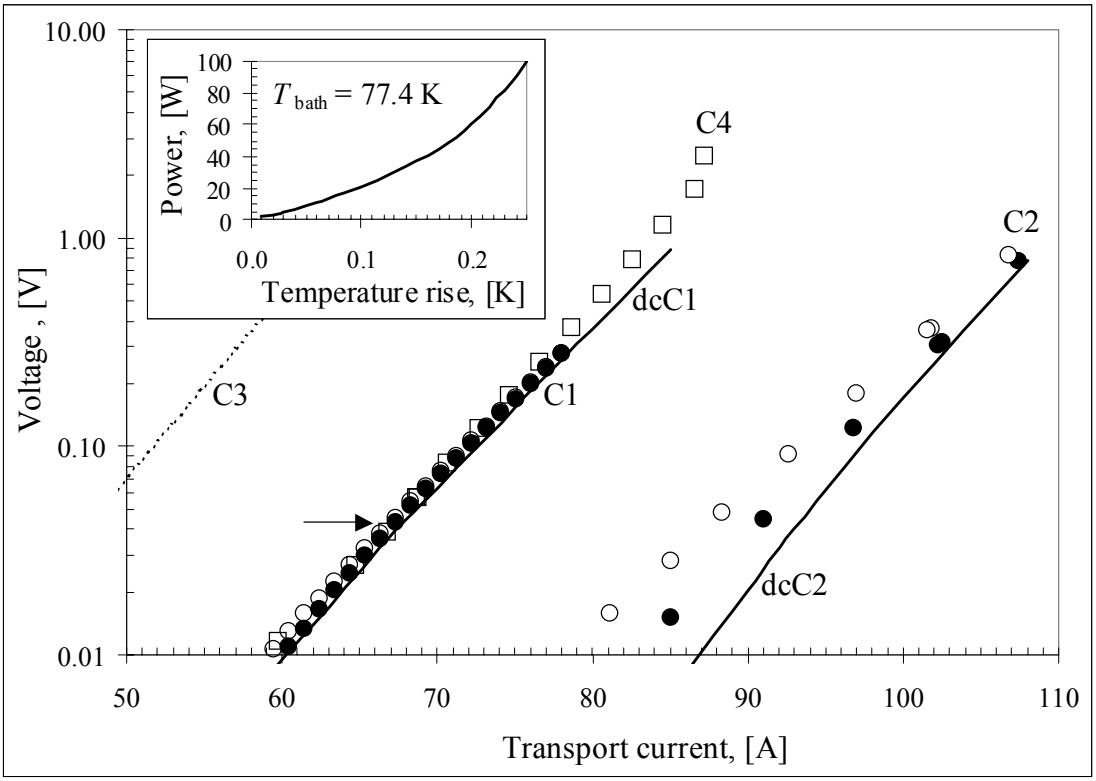

Figure 4.13 Direct logV-I curves of sub-coil 1s at 77 K in cases: C1 and C2, the circles are measured, the lines are calculated; C3 (calculated) and C4 (open boxes, measured).

V-I curves are measured individually for both tapes comprising the sub-coil conductor (shown with the open and filled circles). The inset shows the calibration curve of the thermometers used to derive the conductor losses with the thermal method. The arrow indicates the voltage criterion V_0 = 43.9 mV at which the critical current of the sub-coil is defined (it corresponds to the electric field of 10^{-4} V/m).

The *V-I* curves of the sub-coil in cases C1-C4 are calculated using Equation 4.3, appropriate profiles of magnetic field (Figures 4.10-4.11), magnetic field dependence of the critical currents and *n*-values (Figures 2.11-2.12) and the data for a short sample of tape in self-field (Table 4.4). The *V-I* curves in cases C1 and C4 are found very close to each other. For this reason one of them is shown as the solid line (labelled as dcC1 in the figure). The agreement between the measured points and the calculation is good (the same is valid for sub-coil 3s, see Figure 4.14).

Good agreement between the measurement and the calculation in case C1 indicates that the Bi-2223/Ag tapes in the sub-coils are not damaged. Hence, there is practically no reduction of the critical current all the way from the bare tape delivered by the vendor, through the insulation process, through the coil manufacturing and the successive operation including many thermal cycles between 300 and 77 K. This conclusion is supported by the additional measurements performed on multiple short samples of the tapes taken at various stages of the process.

At present the model used to calculate magnetic field does not account for a residual radial magnetic field caused by the gaps between adjacent turns (a gap between Bi-2223 filaments of two turns is at least 0.3 mm; see Figure 2.2). An enhancement of the model would increase its complexity and is beyond the scope of this study. This explains in part the observed discrepancy between measurements and calculations (line dcC2 in the figure) observed in case C2. Another reason is that the parallel tapes originally have a slightly different critical current. In cases C1 and C4 the radial magnetic field at the coil edge by far exceeds the residual field, the effect vanishes and the agreement between the measurement and calculation improves, see Figure 4.13. For other sub-coils similar results are

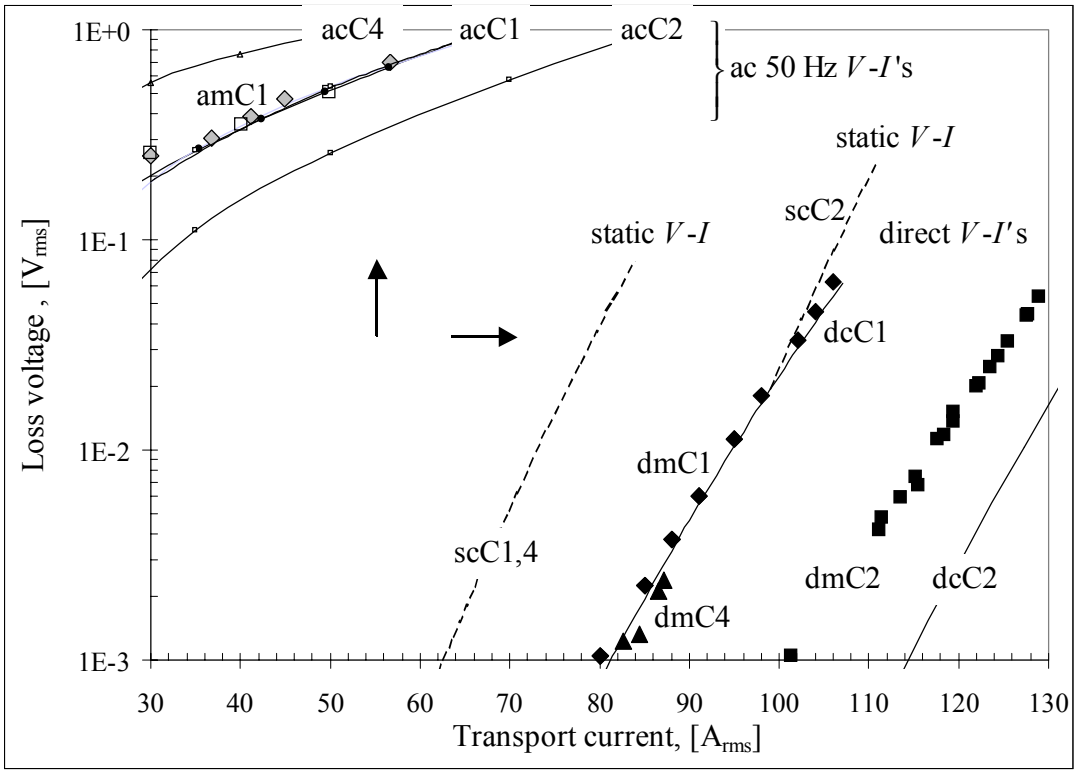

Figure 4.14 Conductor loss logV-I curves of sub-coil 3s at 77 K: the larger symbols indicate the measured points; the lines are calculated; the labels on the curves are m – measured, c – calculated, d – direct, s – static a – alternating, C1-4 are the magnetic arrangements further explained in Table 4.5; the horizontal arrow indicates the voltage criterion V_0=35.9 mV at which the critical current of the sub-coil is defined (it corresponds to the electrical field of 10^{-4} V/m) and the vertical arrow indicates the design value of coil alternating transport current at this temperature.

obtained. The direct *V-I* curves of sub-coils 3s and 4s are very close to each other and show the highest critical currents for all studied magnetic arrangements (as compared to the other sub-coils), see Table 4.4. Though the critical current of sub-coil 2s is somewhat lower (due to the lower critical current of the tape), the sub-coil shows very similar behaviour as compared to the other two sub-coils. As an example, the *V-I* curves of sub-coil 3s are shown in Figure 4.14 and further clarified in Table 4.5. The static and AC *V-I* curves of the sub-coil are explained in the next section.

The electric behaviour of the sub-coil in all the magnetic arrangements qualitatively is rather similar to that of sub-coil 1s. Namely, the sub-coil has the highest critical current in case C2. The critical currents in cases C1 and C4 are lower than in case C2 and they are almost equal to each other (the same picture is seen in Figure 4.13 for sub-coil 1s). It should be noted that the critical current of the sub-coil in case C4 was extrapolated rather than measured. The experimental *V-I* curves in cases C1 and C4 coincide in the range of the measurement from $3 \cdot 10^{-4}$ to $2 \cdot 10^{-3}$ V/m (only partly shown in the figure).

Table 4.5 The V- I curve labels used in Figure 4.14.

Case \ Type of *V- I* curve	direct		static	alternating (50 Hz)	
C1: the sub-coil alone without c- or C-cups	dmC1	dcC1	scC1	amC1	acC1
C2: the sub-coil alone with c- and C-cups	dmC2	dcC2	scC2	amC2	acC2
C4: the 1-MVA coil with c- and C-cups	dmC4	dcC4	scC4	amC4	acC4

The keys: d – direct, s – static, a – alternating; m – measured, c – calculated.

The *V-I* curves of the sub-coil in cases C1, C2 and C4 are calculated using Equation 4.3, appropriate profiles of magnetic field (such as in Figure 4.12b), magnetic field dependence of the critical current and *n*-value (Figures 2.13 and 2.14) and the data for the short sample of tape in self-field (Table 4.4). The calculated *V-I* curves in cases C1 and C4 are found very close to each other. For this reason one of them is shown as a solid line (labelled as dcC1 in the figure). The agreement between the measured points and the calculation is good (the same holds for sub-coil 1s, see Figure 4.13).

The calculated *V-I* curve in case C2 is shown as the solid line labelled dcC2. The calculation correctly predicts an increase of the sub-coil critical current when the iron cups are added. However, the measured critical current is about 8 % lower than calculated. The reason for the discrepancy is the same as for sub-coil 1s: the residual radial magnetic field due to the gaps between adjacent turns unaccounted by the model causes a higher calculated value of the critical current as compared to the measurement. An important dissimilarity in this case is that the current that flows through one tape is very different in sub-coils 3s and 1s (126 A and 43 A at 10^{-4} V/m for sub-coils 3s and 1s respectively). Therefore, the residual magnetic field is also almost 3 times different in magnitude and this explains why the discrepancy between the measurement and the calculation for sub-coil 3s is larger than for sub-coil 1s.

Clearly, a more advanced numerical model that accounts for the effect of residual radial magnetic field due to the gaps between the adjacent turns on the coil critical current could improve the situation. However, such a model is also more complex. From the practical point of view a further improvement of the model is not of primary importance. Indeed, when the magnetic field increases (to characteristic values expected in 1-MVA coil), the discrepancy between the measurement and the calculation vanishes rather rapidly for all sub-coils, see for instance cases C1 and C4 in Figures 4.13 and 4.14.

4.4.2 Sinusoidal transport current

At the frequency limit $f \to 0$, the loss *V-I* curve of a coil (or a tape) asymptotically approaches the static *V-I* curve [Shev99a]. The static *V-I* curve (free of magnetisation current) is not frequency dependent, but depends on the shape of the transport current through the coil. For a sinusoidal transport current with an amplitude I_{tr0} and circular frequency ω the static loss *V-I* curve is calculated as follows (assuming the same density of transport current in any point of the conductor cross-section). For every value of the transport current amplitude I_{tr0} the static loss voltage V_2 is calculated using Equation 4.3: $V_2 = \int_0^{l_t} E_2 dl$ and matching magnetic field profiles, see Figures 4.10 - 4.12. The electric field E_2 is calculated as $E_2 = \frac{Q_{tr2}}{\tau_0 \cdot I_{tr0}}$. The cyclic transport loss Q_{tr2} is found with Equation 3.40: $Q_{tr2} = \int_{\tau_0} E_{tr2} I_{tr} dt$ and the field E_{tr2} is calculated from Equation 2.4. In this case, electric field E_2 can be calculated analytically using Gamma functions:

$$E_2 = E_0 \left| \frac{I_{tr0}}{I_c} \right|^n \frac{1}{2\pi} \int_0^{2\pi} \left| \sin(\omega t) \right|^{n+1} d\omega t . \qquad \textit{Eq. 4.4}$$

4.4.2.1 Outer sub-coil 1s

For a sinusoidal transport current using the data from Figure 4.13 the static *V-I* curves of the sub-coil could be calculated. An example of the static curve in case C2 is shown in

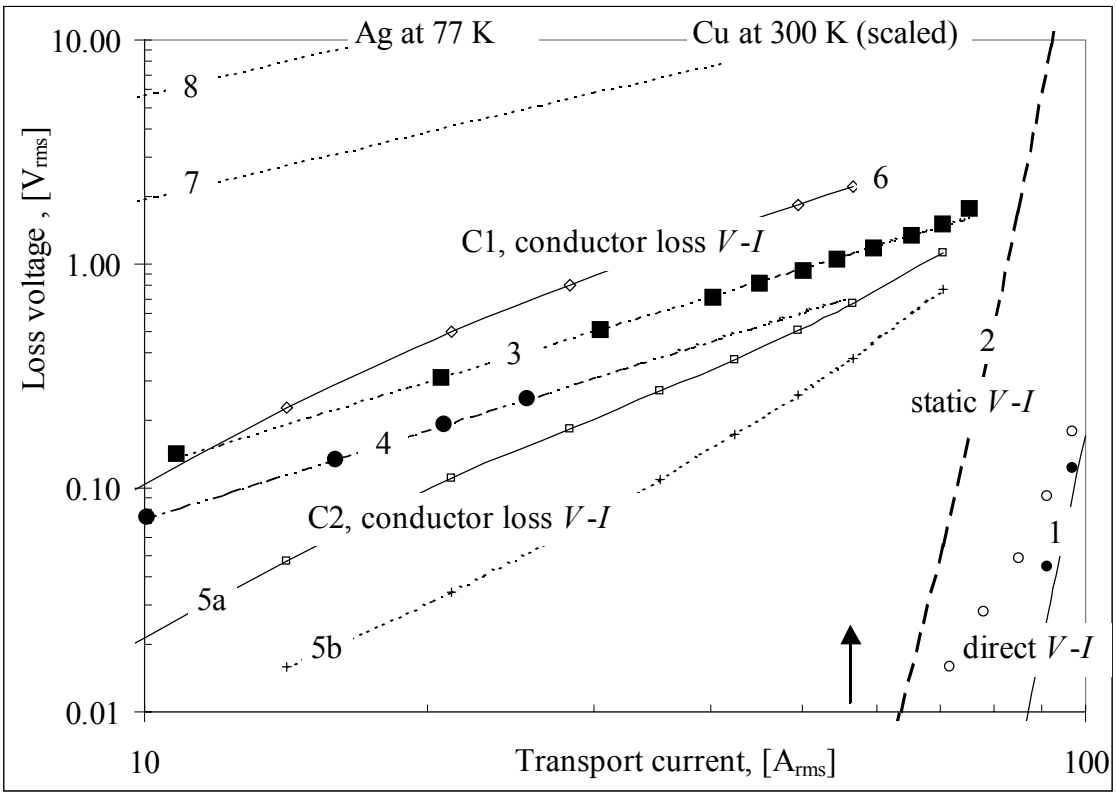

Figure 4.15 Loss logV-logI curves of sub-coil 1s in case C2 at 77 K: lines 1 – direct, line 2 – calculated static; at f = 49 Hz: lines 3 and 4 – measured with the electro-magnetic method, the symbols are measured points and the lines are a guide to the eye; calculated lines 5a – conductor total and 5b – conductor transport; lines 7 and 8 – calculated for an identical coil made with copper and silver conductor and operated at 300 K (scaled by a factor of 20) and at 77 K respectively. Line 6 – calculated total conductor loss in case C1 and shown here for reference. The arrow indicates the design value of coil transport current at this temperature.

Figures 4.15 and 4.16 as line 2. The results obtained for sub-coil 1s in case C2 at 77 K and in the frequency range from 1 to 400 Hz are summarized in Figures 4.15 and 4.16.

The group of points and the line marked as "1" represent the direct *V-I* curve of the sub-coil shown as reference, see Figure 4.13. Line 2 is the static loss *V-I* curve calculated with Equation 4.4. Using the electro-magnetic method, line 3 is measured with the sub-coil placed on the laboratory floor and line 4 is obtained with the sub-coil placed 1 m above the floor. The behaviour suggests that part of the losses might originate from outside the cryostat in the coupled objects (ferro-magnetic structural elements of the building in particular). Therefore, line 4 gives the lower limit of the coil total electro-magnetic losses in this environment. Lines 5a and 5b are calculated using the numerical network model and account only for the sub-coil conductor (5a – for the total losses and 5b – for the transport losses, see Equations 3.40 and 4.3).

Using the numerical method the loss *V-I* curves of the sub-coil conductor are calculated in the frequency range of 1 to 400 Hz and plotted in Figure 4.16. In addition, the conductor loss voltages are measured thermally at 16, 49 and 97 Hz (depicted in the figure with the larger filled symbols) and thus ensure that the agreement of the numerical and thermal methods at 49 Hz is not incidental. Analysis of the data presented in the figure reveals that over the range covered, the loss per cycle of the sub-coil conductor is frequency-dependent. A similar effect is found for the total loss of the same tape, see Figure 3.13 as an example. The dependency is somewhat more pronounced at higher transport currents. While within the narrow range of 50 to 60 Hz the

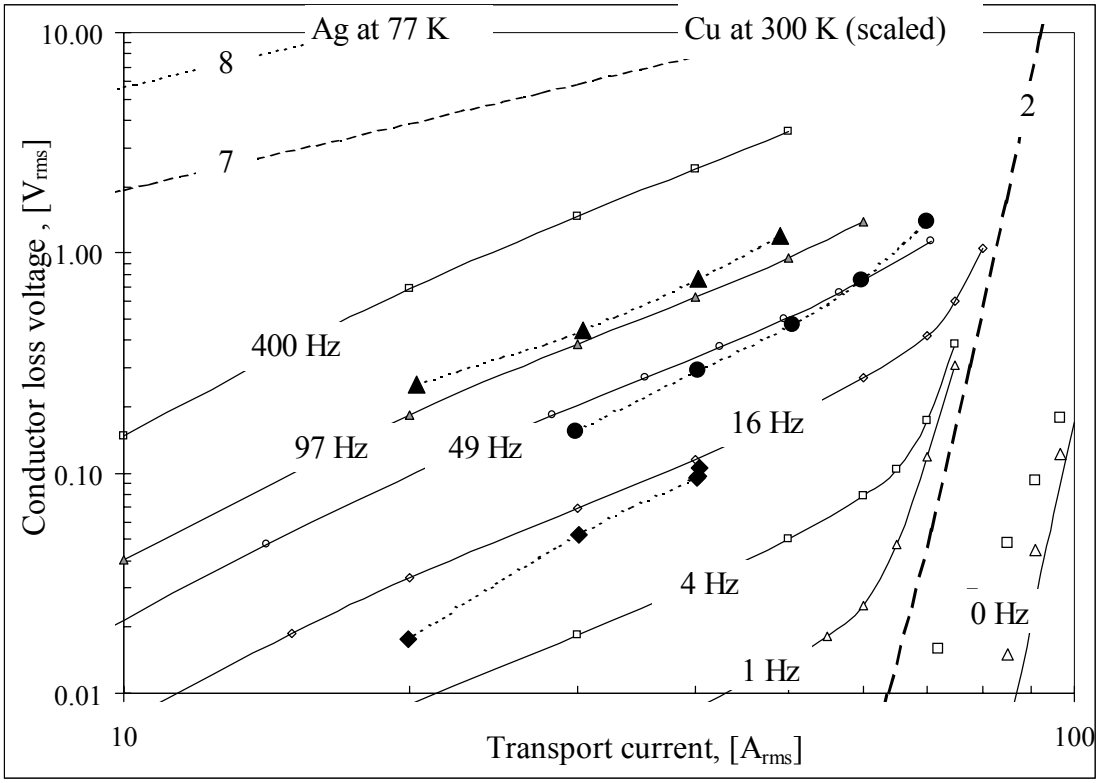

Figure 4.16 Conductor loss logV-logI curves of sub-coil 1s in case C2 at 77 K and the frequency ranging from 1 to 400 Hz: the solid lines are calculated, the labels indicate the frequency; the lines 0 Hz, 2, 7 and 8 are explained in Figure 4.15; the closed symbols represent the points measured with the thermal method.

effect is a few percent only, over the range 1 to 400 Hz it reaches (depending on the transport current amplitude) up to about 50 %.

At the frequency of 49 Hz and design current I_{tr0} of 55 A_{rms} the electro-magnetic, numerical and thermal methods seem to agree well with each other, $V_{\rho t} \approx 0.7$ V_{rms}. This suggests that in this case the dissipation in the iron cups is probably lower than the sub-coil conductor losses. Indeed, obtained from a more detailed measurement (performed with sub-coil 2s in case C2, see [Rabb01a], p. 167) the loss in the iron cups is about 9 W (or the loss voltage of 0.16 V_{rms}) at this current. As reference the calculated total conductor loss voltage in case C1 at 49 Hz is also plotted, line 6. Due to the iron cups the conductor loss voltage in case C2 is reduced by more than 3 times compared to case C1. Hence, the iron cups positively affect both critical current and conductor losses of a Bi-2223/Ag coil. Furthermore, the thermometers show far lower and more uniform temperature increase of the winding, in average 0.15 and 0.5 K at $I_{tr} = 50$ A_{rms} for cases C2 and C1 respectively, see Figure 4.13 and [Gode00b] for more details. Therefore, also the thermal state of the conductor at the sub-coil edges is remarkably improved due to the iron cups.

Based on the data obtained for case C2 at 49 Hz it is found that the electric quality factor of the coil Q_L is 700 at $I_{tr} = 55$ A_{rms}. To illustrate the potential of high-T_c coils, *V-I* curves are shown of identical sub-coils made with copper and operating at 300 K (line 7) and with silver and operating at 77 K (line 8**)**. Such imaginary identical coils differ only in the material of the conductor. To enable the comparison, the loss voltage of the copper sub-coil is divided by the cooling penalty that is taken equal to 20. The conductor loss voltage of the Bi-2223/Ag sub-coil in case C2 at $I_{tr} = 55$ A_{rms} and 50 Hz is 15 and 45 times lower than of the silver and copper sub-coils respectively. At the time when the sub-coil alone was available for the measurements, the gas-tight cryostat was not prepared yet. For this reason the results of the calorimetric measurement of the losses are lacking in the figures.

4.4.2.2 Sub-coils 2s, 3s and 4s

For the sub-coils the same methods as described in section 4.4.2.1 are applied. In-depth analysis of sub-coil 2s losses is published in [Rabb01a]. Since direct *V-I* curves of sub-coils 3s and 4s are very close, only the conductor loss *V-I* curves of sub-coil 3s at the frequency of 50 Hz are shown in Figure 4.14 as an example. The static *V-I* curves of the sub-coil calculated using Equation 4.4 for harmonic transport current are shown in cases C2, C1 and C4 by the dashed lines labelled scC2 and scC1,4 respectively.

The conductor loss *V-I* curves of the sub-coil at 50 Hz are shown in the figure for cases C2, C1 and C4 by solid lines with the small symbols and labelled acC2, acC1 and acC4 respectively. The curves are calculated using the numerical method. The calculations are validated experimentally. The points labelled with amC1 are measured with the calorimetric method (boil-off).

At the design current I_{tr0} = 55 A_{rms}, the calculated conductor loss voltage is 0.34; 0.66 and 1.1 V_{rms} respectively for the cases. The calculated conductor loss voltage is about two times lower in case C2 as compared to case C1 at this current. Note that for sub-coil 1s the calculated conductor loss voltage is three times lower in case C2 as compared to case C1 at this current (about 0.7 and 2.1 V_{rms} respectively, lines 5a and 6 in Figure 4.15). Furthermore, in case C2 the calculated conductor loss voltage of sub-coil 3s is two times lower than that of sub-coil 1s at comparable other conditions (0.34 and 0.7 V_{rms} respectively).

The primary reason is that at comparable thickness and width tape A has more than two times higher critical current than tape V, see Table 2.2. For this reason sub-coils 3s and 1s have respectively two and four tape layers. A periodic pattern of magnetic field ((Figures 4.10-4.12) repeats itself two times for every layer and therefore in sub-coils 1s and 3s it is repeated in total 8 and 4 times respectively, which causes the divergence in loss voltage of the sub-coils. To compare the loss voltages of sub-coils 3s and 1s, the conductor loss *V-I* curve of sub-coil 1s in case C2 is also plotted in Figure 4.14 as a solid line with small filled circles. It is seen that the conductor loss *V-I* curve of sub-coil 1s in case C2 coincides with the conductor loss *V-I* curve of sub-coil 3s in case C1 in the transport current range at least from 30 to 60 A_{rms}.

Note that at the design current I_{tr0} = 55 A_{rms}, the frequency of 50 Hz and temperature of 77 K the conductor loss voltage of the Bi-2223/Ag sub-coil 3s in cases C4 and C2 (about 1 and 0.3 V_{rms}) is 20 and more than 60 times respectively lower than of identical coil made with copper (about 20 V_{rms}). The static *V-I* curves show directly the potential of Bi-2223/Ag tapes as it can be concluded for instance from Figure 4.14. At the transport current amplitude equal to 62 A_{rms} the loss voltage of the sub-coil in case C1 is about 1 V_{rms}. The sub-coil is made from tape with relatively thick and untwisted Bi-2223 filaments. When to make the same sub-coil from tape with fine, twisted and decoupled filaments (that is to eliminate the induced currents without reducing the critical current), the loss voltage at the same current can in principle be reduced to 1 mV, which corresponds to the loss reduction by three orders of magnitude.

In order to assure that the cooling conditions of sub-coils are proper, the following test is performed. Sub-coils 1s and 2s are removed and sub-coils 3s and 4s with c- and C-cups are assembled into the system. Sub-coil 3s is electrically disconnected from and sub-coil 4s is electrically connected to and tested in the resonance circuit. The transport current is varied from zero to 60 A_{rms}. The coil temperature is monitored using the thermometers and the coil losses are measured using the calorimetric and thermal methods. The losses and temperatures in the sub-coil windings are found practically unchanged as compared to case C1.

In conclusion, the behaviour of accurately made relatively large high-T_c sub-coils operating at 77 Kelvin is studied numerically and verified by the experiment. Calculated and measured direct *V-I* curves are in fair agreement, which ensures that the superconducting tape is not damaged. Loss *V-I* curves of the sub-coils operating in liquid nitrogen are calculated using the numerical method and validated by the measurements. Iron c-cups placed around the sub-coil edges simultaneously increase the critical current, reduce the conductor losses and improve the thermal state of a superconducting coil.

4.5 1-MVA resonator coil system

A comparison of measured and calculated *V-I* curves and losses of the sub-coils described in the previous section, has shown expected electrical behaviour of the sub-coils and has validated the numerical method on a coil level. In this section the accent is on the 1-MVA coil system.

In order to reduce the chance of high-voltage break-through the thermometers and the voltage taps are removed from all sub-coils. Subsequently, the thermal method could not be used. Instead, the numerical method is used as the tool for estimating the coil conductor losses. The losses inside the cryostat are measured with the calorimetric method. The electro-magnetic method is substituted by a wattmeter. When the circuit is at resonance (Figure 4.1), it consumes only active power that is measured by the wattmeter. In this case the capacitor loss and the losses in current leads to the coil and connecting cables are also measured.

4.5.1 Numerical estimate of the coil conductor losses

The same method as described in section 4.4 is used here to calculate the conductor loss *V-I* curves of the 1-MVA coil. The method is verified by measurements performed with sub-coils, see section 4.4. At constant transport current in the coil, the conductor loss voltage of the coil is a sum of the loss voltages of the sub-coils comprising the coil. The relevant magnetic field profiles are used to calculate the loss voltage of each sub-coil, see Figures 4.10 - 4.12. At the time when sub-coil 1s was manufactured, the Bi-2223 tape of type A (Tables 4.1 and 2.2) was not yet available on the market. Therefore, two cases are evaluated below. In both cases the four sub-coils are electrically connected in series.

In case VA**,** sub-coil 1s is the same as listed in Table 4.1. The calculated conductor loss *V-I* curves of the sub-coils and of the 1-MVA coil are shown in Figure 4.17 for this case. In case AA it is assumed that sub-coil 1s is replaced with the coil having the same dimensions and number of turns, but made of a single tape A (instead of two tapes in parallel of type V**)** in

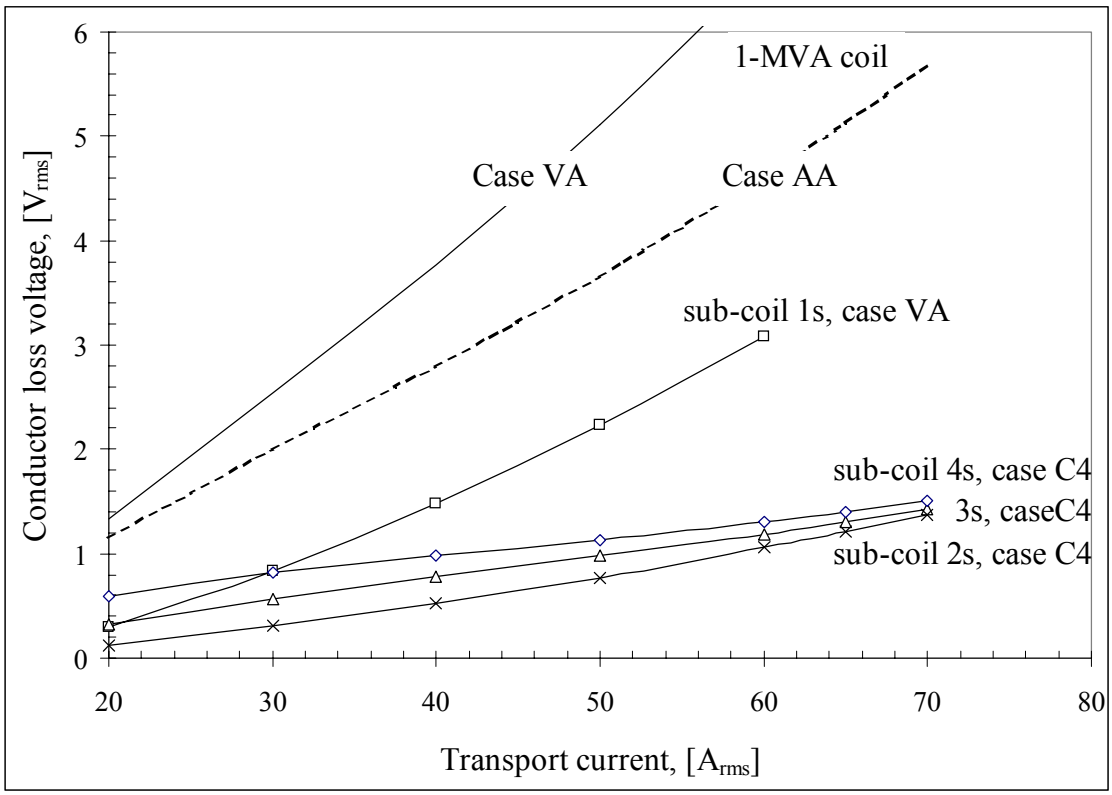

Figure 4.17 Calculated conductor loss V-I curves of the 1-MVA coil and of the sub-coils at 77 K, f = 47 Hz: case VA – as listed in Table 4.1; case AA with sub-coil 1s being upgraded.

the same way as the other three sub-coils. Furthermore, for sake of simplicity it is assumed that the loss *V-I* curve of such modified sub-coil 1s is the same as of sub-coil 2s, see Figure 4.17. The outermost sub-coil 1s operates in the lowest axial and almost the same radial magnetic field compared to other sub-coils, see Figures 4.10 - 4.12. Assuming that all sub-coils are made of an identical conductor, the loss *V-I* curve of sub-coil 1s would probably be below of such curve for sub-coil 2s. The difference in the radial magnetic field of the sub-coils is of minor importance, and hence the observed increase of the loss voltage from sub-coil 2s to 4s is primarily due to the successively increasing axial magnetic field, see Figure 4.17.

The reason for the higher loss in sub-coil 1s is in the conductor used, see section 4.4.2. A single tape V alone cannot carry a full current of the coil and hence two tapes in parallel are laid, Tables 4.1 and 4.4. This implies four conductor layers in the sub-coil instead of two layers in the other sub-coils, Table 4.1. As a result, in sub-coil 1s the periodic pattern of the magnetic field repeats itself along the tape length twice as much compared to the other sub-coils. The total length of the Bi-2223 tape used in sub-coil 1s is more than twice the tape length in the other sub-coils. In agreement with Equation 4.3, in case VA this implies higher losses of sub-coil 1s as it is shown in Figure 4.17. For instance, at the transport current of 55 A_{rms} the conductor loss voltage of sub-coil 1s is almost 3 times higher than that of the other sub-coils. As a result, the loss voltage of sub-coil 1s contributes almost 50 % to the total conductor loss voltage of the 1-MVA coil. Hence in case AA, when sub-coil 1s is upgraded, the loss voltage of the 1-MVA coil is reduced by about 30 % at the transport current of 55 $A_{rms,}$ Figure 4.17. Furthermore, the maximum current of the 1-MVA coil could increase, as it will be limited to about 65 A_{rms} by sub-coil 2s and not to about 47 A_{rms} by sub-coil 1s as at present, Table 4.4. All *V-I* curves presented in Figure 4.17 follow reasonably well the power law:

$$V_{\rho t} = C_{\rho t} \cdot I^{m}, \qquad \textit{Eq. 4.5}$$

with $C_{\rho t}$ and *m* constants determined by fitting and listed in Table 4.6.

Table 4.6 Values of the fitting constants in Equation 4.5 for Bi-2223 coils (T = 77 K, f = 50 Hz).

Coil	$C_{\rho t}$, [V_{rms}/A_{rms}^{m}]	*m*, [-]
Case C4: sub-coil 1s	$5.55 \cdot 10^{-4}$	2.12
Case C4: sub-coil 2s	$4.34 \cdot 10^{-4}$	1.91
Case C4: sub-coil 3s	$1.02 \cdot 10^{-2}$	1.17
Case C4: sub-coil 4s	$6.90 \cdot 10^{-2}$	0.72
Case VA C4: 1-MVA coil	$1.79 \cdot 10^{-2}$	1.45
Case AA C4: 1-MVA coil	$2.75 \cdot 10^{-2}$	1.25

4.5.2 Experimental verification of the design

The measured value of the self-inductance for each sub-coil alone (and without C-cups) is listed in Table 4.1. For the 1-MVA coil in case VA the inductance of about 0.28 H is measured at a sinusoidal transport current, see Table 4.7. As expected, a relatively uniform distribution of the voltages across sub-coils is achieved. To ensure a safe measurement, non-destructive AC high-voltage tests of the 1-MVA coil are performed at 50 Hz, both at room temperature and at 77 K. First, the voltage of up to 10 kV_{rms} is applied to the floating coil. Then, the voltage of up to 5 kV_{rms} is applied between the sub-coils. In both cases at 77 K the tests show no sign of partial discharge. Hence, it is concluded that the sub-coil-to-sub-coil and the coil-to-ground insulation are sufficient. Layer-to-layer insulation is provided by at least two layers of KAPTON wrapped around Bi-2223/Ag tapes and tested separately, see Table 2.6.

Table 4.7 V-I characteristics of the 1-MVA coil at T = 77 K and f = 47 Hz.

Coil	I_{tr}, [A_{rms}]	V, [V_{rms}]	Z, [Ω]
Case C4: sub-coil 1s	4.2	98	23
Case C4: sub-coil 2s	4.1	86	21
Case C4: sub-coil 3s	4.0	82	20
Case C4: sub-coil 4s	4.1	73	18
Case VA C4: 1-MVA coil	4.1	339	83

Two cases studied experimentally are summarised in Table 4.8. In case VA sub-coils 1s, 2s, 3s and 4s are connected in series and powered. In case A_2A_4 sub-coils 2s, 3s and 4s are connected in series with sub-coil 1s being physically present, but electrically disconnected (not powered). It can be concluded from Table 4.4 that in cases VA and A_2A_4 the sub-coils 1s and 2s limit the maximum operating current of the 1-MVA coil to about 47 and 65 A_{rms} respectively at 77 K. At these values the amplitude of the transport current is equal to the critical currents of the sub-coils. The measured *V-I* curves of the 1-MVA-coil in case VA at constant frequency but at bath temperatures of 77 K and 64.5 K are depicted in Figure 4.18. It is seen that at both temperatures the inductance of the coil is about 0.28 H. The maximum power that has been reached at 77 K is 256 kVA, close to the design value of 0.25 MVA at this temperature. During the experiment the coil current was limited to about 50 - 55 A_{rms} for several reasons. The open boxes show the loss *V-I* curve of the *LC*-circuit (see Figure 4.1)

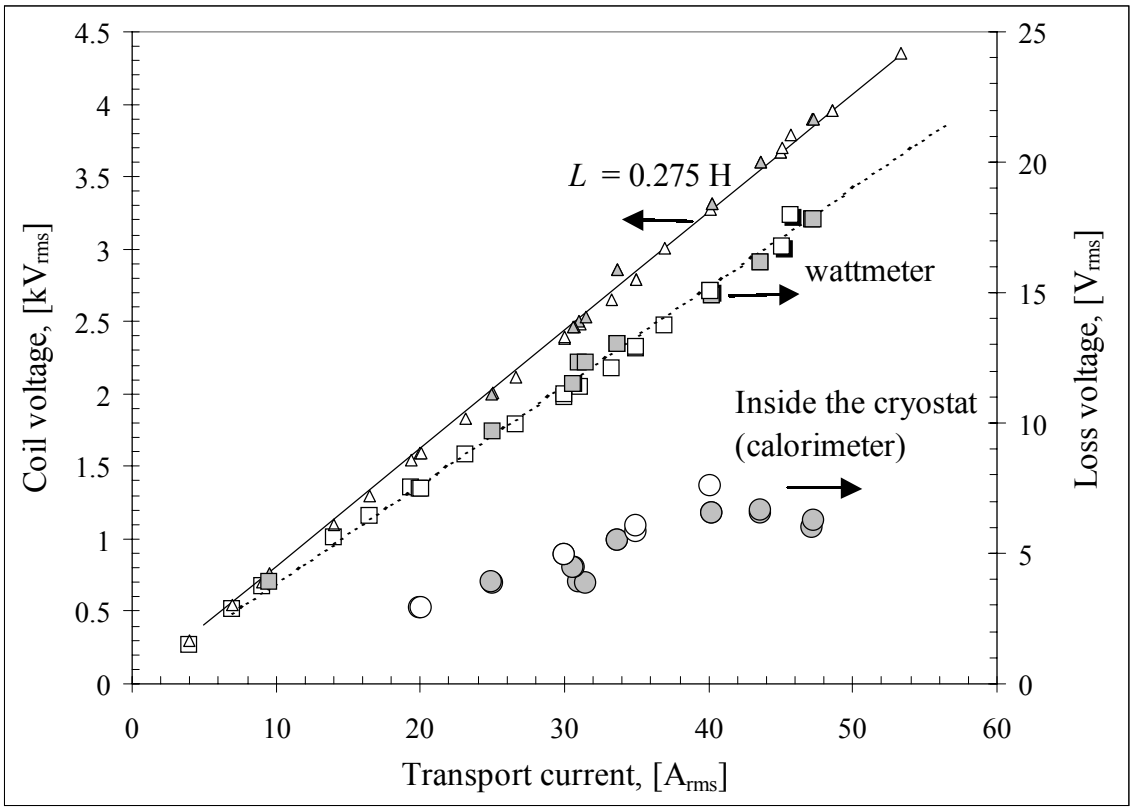

Figure 4.18 V-I curves of the 1-MVA coil in case VA at f = 47 Hz and T_{bath} = 77 K (open symbols) and 64.5 K (filled symbols) and loss V-I curves of the LC circuit for the same conditions, the symbols are the measured points: the coil voltage is represented by the triangles, the solid line is the inductive voltage calculated for L = 0.275 H; the loss measured with the wattmeter is represented by the boxes. The dashed line is the voltage of the losses both inside and outside the cryostat (calculated assuming R =0.38 Ω). The circles represent the coil loss voltage measured calorimetrically (boil-off); the arrows show the proper vertical axes.

Table 4.8 Parameters of the 1-MVA circuit used during the experiments.

Parameter	Case VA	Case A_2A_4
Capacitance C, [μF]	40.9	40.9
Inductance L, [H] (nr. of turns)	0.28 (1124)	0.14 (828)
Resonant frequency f_0 [Hz]	47.1	65.9
Bath temperature T_b, [K]	77 and 64	77 and 70
Circuit current I_{tr} [A_{rms}]	55 and 55	65 and 85
Voltage across the coil V_{coil} [kV_{rms}]	4.55 and 4.55	3.85 and 5.1
Inductive power P_{coil} [MVA]	0.25 and 0.25	0.25 and 0.43

measured by the wattmeter with the coil being at 77 K. The electric power consumed by the *LC*-circuit is found to be almost proportional to the square of the coil current, hence indicating substantial ohmic (eddy current) losses in the objects coupled to the coil both outside and inside the cryostat.

A rather high effective value of the overall loss resistance $R = 0.38\ \Omega$ is found with a corresponding quality factor of about 230, see Figure 4.18. The loss outside the cryostat occurs in the objects electro-magnetically coupled to the coil (structural ferromagnetic and conducting elements, such as iron in the floor of the building, metal wheels and other metal parts of the cryostat, like piping, flanges and bolts), the capacitor and the wiring. Consequently, it is important to reduce the amount of magnetic and conducting parts around the coil in the future. A stable operation of the system, sufficient to perform the calorimetric measurement (demanding about 30 min per point), was possible at a transport current below 40 - 48 A_{rms}.

The loss *V-I* curves derived through the calorimetric measurement at 77 and 65 K are shown with the open and filled circles respectively. This part of the loss voltage is due to the losses in the coil conductor, iron cups, current leads and other conducting components inside the cryostat. It is seen that the loss inside the cryostat is only a fraction of the active power consumed by the *LC*-circuit at resonance. At 65 K the critical current of the coil increases in agreement with

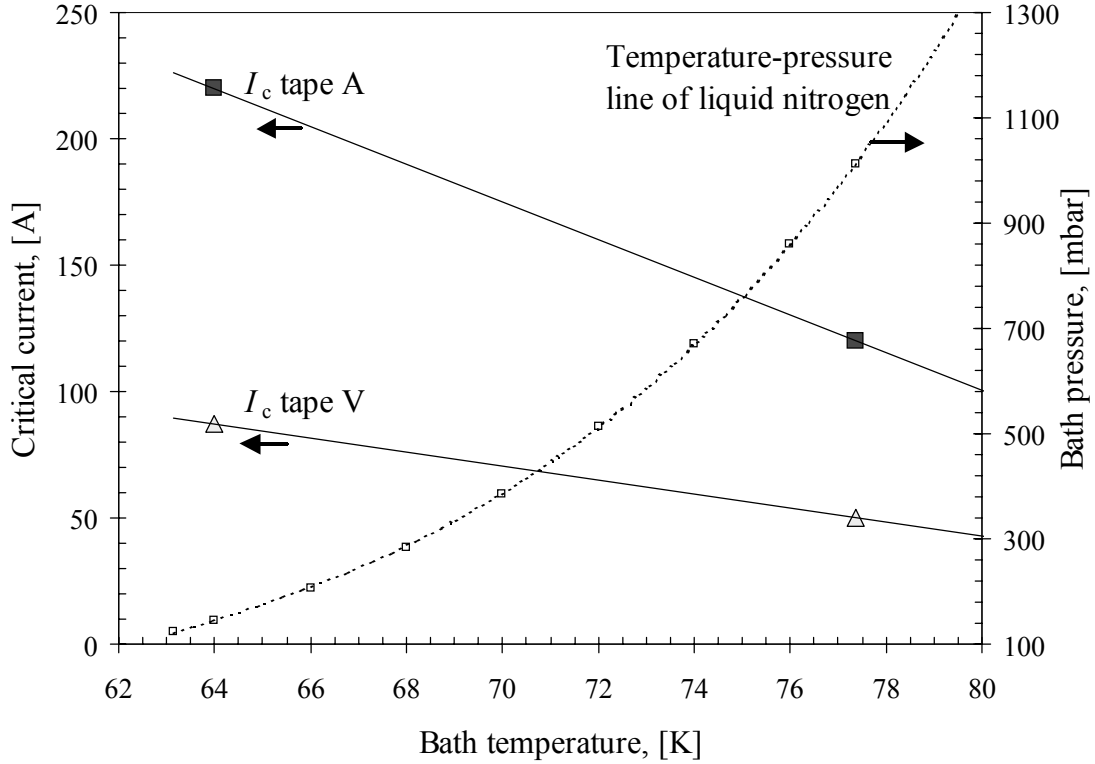

Figure 4.19 Critical currents of the Bi-223/Ag tape samples V and A and the bath pressure as functions of the bath temperature inside the cryostat.

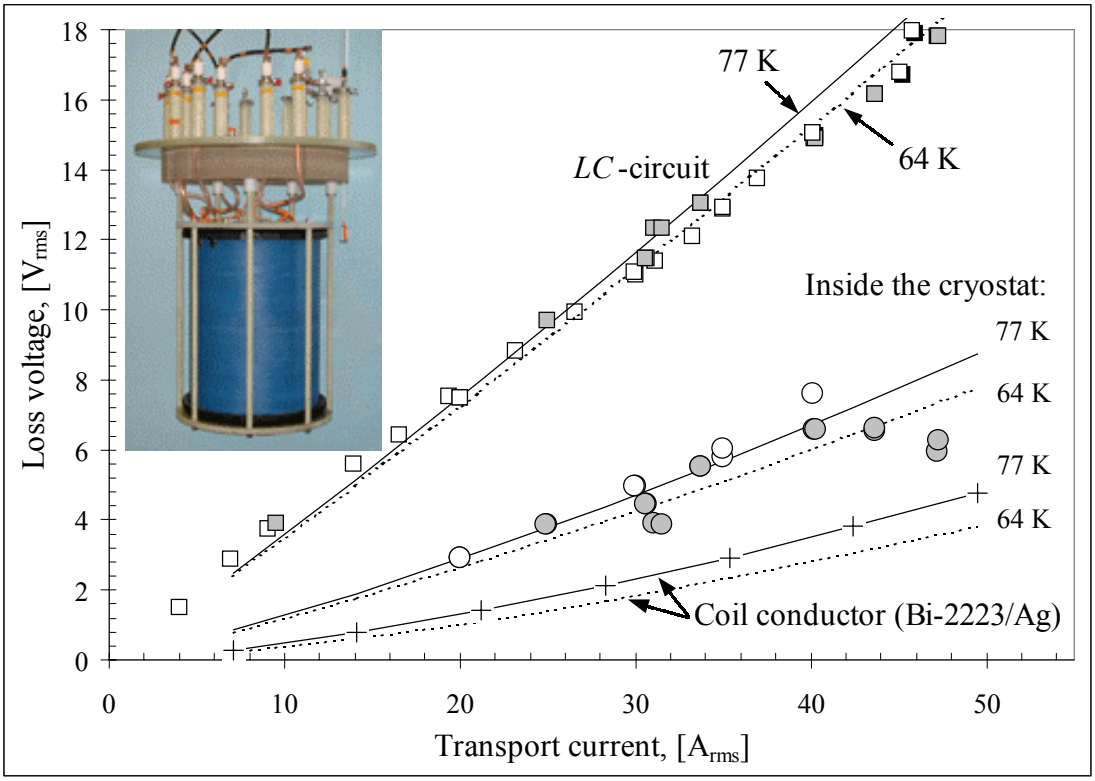

Figure 4.20 Loss V-I curves of the 1-MVA Bi-2223/Ag coil in case VA at f = 47 Hz, T_{bath} = 77 K and 64.5 K, the symbols represent the measured points, the lines are calculated, the inset shows the photo of the completed 1-MVA coil.

Figure 4.19. Hence the direct, static and loss *V-I* curves of the coil at this temperature shift to the right correspondingly. The filled circles in Figure 4.18 represent the experimental data obtained with the calorimetric method at 65 K, see section 4.5.3 for more details. The voltage due to the loss inside the cryostat is only a fraction of the loss measured with the wattmeter. Therefore, it is concluded that the major part of the losses in the *LC*-circuit (measured with the wattmeter) takes place outside the cryostat. The conclusion is supported by earlier measurements on sub-coils, lines 3 and 4 in Figure 4.15.

The measured loss *V-I* curves of the coil are analysed in more detail in Figure 4.20. The calculated loss voltage of the coil conductor at 77 K is inserted from Figure 4.17 and at 65 K it is derived using Figure 5.4. In both cases the difference in the operating frequency (between the calculation at 50 Hz and the measurement performed at 47 Hz) is accounted for by the proper scaling. The loss voltage inside the cryostat is calculated using the conductor loss *V-I* curves of the coil, the calculated loss in iron cups and current leads.

To account for the losses due to the c- and C-cups, current leads, and other structural conducting elements, the effective value of the resistance $R_1 = 0.08\ \Omega$ is assumed at both temperatures. Analysis of the losses in the C-cups indicates that the eddy current loss (Equation 3.24) is dominating the magnetisation loss. The largest characteristic dimension of the C-cup in the present design is about 6 cm, while the skin depth of the eddy currents is estimated at about 3 cm. Further lamination of the C-cups (down to about 2 cm) will provide the reduction of the resistance R_1 to the desired level. Avoiding unnecessary current loops in parallel branches can reduce the loss in the current leads. These (technically simple) options are however beyond the scope of the study.

To obtain the loss *V-I* curves inside the cryostat at both temperatures, the calculated loss voltage based on the resistance R_1 is added to the conductor loss voltage. The agreement with the calorimetric measurement is fair (Figure 4.20). In the same way, the loss voltage of the *LC*-circuit (hence both inside and outside the cryostat) is obtained assuming an additional resistance

$R_2 = 0.23\ \Omega$. The resulting lines are shown in Figure 4.20 for both bath temperatures. The corresponding budget of the coil losses (at 77 K and 47 Hz in case VA) can be summarised as following. The loss outside the cryostat amounts to 61 %; in the iron cups and current leads 21 % and of the coil conductor 18 % of the total loss.

In case A_2A_4, the inductive power of 0.25 MVA is reached at a transport current of 65 A_{rms} using three sub-coils connected in series, see Table 4.8. At the bath temperature reduced down to 70 K the inductive power of 0.43 MVA is reached at the transport current through the coil equal to 85 A_{rms}. Further experiments aiming at higher transport current through the coil are on the way.

4.5.3 Cooling of the coil

Each sub-coil alone is characterised at 77 K, while the 1-MVA coil is characterised both at 77 and 65 K. In the present set-up, reduced bath temperature is obtained by reducing the pressure inside the cryostat. The effect is illustrated in Figure 4.19. When the pressure inside the cryostat is kept equal to an atmospheric pressure of about 1013 mbar, the liquid nitrogen boils at 77.4 K. The self-field critical current of the tapes V and A is equal to about 50 A and 120 A respectively, see Table 2.2. When the bath pressure is reduced to 146 mbar, liquid nitrogen starts to boil at 64 K. The self-field critical currents of the tapes increase linearly with the temperature in this range and at 64 K they are equal to 87 and 220 A respectively, see Figure 4.19. The critical currents of the sub-coils increase correspondingly. Further lowering of the pressure might cause complications, as at about 63 K nitrogen becomes solid.

The hardware used to lower the pressure inside the cryostat is sketched in Figure 4.21. The temperature T_2 measured with a thermocouple is kept close to 20°C by means of a heater. The valve controls both the pressure inside the cryostat P_1 and the gas flow from the cryostat, while the vacuum pump does the actual job of reducing the pressure. The calibration of the hydraulic circuit is performed with the gas counter connected instead of the cryostat. The calibration of the vacuum pump against the gas counter shows the following. When the temperature of the inlet nitrogen gas is constant, the inlet pressure of the vacuum pump in the range from 20 to 1020 mbar is directly proportional to the volume flow rate of the gas through the pump. It is found that at a constant temperature T_2 the pressure P_2 is directly proportional to the gas flow rate measured by the flow meter with a reasonable accuracy. Therefore, the calibration curve is derived from the measurement and the reading of the pressure sensor P_2 is used to measure the flow rate of the boil-off nitrogen gas during the experiment.

In the future, the best option for the cooling of resonator coils might be a re-fill of the cryostat with sub-cooled liquid nitrogen at atmospheric pressure and 64 K attained separately. The ambient heat leak into the plastic cryostat (about 60 W) could be easily intercepted with an intermediate shield cooled for instance by liquid nitrogen at 77 K (with liquid nitrogen boil-off being of about 1 litre/hour for 1-MVA coil cryostat). The vacuum pump will be needed still, but the preparation time to operate the coil at 64 K would be significantly reduced.

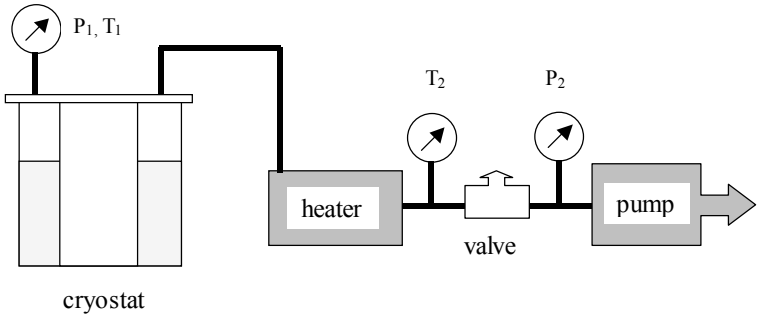

Figure 4.21 Hydraulic circuit of the coil used to control the pressure inside the cryostat.

4.5.4 Specifications of the coil

A resonant circuit as shown in Figure 4.1 may be used for the testing of power cables and capacitors. The operating frequency of the power supply is adjustable, as it must be tuned to the resonant frequency of an *LC* – circuit. When a copper coil is used as a 1-MVA inductor, the electric quality factor is about 20 and the power supply must deliver up to about 50 kW. At this kind of rating, the costs of the power supply are significant. For the field tests of power cables, considerations regarding the primary energy source are of importance. When a high-T_c coil replaces the copper coil, the power supply must deliver only a few kW (assuming a non-magnetic environment for the coil). To perform an hour-long field test, a few car batteries or a small generator can be sufficient as the primary source. Hence the saving provided by a smaller power supply potentially covers extra investment in the inductor.

The photograph of the completed 1-MVA resonator coil lifted above the cryostat is shown in Figure 4.22. The estimated specifications of the high-T_c 1-MVA coil based on the measurements and the calculations are listed in Table 4.9. The electric quality factor of a coil Q_{coil} is the ratio of inductive power and conductor loss power of a coil. For the 1-MVA coil in case VA at bath temperature of 77 K and frequency of 50 Hz the overall value of Q_{coil} of about 800 is found, see Figure 4.17. Using the voltage distribution across and the losses of individual sub-coils, see Table 4.7 and Figure 4.17, one finds the quality factors equal to 520; 1264; 1064 and 856 for sub-coils 1s, 2s, 3s and 4s respectively under the same conditions. Therefore, in case AA (when the sub-coil 1s is upgraded with the modern tape A**)** the value of the overall quality factor for the 1-MVA coil is 1140.

The loss inside the cryostat is important because it is multiplied by the cooling penalty factor (Equation 5.5) and contributes to the running costs. In addition to the coil conductor, the loss of the iron cups, current leads and heat leak into the cryostat contribute to evaporation of liquid nitrogen and should be minimised. Though technically important, the reduction of the losses in these components of the coil system is a trivial task from the scientific point of view (lamination of iron cups, optimisation of the current leads and better design of the plastic cryostat). Hence, only the reduction of the coil conductor losses is addressed here. Liquid nitrogen consumption of the 1-MVA coil system at full power contributes to the running costs

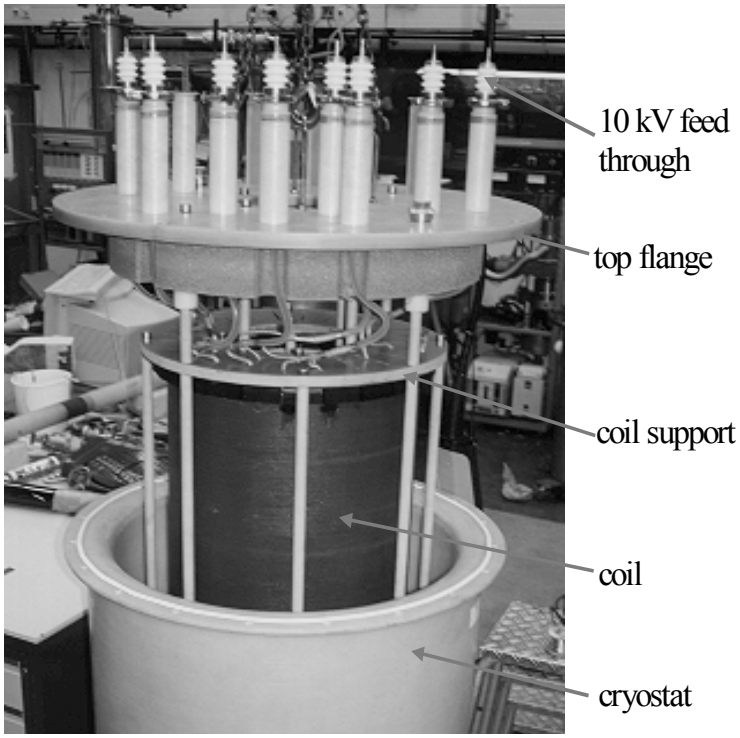

Figure 4.22 The 1-MVA resonator Bi-2223/Ag coil lifted above the plastic cryostat.

at a rate of about 4 US$/hour, see Table 4.9. As it follows from the table, the effective resistance of the conductor for an advanced 1-MVA Bi-2223/Ag coil is at present about 0.1 Ω. To compare with the existing technology, a resistance at room temperature of 1-MVA copper resonator coil is at least 1 Ω and in practice ranges up to about 5 Ω, see the introduction. To carry 100 A_{rms}, about 33 mm^2 of copper is required. Therefore, the active power required to operate the resonator coil is reduced by factor 10 (from about 50 to below 5 kW) when the superconductor replaces copper. Care must be taken to provide superconducting power coils with low-loss electro-magnetic environment as it results in a smaller power supply. For copper coils this is less critical, since the environment loss is much smaller than the conductor loss.

Table 4.9 Estimated specifications of Bi-2223/Ag based 1-MVA resonator coil system.

Parameter	Unit	Value	Value
Coil:			
Reactive power	[kVA]	250	1000
Voltage	[kV_{rms}]	5	9
Current	[A_{rms}]	55	110
Frequency	[Hz]	50	50
Inductance	[H]	0.28	0.28
Quality factor (conductor losses only)	[-]	806 (1140)	750 (1000)
Liquid nitrogen consumption at full power	[ltr/h]	10	40
Number of the sub-coils	[-]	4	4
Number of turns	[-]	1124	1124
Wet weight (incl. cryostat, nitrogen and pump)	[kg]	300	300
Cooling (cryostat and vacuum pump):			
Bath temperature	[K]	77	64
Bath pressure	[mbar]	1013	146
Liquid nitrogen consumption at zero current	[ltr/h]	1.5	2
Volume of liquid nitrogen to refill the cryostat	[m^3]	0.2	0.3
Costs of liquid nitrogen	[US$/$m^3$]	100	100
Method to reach the bath temperature	[-]	-	by pumping boil-off nitrogen gas
Electric power consumed by the vacuum pump	[kW]	0	2.5
Electric power consumed by the heater	[kW]	0.1	0.5
Power supply:			
Voltage	[V_{rms}]	40	40
Current	[A_{rms}]	55	110
Weight	[kg]	46	46

4.6 Conclusions

The resonant circuit for testing cables and capacitors at full power presents an example of a practically important technical system in which a superconducting coil made with the Bi-2223/Ag tape and operated in liquid nitrogen may be used. For this type of applications a lower cost of the power supply feeding the circuit may compensate for the higher cost of the coil (as compared to the case when conventional copper coil is used).

The advanced 1-MVA high-T_c coil system for testing power cables and capacitors is described. The optimization of the coil design has lead to a circular coil that consists of four long and thin concentric solenoids of large diameter made with insulated Bi-2223/Ag tape. To compensate for the negative effect of the radial component of the magnetic field on the

critical current in Bi-2223/Ag tapes and to increase the electric quality factor of coils, it is proposed to surround coil edges with laminated ferro-magnetic C-cups. Application of the cups simultaneously increases the critical current, reduces the AC conductor losses and provides more uniform thermal state of the coil windings.

As a result of the research and technical effort, the knowledge, the infrastructure and technology that allow the manufacturing of power Bi-2223/Ag coils in industrial conditions are developed. The insulation of Bi-2223/Ag tapes and the coil manufacturing technology have been adopted at Smit Wire Nijmegen and at Smit Transformatoren B.V. respectively. All tapes are insulated and all sub-coils are made by the companies personnel. Close cooperation between the university and the industry has created conditions that facilitate technical applications of high-T_c superconductors and resulted in manufacturing the 1-MVA coil system.

Two methods are used for studying *V-I* curves of the sub-coils: numerical and experimental. The latter includes thermal, calorimetric and electro-magnetic methods, which are complementary to each other and allow accessing various components of the coil loss voltage.

To enable the numerical method, magnetic field in the coil windings is calculated using commercial software for various configurations of sub-coils and C-cups. The distribution of the magnetic field along the tape length for each magnetic configuration of the coil is derived from the calculations. Using magnetic field profiles and the network model, the conductor loss voltage is calculated for various magnetic configurations of the sub-coils and for the 1-MVA coil.

The direct voltage-current curves measured and calculated at 77 K for three magnetic configurations of the sub-coils comprising the 1-MVA coil system are presented. The calculations use the effective critical currents and *n*-values along with the data extracted from the tape short sample measurements. The gain in critical current due to the application of the iron cups is clearly seen from the presented data.

The AC loss *V-I* curves of the sub-coils are measured with the electro-magnetic, thermal and calorimetric methods. Because of the high voltage restrictions, AC loss *V-I* curves of the 1-MVA coil are measured with the calorimetric method and using the wattmeter. The coil design is verified with the experiments.

The *V-I* curves obtained using the network model are compared with the experimental data for various magnetic configurations of the sub-coils. A fair agreement of the experimental and calculated data is found and it proves the harmless tape treatment during the coil manufacturing and subsequent operation. At the same time, the agreement validates the developed numerical method itself. This allows numerical characterization of power coils in cases when experiments are difficult or impossible to perform.

Due to the high electric quality factor of the 1-MVA superconducting coil (above 500), the advanced resonant circuit for testing power cables and capacitors at full power consumes only few kW (with sound consumption of liquid nitrogen) as compared to 50 kW in the case when a copper coil is used.

Chapter 5

OUTLOOK FOR SUPERCONDUCTING POWER TRANSFORMERS

In this chapter conventional and superconducting transformers are compared and the viability of superconducting transformers from the economical and technical points of view is dealt with. The essential properties of a superconducting transformer are: electro-magnetic behaviour, costs and reliability, weight and volume as well as environmental and economical impacts. The crucial question for future applications: "at which cost-effective conditions can the overall efficiency of a superconducting transformer be made higher than that of a conventional one?" is dealt with and answered in the chapter. Other less important issues are briefly discussed. Perspectives and problems are underlined. Before further development can be justified, an economical benefit must be certain. When the cost break-even point is passed, the expected advantages of a superconducting transformer are: more efficient, environmentally friendly and compact. More efficient meaning reduced total ownership costs. Environmentally friendly meaning eliminating oil spills and fire hazard. More compact meaning less volume, smaller footprint and lighter. The electrical properties among many others include: power rating, primary and secondary voltages and currents, efficiency, frequency, number of phases, high-voltage withstand, impedance voltage, over-current and over-voltage behaviour. Potential problems are foreseen in fault and short-circuit modes. For a power transformer, the technical and economical parameters are tightly linked due to the fact that copper transformers are produced for almost a century and have reached physical and technological limits in many aspects.

5.1 Introduction

5.1.1 Previous studies

This section summarises the feasibility studies made for superconducting transformers. To enable a comparison with conventional devices, reference data of copper-based transformers are included. Power transformers based on low temperature superconductors never came to life due to poor efficiency (the product of losses and cooling penalty is too high) and maintenance costs of the helium cooling systems. The studies performed over the years 1961-1986 are summarised in [Over86]. A different future for high temperature superconducting power devices is expected. A market penetration trend for the power devices has been forecasted recently [Shea01], [Lawr00]. During the next 20 years, very optimistically, market penetration of 65, 60, 35 and 30 % are predicted for superconducting transformers, motors, generators and cables respectively. For high temperature superconducting transformers the prospects are discussed, for instance in [Meht97], [McCo00], [Funa00a], [Funa00b], [Oome00] and [Hass01]. An overview of the recent research activities is given in Table 5.1. The latest developments are presented in [Schl02], [Mein02]. Most of the studies are aiming at 20-30 MVA utility transformers and 10 MVA traction transformers for trains.

Table 5.1 Recent research activities on high-T_c transformer demonstrators and prototypes.

Group \ Year	1996	1997	1998	1999	2000	2001 ⇒ beyond
Kyushu University, Japan [Funa00]	0.8 MVA 1-phase →				1 MVA 1-phase	3 ⇒ 20 MVA: 3-phase for underground substations
ABB, Switzerland EDF, France ASC, USA [Serr00]		0.6 MVA 3-phase →			On hold	30 MVA systems 3-phase: utility
IGC - Waukesha, USA [Inte01]			1 MVA 1-phase →		5 MVA 3-phase	5 ⇒ 30 MVA 3-phase
Siemens, Germany [Kumm99]				0.1 MVA 1-phase →		1 ⇒ 10 MVA: trains, distribution

A brief summary of the studies is as follows. The world market for copper transformers is estimated at about 10^9 US $. A 30-MVA transformer represents about ½ of the US market. Urban areas need smaller, lighter and free of hazard devices. The expected benefits of high-T_c over copper transformers are: improved energy efficiency; reduced fire and spill risks and hence more environment-friendly, possibly smaller and lighter devices. The likely problems are in conductor losses and fault behaviour. The relation remains uncertain between the practical characteristics of an AC superconductor such as critical current, operating temperature, losses, cooling, electro-mechanics, insulation issues, reliability and price on one hand and the expected benefits of a high-T_c transformer on the other hand, which makes the forecasting fairly complicated.

Here the focus is on power coils and utility transformers in particular. An effort is made to minimize both capital and operating costs of a future high temperature superconducting transformer. For a copper transformer both capital and total costs are very important. For this reason they are included in the consideration. A fair discussion on overload and fault behaviour is beyond the scope of this study.

5.1.2 Arrangement of a transformer

A 3-phase power transformer consists mainly of coils, cooling system, iron core, bushings and main tank. A simple sketch of the essential parts is presented in Figure 5.1. The characteristic dimensions of the iron core are also shown. Transformer windings carry an alternating transport current and are exposed to an alternating magnetic field. Both current and field are sinusoidal; they alternate at the same frequency (50-60 Hz) and in phase. The amplitudes of the current and the field are coupled via the magnetic filed constant. Compared to a DC magnet, much more energy is dissipated in the transformer conductor due to changing magnetic field at the same transport current. Compared to a cable, the amplitude of the changing magnetic field is higher, the direction and phase are different and the loss behaviour is altered. The distinction in operating conditions will influence the costs of and the energy consumed by the device as well as the operating temperature.

The operating temperature of the iron core of a conventional transformer is close to room temperature T_P. A liquid normally cools both the core and the copper or aluminium coils. Oil is commonly used for both electrical insulation and cooling. Oil and cooling radiators add substantially to the mass and volume of a transformer mainly determined by the core and coils.

A schematic layout of a future 3-phase high-T_c power transformer is presented in Figure 5.2 [Amer01]. The iron core of a superconducting transformer is also at room temperature T_P. The superconducting coils operating at a temperature $T_Q << T_P$, are placed in cryostats and are connected by current leads to the bushings at T_P. Cooling of the coils is provided by a refrigerator.

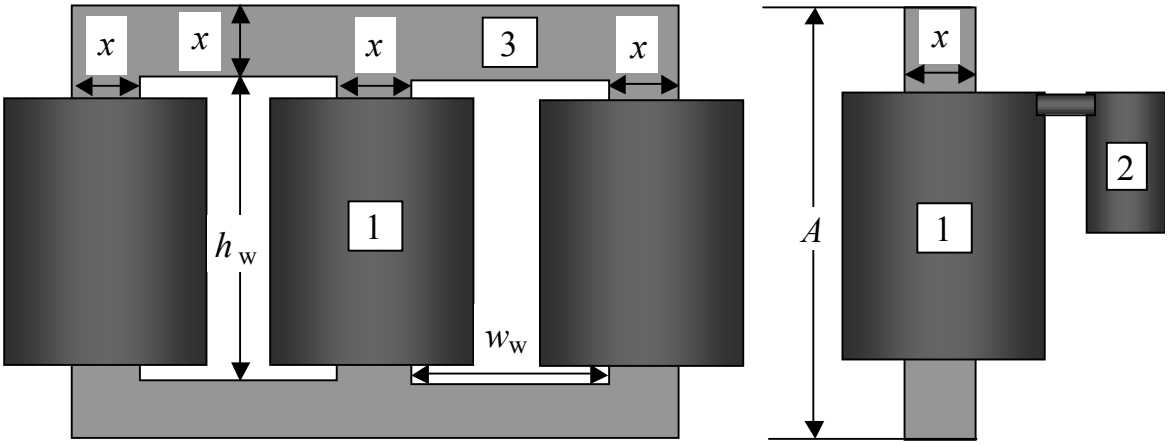

Figure 5.1 Essential parts of a 3-phase transformer: 1- coils, 2- cryo-cooler and 3- iron core.

5.1.3 Overview of the essential parameters

Characteristic specifications of copper based transformers rated at 20-780 MVA and the estimated cost are listed in Table 5.2. The values shown in bold are actual published values, while the others are inter- or extrapolated values. The transformers operate at mains frequency of 50-60 Hz. Voltage and current during normal operation range from 7 to 410 kV_{rms}, and from 120 A_{rms} to 12.4 kA_{rms} respectively. No-load and conductor losses are separated in order to enable a direct comparison with a superconducting transformer. Both capital C_{CAP} and total C_{TOC} costs rise with the power rating P_{3p} almost linearly over the whole range. The fitting equations with costs in thousands of US $ and the power rating in MVA are respectively

$$C_{CAP} = 5.3 \cdot P_{3p} + 140 \text{ and } C_{TOC} = 7.15 \cdot P_{3p} + 235 . \qquad \textit{Eq. 5.1}$$

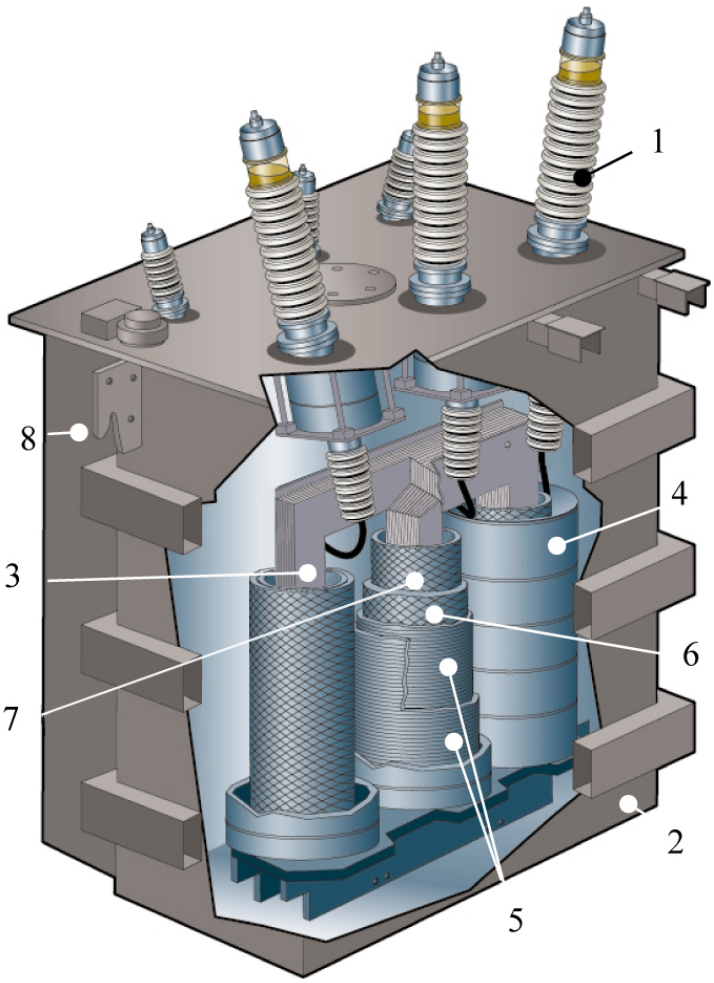

Figure 5.2 Conceptual layout of a superconducting transformer: 1 – bushing, 2 – main tank, 3 - iron core, 4 – outer shell of the coil cryostat, 5 – single-phase sub-set of the primary and secondary coils, 6 - coil former of the inner coil, 7 – inner shell of the coil cryostat and 8 – cold box with the cryo-cooler and control.

Table 5.2 Characteristic specifications of conventional 3-phase copper based transformers.

Transformer label	1	2	3	4	5	6	7	8
Reference	[Funa00]	[Meht97]	[Bonm00]	this study	[Bonm00]	[Syku00]	this study	[Over86]
Power Rating, [MVA]	**20**	**30**	**36**	77	**100**	**240**	450	**780**
Frequency, [Hz]	**60**	**60**	**50**	50	**50**	**50**	50	**50**
Primary Voltage, [kV_{rms}]	**66**	**138**	**63**	158	**225**	**400**	345	**410**
Primary Current, [A_{rms}]	**175**	126	330	162	257	346	753	1098
Secondary Voltage, [kV_{rms}]	**7**	**38**	**21**	12	**20**	**132**	138	**21**
Secondary Current, [A_{rms}]	**966**	263	571	2213	1667	606	1087	12381
No-load loss, [kW]	**11**	**14**	**15**	28	27	54	95	158
Conductor loss, [kW]	**111**	**137**	**140**	288	**270**	546	960	**1080**
Total loss, [kW] at full load	122	150	155	316	**297**	**600**	1055	1769
Capital cost, [US k$]	247	**300**	332	550	673	**1420**	2539	4297
Energy cost, [US k$]	132	150	161	236	278	531	915	1515
Total Ownership Costs,[k$]	379	**450**	493	786	951	1951	3453	5813

The total ownership costs depend on the lifetime (typically 30-40 years), on the load-duration curve and usually amount to 135 - 150 % of the capital cost. The capital and total costs are very important for conventional transformers and for this reason they are included in the study. For an introduction to other important parameters of a transformer such as: impedance voltage, overload behaviour and reliability, the reader is referred to [Over86], [Bonm00] and [Funa00b].

5.1.4 Costs of a transformer (in thousands of US dollars)

Crucial questions for the assessment of future applications are: "is it possible today to design a superconducting transformer that has a higher overall efficiency during normal operation than the conventional transformer of the same rating and what is required to reach this goal?". Once the economical potential of a future power device is clear, the relevant physical and technical problems can be solved in most cases. As an introduction, both conventional and superconducting versions of a 30-MVA transformer are considered below. The Total Ownership Cost (TOC) C_{TOC} is defined as:

$$C_{TOC} = C_{CAP} + C_{OP}, \qquad \textit{Eq. 5.2}$$

where C_{CAP} is the capital (investment) cost and C_{OP} is the operating cost (of the energy consumed during the device life cycle of 30 years). For a copper based 30 MVA transformer typical published values are: $C_{TOC} = 450$ k\$, $C_{CAP} = 300$ k\$ and $C_{OP} = 150$ k\$, see Table 5.2. For the capital costs one may write:

$$C_{CAP} = \sigma_{CAP}(C_{CN} + C_{RF}), \qquad \textit{Eq. 5.3}$$

where the term between the brackets is conductor-related material costs; C_{CN} is the cost of the conductor and turn-to-turn insulation and C_{RF} is the cost of the cooling and coil-to-coil insulation. The factor $\sigma_{CAP} \approx 2.5$ accounts for other than material costs (such as labour and installation) and for other than conductor-related material costs (like iron and bushings). For a copper transformer the costs may include: copper, insulation and coil formers; oil, radiators, main tank and the associated civil work.

The costs of a conventional 30-MVA transformer include costs of materials (~ 150 k\$) and other costs (~ 150 k\$). The conductor-related cost $C_{CN} + C_{RF}$ is 120 k\$. For a high-T_c transformer the conductor-related costs include superconductor, insulation, coil formers and current leads. The cooling and coil-to-coil insulation costs include the refrigerator, cooling liquid and cryostats. The conductor related material costs of a high-T_c transformer must be at least comparable to those of a conventional counterpart with the same rating. For the operating (energy) costs over the lifetime one can define [Syku00]:

$$C_{OP} = c_{NL}(P_{NL} + f_L^2 \cdot P_{FL}), \qquad \textit{Eq. 5.4}$$

with P_{NL} the power consumed by a device at no-load and P_{FL} the power consumed at full-load conditions. The coefficient $c_{NL} = 2.5$ k\$ / kW reflects the energy costs over the lifetime at no-load and f_L is the load factor. In practice, the load factor f_{LA} averaged over the lifetime is about 0.5 [Shea01]. Then for a 30-MVA copper transformer operated at 60 Hz [Meht97], [McCo00] and [Funa00a] one finds $P_{NL} = 13$ kW and $P_{FL} = 145$ kW, which results in $C_{OP} = 150$ k\$ at $f_{LA} = 0.55$ and $C_{OP} = 223$ k\$ at $f_{LA} = 0.7$. According to the DOE/EIA Annual Energy Outlook 1999 (and 2001) the expected price of electric energy is between 5.60 and

6.75 US $ cents / kWh for the next 20 years [Lawr00]. Taking into account the bank interest rates over the lifetime of 30 years, the effective energy price for a transformer is only ~ 1 US $ cent / kWh. In order to calculate the costs it is required to know energy consumed by the device at no-load and at full load conditions.

5.1.5 Normal operation modes

A power transformer connected to the grid normally works as a voltage source with the power limited by the transformer rating. This means that the voltage generated by a transformer is practically constant and the current depends on the load. For this reason AC loss in the iron core of the transformer is present as soon as the voltage is present, therefore continuously. Once a load is connected, currents flows in the transformer coils and consequently in addition to the core losses P_{Fe} the conductor losses appear, see Table 5.2. In the no-load mode, the electric power consumed by the device consists mostly of the core losses:

$$P_{NL} = P_{Fe} + \dot{Q}_{NL}\ (\varepsilon - 1) = \sigma_{NL} P_{Fe}\,, \qquad \textit{Eq. 5.5}$$

where $\varepsilon = \varepsilon(T_Q, \dot{Q}) = (\frac{T_P / T_Q - 1}{\eta} + 1)$ is the cooling penalty additionally defined in section 5.2.5. The cooling power $\dot{Q}_{NL}$ required to keep the superconductor temperature close to T_Q under no-load condition, is mostly due to the heat leak into the cryostats and of the current leads see [Seeb98], ch. D10.

The coefficient σ_{NL} controls an increase of the no-load losses due to the "cold part". For a 30-MVA superconducting transformer with $\sigma_{NL} = 1.3$, a 30 % increase of the no-load loss is allowed. The condition sets the demands to the cryostat(s) and to the current leads. For instance, $\dot{Q}_{NL}$ = 0.25 kW at P_{Fe} = 13 kW, η = 0.2 and T_Q = 65 K. A lower value of σ_{NL} will cause a decrease of the operating costs according to Equation 5.4. It also increases the capital costs of both the cryostat and the leads included in σ_{RF} of Equation 5.19. The core losses are dealt with in section 5.2.6. In full-load mode, the electric power consumed by a device consists mostly of the conductor losses and the cooling:

$$P_{FL} = P_{CN} + \sigma_{FL} P_{Fe} = \sigma_{FE} P_{CN} = \sigma_{FE} (\varepsilon - 1) \cdot \dot{Q}_{CN}\,, \qquad \textit{Eq. 5.6}$$

where $\dot{Q}_{CN}$ is the conductor losses at T_Q and the factor $\sigma_{FL} \approx 1.4\,\sigma_{NL}$ accounts for an increase of the losses (the leads and the cryostat) at full current; therefore the factor $\sigma_{FE} \approx 1.14$. The conductor losses are addressed in sections 5.2.2 and 5.2.3.

5.2 Components of a superconducting transformer

5.2.1 Coils

A single-phase sub-set of coils in a high-T_c transformer consists of primary and secondary solenoidal coils surrounding the leg and surrounded by a glass fibre-epoxy cryostat (to avoid eddy current loss) with a room temperature bore, see Figure 5.2. The coils are connected to the room temperature bushings via the current leads. Each coil is a matrix of strand turns $N_{1ps} = N_r \times N_z$. Here N_r and N_z are the radial and axial number of turns respectively. Each coil consists of a number M_{1p} of sub-coils with the same direction of the transport current (connected in series or in parallel). Each sub-coil consists of a single layer of conductor, wound with insulated Bi-2223 tape(s) on a (separate) coil former. Iron c-cups are applied around the coil edges to suppress locally the radial component of the magnetic field, section 4.3. In order to

match the coefficients of thermal contraction, Bi-2223 tapes are usually wound on a G-10 like coil former with suitable direction of the glass fibres, section 2.2. The insulating and cooling properties of bubble-free liquid nitrogen are comparable to oil and it is therefore natural to use it for both coil-to-coil insulation and cooling.

A high voltage withstand requirement forces the designer to use single layer wound coils on separate coil formers [Funa00b]. In the radial direction the conductor layer is comprised of only few strands in order to attain a uniform temperature within the windings. Intra coil layers of liquid nitrogen separate the conductor layers and provide the required insulation and cooling. Each sub-coil is a matrix of N_{ssu} turns. The primary conductor has N_{ps} parallel tapes. The total number of the turns N_{1ps} per coil is:

$$N_{1ps} = N_{ps} P_{3p} / (3 I_{1p} v_{1p}) . \qquad \textit{Eq. 5.7}$$

With the height of a (sub-) coil h_{cl} and the number of strand turns per unit height of a coil N_{sh}, the number of turns wound in the axial direction is:

$$N_z = h_{cl} N_{sh} . \qquad \textit{Eq. 5.8}$$

The number of turns wound in radial direction is:

$$N_r = N_{1ps} / N_z . \qquad \textit{Eq. 5.9}$$

The number of primary sub-coils per phase is therefore:

$$M_{1p} = N_{1ps} / N_{ssu} . \qquad \textit{Eq. 5.10}$$

The height of a (sub-) coil and the relevant cryostat dimensions (including both the top and the bottom walls) define the height h_{w} of the core window, as shown in Figure 5.1. The thickness of two single-phase sub-sets of the coils together with insulation and cooling gaps, cryostat(s) walls and the spacing between adjacent cryostats defines the width w_{w} of the core window, see Figures 5.1 and 5.2. The specifications of the high-T_{c} power coils used in the study are listed in Table 5.3. Tapes A, V and Sm and coils 1s and 3s are discussed in more details in Chapters 2 (Table 2.2) and 4 (Tables 4.1 and 4.4) respectively, tape Sm and coil 1f are further described in [Funa00b] and [Iwak00].

Table 5.3 Specifications of the model solenoidal coils used in the study.

Parameter \ Label Reference	Coil 3s this study	Coil 1s this study	Coil 1f [Funa00b]
Manufacturer of Bi-2223/Ag strand	A	V	Sm
Strand total length, [m]	359	880	4700
Dimensions of bare strand (width × thickness), [mm^2]	4.1 × 0.28	3.9 × 0.26	3.8 × 0.25
Nr. of parallel strands in the coil conductor	1	2	2 and 6
Number of the conductor turns per sub-coil	278	296	140 and 88
Number of the conductor layers per sub-coil	2	4	1
Height of the coil winding package, [m]	0.614	0.614	0.994
Inner \ outer diameter of the winding package, [m]	410 \ 412	470 \ 474	0.528 \ 0.818
Number of the sub-coils	1	1	6
Critical current, [A] of a coil at 77 K and 10^{-4} V/m	126	86	62 and 187

5.2.2 Conductors

It is customary to describe a transformer conductor in terms of the length l and the current I_{tr} of a single strand (tape or wire). The total amount of Ampere-turns is defined by the power rating of a transformer P_{3p}:

$$l \cdot I_{tr} = 2P_{3p} / E_{1p} , \qquad \textit{Eq. 5.11}$$

where E_{1p} is the source electric field defined by Equation 5.22. With the given specific price of a strand c_{CN} expressed in \$/A_{rms}/m, one may find the conductor costs C_{CN} in US \$:

$$C_{CN} = c_{CN} \cdot l \cdot I_{tr} \approx c_{CN} \cdot l \cdot I_{c0} / \sqrt{2} . \qquad \textit{Eq. 5.12}$$

The electric field of the losses expressed in $mV_{rms}/m \equiv mW/(A_{rms}m)$ leads to the conductor loss $\dot{Q}_{CN}$. The conductor loss power averaged over the (electric) cycle at full-load is proportional to the loss electric field E_ρ, [V_{rms}/m], the conductor length l, [m] and the transport current I_{tr}, [A_{rms}]:

$$\dot{Q}_{CN} = E_\rho \cdot l \cdot I_{tr} . \qquad \textit{Eq. 5.13}$$

5.2.3 Strands

The performance and costs of various long wires available from vendors are compared in Figure 5.3 and are summarized in Table 5.4. Copper wire is produced since many decades and forms the basis of conventional power applications. At full load the typical value of the current density in coils is $J_{Cu} = 3$ A_{rms}/mm^2 and the specific price of copper is about 10 \$/kA_{rms}/m [Malo99], [Bonm00]. The DC resistance of copper sets the lower limit of the losses. The resistivity ρ of copper depends on temperature [Wils83], at full load for a typical transformer coil: $T_Q = 350$ K and $\rho_{Cu} = 2 \cdot 10^{-8}$ Ωm. The loss electric field at full-load is therefore: $E_{FL}^{Cu} = 60$ mV_{rms}/m [Bonm00].

Long Bi-2223/Ag tapes are produced for about 7 years, still are under development and the tape is rather expensive at the moment. The performance and costs of high-T_c superconductors are usually described in terms of the critical current, specific loss, specific price and dimensions. By convention, the direct critical current I_{c0} of a superconductor is measured at 77 K and self-field conditions at the electric field $E = 10^{-4}$ V/m. Typical value of the current density corresponds to about 50 A_{rms}/mm^2. The critical current depends on magnetic field (both amplitude and direction in respect to the tape surface) and temperature, see section 2.4, and strain [Vase00]. The price is frequently expressed in \$/m or in \$/kA/m employing the I_c. Parameters of bare and insulated tapes potentially suitable for power applications are listed in Tables 2.1, 2.2 and 2.6.

In Figure 5.3 the performance and costs of a long Bi-2223/Ag tape (presently available) are compared with the other known conductors. In four years (1997-2001) the specific price of Bi-2223 tapes has changed from 1000 to 200 \$/kA/m. It is expected that the price will reach 100 and 70 \$/kA/m in the year 2002 and 2004 respectively due to the up scaling of the tape production. The critical current of a 1-mm^2 single tape at 77 K and self-field conditions has increased from 70 to 120 A in the years 1999 and 2001 respectively and it is expected to reach 150 A in the year 2004 [Malo02]. It is clear from Figure 5.3 that at 50 \$/kA/m Bi-2223/Ag conductor operated at $T_Q \leq 70$ K will become comparable in price with copper and will enable further penetration of Bi-2223/Ag tapes into the power market.

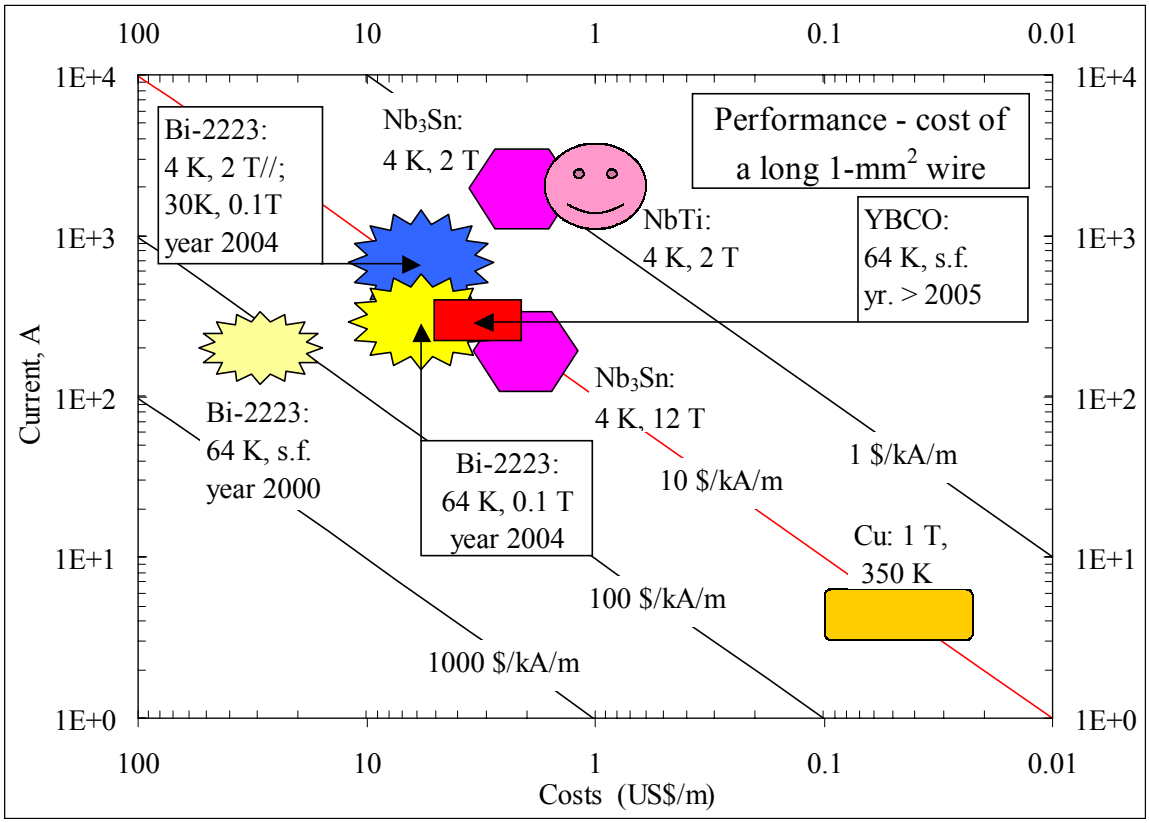

Figure 5.3 Critical current and cost of a long 1-mm² wire made of various conductors.

Total losses per meter of a tape depend on operating current, magnetic field, frequency and temperature, see sections 3.4 and 3.5 and [Rabb00], [Magn01]. Bi-2223 tapes existing today and used for power coils are still rather primitive DC conductors, with relatively thick and non-twisted filaments embedded in a pure Ag matrix surrounded by AgMn-alloy or pure Ag outer sheath. In addition the tape may be reinforced with parallel stainless steel tapes.

In a coil multiple tape turns are coupled together. This creates a different electro-magnetic environment as compared to a single tape or stack of tapes in uniform magnetic field [Oome00], [Iwak00]. Therefore, the loss is estimated using the experimental data for coils. At full load, the conductor loss electric field $E_{sc} = 1.5$ mV$_{rms}$/m is found experimentally for 1-MVA high-T_c transformer coils operating at $B_{x,mx} \approx 50$ mT and $B_{r,mx} \approx 30$ mT, 60 Hz and 65 K [Iwak00]. Here the loss electric field is obtained by dividing the total loss of a coil (159 W) by the operating current and the total length of a single strand (22.5 A$_{rms}$ and 4700 m respectively). Most of the losses in this case (about 75 %) is due to the radial component of magnetic field B_r [Iwak00]. A similar value of the conductor loss electric field and namely 2 mV$_{rms}$/m (at $B_{x,mx} \approx 25$ mT, $B_{r,mx} \approx 30$ mT, $I_{tr} = 55$ A$_{rms}$, 50 Hz and 77 K) is found for sub-coil 3s in case C1, as dealt with in section 4.4, see Figure 4.14. When iron cups are applied around the coil edges, the radial component of magnetic field is reduced ($B_{r,mx} \approx 4$ mT) and the conductor loss electric field of 1 mV$_{rms}$/m is found in case C2 (at equal other conditions).

Table 5.4 Expected specifications of long 1-mm² tapes at full load and frequency 50-60 Hz.

Material	J, A$_{rms}$/mm² at T_Q	E_p, mV$_{rms}$/m at T_P	Price, \$/kA$_{rms}$/m	
Copper	3 at 350 K	60 at 350 K	10	[Bonm00]
Bi-2223/Ag, year 2000	60 at 65 K	30♣ at 300 K	420	[Masu99]
Bi-2223/Ag, year 2004	75 at 65 K	20-30♣ at 300 K	50	[Masu99]
Bi-2223/Ag, beyond year 2004	100 at 65 K	10♣ at 300 K	≤ 35	[Malo99]

♣The averaged over the tape length loss is calculated for coil 1s operated at the temperature of 77 K and the transport current of 55 A$_{rms}$. The cooling penalty equal to 15 is included.

Assuming a loss electric field of 2 mV_{rms}/m and the cooling penalty equal to 15, one gets for the Bi-2223/Ag tapes the loss electric field (scaled to room temperature): $E_{FL}^{SC} = 30\ mV_{rms}/m$. The value is two times lower than the established limit for a copper conductor: E_{FL}^{Cu}. This result shows that high-T_c power technology has the ability to compete with the conventional Cu-based technology regarding the efficiency already today. In the future, AC superconductors with many fine twisted and decoupled filaments and lower losses will become commercially available. Potentially, the loss may be reduced by more than two orders of magnitude, see Figure 4.14. However, these developments may take considerable time, as the development is to be combined with the mentioned reduction of the tape price.

The critical current of a tape depends on the magnetic field (both amplitude and direction), see section 2.4. The axial magnetic field usually does not exceed 0.1 T in transformer windings. The radial magnetic field increases at the coil edge. The care must be taken to keep it at an acceptable level (approximately 10 times lower than the axial field, see section 4.1.1). With the axial magnetic field in the transformer coil windings of 0.1 T and the radial component of magnetic field suppressed by the iron c-cups down to about 10 mT (section 4.3), for coils made with tapes A the expected reduction of the critical current in magnetic field is within 10 % as compared to a short sample in the self-field, see Table 2.2.

5.2.4 AC loss versus temperature and transport current

The critical current of a superconductor depends on temperature. At zero external magnetic field B_e (but in the presence of a self-field) the temperature dependence of the critical current according to [Angh98] is:

$$I_c(T, B_e)/I_c(77K, B) = 6.75 \cdot (1 - T_Q/T_c(B_e))^{1.4}, \qquad \textit{Eq. 5.14}$$

with $T_c = T_c(B_e)$ the critical temperature, $I_c(77K, B_e)$ the critical current measured at $T_Q = 77$ K with both the external magnetic field and the self-field present. When the external magnetic field is far below the second critical field, the dependence of the critical temperature on the magnetic field can be neglected and $T_c(B_e) = 104\ K$ is assumed further on.

Coil losses depend on temperature [Iwak00]. To establish the dependence, the loss of a coil is calculated using the network model. The validity of the numerical model is demonstrated for both a tape and a coil, see sections 3.4 and 4.4. Using Equation 5.14 and the numerical model the loss voltage of coil 1s in Table 5.3 is calculated at various operating temperatures, constant frequency of 50 Hz and a sinusoidal transport current of 55 A_{rms}.

The numerical result is shown in Figure 5.4 as boxes. The scaled loss of the coil depends on the operating temperature. The calculated dependence is fitted by the 2-nd order polynomial as depicted in the figure by the solid line

$$\dot{Q}_{CN}/\dot{Q}_{77K} = 1.12 \cdot 10^{-4} \cdot T_Q^{\,2} - 3.12 \cdot 10^{-3} \cdot T_Q + 0.565. \qquad \textit{Eq. 5.15}$$

The scaling factor represents the loss of the coil at 77.4 K: $\dot{Q}_{77K} = \dot{Q}_{CN}(77K) = 39\ W$, see Figure 4.15. The result is in agreement with a relevant experiment [Iwak00] performed in the temperature range from 64 to 78 K and shown as triangles in Figure 5.4, as well as with the self-field loss measurements [Past99] performed at 45 to 70 K (not shown in the figure).

In addition, calculations assuming the temperature dependence of the critical current shown in Figure 2.19, are performed for sub-coil 3s at 77 and 65 K in several magnetic arrangements. The calculations show that in cases acC1, acC2 and acC4 (Table 4.5) the ratio $\dot{Q}_{CN}(65K)/\dot{Q}_{77K}$ is equal to 0.4; 0.5 and 1 respectively for the sub-coil. In case acC4 most of

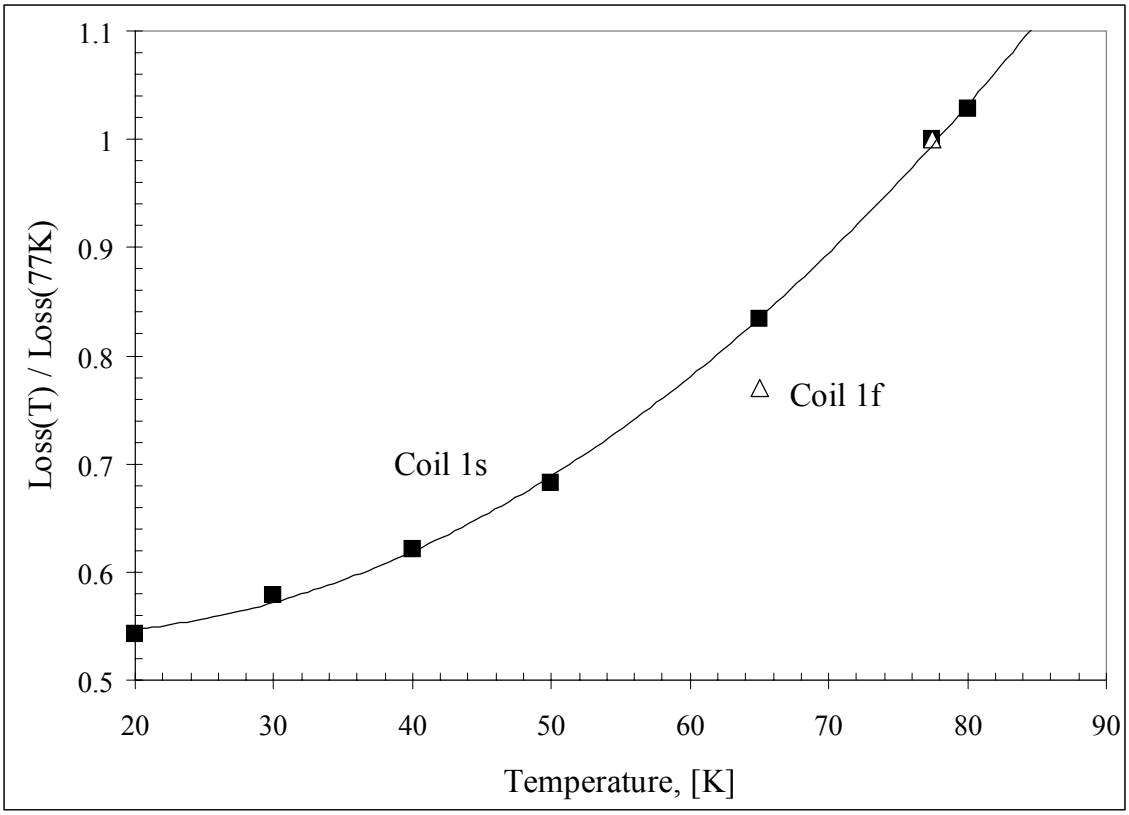

Figure 5.4 Temperature dependence of the coil losses: boxes and triangles are for coils 1s (calculated) and 1f (measured) respectively.

the sub-coil windings operate in magnetic field B_x above 50 mT and B_y below 8 mT (Figure 4.12). Consequently, the sub-coil loss is dominated by the magnetisation loss due to B_x, which is almost independent of temperature [Oome00]. Therefore, depending on the magnetic field amplitude, direction and distribution in the windings, Bi-2223/Ag coils show different temperature dependence of total losses. When operating temperature of a coil is reduced from 77 to 65 K, the total loss may reduce as much as two times or it may stay unchanged.

In a coil the transport current and the transverse magnetic field are coupled via the magnetic field constant. The direction of the magnetic field with respect to a Bi-2223 tape (Figure 3.1) and the magnetic field constant are spatially dependent. For the coils listed in Table 5.3 the following dependence of the losses on the magnitude of sinusoidal transport current is obtained at constant temperature:

$$\dot{Q}_{CN}(I_{tr}) / \dot{Q}_{CN}(I_{tr0}) = (I_{tr} / I_{tr0})^m , \qquad \textit{Eq. 5.16}$$

with m being dependent on the magnetic field constant of a coil. For coils 1s, 3s and 1f in Table 5.3 and at 77 K m = 3.12; 2.9 and 2.35 when the characteristic values of the maximum axial magnetic field constant are B_{zmx} / I_{tr} = 1.37; 0.48; and 1.1 mT/A respectively. The spatial distribution of the magnetic field (amplitude, direction) in the windings is rather different for the coils due to the altered electro-magnetic arrangements: same direction of the current and iron cups for coils 1s and 3s, but opposite direction of the currents (in the sub-coils) and iron core for coil 1f. For other coils the values of the empirical constants can be found in Table 4.6.

5.2.5 Cooling

In the case of not continuous use of the device like a resonator coil for testing cables and capacitors or a prototype transformer, a cooling liquid supplied from a remote source is an

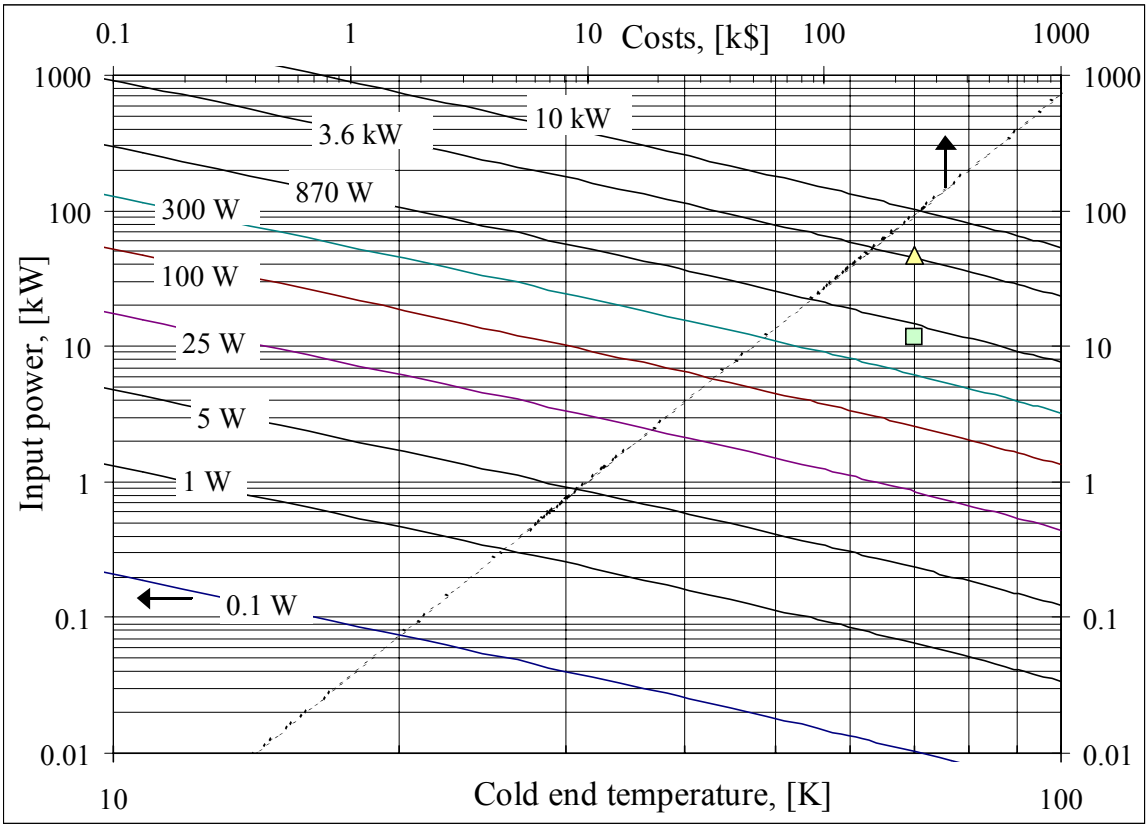

Figure 5.5 Input power and capital costs of a refrigerator at $A_{RF} = 0.095\ W^{-0.2}$ *and* $\sigma_{RF} = 10$ *US k$/kW*$^{0.7}$.

option. In this case the investment cost is reduced, but the cost of the cooling liquid of about 100 US \$/m^3 for nitrogen will increase the operating costs.

For 10 - 100 MVA range superconducting coils operated continuously, stand-alone refrigeration units seems to be the only option. To carry out a refrigeration cycle with a cooling power $\dot{Q}$ removed at the temperature T_Q of a cold end, the input power P consumed by the cooling device at the so-called rejection temperature $T_P = 300\ K$ is

$$P = \dot{Q}\left(\frac{T_P/T_Q - 1}{\eta}\right) = \dot{Q}(\varepsilon - 1)\ . \qquad \textit{Eq. 5.17}$$

Here $\eta = \eta(T, \dot{Q})$ is the relative efficiency of a real cycle compared to an ideal thermodynamic Carnot cycle. For the latter cycle $\eta \equiv 1$ holds. From [Angh98] and the references therein the efficiency of a real cycle can be approximated as follows

$$\eta = A_{RF} \cdot \dot{Q}^{0.2}(T_Q/T_P)^{0.43}, \qquad \textit{Eq. 5.18}$$

with A_{RF} an empirical constant to adjust for particular combinations of $\dot{Q}$ and T_Q. For $T_Q = 20$-80 K and $\dot{Q} > 100\ldots500$ W, the Brayton-Claude cycle [Seeb98] or Stirling cycle [Stir00] provides the highest efficiency: $\eta = 0.15 - 0.35$ or $\eta = 0.25 - 0.35$ respectively. Therefore one may expect $0.09 < (A_{RF}, [\mathrm{W}^{-0.2}]) < 0.16$.

The investment cost C_{RF}, in thousands US \$ and the input power P, in kW of a refrigerator are related as following [Stro69]:

$$C_{RF} = \sigma_{RF} P^{0.7}, \qquad \textit{Eq. 5.19}$$

with $\sigma_{RF} = 6$ US k\$/kW$^{-0.7}$. More recent surveys show higher values of σ_{RF} close to about 10 US k\$/kW$^{-0.7}$ [Angh98]. As an example, the input power of a refrigerator as function of the cold end temperature at a certain cooling power with $A_{RF} = 0.095$ W$^{-0.2}$ calculated according to Equations 5.17 and 5.18 is displayed in Figure 5.5 as solid lines (the axis is indicated by the horizontal arrow). The corresponding values of the cooling power $\dot{Q}$ are shown near the lines. The two symbols at $T_Q = 70$ K and $\dot{Q} = 0.87$ and 3.6 kW are for existing Stirling cryo-coolers [Stir00]. The capital costs of a refrigerator versus the input power calculated from Equation 5.19 at $\sigma_{RF} = 10$ US k\$/kW$^{-0.7}$ are shown by the dotted line in the same figure (the axis is indicated by the vertical arrow).

5.2.6 Iron core

The transformer iron core usually operates at room temperature. For a 3-phase transformer it consists of 3 legs around which the coils are positioned and (rectangular) yokes connecting the legs as depicted in Figures 5.1 and 5.2. The mass, the lamination, the operating frequency f and the amplitude of the induction in the core B_{Fe} define the bulk of the loss in the iron core. The design of the core is also based on a given voltage-per-turn ratio v_{1p} and the filling factor φ_m (cross-section of iron divided by the total cross-section of the core). The cross-sections of the legs and of the yokes are usually equal

$$S_{Fe} = \frac{v_{1p}}{\sqrt{2}\pi \cdot f \cdot \varphi_m \cdot B_{Fe}}. \qquad \textit{Eq. 5.20}$$

The average length of a conductor turn l_{1p} is determined by the radius of the round leg and the additional radial spacing r_c

$$l_{1p} = (2^{3/4}\sqrt{v_{1p}/(f \cdot \varphi_m \cdot B_{Fe})} + 2\pi r_c). \qquad \textit{Eq. 5.21}$$

The spacing r_c is proportional to the thickness of the coils, coil formers, cryostat walls, cooling channels and insulation. Its contribution to the l_{1p} (relative to the core) is about 50 %. The source electric field per phase is

$$E_{1p} = \frac{v_{1p}}{l_{1p}}. \qquad \textit{Eq. 5.22}$$

The height h_w and the width w_w of the core windows are primarily influenced by the height and the thickness of the transformer coils as described in section 5.2.1. The volume of the core [Siss00] is

$$V_{Fe} = \varphi_m S_{Fe}(6\sqrt{\varphi_m S_{Fe}} + 4w_w + 3h_w). \qquad \textit{Eq. 5.23}$$

Assuming a peak field in the iron core of $B_{Fe} = 1.6$ T and $f = 50$ Hz, the loss of a 0.27 mm thick laminate of electro-technical steel is about 1.3 W/kg. The cost of the assembled core is about 2 \$/kg and the density of the steel is 7600 kg/m^3. This information allows to calculate the core losses and weight.

5.3 Costs and performance of a superconducting transformer

5.3.1 Basic assumptions

The most important assumptions used here are listed in Table 5.5 and compared to those made in a previous study [Oome00]. Other assumptions are clarified in the text. To account for the temperature dependence of the losses, Equation 5.15 is used. The importance of realistic assumptions is evident. For example, in section 5.1.4 it is shown that due to the bank interest rates included into the consideration (see assumption 2 in Table 5.5) the effective energy price for a power transformer is only about 1 US $ cent / kWh and it is far lower than the expected energy price of 5.60 - 6.75 US $ cents / kWh.

Table 5.5 Overview of basic assumptions when assessing cost and performance of a superconducting transformer.

Nr.	Assumption \ Reference	This study	[Oome00]
1	The operating cost is proportional to the energy consumption	+	+
2	The energy cost over lifetime includes bank interest rate	+	-
3	The energy consumption consists of full-load and no-load losses	+	-
4	The load factor f_L describes the actual energy consumption	+	-
5	The losses of iron core, cryostat and current leads are included	+	-
6	The capital costs include both superconductor and cooling	+	-
7	Conductor-related material costs are ~ 0.4 of the capital costs	+	-
8	The overload capability is included	+	-
9	Arbitrary direction of the transverse magnetic field is allowed	+	-
10	The magnetic field is below and above the penetration field	+	-
11	The amplitudes of magnetic field and transport current are coupled	+	-
12	The T-dependence of the I_c is independent on magnetic field	+	+
13	Superconducting filaments are non-twisted and coupled	+	+
14	The superconductor loss is evaluated numerically beyond the Critical State Model; the loss depends on I_{tr} and T	+ +	- -
15	The T-dependence of the losses is independent on the I_{tr}	+	-
16	The nr. of superconducting strands connected in parallel is integer	+	-
17	Coils may operate in the temperature range $20K \le T_Q \le 90K$	+	-
18	The refrigerator efficiency η is a function of Q, T_Q, T_P and A_{RF}	+	-
19	The refrigerator operates steadily at 70 % of the full load	+	-
20	The cooling penalty is a smooth function of T_Q	+	+
21	A comparison with a Cu-based device of the same rating is made	+	-

5.3.2 Brief summary of the model

The model based on Equations 5.1 - 5.23 is applied to a 3-phase, 30-MVA transformer. The specifications of the transformer are listed in Table 5.6. Four basic cases are eminent in the study. A copper-based device is compared with three variants of a Bi-2223 based transformer of the same rating:

(0) Cu-based transformer;
(1) HTS1, with the same iron core and the same amount of Ampere-meters as (0) with a specific costs of superconducting tape c_{cn} = 50 $/kA/m;
(2) HTS2, with the same weight as (0), but less conductor at c_{cn} = 50 $/kA/m;
(3) HTS3, with the same weight as (0), but less conductor and c_{cn} = 25 $/kA/m.

For the 30-MVA copper transformer the main specifications are presented in Table 5.6. The values of the constants are given in Table 5.7 and used throughout the study unless stated otherwise.

Table 5.6 Specifications of a 30-MVA transformer.

Parameter	Primary side	Secondary side
Rated Power P_{3p}, MVA per 3 phases	30.0	29.9
Voltage, V_{p1}, kV_{rms} per phase	79	38.0
Current I_{p1}, A_{rms} per phase	126	263
Frequency, Hz	60	60

Table 5.7 Constants used in the comparative study.

Symbol	Unit	Value	Equation
σ_{CAP}	-	2.5	(5.3)
c_{NL}	US k$ / kW	2.5	(5.4)
f_{LA}	-	0.55	(5.4)
σ_{NL}	-	1.3	(5.5)
σ_{FE}	-	1.14	(5.6)
I_c	A	95	(5.12; 5.14)
E_ρ	mV_{rms} / m	1.1 - 1.6*	(5.13)
T_P	K	300	(5.17; 5.18)
A_{RF}	$W^{-0.2}$	0.095	(5.18)
σ_{RF}	US k$ / $kW^{-0.7}$	11	(5.19)

* under conditions typical for the existing coils, see Table 5.3.

5.3.3 Total ownership costs (TOC)

The total cost includes the capital cost and the energy cost. An overview of the main results is given in Table 5.8. It is clear, that variant HTS1 due to the higher costs has limited chance of application. The penetration of superconducting transformers into the market will happen in two stages. During the initial stage the same total costs for both Cu-based and HTS devices of the same rating will be achieved, but capital cost of an HTS transformer will be 20 % higher. This disadvantage will be balanced by the specific operational advantages of the HTS transformer. This stage of the penetration will become economically feasible at a conductor price of $c_{CN} \approx 50$ $/kA/m expected around year 2004. The iron core of the relevant transformer HTS2 is about 50 % heavier, but the total volume and mass are the same.

During the final penetration stage the transformer HTS3 will have lower capital and total costs than the copper-based version. This stage will happen at $c_{CN} \leq 25$ $/kA/m. During this stage it will be allowed to reduce the weight of the iron core to (or beyond) the one of the copper based transformer. In all cases the superconducting transformer will have a higher overall efficiency than the copper-based version. The higher capital costs in cases HTS1 and HTS2 cancel out the lower energy costs. Only in the case of HTS3 (and beyond) lower energy costs lead to reduced

Table 5.8 Summary of the results for a 30-MVA transformer.

Variant	Coils T_Q, [K]	Capital costs, [k$]	Energy costs, [k$]	TOC, [k$]
Cu-based (0)	340	300	150	450
HTS1	70	426	106	532
HTS2	65-76	354	88	442
HTS3	74-76	298	88	387

total costs. The results are based on the properties of existing coils made with existing conductors and are rather insensitive to a further reduction of conductor losses.

For instance, in the case HTS3 keeping equal all other conditions an additional decrease of the conductor losses by 2 times will reduce the conductor-related costs with 9 %, capital costs with 3 % and total ownership costs with 4 %. If this step is accompanied by 20 % increased conductor costs, the gain in costs is zero. The expected dependence of the total costs on the operating temperature T_Q of the coils is depicted in Figures 5.6 and 5.7 for the variants HTS2 and HTS3 respectively. The steps in the curves are due to the integer number of tapes connected in parallel; see assumption 16 in Table 5.5. The range of the operating temperature accessible with liquid nitrogen is indicated on the horizontal axis by the grey box. The vertical arrows show the position of the minima in the costs. The costs and temperature at the minimum are different for the total costs and for the capital costs due to the energy costs involved. The only difference between the cases HTS2 and 3 is in the costs of the tape c_{CN}. It is seen that reduction of the tape costs lowers the values of both total and capital costs. At the same time, it shifts the minima in the costs towards a higher operating temperature.

5.3.4 Capital cost

The capital cost includes the conductor related material cost and the other costs, see Equation 5.3. The expected dependence of the capital cost on the operating temperature T_Q is depicted in Figures 5.6 and 5.7 for the variants HTS2 and HTS3 respectively. The minimum in capital cost is governed primarily by the cost of conductor and cooling. The breakdown of the conductor related material cost is presented in Figure 5.8 for the case HTS3 and labelled as "Capital 1". The cost of the conductor C_{CN} is labelled as "Conductor" and it increases with T_Q. The cost of the cooling C_{RF} is labelled as "Cryogenics" and it decreases with T_Q. This behaviour leads to the minimum in costs "Capital 1".

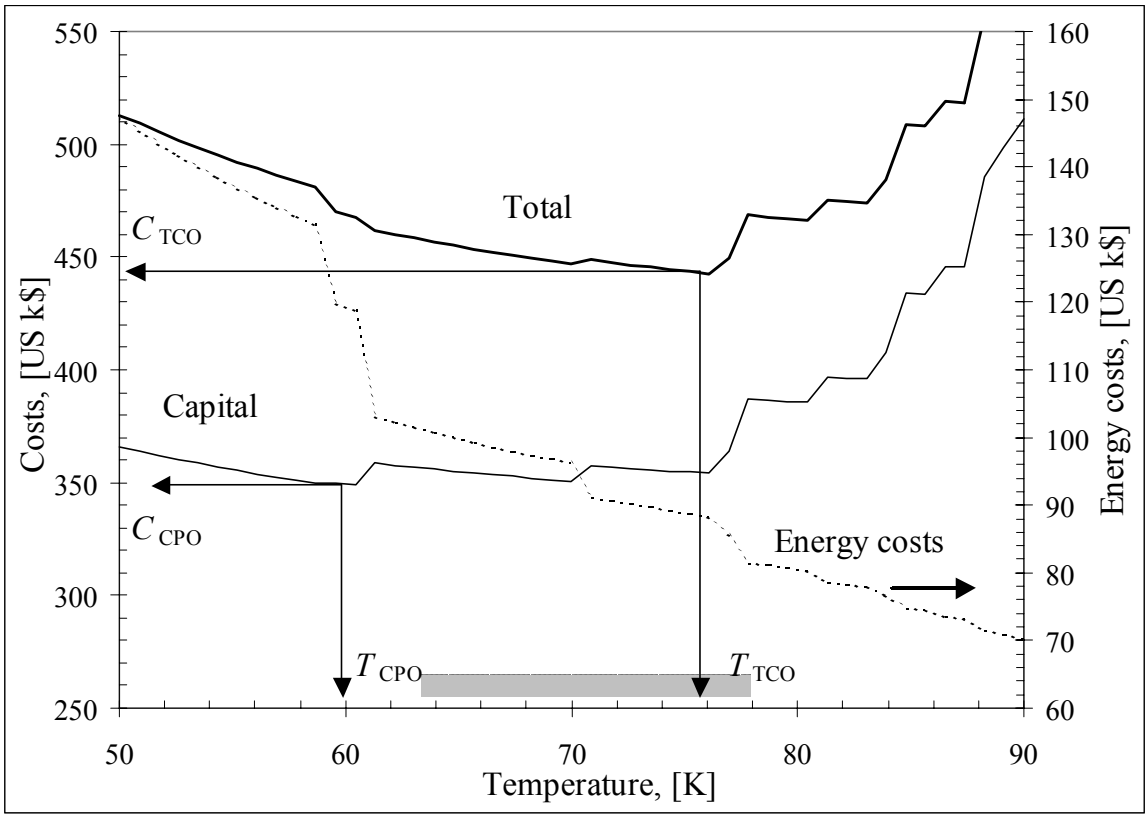

Figure 5.6 Total, capital and energy costs of the 30-MVA superconducting transformer HTS2 as function of the coils operating temperature.

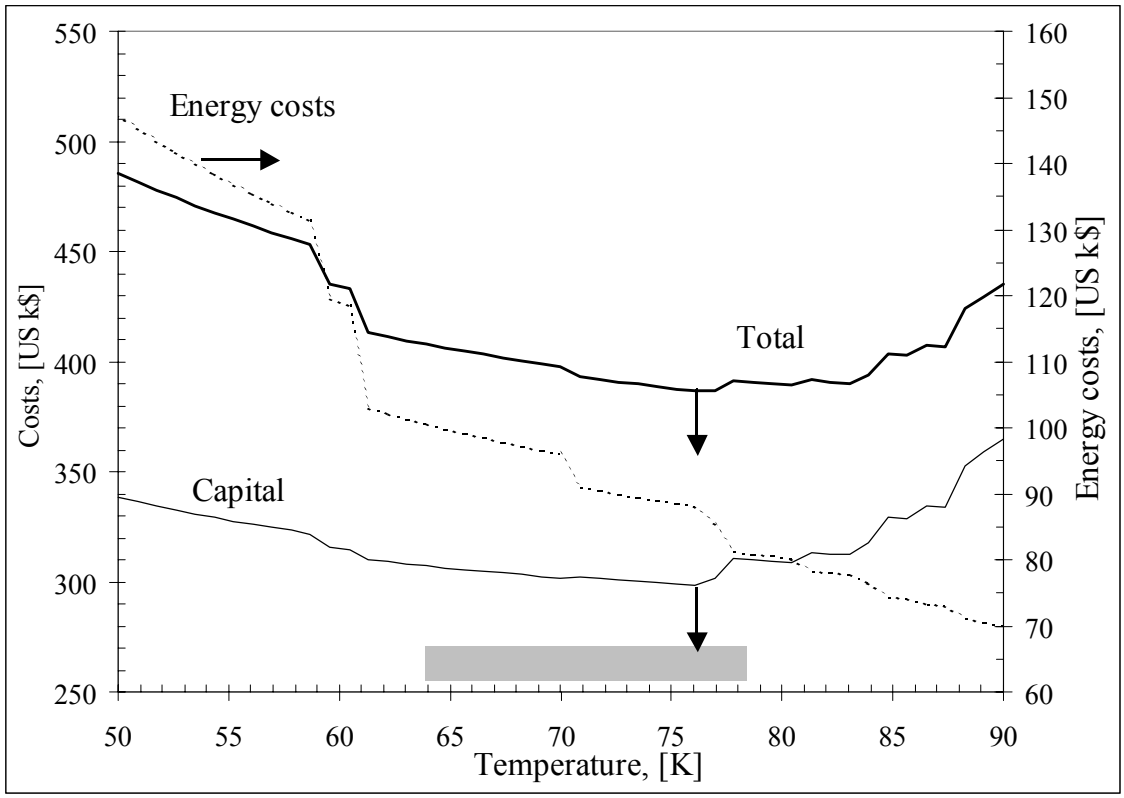

Figure 5.7 Total, capital and energy costs of the 30-MVA superconducting transformer HTS3 as function of the coils operating temperature.

Again, the coordinates of the minimum point are governed by the cost of conductor and cooling. At the minimum the costs of conductor and of cryogenics are comparable, see Figure 5.8. For this reason the capital cost of cooling cannot be ignored. When operating at higher temperature $T_{Q,}$ the critical current of a single strand will decrease and more strands have to be connected in parallel in order to meet the operating current of the transformer. This usually leads to lower operating current per strand and lower losses per coil. As a result, the "Conductor" cost will increase, but the "Cryogenics" cost will decrease primarily due to reduced losses as it happens for instance at $T_Q \approx 60$ K in Figure 5.8. Consequently the step of the cost "Capital 1" is relatively small. A larger iron core as in the cases HTS2 and 3 has little effect on the costs, as the transformer core is relatively cheap.

5.3.5 Energy cost

The operating cost of a transformer is the energy cost calculated over the lifetime of the device (30 years). The energy cost comprises of the losses in iron core and in cryogenic coils including refrigerator, cryostats and current leads. The energy cost of a 30-MVA superconducting transformer compared to the copper-based device is reduced by: 30, 41 and 41 % in the transformers HTS1, 2 and 3 respectively, see Table 5.8. The energy costs are practically the same for the transformers HTS2 and 3. The costs are rather sensitive to the number of parallel strands in the coil conductor; see Figures 5.6 - 5.7 and Table 5.10.

5.3.6 Operating temperature

Optimal values of the capital and total costs and of the corresponding temperatures C_{CPO} ,T_{CPO} and C_{TCO} ,T_{TCO}, see Figure 5.6 follow from the equations:

$$\frac{dC_{CAP}}{dT} = 0, \Rightarrow C_{CPO}, T_{CPO} \text{ and } \frac{dC_{TOC}}{dT} = 0, \Rightarrow C_{TCO}, T_{TCO}. \qquad \textit{Eq. 5.24}$$

The result shows two optima for the operating temperature: one optimum is found for the capital cost and a second is for the total cost. For this reason, the operating temperature T_{CQ} of transformer coils can be determined by preferences of the customer within a certain range. In most of the cases the following range holds for the operating temperature

$$T_{CPO} \le T_{CQ} \le T_{TCO}. \qquad \textit{Eq. 5.25}$$

Both temperatures T_{CPO} and T_{TCO} are governed primarily by the conductor specific price. At a high conductor price the difference between T_{CPO} and T_{TCO} is larger and the values are shifted to lower operating temperature. For instance, at a tape specific cost of 100 \$/kA/m both minima are below 63 K and hence are beyond the possibility of cooling with liquid nitrogen. At low conductor price the difference becomes smaller and the operating temperature increases.

Remarkably, for HTS3 the minima of the total and capital costs are practically at the same temperature $T_{CQ} \approx 76$ K, which is close to the boiling temperature of liquid nitrogen at atmospheric pressure (77.4 K), see Figures 5.7 and 4.19.

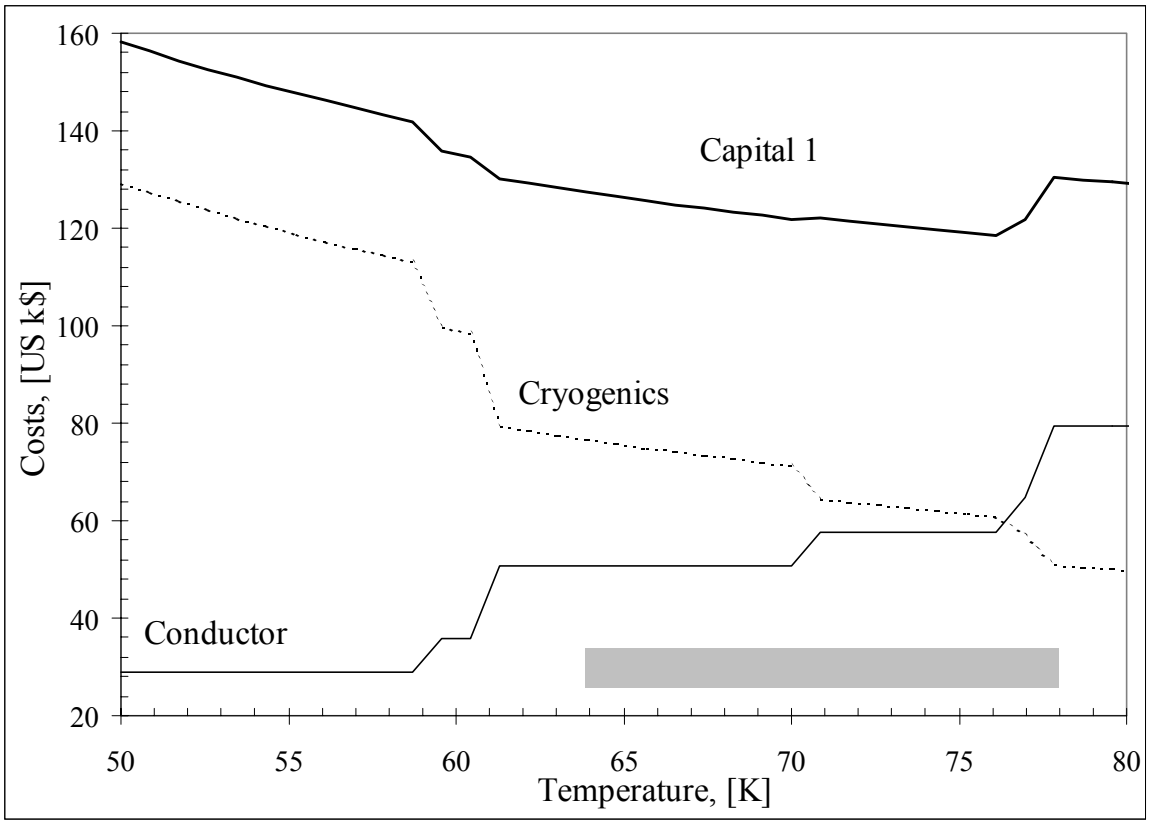

Figure 5.8 Conductor related material costs of the 30-MVA transformer HTS3 as function of the coils operating temperature.

5.3.7 Strands, conductor, coils, cooling and iron core

The estimated total amount of conductor for a 30-MVA transformer in Mega Ampere-meters is 2.26 for the Cu–based and for the HTS1 transformers and 1.65 for the HTS2 and for the HTS3 transformers respectively. The main specifications of superconducting coils (that are the same for the cases HTS2 and HTS3) are shown in Table 5.9. The number of parallel strands in the coil conductor that has to carry the rated current depends on the operating temperature, see Equations 5.12 and 5.14.

The cooling power also depends on temperature as given by Equation 5.15. Both dependencies are illustrated in Table 5.10 for the case HTS3. The number of strands is per phase; the cooling power is per transformer. The values shown in bold are closest to the minimum of the costs, see Figure 5.7. Note, that for a 30-MVA transformer the required cooling power is comparable to that of the 1-MVA resonator coil (about 1 kW, see section 4.5). The cooling power is within the range of the existing cryo-coolers see Figure 5.5. The main parameters of the iron cores for all cases studied are listed in Table 5.11.

Table 5.9 Specifications of the primary coil (per phase, cases HTS2 and 3).

Parameter	Unit	Value
Number of sub-coils	-	2
Average winding diameter	m	2.9
Height of sub-coil	m	1.7
Number of strand turns per sub-coil	-	756
Number of conductor layers per sub-coil	-	1
Axial magnetic field constant	mT/A	1.1

Table 5.10 Number of parallel strands in a coil conductor (per phase) and the cooling power.

Temperature T_Q, [K]	Primary side N_{ps}	Secondary side N_{ss}	Cooling power Q, [kW]
58.7	1	2	1.35
61.3	2	3	0.79
70.9	**2**	**4**	**0.74**
76.1	**2**	**4**	**0.78**
77.8	3	5	0.60
84.8	4	7	0.49

Table 5.11 Specifications of the iron core for a 30 - MVA transformer.

Parameter	Unit \ Value	Cases Cu and HTS1	Cases HTS2 and 3
Voltage-per-turn ratio v_{1p}	[V/turn]	70	105
Filling factor φ_m	-	0.9	0.9
Cross-section of the leg S_{Fe}	[m^2]	0.18	0.28
Width of the window w_w	[m]	0.75	0.67
Height of the window h_w	[m]	1.87	1.87
Avg. length of conductor turn	[m]	2.50	2.71

5.4 Conclusions

At present a few transformers already constructed are being investigated and have demonstrated various aspects of (sub)1-MVA class of high-T_c transformers. New model transformers rated at 3-5 MVA are under construction. The long term R&D activity aims to replace conventional 20-30 MVA utility transformers and 10 MVA traction transformers.

In order to investigate the applicability, a realistic model of a high-T_c transformer has been developed. The model links together the coils, the cooling and iron core; the efficiency, the dimensions, weight and the costs.

The model predicts two characteristic points of the market penetration for 30-MVA superconducting transformers. On one hand, the losses of existing power superconductors operated in liquid nitrogen are already low enough to compete with conventional conductors such as copper and aluminium. As a result, the energy costs of a high-T_c transformer are lower than of conventional transformer. On the other hand, the specific price of superconductors is too high at the moment. At 50 US$/kA/m the model predicts a competitive total cost of high-T_c transformers. Competitive capital costs will become a reality at conductor cost below 25 US$/kA/m.

The estimates used for a utility superconducting transformer employ rather conservative assumptions (based on the results achieved in existing coils, cryo-coolers, cryostats and current leads). The improvement of high-T_c tapes in terms of critical current, specific loss and cost continues. This lays a basis for even better technical and economical characteristics than presented here.

It is expected that high-T_c power transformers will become feasible and the break-even point will be reached in the next few years, certainly for special applications such as traction transformers in trains. Further research on power superconductors and coils (high current density and low losses combined with high voltage, the fault and short –circuit behaviour) is required in order to turn the prediction into technical reality.

Chapter 6

CONCLUSIONS

The key conclusions of the previous chapters are summarised. First, the main results of the study are outlined. Next, the modern technical Bi-2223/Ag superconductors are assessed. The concluding remarks regarding the network model development are laid down. The model is used to calculate voltage-current curves of advanced Bi-2223/Ag power coils. The essentials of high-T_c power coils and transformers are emphasized. Finally, existing opportunities for further research are listed.

6.1 Main results of the study

The aim of the study is to develop the basic knowledge of high-quality superconducting power coils made with Bi-2223/Ag tapes and to demonstrate the validity of the approach with a practical example.

When the perpendicular component of the external magnetic field is reduced from 50 to 10 mT, the critical current of a single Bi-2223/Ag tape increases by more than 30 % (section 2.4) and the corresponding total cyclic loss is reduced more than 10 times, see section 3.4.

When coil edges are surrounded with laminated ferro-magnetic C-cups, the perpendicular component of the magnetic field in the coil windings is reduced from about 55 to about 10 mT at the transport current of 50 A, see section 4.3. As expected, the critical current of such advanced coils increases and the conductor local and total losses decrease substantially, see section 4.4.

Therefore, application of the C-cups simultaneously causes an increase of the critical current, reduces the AC conductor losses and provides a more uniform thermal state in the windings of advanced Bi-2223/Ag coils. This main result is demonstrated using 1-MVA resonator coil as an example by the means of measurement and calculation.

The competitive costs of a 30-MVA high-T_c utility transformer will become a reality at a superconductor cost of below 25 US $/kA/m. For special applications, such as resonator coils and traction transformers, there is a market possibility already today.

6.2 Modern technical Bi-2223 superconductors

A quantitative description of direct *E-I* curves for technical Bi-2223 superconductors consistent with theory is proposed, which takes into account the effect of external magnetic field amplitude and direction with respect to the tape surface.

The essential properties of technical multifilament Bi-2223/Ag tapes are summarized. The spread along the length of outer dimensions and critical currents for Bi-2223/Ag tapes is kept within a few percent at present. The demonstrated constantly improving technical parameters of the tapes promise interesting opportunities for future scientific and technical applications.

Constitutive equations linking magnetic field strength and induction as well as electric field strength and current density for superconducting tape are introduced. The electric resistivity of Bi-2223/Ag tapes depends on the current density, magnetic field, temperature and conductor interior arrangement.

Measured direct Voltage-Current Curves of several tapes are analysed as function of external magnetic field (magnitude and angle with respect to the tape surface) and temperature using the power law. The angle dependencies of the critical current and the power index are described by a single correction factor. The factor depends only on the direction of the magnetic field and is autonomous for the field magnitude. As a result, a compact description for the effect of the magnitude and the direction of magnetic field on the critical current and the power index at constant temperature is provided. The *E-I* curves provide the input for the numerical model.

An empirical scaling relation known for Nb_3Sn wires describing the dependence of the critical current on external magnetic field and temperature is applied for Bi-2223/Ag tapes. The relation is modified to account for the dependence of experimental *E-I* curves on the magnetic field angle and for the irreversibility field. Using the novel relation, the dependence of the critical current on magnetic field and temperature is calculated and presented for one of the tapes.

A new method to insulate a superconducting tape without reduction of the critical current is proposed and implemented. Properties of insulated tapes are studied and described. Commercial heavy-duty insulation of Bi-2223 tapes has become available as a result of the research. Several km of diverse high-T_c tapes are already insulated and successfully operated in various devices. Here the insulated tapes are used in the 1-MVA high-T_c superconducting coil presented in Chapter 4.

6.3 New numerical network model and AC loss of single Bi-2223 tapes

The total AC loss of a single Bi-2223/Ag tape with non-twisted filaments can be accurately calculated using the network model and a direct *E-I* characteristic of the same (representative) tape measured as function of uniform external magnetic field and temperature. The uncertainty margin of about 7 % is found by comparing the measurement and the calculation. Though the comparison is confined to the losses, many other important characteristics of tapes can be calculated using the network model.

The existing physical and numerical models describing the electro-magnetic behaviour of high-T_c superconductors are reviewed. An advanced formulation of the classical eddy current problem is developed that links directly the current density and electrical field inside the superconductor and forms the basis of the presented electro-magnetic model. The formulation consists of the basic equations derived for the 3-dimensional quasi-static case of a high-T_c tape with non-twisted superconducting filaments and also for the case of time-harmonic source fields.

The network model allows a simple and clear derivation of the governing equations in the 2-dimensional case. Explicit formulas are found for calculating the inductances of the rectangular cells and the magnetic fields of the currents through the cells. The approach eliminates errors caused by making a step between the cells of finite size and the line cells.

The model is verified against available experimental data for high-T_c tapes (two cases: of both direct transport current and magnetic field present and of both time-harmonic transport current and magnetic field present are considered). In the former case, the calculated critical current-external magnetic field characteristics with and without the self-field correction are found to be in agreement with the measured one's, thus confirming the consistency of the model. In the latter case at 77 K and 48 Hz, the calculated and the measured total cyclic losses for a tape agree with the average relative uncertainty below 7 % over the whole measurement range thus proving that the assumptions of the network model are correct and that the total losses can be accurately calculated from the measured direct voltage-current curves. When the perpendicular component of the external magnetic field is reduced from 50 to 10 mT, the corresponding total cyclic loss is reduced more than 10 times independent of the transport current.

Though the comparison is confined to the total cyclic loss alone and in rather specific conditions, the model allows to compute the current distribution and losses in many other cases (such as the few mentioned in section 3.4) as well as many other important characteristics of tapes. A few selected examples (time dependence of the total, induced and transport currents at 48 Hz and frequency dependence of the total, magnetisation and transport current losses for tape A) are discussed. The purpose of the network model is to serve as a tool for calculating the loss voltage-current curves of coils, since for various reasons the number of options to measure losses is very limited for coils.

6.4 Advanced superconducting power coils

The resonant circuit for testing cables and capacitors at full power presents an example of a practically important technical system in which a superconducting coil made with Bi-2223/Ag tapes and operated in liquid nitrogen may be used. For this type of applications a lower cost of

the power supply feeding the circuit may compensate for the higher cost of the coil (as compared to the case when conventional copper coil is used).

The advanced 1-MVA high-T_c coil system for testing power cables and capacitors is described. An optimization of the coil design has led to a circular coil that consists of four long, thin concentric solenoids with a large diameter made with insulated Bi-2223/Ag tapes. To compensate for the negative effect of the radial component of magnetic field on the critical current in the Bi-2223/Ag tapes and to increase electric quality factor of coils, it is proposed to surround the coil edges with laminated ferro-magnetic C-cups. Application of the cups simultaneously increases the critical current, reduces the AC conductor losses and provides a more uniform thermal state of the coil windings. The losses in iron C-cups can be kept at an adequate level by means of sufficient lamination.

As a result of the research and technical effort, the knowledge, the infrastructure and technology are developed that allow manufacturing of power Bi-2223/Ag coils under industrial conditions. The insulation of Bi-2223/Ag tapes and the coil manufacturing technology are adopted at Smit Wire Nijmegen and at Smit Transformatoren B.V. respectively. All tapes are insulated and all sub-coils are made by the companies' personnel. A close cooperation between the university and the industry has created conditions facilitating technical applications of high-T_c superconductors and resulted in the manufacturing of the 1-MVA coil system.

Two methods are used for studying voltage-current curves of the sub-coils: numerical and experimental. The latter includes thermal, calorimetric and electro-magnetic methods, which are complementary to each other and allow accessing of various components of the coil loss voltage.

To enable the numerical method, the magnetic field in the coil windings is calculated using commercial software for various configurations of sub-coils and C-cups. The distribution of the magnetic field along the tape length for each magnetic configuration of the coil is derived from the calculations. Using magnetic field profiles and the network model, the conductor loss voltage is calculated for various magnetic configurations of the sub-coils and for the 1-MVA coil.

The direct voltage-current curves measured and calculated at 77 K for three magnetic configurations of the sub-coils comprising the 1-MVA coil system are presented. The calculations use the effective critical currents and *n*-values along with the data extracted from the tape short sample measurements. The gain in critical current due to application of the iron cups is clearly seen from the presented data.

The AC loss voltage-current curves of the sub-coils are measured with the electro-magnetic, thermal and calorimetric methods. Because of the high voltage restrictions, AC loss voltage-current curves of the 1-MVA coil are measured with the calorimetric method and using the wattmeter. The coil design is verified with the experiments and calculations.

The voltage-current curves obtained using the network model are compared with the experimental data for various magnetic configurations of the sub-coils. A fair agreement of the experimental and calculated data is found and it proves the harmless (in respect to the critical current) tape treatment during the coil manufacturing and subsequent operation. At the same time, the agreement validates the developed numerical method itself. This allows numerical characterization of power coils in cases when experiments are difficult or impossible to perform.

Due to the high electric quality factor of the 1-MVA superconducting coil (above 500), the advanced resonant circuit for testing power cables and capacitors at full power consumes only a few kW (with sound consumption of liquid nitrogen) as compared to 50 kW in the case when a copper coil is used.

6.5 Outlook for superconducting power transformers

At present a few transformers already constructed are being investigated and have demonstrated various aspects of (sub)1-MVA class of high-T_c transformers. New model transformers rated at 3-5 MVA are under construction. The long and mid-term R&D activities

are aiming to replace coils of conventional 20-30 MVA utility transformers and traction transformers respectively.

A realistic model of the high-T_c transformer has been developed. The model links together the coils, the cooling and iron core; the efficiency, the dimensions, weight and the costs.

The model predicts two characteristic points of market penetration for the 30 - MVA superconducting utility transformers. On the one hand, the losses of existing power superconductors operated in liquid nitrogen are already low enough to compete with conventional conductors such as copper and aluminium. As a result, the energy costs of a high-T_c transformer are lower than those of a conventional transformer. On the other hand, the specific price of superconductors is too high at the moment. At 50 US $/kA/m the model predicts a competitive total cost of high-T_c transformers. Competitive capital costs will become a reality at conductor cost of below 25 US $/kA/m.

The estimates used for a utility superconducting transformer employ rather conservative assumptions (based on the results achieved in existing coils, cryo-coolers, cryostats and current leads). The improvement of high-T_c tapes in terms of critical current, specific loss and cost continues. This lays a basis for even better technical and economical characteristics than presented here.

The break-even point in costs for high-T_c power transformers is expected in the next few years, certainly for special applications such as traction transformers in trains. Further research on power superconductors and coils is required in order to turn the prediction into technical reality.

6.6 Opportunities for further research

The most important topics for further research are listed below. Measurement of direct voltage-current characteristics of Bi-2223/Ag tapes as function of external magnetic field and temperature (and controlled strain), also with suppressed perpendicular component B_y of the self-field. Systematic study of the temperature dependence of direct *E-I* characteristics and of the losses for the same tape enabling the comparison with the calculations is required.

The network model can be extended to tapes with twisted filaments as well as to arrays of (insulated) tapes and cables. The model should have better resolution in order to account for the residual component of magnetic field between the adjacent turns.

Research aiming at a higher critical current density in combination with reduced specific costs and lower AC losses (achieved by creating a Bi-2223/Ag tape with many fine and electro-magnetically decoupled superconducting filaments) is important.

Fundamental principles of science and technology for advanced high-T_c power coils laid down in this study, should be further developed. The method to calculate voltage-current curves of power coils should be applied to transformer coils. New reliable methods to study voltage-current curves of power coils are required. Various magnetic configurations and operating modes typical for power coils and transformers (higher operating voltages; ability to pass over-current and over-voltage tests, etc.) should be further explored both by measurement and calculation.

List of symbols

Convention: bold symbols are used for matrices or vectors. Quantities marked as [-] are dimensionless. Symbols used for curves are not listed.

a_c	dimension in *x*-direction (width) of the filamentary core	[m]
b_c	dimension in *y*-direction (thickness) of the filamentary core	[m]
k_m	magnetic field constant	[T/A]
$\dot{Q}_{CN}$	conductor loss	[W]
$\dot{Q}$	cooling power	[W]
a	dimension in *x*-direction (width)	[m]
A	magnetic vector potential	[Wb/m]
A	height of transformer	[m]
A_{RF}	empirical constant to fit $\dot{Q}$ and T_Q of a refrigerator	[$W^{-0.2}$]
a_{tb}	characteristic dimension perpendicular to the direction of magnetic field	[m]
b	dimension in *y*-direction (thickness)	[m]
B	magnetic induction, magnetic field, magnetic flux density	[T]
b	magnetic field	[-]
C	capacitance	[F]
C_{CAP}	capital cost	[US $]
C_{CN}	conductor cost	[US $]
c_{NL}	dimensional factor related to the energy costs at no-load conditions	[$/W]
C_{OP}	operating cost	[US $]
C_{RF}	cooling cost	[US $]
C_{TOC}	total cost	[US $]
d	distance	[m]
E	electric field (strength)	[V/m]
f	frequency	[Hz]
F	pinning force	[N/m]
$f(\alpha)$; f_α	correction factor for misalignment angle	[-]
f_{bir}	pinning force	[-]
f_L	load factor	[-]
f_{LA}	load factor average over the lifetime	[-]
g	mean geometric distance	[m]
g	size of an air gap	[m]
h	height	[m]
H	magnetic field strength	[A/m]
I	current	[A]
i	critical current	[-]
J	current density	[A/m^2]
k	the Ginzburg-Landau parameter	[-]
$K_{t,\varepsilon}$	temperature and strain dependent coefficient	[-]
L	self-inductance	[H]
l, ℓ_v	dimension in *z*-direction (length)	[m]
m	integer number (of cell currents, for instance)	[-]
$M(B)$	magnetisation	[T]

M, M_G	mutual inductance, Green's function	[H]
M_{1p}	number of sub-coils with the same direction of the transport current	[-]
N	number of coil turns	[-]
n	power index, $n_1 = n^{-1}$	[-]
p	power index	[-]
P_{3p}	electric power rating	[VA]
P_{Fe}	electric power dissipated in iron core	[W]
P_{FL}	electric power consumed by a transformer at full-load conditions	[W]
P_{NL}	electric power consumed by a transformer at no-load conditions	[W]
q	power index	[-]
Q	loss per cycle per meter tape	[J/m]
r	radius, position	[m]
S	surface area (of a superconductor)	[m^2]
S_c	electrical cross-section area of (tape) conductor	[m^2]
S_ε	strain factor	[-]
T	temperature	[K]
t	time	[s]
T_Q	temperature of refrigerator cold end	[K]
t_ε	temperature	[-]
V	voltage	[V]
w	width	[m]
X	magnetic field constant in x-direction	[T/A]
x, y, z	Cartesian coordinates	[m]
Y	magnetic field constant in y-direction	[T/A]
Z	impedance of a coil	[Ω]
α	angle between the direction of magnetic field and y-direction	[°]
α_0	misalignment angle	[°]
$\beta_{t,\varepsilon}$	temperature and strain dependent factor	[-]
Φ	magnetic flux	[Wb]
Φ_0	magnetic flux quantum	[Wb]
γ	superconductor to total filling factor	[-]
γ	power index	[-]
φ	electric scalar potential	[V]
φ_m	filling factor (iron core)	[-]
λ	magnetic field penetration depth	[m]
μ	permeability	[H/m]
η	efficiency of the real cooling cycle	[-]
η	density of the magnetic flux lines	[m^{-2}]
η_1	distance between two cells	[m]
η	size of an air gap	[-]
ε	cooling penalty	[-]
ε	strain	[-]
θ	current vector potential	[A/m]
ρ	electrical resistivity	[Ωm]
σ	electrical conductivity $\sigma = \rho^{-1}$	[S/m]
σ	radius	[-]
σ_{CAP}	factor related to material costs	[-]
σ_{NL}	factor accounting the loss at no-load (the leads and the cryostat)	[-]
σ_{FL}	factor accounting for the loss increase at full load (leads and cryostat)	[-]

ω	circular frequency	[Hz]
Ω	magnetic scalar potential	[A]
ξ	angle between the positive direction of x-axis and the vector $\boldsymbol{r}_i - \boldsymbol{r}_k$	[°]
ξ	coherence length	[m]
ς	power index	[-]
χ	coil height	[-]
χ	power index	[-]
τ_0	duration of a cycle	[s]
Δ	small change	[-]
ν	power index	[-]
ν_{lp}	given voltage per turn ratio	[V_{rms}/turn]

subscripts

α	angle
ε	strain
ρ	resistivity; resistive
B, b	magnetic field
bath	bath
c	critical (for electric or magnetic quantity), core (for dimensions)
c2	the upper critical
d	drain; direct; depairing
e	external
ef	effective
Fe	iron
i	insulation; inductive
i, k	integer counters: $i = 1,2,...m$ and $k = 1,2,...m$
ir, bir	irreversibility
J	self-field
m	matrix
mx	maximum
P	room
Q	coil
r	relative; resistive
rms	root mean square
s	superconductor; source
st	superconductor to total
T	temperature
t	tape
tot, tt	total
tr	transport
ts	total static
v	voltage
w	window
x, y, z	*x, y, z* – direction respectively

superscripts

*	corrected (for errors in direction of magnetic field)
◊	rectangular cell of final dimensions
0	absolute; amplitude

References

Convention: each book is listed here only once. The page or chapter number in a book is given in the main text as p. 100 or ch. 3. Conference papers have the year of publishing of the conference proceedings. If these are not yet published, the papers have the year of the conference itself. When the number of the authors exceeds 12, only 1-st name is listed. The label of a website address contains the year during which the cited information is acquired.

[Akhm98] A. Akhmetov: *Network models of superconducting cables and the results of the matrix approach to their description*, Physica C **310**, p. 309 (1998).

[Amem98] N. Amemiya, S. Murasawa, N. Banno and K. Miyamoto: *Numerical modelling of superconducting wires for AC loss calculations*, Physica C **310**, p. 16 (1998).

[Amer01] website address: http://www.amsuper.com/.

[Angh98] A. Anghel, G. Pastor, R. Wesche, B. Jakob and G. Vecsey: *Neon refrigeration for high temperature superconducting power transmission cables*, presented at ICEC'98, Proceedings of 17-th International Cryogenic Engineering Conference ICEC17, eds. D. Dew Hughes, R. Scurlock and J. P. Watson, p. 337 (1998).

[Ashw00] S. P. Ashworth, M. Suenaga: *Experimental determination of the losses produced by the interaction of AC magnetic fields and transport currents in HTS tapes*, Physica C **329**, p. 149 (2000).

[Bedn86] J. G. Bednorz, K. A. Müller: *Possible high-T_c superconductivity in the Ba-La-Cu-O system*, Z. Phys. B **64**, p.189 (1986).

[Bonm00] D. Bonmann: *Supraleitende transformatoren – chansen und herausforderungen*, presented at DPG-2000; available at: http://w3.infp.fzk.de:8080/extern/hotline

[Bosc91] H. Boschman: *On the resistive transition of composite superconductors*, PhD thesis University of Twente, Enschede, The Netherlands (1991).

[Bott00] L. Bottura: *A practical fit for the critical surface of NbTi*, presented at MT-16'99, IEEE Transactions on Applied Superconductivity **10**-1, p. 1054 (2000).

[Bran96] E. H. Brandt: *Superconductors of finite thickness in a perpendicular magnetic field: Strips and slabs*, Physical Review B **54**, p. 4246 (1996).

[Carr83] W. J. Carr, Jr.: *AC Loss and macroscopic theory of superconductors*, Gordon and Breach, New York, USA (1983).

[Chiba99] T. Chiba, Q. Li, S. P. Ashworth and M. Suenaga: *Angular dependence of AC losses at power frequencies for a stack of Bi2223/Ag tapes*, presented at ASC '98, IEEE Transactions on Applied Superconductivity **9**-2, p. 2143 (1999).

[Chri95] C. J. Christopherson and G. N. Riley, Jr.: *Development of twisted high-temperature superconductor composite conductors*, Applied Physics Letters **66**, p. 2277 (1995).

[Clerc95] St. H.-R. Clerc: *AC losses of mono- and multifilamentary high-T_c superconducting (Bi, Pb)$_2$Sr$_2$Ca$_2$Cu$_2$O$_{10}$/Ag tapes,* PhD thesis, Swiss Federal Institute of Technology, Zurich, Switzerland (1995).

[Cool96] L. D. Cooley, P. J. Lee and D. C. Larbalestier: *Flux-pinning mechanism of proximity-coupled planar defects in conventional superconductors…*, Physical Review B **53**, p. 6638 (1996).

[Däum97] M. Däumling: *Numerical calculation of ac losses, field and current distributions for specimens with demagnetisation effect*, presented at EUCAS '97, Institute of Physics Conference Series **158**, p. 1413 (1997).

[Dema97] A. Demarmelis, S. Hörnfeld, F. König, J. Rhyner and J. M. Rivera: *Superconducting coil*, United States Patent nr. 5,689,223. Dated: Nov. 18, 1997.

[DeVr92] P. L. DeVries: *A first course in computational physics*, John Wiley & Sons, Inc., New York, 1992.

[Djur01] D. Djurek, Z. Medunić, A. Tonejc and M. Paljević: *$PbCo_3 \cdot 2PbO + Ag_2O$ and $PbCo_3 \cdot PbO + Ag_2O$ (PACO) systems: route for novel superconductors*, Physica C **351**, p. 78 (2001).

[Evet00] J. E. Evetts and B. A. Glowacki: *Superconducting materials – the path to applications*, Superconductor Science and Technology **13**, p. 443 (2000).

[Evet92] *Concise encyclopedia of magnetic & superconducting materials*, Ed.: J. Evetts, Pergamon Press, Oxford, 1992.

[Fisc99] B. Fischer, S. Kautz, M. Leghissa, H.-W. Neumüller and T. Arndt: *Fabrication and properties of Bi-2223 tapes*, presented at ASC '98, IEEE Trans. on Applied Superconductivity **9**-2, p. 2480 (1999).

[Fles99] S. Fleshler, M. Fee, S. Spreafico and A. P. Malozemoff, *Self-field effect in high critical current density BSCCO tapes*, submitted 10/18/99 to ISS'99, the pre-print is available at [Amer00].

[Fuch95] G. Fuchs, E.S. Vlakov, K. A. Nenekov, T. Staiger and A. Gladun: *Irreversibility line of polycrystalline Bi-2223 samples*, Physica C **247**, p. 340 (1995).

[Funa00] K. Funaki and M. Iwakuma: *Recent activities for application to HTS transformers in Japan*, Superconductor Science and Technology **13**, p. 60 (2000).

[Funa01] K. Funaki, e. a.: *Development of a 22 kV/6.9 kV single-phase model for a 3 MVA HTS power transformer cooled by liquid nitrogen,* presented at ASC '2000, IEEE Trans. on Applied Superconductivity **11**-1, p. 1578 (2001).

[Funa98] K. Funaki, K. Kajikawa, H. Shiraishi, M. Iwakuma, S. Miyake, T. Kumano and T. Hasegawa: *A simple electromagnetic method of AC loss measurement for superconducting wires carrying DC/AC transport current in an AC transverse magnetic field*, Physica C **310**, p. 132 (1998).

[Funa98a] K. Funaki, e. a.: *Development of a 500 kVA-class oxide-superconducting power transformer operated at liquid-nitrogen temperature*, Cryogenics **38**, p. 211 (1998).

[Garb89] M. Garber, A. K. Ghosh and W. B. Sampson, *The effect of self field on the critical current determination of multifilamentary superconductors,* IEEE Trans. on Magnetics **25**-2, p. 1940 (1989).

[Gode00a] A. Godeke, H. J. G. Krooshoop, O. A. Shevchenko, B. ten Haken, H. H. J. ten Kate, A. M. A. Scholten, and P. C. H. Klein Schiphorst: *Method of insulating an elongated conductor comprised of high-temperature superconductive, substantially ceramic material and an apparatus for the implementation of the method*, European patent EP1089300, publication date: 2001-04-04, available at: http://ec.espacenet.com/espacenet/ .

[Gode00b] A. Godeke, O. A. Shevchenko, H. J. G. Krooshoop, B. ten Haken, H. H. J. ten Kate, G. Rutten, B. Broeren, C. J. G. Spoorenberg, A. M. A. Scholten, P. Klein Schiphorst and G. C. Damstra: *An optimised BSCCO/Ag resonator coil for utility use,* presented at MT-16, IEEE Transactions on Applied Superconductivity **10**-1, p. 849 (2000).

[Gode01] A. Godeke, O. A. Shevchenko, J. J. Rabbers, B. ten Haken, C. J. G. Spoorenberg, P. Klein-Schiphorst, G. C. Damstra and H. H. J. ten Kate: *Construction and test of a 1 MVA-class BSCCO resonator coil*, presented at ASC '2000, IEEE Trans. on Applied Superconductivity **11**-1, p. 1570 (2001).

[Gode01a] A. Godeke, H. J. G. Krooshoop, H. G. Knoopers, B. ten Haken, and H. H. J. ten Kate: *Experimental verification of the temperature and strain dependence of the critical properties in Nb_3Sn wires*, presented at ASC '2000, IEEE Trans. on Applied Superconductivity **11**-1, p. 1570 (2001).

[Gode99] A. Godeke, B. ten Haken and H. H. J. ten Kate: *Scaling of the critical current in ITER type niobium-tin superconductors in relation to the applied field, temperature and uni-axial applied strain*, presented at ASC '98, IEEE Trans. on Applied Superconductivity **9**-2, p. 161 (1999).

[Good01] L. F. Goodrich and T. F. Stauffer: *Hysteresis in transport critical-current measurements of oxide superconductors*, Journal of research of the National Institute of Standards and Technology, **106**-4, p. 657 (2001).

[Gras97] G. Grasso, F. Marti, Y. Huang, A. Perin and R. Flükiger: *Correlation between the normal-state resistivity and the critical current density of Ag-sheathed Bi(2223) tapes*, Physica C **281**, p. 271 (1997).

[Grov46] F. W. Grover: *Inductance calculations: working formulas and tables*, Dover Publ. Inc., NY, (1946).

[Gure97] A. V. Gurevich, R. G. Mints and A. L. Rakhmanov: *The physics of composite superconductors*, Begell House, Inc. N. Y. 1997.

[Hart89] R. A. Hartmann: *A contribution to the understanding of AC losses in composite superconductors*, PhD thesis, University of Twente, Enschede, The Netherlands (1989).

[Hass01] W. V. Hassenzahl: *Superconductivity, an enabling technology for 21st century power systems?*, presented at ASC '2000, IEEE Trans. on Applied Superconductivity **11**-1, p. 1447 (2001).

[Hilg95] H. Hilgenkamp: *High-T_c DC SQUID magnetometers*, PhD thesis, University of Twente, Enschede, The Netherlands (1995).

[Hofm01] C. Hofmann: *A high-T_c superconductor material model for time harmonic numerical simulations*, Superconductor Science and Technology **14**, p. 41 (2001).

[Inte01] website address: http://www.igc.com.

[Iwak01] M. Iwakuma, e. a.: *AC loss properties of a 1MVA single-phase HTS power transformer*, presented at ASC '2000, IEEE Trans. on Applied Superconductivity **11**-1, p. 1482 (2001).

[Iwak96] M. Iwakuma, e. a.: *AC loss and current distribution in parallel conductors for Bi2223 HTS transformer windings*, Proceedings of ICEC/ICMC **16**, p. 1329 (1996).

[Iwak98] M. Iwakuma, Y. Tajika, K. Kajikawa, K. Funaki, T. Matsushita, E. S. Otabe, N. Ayai, K. Hayashi and K. Sato: *Twist effect on hysteresis loss in Bi2223 multifilamentary wires exposed to an AC magnetic field*, Physica C **310**, p. 155 (1998).

[Iwas94] Yu. Iwasa: *Case studies in superconducting magnets, design and operational issues*, Plenum Press, New York and London (1994).

[Jin97] J. X. Jin, S. X. Dou and H. K. Liu: High voltage generation with high-T_c superconducting resonant circuit, presented at ASC'1996, IEEE Transactions on Applied Superconductivity **7**-2, p. 881 (1997).

[Kaji01] K. Kajikawa, A. Takenaka, K. Kawasaki, M. Iwakuma and K. Funaki: *Numerical simulation for AC losses of HTS tapes in combined alternating transport current and external magnetic field with fase shift*, presented at ASC'2000, IEEE Trans. on Applied Superconductivity **11**-1, p. 2240 (2001).

[Kane99] T. Kaneko, T. Hikata, M. Ueyama, A. Mikumo, N. Ayai, S. Kobayashi, N. Saga, K. Hayashi, K. Ohmatsu and K. Sato: *Status of Bi-2223 tapes performance and development*, presented at ASC '98, IEEE Transactions on Applied Superconductivity **9**-2, p. 2465 (1999).

[Kate01] H. H. J. ten Kate: *The superconducting magnet system for the ATLAS detector at CERN*, IEEE Transactions on Applied Superconductivity **10**-1, p. 347 (2000).

[Kate94] H. H. J. ten Kate: *Superconducting rectifiers*, PhD thesis, University of Twente, Enschede, The Netherlands (1984).

[Kim62] Y. B. Kim, C. F. Hempstead and A. R. Strnad: *Critical persistent currents in hard superconductors*, Physical Review Letters **9**, p. 306 (1962).

[King96] C. King, K. Herd, T. Laskaris and A. Mantone: *Evaluation of strengthening and insulation system for high temperature BSCCO-2223 superconducting tapes*, Advances in Cryogenic Engineering **42** p. 855 (1996).

[Klop93] B. Klopman: *High-frequency properties of high-temperature superconductors*, PhD thesis, University of Twente, Enschede, The Netherlands (1993).

[Koba96] S. Kobayashi, T. Kaneko, T. Kato, J. Fujikami and K. Sato: *A novel scaling of magnetic field dependencies of critical currents for Ag-sheathed Bi-2223 superconducting tapes*, Physica C **258**, p. 336 (1996).

[Kumm99] P. Kummeth, R. Schlosser, P. Massek, H. Schmidt, C. Albrecht, D. Breitfelder and H.-W. Neumüller: *Development and test of a 100 kVA superconducting transformer operated at 77 K*, presented at EUCAS '99, Superconductor Science and Technology **13**, p. 503 (2000).

[Kwas98] A. Kwasnitza, St. Clerc, R. Flükiger and Y. B. Huang: *Alternating magnetic field losses in high-T_c superconducting multifilament tapes with a mixed matrix of Ag and $BaZrO_3$*, Physica C **299**, p. 113 (1998).

[Larb01] D. C. Larbalestier, e. a.: *Strongly linked current flow in polycrystalline forms of new superconductor MgB_2*, Nature **410**, p. 186 (2001).

[Larb97] D. C. Larbalestier: *The road to conductors of high temperature super-conductors: 10 years do make a difference!* IEEE Trans. on Applied Superconductivity **7**-2, p. 90 (1997).

[Lawr00] L. R. Lawrence, Jr., C. Cox and D. Broman: *High temperature super-conductivity: the products and their benefits*, Alexandria, Virginia, USA, Report ORNL/Sub/4500006921 (2000).

[Leyb01] website address: http:///www.leyboldvac.de.

[Magn01] N. Magnusson: *Semi-empirical model of the losses in HTS tapes carrying AC currents in AC magnetic fields applied parallel to the tape face*, Physica C **349**, p. 225 (2001).

[Malo02] the presentation is available at: http://www.amsuper.com/doewireworkshop.htm.

[Malo99] A. P. Malozemoff, e. a.: *HTS wire at commercial performance levels,* presented at ASC'98, IEEE Trans. on Applied Superconductivity **9**-2, p. 2469 (1999).

[Mart96] L. Martini, A. Gandini, L. Rossi, V. Ottoboni and S. Zannella: *Anisotropy of Bi-2223/Ag tapes by electrical and magnetic characterizations*, Physica C **261**, p. 196 (1996).

[Masl97] M. Maslouh, F. Bouillault, A. Bossavit and J.-C. Vérité: *From Bean's model to the $H-M$ characteristic of a superconductor: some numerical experiments*, IEEE Trans. on Applied Superconductivity **7**-3, p. 3797 (1997).

[Masl98] M. Maslouh, F. Bouillault, A. Bossavit and J.-C. Vérité: *Numerical modelling of superconductor materials using an anisotropic Kim law*, IEEE Trans. on Magnetics **34**, p. 3064 (1998).

[Masu99] L. J. Masur, e. a.: *Long length manufacturing of BSCCO-2223 wire for motor and cable applications*, presented at CEC / ICMC'99, Montreal, Canada, July12-16, (1999).

[McCo00] B. W. McConnell: *Transformers – a successful application of high temperature superconductors*, IEEE Trans. on Applied Superconductivity **10**-1, p. 716 (2000).

[Meht97] S. P. Mehta, N. Aversa and M. Walker: *Transforming transformers*, IEEE Spectrum, p. 43 (July 1997).

[Mein02] M. Meinert, M. Leghissa, R. Schlosser and H. Schmidt: *System test of 1-MVA-HTS-transformer connected to a converter-fed drive for present rail vehicles*, presented at ASC '2002.

[Muld88] G. Mulder: Increasing the operating frequency of superconducting rectifiers, PhD thesis University of Twente, Enschede, The Netherlands (1988).

[Müll99a] K.-H. Müller: *AC losses in stacks and arrays of YBCO/hastelloy and monofilamentary Bi-2223/Ag tapes*, Physica C **312**, p. 149 (1999).

[Naga01] J. Nagamatsu, N. Nakagawa, T. Muranaka, Y. Zentani and A. Akimitsu: *Superconductivity at 39 K in magnesium diboride*, Nature **410**, p. 63 (2001).

[Naka96] S. Nakamae and J. Schwartz: *Magnetoresistivity of Ag tape co-processed with Bi1.4 Pb0.6 Sr2 Ca2 Cu3Ox superconductor*, Cryogenics **36**, p. 395 (1996).

[Namj88] K. V. Namjoshi and P. P. Biringer: *Low-frequency eddy current loss estimation in long conductors by using the moment of inertia of cross-sections*, IEEE Trans. on Magnetics **24**, p. 2181 (1988).

[Neum99] H.-W. Neumüller and W. Schmidt: *Development of resistive fault current limiters: status and prospects for the YBCO coated switching element concept*, presented at CEC / ICMC '99, Montreal, Canada (1999).

[Nibb01] N. Nibbio, S. Stavrev and B. Dutoit: *Finite element method simulation of AC loss in HTS tapes with B-dependent E-J power law*, IEEE Trans. on Applied Superconductivity **11**-1, p. 2631 (2001).

[Nibb99] N. Nibbio: *Non-linear electromagnetic modelling of high temperature superconducting tapes*, PhD thesis N 2031, École Politechnique Fédérale de Lausanne, Lausanne, Switzerland (1999).

[Nord01] website address: http://www.nst.com.

[Onne11] H. K. Onnes: *The disappearance of the resistance of mercury*, Comm. Phys. Lab. Univ. Leiden **122 B** (1911).

[Oome00] M. P. Oomen, B. ten Haken, M. Leghissa and J. Rieger: *Optimum working temperature of power devices based on Bi-2223 superconductors*, Superconductor Science and Technology **13**, p. L19 (2000).

[Oome00a] M. P. Oomen: *AC loss in superconducting tapes and cables*, PhD thesis University of Twente, Enschede, The Netherlands (2000).

[Over86] F. van Overbeeke: *On the application of superconductors in power transformers*, PhD thesis University of Twente, Enschede, The Netherlands (1986).

[Paas98] J. Paasi, J. Lehtonen, M. Lahtinen and L. Kettunen: *Computation of AC losses in high-temperature superconductors*, Physica C **310**, p. 63 (1998).

[Paas98a] J. Paasi and M. Lahtinen: *AC losses in high-temperature superconductors: revisiting the fundamentals of the loss modelling*, Physica C **310**, p. 57 (1998).

[Pan00] S. H. Pan, E.W. Hudson, K.M. Lang, H. Eisaki, S. Uchida and J. C. Davis: *Imaging the effects of individual zinc impurity atoms on superconductivity in* $Bi_2Sr_2Ca_1Cu_2O_{8+}$, Nature **403**, p. 746 (2000).

[Past99] G. Pastor, A. Anghel, A. M. Fuchs, B. Jakob, D. Trajkovic, G. Vecsey, R. Wesche and R. Schindler: *Manufacture and testing of a neon gas-cooled HTS prototype cable for power transmission*, presented at EUCAS '99, Institute of Physics Conference Series **167**, p. 1119 (1999).

[Pedy96] M. V. Pedyash: High-T_c superconducting nanobridges in $YBa_2Cu_3O_{7-\delta}$ thin films", PhD thesis University of Twente, Enschede, The Netherlands (1996).

[Quic01] website address: http://www.quickfield.com.

[Rabb01] J. J. Rabbers, B. ten Haken, O. A. Shevchenko and H. H. J. ten Kate: *An engineering formula to describe the AC loss of BSCCO/Ag tape*, presented at ASC '2000, IEEE Trans. on Applied Superconductivity **11**-1, p. 2623 (2001).

[Rabb01a] J. J. Rabbers, *AC loss in superconducting tapes and coils* PhD thesis University of Twente, Enschede, The Netherlands (2001).

[Rabb98] J. J. Rabbers, B. ten Haken and H. H. J. ten Kate: *Measuring transport current loss of BSCCO/Ag tapes exposed to external AC magnetic field*, Physica C **310**, p. 101 (1998).

[Rabb99] J. J. Rabbers, O. v. d. Meer, W. F. A. Klein Zeggelink, O. A. Shevchenko, B. ten Haken and H. H. J. ten Kate: *Magnetisation loss of BSCCO/Ag tapes in uni-directional and rotating magnetic field*, Physica C **325**, p. 1 (1999).

[Rabb99a] J. J. Rabbers, D. C. van der Laan, B. ten Haken and H. H. J. ten Kate: *Magnetisation and transport current loss of a BSCCO/Ag tape in an external AC magnetic field carrying an AC transport current,* presented at ASC'98, IEEE Trans. on Applied Superconductivity **9**-2, p. 1185 (1999).

[Rabb99b] J. J. Rabbers, B. ten Haken, O. A. Shevchenko and H. H. J. ten Kate: *Total AC loss of BSCCO/Ag tape in different orientations of the external AC magnetic field,* presented at EUCAS '99, Institute of Physics Conference Series **167**, p. 859 (1999).

[Radc82] D.J. Radcliffe and H. M. Rosenberg: The thermal conductivity of glass-fibre and carbon fibre composites from 2 to 80 K, Cryogenics, p. 245 (1982).

[Rhyn98] J. Rhyner: *Calculation of ac losses in HTSC wires with arbitrary current voltage characteristics*, Physica C **310**, p. 42 (1998).

[Schl02] R. Schlosser, H. Schmidt, M. Leghissa, B. Gromoll, J. Rieger and M. Meinert: *Development of high-temperature superconducting transformers for railway applications*, presented at ASC '2002.

[Schm00] C. Schmidt, Calorimetric ac-loss measurement of high T_c-tapes at 77 K, a new measuring technique, Cryogenics **40**, p. 137 (2000).

[Schw02] S. W. Schwenterly, M. J. Cole, D. W. Haselton and E. F. Pleva: *Performance of a prototype HTS power transformer cooling module*, presented at ASC '2002.

[Seeb98] B. Seeber: *Handbook of Applied Superconductivity*, Institute of Physics Publishing, Bristol UK (1998).

[Serr00] E. Serres, e. a.: *Current limitation in high temperature superconducting transformers and impact on the grid*, CIGRÉ 2000, Paris, session paper 12-205.

[Shea01] T. P. Sheahen, B. W. McConell and J. W. Mullholland: *Method for estimating future markets for high temperature superconducting power devices*, presented at ASC '2000; an extended version of this document is currently available at: www.ornl.gov./HTSC/pdf/Mulholland%20Report.pdf.

[Shea94] T. P. Sheahen: *Introduction to high-temperature superconductivity*, Plenum Press, New York (1994).

[Shev01] O. A. Shevchenko, J. J. Rabbers, A. Godeke, B. ten Haken and H. H. J. ten Kate: *V-I curves of a 100-kVA class high-T_c resonator coil*, presented at ASC '2000, IEEE Trans. on Applied Superconductivity **11**-1, p. 2204 (2001).

[Shev97] O. A. Shevchenko, H. G. Knoopers, H. H. J. ten Kate and G. C. Damstra: *Loss reduction in a high quality superconducting coil,* presented at EUCAS '97, Institute of Physics Conference Series **158**, p. 1555 (1997).

[Shev98] O. A. Shevchenko, J. J. Rabbers, A. Godeke, B. ten Haken and H. H. J. ten Kate: *AC loss in a high-temperature superconducting coil*, Physica C **310**, p. 106 (1998).

[Shev99] O. A. Shevchenko, J. J. Rabbers, A. Godeke, B. ten Haken and H. H. J. ten Kate: *Angle dependency of AC losses in a BSCCO-2223 tape – simulation and experiment*, presented at EUCAS '99, Institute of Physics Conference Series **167**, p. 879 (1999).

[Shev99a] O. A. Shevchenko, J.J. Rabbers, H. J. G. Krooshoop, B. ten Haken and H. H. J. ten Kate: *Characterization of a high-T_c coil using short sample data*, presented at ASC'98, IEEE Trans. on Applied Superconductivity **9**-1, p. 1331 (1999).

[Shev99b] O. A. Shevchenko, A. Godeke, H. J. G. Krooshoop, J.J. Rabbers, B. ten Haken, G. C. Damstra, G. Rutten, C. J. Spoorenberg and H. H. J. ten Kate: *A high-T_c resonator coil with an air-gap iron yoke*, presented at EUCAS '99, Institute of Physics Conference Series **167**, p. 1147 (1999).

[Siss00] E. Sissimatos, G. Harms and B. R. Oswald: *Optimisation of high-temperature superconducting transformers,* presented at ASC '2000, IEEE Trans. on Applied Superconductivity **11**-1, p. 1574 (2001).

[Sjös00] M. Sjöström, D. Djukic, and B. Dutoit*: Parameterized hysteresis model for high-temperature superconductors,* IEEE Trans. on Applied Superconductivity **10**-2, p. 1585 (2000).

[Spre99] S. Spreafico, L. Gerardi, S. Fleshler, D. Tatelbaum, J. Leone, D. Yu, and G. Snitchler: *The effects of self-field on current capacity in Bi-2223 composite strands*, IEEE Trans. on Applied Superconductivity **9**-2, p. 2159 (1999).

[Stav98] S. Stavrev and B. Dutoit: *Frequency dependence of AC loss in Bi/2223/Ag-sheathed tapes*, Physica C **310**, p. 86 (1998).

[Stee97] C. W. Steele: *Numerical computation of electric and magnetic fields*, Chapman & Hall, NY (1997).

[Stir00] website address: http://www.stirling.nl.

[Stro69] T. R. Strobridge: *Refrigeration for superconducting and cryogenic systems*, IEEE Trans. Nucl. Sci., NS-**16,** p. 1104 (1969).

[Sumi99] F. Sumiyoshi, R. Kinoshita, Y. Miyazono, A. M. Campbell and K. Ohmatsu: *Proposal of new type Ag-BSCCO tapes and wires with low losses*, presented at ASC '98, IEEE Trans. on Applied Superconductivity **9**-2, p. 2549 (1999).

[Syku00] J. K. Sykulski, R. L. Stoll, C. Beduz, A. J. Power, K. F. Goddard and M. K. Al-Mosawi: *The design, construction and operation of high temperature superconducting transformers – practical considerations*, CIGRÉ 2000, Paris, session paper 12-203.

[Tan01] T. T. Tan, S. Li, J. T. Oh, W. Gao, H. K. Liu and S. X Dou: *Crystallographic orientation mapping with an electron backscattered diffraction technique in $(Bi, Pb)_2Sr_2Ca_2Cu_3O_{10}$ superconducting tapes,* Superconductor Science and Technology **14**, p. 78 (2001).

[Tana99] T. Tanaka, M. Hara and J. Gerhold: *Electrical insulation in HTS power cables, fault-current limiters and transformers*, Electra **186**, p. 11, October (1999).

[Ušák01] P. Ušák, L. Janšák and M. Polák: *Hysteresis of V-I curve of BSCCO-2223 tape*, Physica C **350**, p. 139 (2001).

[Vacu01] website address: http:///www.vacuum.de.

[Vase00] P. Vase, R. Flükiger, M. Leghissa and B. Glowacki: *Current status of high-T_c wire*, Superconductor Science and Technology **13**, p. R71 (2000).

[Verw95] A. P. Verweij: *Electrodynamics of superconducting cables in accelerator magnets*, PhD thesis, University of Twente, Enschede, The Netherlands (1995).

[Wesc98] R. Wesche: *High-temperature superconductors*, Kluwer Academic Publishers, Boston/Dordrecht/London (1998).

[Wils83] M. N. Wilson: *Superconducting magnets*, Clarendon Press, Oxford, UK (1983).

[Wils99] M. N. Wilson: *Superconductivity and accelerators: the good companions*, presented at ASC '98, IEEE Trans. on Applied Superconductivity **9**-2, p. 111 (1999).

[Yang99] Y. Yang, E. Martinez and C. Beduz: *Numerical modelling of the critical state and calculation of AC losses and current profiles in multi-filamentary Bi-2223 tapes*, presented at EUCAS '99, Institute of Physics Conference Series **167**, p. 855 (1999).

[Yaza00] T. Yazawa, J. J. Rabbers, O. A. Shevchenko, B. ten Haken, H. H. J. ten Kate and H. Maeda: *Modelling the current distribution in HTS tapes with transport current and applied magnetic field,* presented at ASC '98, IEEE Trans. on Applied Superconductivity **9**-2, p. 797 (1999).

[Yaza98] T. Yazawa, J. J. Rabbers, B. ten Haken, H. H. J. ten Kate and Y. Yamada: *Numerical calculation of current density distributions in high temperature superconducting tapes with finite thickness in self field and external field,* Physica C **310**, p. 36 (1998).

[Yoko95] H. Yokoyama: *Thermal conductivity of polyimide film at cryogenic temperature*, Cryogenics **35**, p. 799 (1995).

Appendix A

A.1 Basics of type-II superconductivity

In this section the basic concepts of low-T_c superconductivity are briefly introduced. Above the so-called critical temperature a type-II superconductor usually has relatively high electrical resistivity compared to the pure metals. Below the critical temperature the resistivity vanishes abruptly and hence a certain current can flow through a superconductor at (almost) zero voltage. The external magnetic field is (partially) expelled from a superconductor due to the induced currents. In other words, a condition $\boldsymbol{B} \approx 0$ takes place.

A.2 Quantization of magnetic flux

Ginzburg-Landau and Abrikosov explained the phenomenology of type-II superconductivity, a summary of the theory is given in [Seeb98]. When a type II superconductor is exposed to a sufficiently high magnetic field, around each field line an Abrikosov vortex is formed. Equally one may say that magnetic flux in a superconductor is quantized and it exists as a number of distinct flux lines. Each flux line (or a fluxoid, or a vortex) carries one quantum of magnetic flux Φ_0. A fluxoid consists of normal conducting core and superconducting current around the core.

Two characteristic dimensions of a fluxoid are important: a coherence length ξ and a magnetic field penetration depth λ. The former and the later have the order of the core and of the superconducting current whirl radii respectively. For type-II superconductors the Ginzburg-Landau parameter reads: $k = \lambda/\xi > 1$. In absence of any fluctuations, fluxoids form a periodic triangular lattice. In magnetic field B the distance d between adjacent fluxoids is defined by the expression [Wils93]: $d^2 = \sqrt{\frac{4}{3}}\frac{\Phi_0}{B}$.

As the magnetic field B increases, so does the density of the flux lines: $\eta = \frac{B}{\Phi_0}$. At a certain value of magnetic field the fluxoids start to overlap (thermodynamic critical magnetic field). At the 2-nd (upper) critical magnetic field B_{c2} the cores of the fluxoids overlap and a normal conducting state is restored. When an external current flows through the vortex system, flux lines move. The driving Lorenz force is counteracted by the friction and by the pinning forces.

A.3 Outline of the theory

According to the microscopic quantum theory summarised in [Seeb98] and [Evet92], temperature-dependent coherence length:

$$\xi(T) = \sqrt{\frac{\Phi_0}{2 \cdot \pi \cdot B_{c2}(T)}} \qquad \text{and} \qquad \xi(T)/\xi(0) = \sqrt{B_{c2}(0)/B_{c2}(T)} \qquad \textit{Eq. A1.1}$$

with Φ_0 magnetic flux quantum. The Ginzburg-Landau parameter and the penetration depth are respectively:

$$k(T) = \lambda(T)/\xi(T) \quad \text{and} \quad \frac{\lambda(T)}{\lambda(0)} = \frac{k(T)}{k(0)} \cdot \frac{\xi(T)}{\xi(0)}. \qquad \textit{Eq.A1.2}$$

Note that the GL parameter is allowed here to be temperature-dependent [Gode99]). The thermodynamic and 2-nd critical fields $B_c(T)$ and $B_{c2}(T)$ are respectively:

$$B_c(T) \cdot \sqrt{2} = B_{c2}(T)/k(T) \quad \text{and} \quad \frac{B_c(T)}{B_c(0)} = \frac{B_{c2}(T)}{B_{c2}(0)} \cdot \frac{k(0)}{k(T)}. \qquad \textit{Eq. A1.3}$$

The Ginzburg-Landau depairing critical current density is expressed by:

$$J_d(T) = \frac{1}{\pi \cdot 3\sqrt{6}} \cdot \frac{B_c(T)}{\mu_0 \cdot \lambda(T)} \quad , \qquad \textit{Eq. A1.4}$$

with μ_0 permeability of vacuum.
Making use of Equations A1.2 - 1.4, one gets:

$$\frac{J_d(T)}{J_d(0)} = \left[\frac{B_{c2}(T)}{B_{c2}(0)}\right]^{3/2} \cdot \left[\frac{k(T)}{k(0)}\right]^{-2}. \qquad \textit{Eq. A1.5}$$

In addition, the theory states for a superconductor a reversible magnetization curve:

$$[B_c(T)]^2 = -8\pi \cdot \int_0^{B_{c2}(T)} M(B,T) \cdot dB \quad \text{and} \quad \frac{B_c(T)}{B_c(0)} = \left[\frac{\int_0^{B_{c2}(T)} I_c(B,T) \cdot dB}{\int_0^{B_{c2}(0)} I_c(B,0) \cdot dB}\right]^{1/2}, \qquad \textit{Eq. A1.6}$$

with *M(B,T)* magnetization that is directly proportional to the critical current. It is assumed here that the magnetization curve is obtained at the same electric field E_0 at which the critical current is defined as it is explained in the next section.

A.4 Empirical relations

Transport electro-magnetic properties of a superconductor are usually described by the voltage-current (*V-I*) characteristic. The *V-I* curve of a superconductor depends on many variables: temperature, magnetic field, strain, material properties, geometry, and frequency. A power law usually describes the direct *V-I* curve obtained in a transport measurement, Equation 2.4. At the fixed electrical field $E = E_c$ it is said that a critical current flows through the superconductor, though other definitions are also in use [Bosc91].

Both amplitude and direction of the magnetic field with respect to the transport current are important. In many practical cases (coils and cables) a wire carrying a transport current is exposed to the transverse magnetic field. Consider a long round wire that has a number of (round) superconducting filaments embedded in a normal metal matrix and that carries a direct transport current at a certain temperature. Both static uni-axial strain and a transversal

magnetic field are applied to the wire. In this case the dependence of the critical current on relevant parameters is well established for practical NbTi [Bott99] and Nb_3Sn wires. The critical current of a Nb_3Sn wire is described by the empirical relation [Gode99]:

$$I_c(B,T,\varepsilon) = \frac{C\beta_{T,\varepsilon}^{\nu}}{B \cdot K_{T,\varepsilon}^{\gamma}} \cdot S_\varepsilon^n \cdot f_b \quad , \qquad \textit{Eq. A1.7}$$

with B applied magnetic field, T temperature, ε strain, $I_c(B,T,\varepsilon)$ critical current. Here $T_{c\varepsilon} = T_{cm} \cdot S_\varepsilon^{1/w}$; $t = T/T_{c\varepsilon}$; $K_{T,\varepsilon} = 1 - 0.31 \cdot t^2 \cdot (1 - 1.77 \cdot \ln t)$; $\beta_{T,\varepsilon} = (1-t^2) \cdot K_{T,\varepsilon}$; $B_{c2} = B_{c2}(T,\varepsilon) = B_{c2m} \cdot S_\varepsilon \cdot \beta_{T,\varepsilon}$; $B_{c2m} = B_{c2}(T=0,\varepsilon=0)$; $b = B/B_{c2}$ and $f_b = b^p(1-b)^q$. The strain function S_ε and the material constants C, T_{cm}, B_{c2m}, ν, γ, w, n, p and q are further specified in [Gode99] and [Gode01a].

To establish a dependence of the critical current on temperature, consider the case of a low applied magnetic field $B = B_1$ set by the condition: $b \ll 1$ and a proper strain $\varepsilon = \varepsilon_1$ set by the condition $S_\varepsilon = const$. In this case Equation A1.7 can be simplified to:

$$\frac{I_{c,T}}{I_{c,0}} = \beta_{T,\varepsilon_1}^{\nu-p} \cdot K_{T,\varepsilon_1}^{-\gamma} \quad , \qquad \textit{Eq. A1.8}$$

with $I_{c,T} = I_c(B_1,T,\varepsilon_1)$ and $I_{c,0} = I_c(B_1,0,0) = C \cdot \frac{B_1^{p-1}}{B_{c2m}^{p}}$.

The empirical data analysed in [Gode99] show for all Nb_3Sn samples studied with a good accuracy the following empirical relations hold at any magnetic field and strain, Table A1.1:

$$\nu - p = 3/2 \text{ and } \gamma = 1. \qquad \textit{Eq. A1.9}$$

The values of other relevant constants are listed in Table A1.1. The values of p and q come from the transport measurement in high magnetic field ($0.3 << b < 0.9$) [Gode99].

Table A1.1 Power indices for Equation A1.7.

Material \ Index	γ	$\nu - p$	ν	p	q	χ	ς
Nb_3Sn	1	3/2	2	1/2	2	1	-3/2
Bi-2223	-1	3/2	2.2	0.7	2.9	7/3	-7/2

A.5 Link to theory

Though a critical surface for a practical Nb_3Sn wire is relatively well studied, the relation to the basic theory is less understood. Equation A1.5 is derived for a depairing current, while Equation A1.8 for a critical current. In the limit of low magnetic field and strain it is reasonable to assume that both currents have the same-scaled temperature dependence:

$$\frac{I_{c,T}}{I_{c,0}} = \frac{J_d(T)}{J_d(0)} . \qquad \textit{Eq. A1.10}$$

Comparing Equations A1.5 with A1.8 and bearing in mind Equations A1.9 and A1.10, one may write:

$$\frac{I_{c,T}}{I_{c,0}} = K_{T,\varepsilon_1}^{-1}\left[\frac{B_{c2}(T)}{B_{c2}(0)}\right]^{v-p} \quad \text{and} \qquad \textit{Eq. A1.11}$$

$$\frac{B_{c2}(T)}{B_{c2}(0)} = (1-t_{\varepsilon_1}^2)\cdot K_{T,\varepsilon_1}^{\chi}, \qquad \textit{Eq. A1.12}$$

where $\chi = 1+\frac{1-\gamma}{v-p} = 1+\frac{2}{3}(1-\gamma)$ and

$$\frac{k(T)}{k(0)} = K_{T,\varepsilon_1}^{\frac{1}{2}}. \qquad \textit{Eq. A1.13}$$

In addition, from Equation A1.3 it follows:

$$\frac{B_c(T)}{B_c(0)} = (1-t_{\varepsilon_1}^2)\cdot K_{T,\varepsilon_1}^{\chi-\frac{1}{2}}. \qquad \textit{Eq. A1.14}$$

For Nb_3Sn according to Equation A1.9 $\gamma = 1$, therefore $\chi = 1$. The value of γ is material-dependent and for $Bi-2223$ tapes a different value: $\gamma = -1$ is found as it is explained in Chapter 2. The value of $v-p = 3/2$ is material independent (holds as long as Equation A1.10 is valid). In theory the GL parameter is assumed to be temperature independent. In practice slight temperature dependence is allowed to obtain a better fit to the experimental data, Equation A1.7. Both the fitting factor, which for Nb_3Sn is:

$$K_{T,\varepsilon_1} = 1-0.31\cdot t_{\varepsilon_1}{}^2\cdot(1-1.77\cdot \ln t_{\varepsilon_1}) \qquad \textit{Eq. A1.15}$$

and the power index γ are therefore empirical. To keep the consistency of the approach, one may assume that Equation A1.15 holds for other superconductors as well. In this case from Equations A1.8, A1.11 and A1.12 it follows:

$$I_{c,0} = C\cdot\frac{B_1^{p-1}}{B_{c2m}^{p}} = I_{c,T}\cdot K_{T,\varepsilon_1}^{\varsigma}\cdot(1-t_{\varepsilon_1}^2)^{p-v}, \qquad \textit{Eq. A1.16}$$

where $\varsigma = (p-v)\cdot\chi$. With the power indices known, see Table A1.1 and the $I_{c,T}$ measured, one may find the (material dependent) constant $I_{c,0}$.

A.6 Verification of the method

Consider a practical example using the data for Nb_3Sn superconductor in order to verify the assumptions of this Appendix. In this case Equation A1.7 is the source of experimental data, in particular of the data for sample A placed on Ti-holder [Gode99]. Therefore, at applied axial strain equal to zero, the remaining strain (caused by the mismatch in thermal contraction) is 0.12 % in the case. In general, the remaining strain depends on temperature. However, for Nb_3Sn the condition $S_\varepsilon = const$ is accurate over the temperature range studied (4 - 10 K). The critical temperature and the upper magnetic field of the material are 17.8 K and 33.3 T respectively. For the material K_{T,ε_1} is set by Equation A1.15.

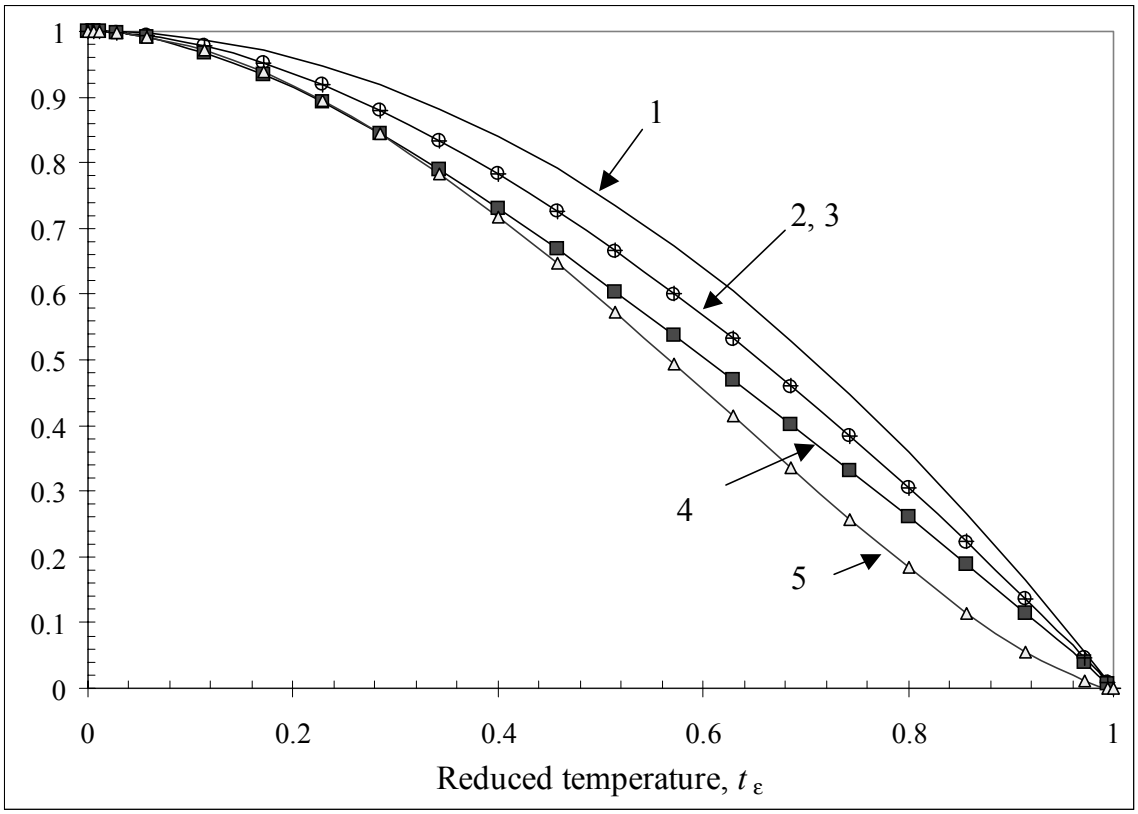

Figure A1.1 Calculated temperature dependence of scaled critical current and the fields for Nb_3Sn.

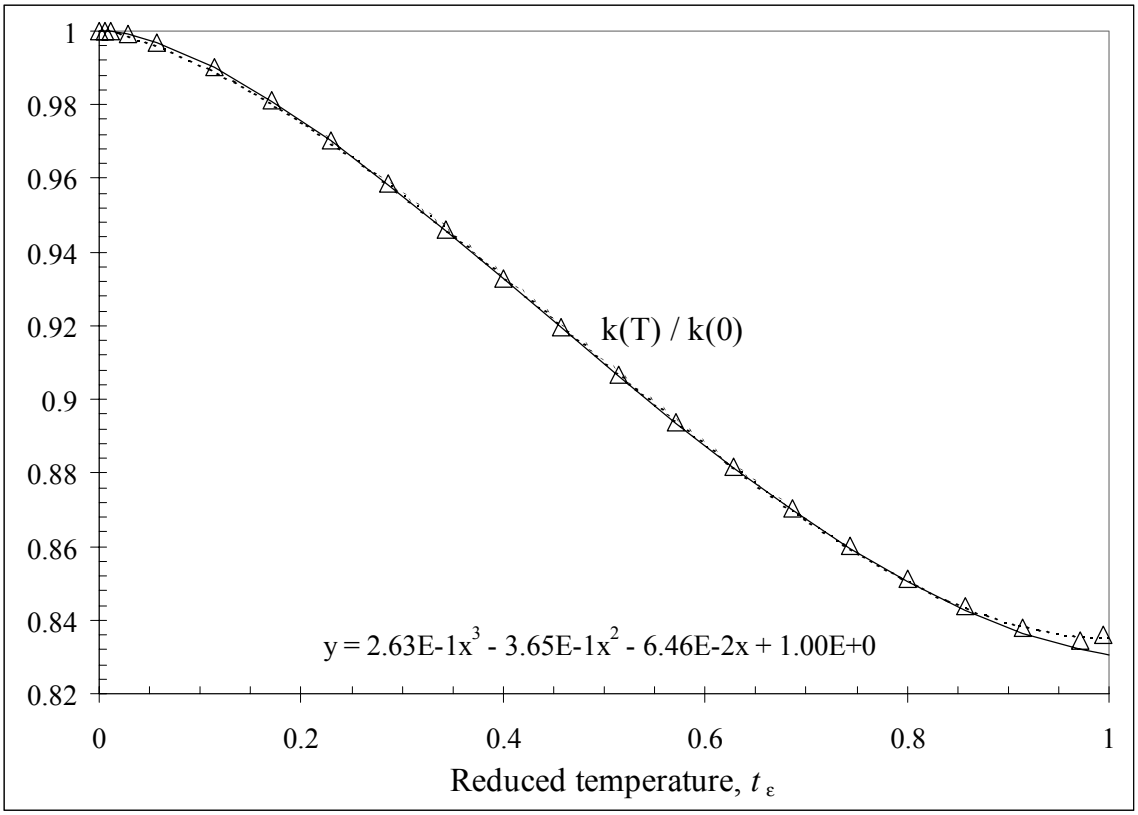

Figure A1.2 Calculated temperature dependence of the Ginzburg-Landau parameter for Nb_3Sn.

The power indices are defined in Table A1.1 [Gode99]. Therefore Equations A1.11 to A1.14 can be verified.

A.6.1 Critical current and the fields

The dependence of several scaled parameters on (scaled) temperature t_{ε_1} is presented in Figure A1.1. Line 1 is simply the equation: $(1-t_{\varepsilon_1}{}^2)$ shown here as the reference. Lines 2 and 3 represent the thermodynamic critical field calculated from Equations A1.14 and A1.6 respectively. Here Equation A1.6 uses the critical current defined by Equation A1.7 at $\varepsilon = \varepsilon_1$. The integration over the magnetic field is performed for each value of the temperature. Equation A1.14 uses the assumption expressed by Equation A1.10. It is seen that agreement between the lines 2 and 3 calculated with different methods is very good. This validates the Equation A1.10 as well as the applicability of the theory - Equation A1.6 in particular, to Nb_3Sn. Lines 4 and 5 represent the upper critical field and the critical current calculated from Equations A1.12 and A1.11 respectively.

The temperature dependence of the Ginzburg-Landau parameter is shown in Figure A1.2. The solid line is calculated using Equations A1.13 and A1.15. To calculate the line indicated by the triangles Equations A1.3, A1.6 and A1.7 are engaged. The dashed line is a polynomial fit to the latter; the equation is shown in the Figure. Indeed, over the whole temperature range the GL-parameter changes only slightly (±8% around the average value of 0.92). This is in fair agreement with the theory that assumes a constant. Therefore, Equation A1.10 is verified.

A.6.2 The coherence length and the penetration depth

From Equations A1.1 and A1.12 one obtains for the coherence length:

$$\xi(T)/\xi(0) = (1-t_{\varepsilon_1}{}^2)^{-1/2} \cdot K_{T,\varepsilon_1}^{-\chi/2} . \qquad \textit{Eq. A1.17}$$

For the penetration depth it follows from Equations A1.1, A1.13 and A1.17 and Table A1.1:

$$\lambda(T)/\lambda(0) = K_{T,\varepsilon_1}^{\frac{1-\chi}{2}} (1-t_\varepsilon^2)^{-1/2} = (1-t_\varepsilon^2)^{-1/2} . \qquad \textit{Eq. A1.18}$$

The relevant temperature dependencies of scaled parameters are displayed in Figure A1.3.

Line 1 for the coherence length is calculated from Equation A1.17. Line 2 for the London penetration depth is calculated from Equation A1.18. The reduced penetration depth is indeed in a qualitative agreement with that calculated from BCS - theory in the dirty limit [Seeb98]. It is also in perfect quantitative agreement (same formula) with both the experiment for Y-123 magnetometers and striplines [Hilg95], nanobridges and the two-fluid model [Pedy96]. For NbTi in fact the same temperature dependency is used, as it is assumed that the GL-parameter is temperature independent for this material [Cool96]. Therefore, the analysis shows the consistency of the theory, the empirical approach and Equations A1.18 and A1.10 in particular for Nb_3Sn.

A.7 Example of application to Bi-2223 tapes

A.7.1 Experiment

In general, the applicability of the theory to Bi-2223 tapes remains unclear and an empirical approach is in use [Kane99], [Vase00]. In Table 2.2 the specifications are listed of several modern multifilamentary tapes manufactured in large quantities. It is generally accepted that the critical temperature of Bi-2223 superconductor is about 110 Kelvin. Measurements of the critical current versus temperature (with self-field present and zero applied magnetic field and

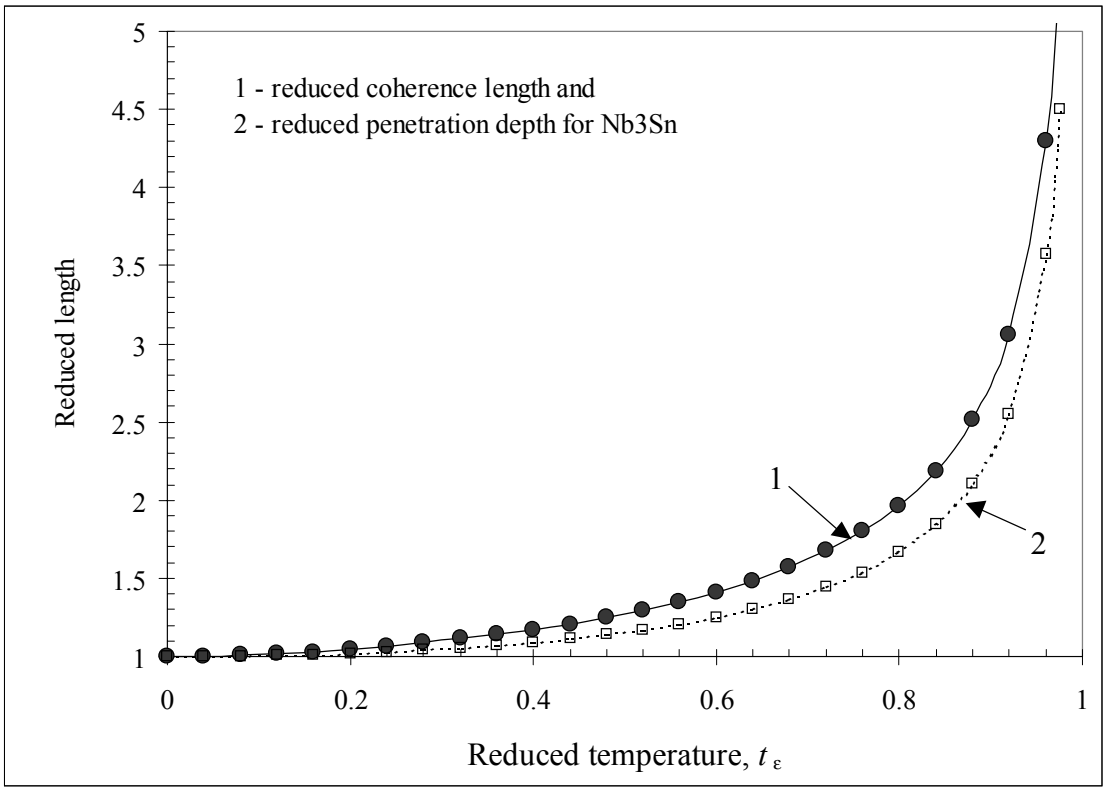

Figure A1.3 Temperature dependence of the coherence length and penetration depth for Nb_3Sn.

strain) are performed in [Amer01], [Vacu01] and [Kane99]. The example dependence is shown in Figure A1.4 for the same samples as listed in the Table. The data for samples A1 and A2 are shown as boxes using the right vertical axis; for samples V1 and V2 – as triangles and for sample Sm1 – as circles using the left vertical axis. The markers in all figures in this section are kept the same. At lower temperature the critical current is higher and so is the influence of the self-field. In presence of the self-field the critical current is reduced, the influence is higher at higher currents. The effect is treated in more detail in Chapter 3. The material of a sample holder is not reported, for this reason the influence of the remaining strain cannot be evaluated. If there is any, it is present as an error.

The method as described in sections A4 to A6 is applied to Bi-2223 tapes using the experimental data from Figure A1.4. The power indices are listed in Table A1.1. The values of p and q are obtained from the measurements in presence of high external magnetic field as it is explained in Chapter 2. With the values of p known and $\nu - p$ fixed, the value of ν is found. The only unknown empirical constant in the analysis is γ. For all tapes studied the value $\gamma = -1$ is found. Using Equation A1.16 the critical current at zero Kelvin is calculated, the values are given in Figure A1.4. To keep the value of the current constant for each sample, a slight deviation from Equation A1.15 is allowed as it is shown in Figure A1.5.

A.7.2 Ginzburg-Landau parameter

The temperature dependence of the reduced parameter for all samples is shown in Figure A1.5. The GL-parameter calculated using Equations A1.13 and A1.15 is shown as solid line. As the critical temperature for all tapes is practically the same, the scaling of the temperature is omitted for the sake of clarity. The figure shows that for each sample it is possible to simultaneously keep constant the critical current at zero Kelvin with reasonable deviation of the experimental data from Equation A1.15. For expediency, the ±3 % error bars are also shown in the figure.

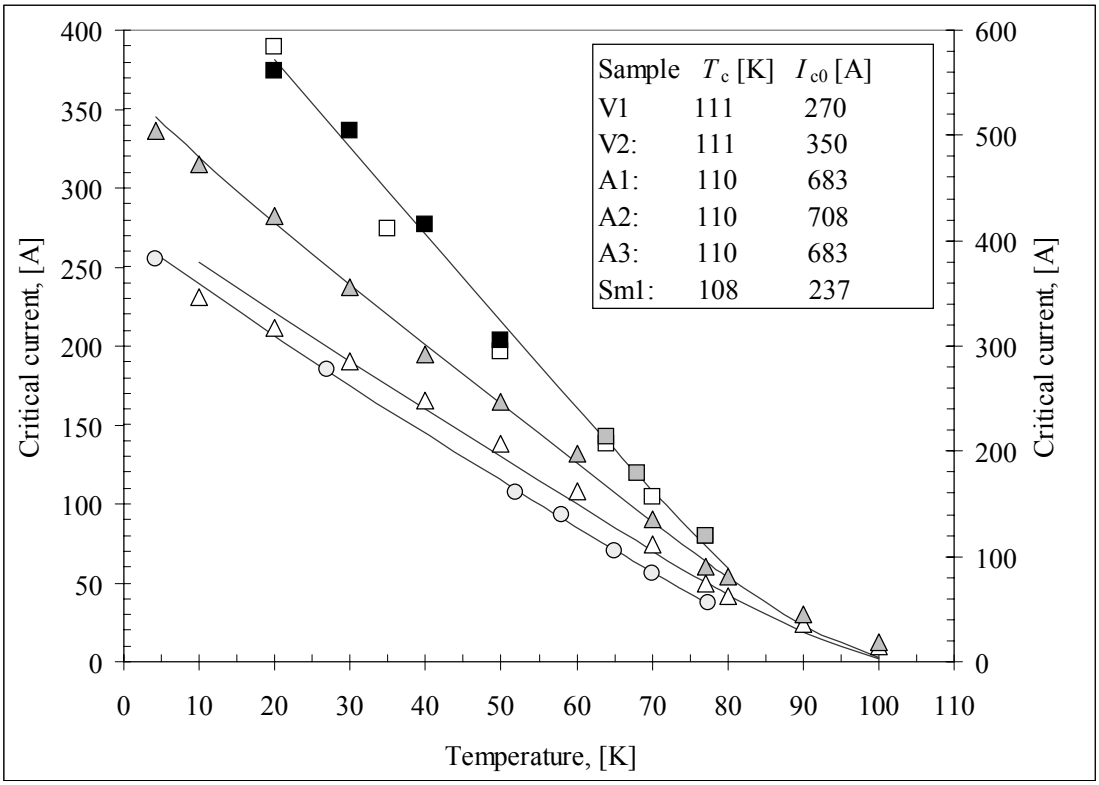

Figure A.1.4 Temperature dependence of the critical current for Bi-2223/Ag tapes.

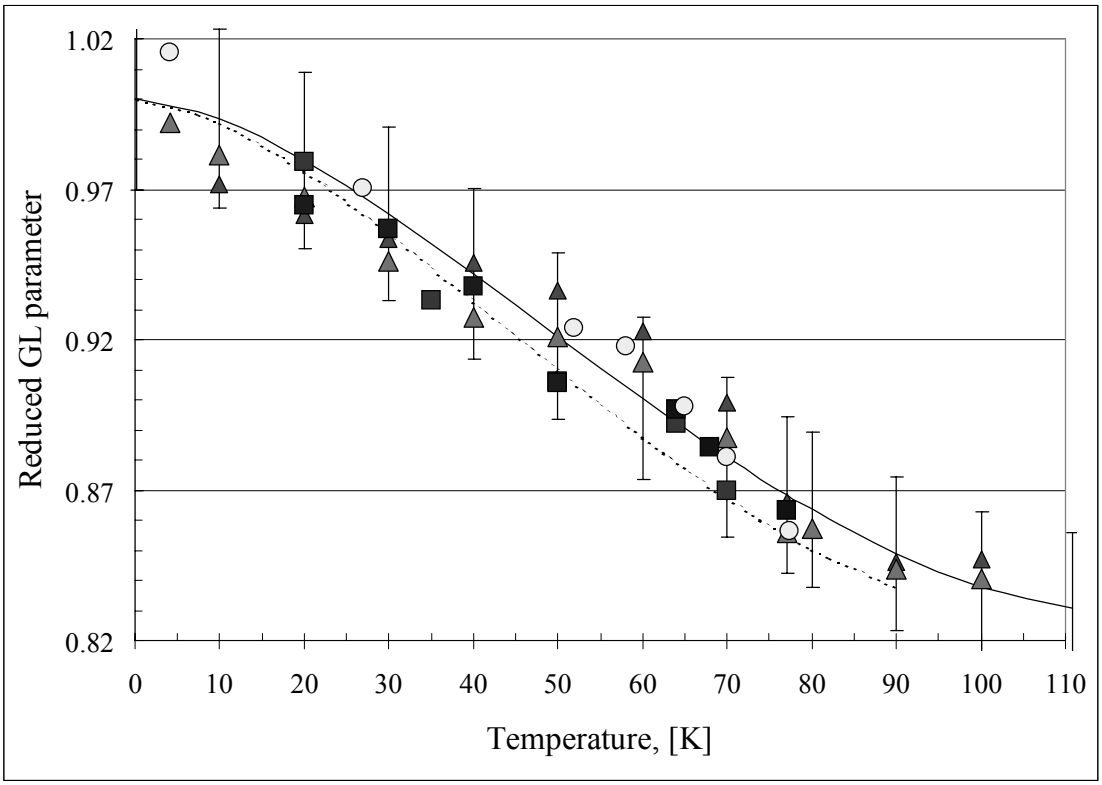

Figure A1.5 Temperature dependence of the Ginzburg-Landau parameter for Bi-2223 tapes, ± 3 % error bars are shown.

A.7.3 The upper critical magnetic field

Temperature dependence of the scaled magnetic field calculated from Equation A1.12 is shown in Figure A1.6. The solid line is calculated using Equation A1.15, the data point use actual values of the GL-parameter as shown in Figure A1.5. It is seen that the properties of all Bi-2223 tapes allow scaling with a reasonable error (±10 % error bars are shown in the Figure). Note that both the self-field and the remaining strain contribute to the error. The concave shape of the curve is due to the different value of $\gamma = -1$, Table A1.1.

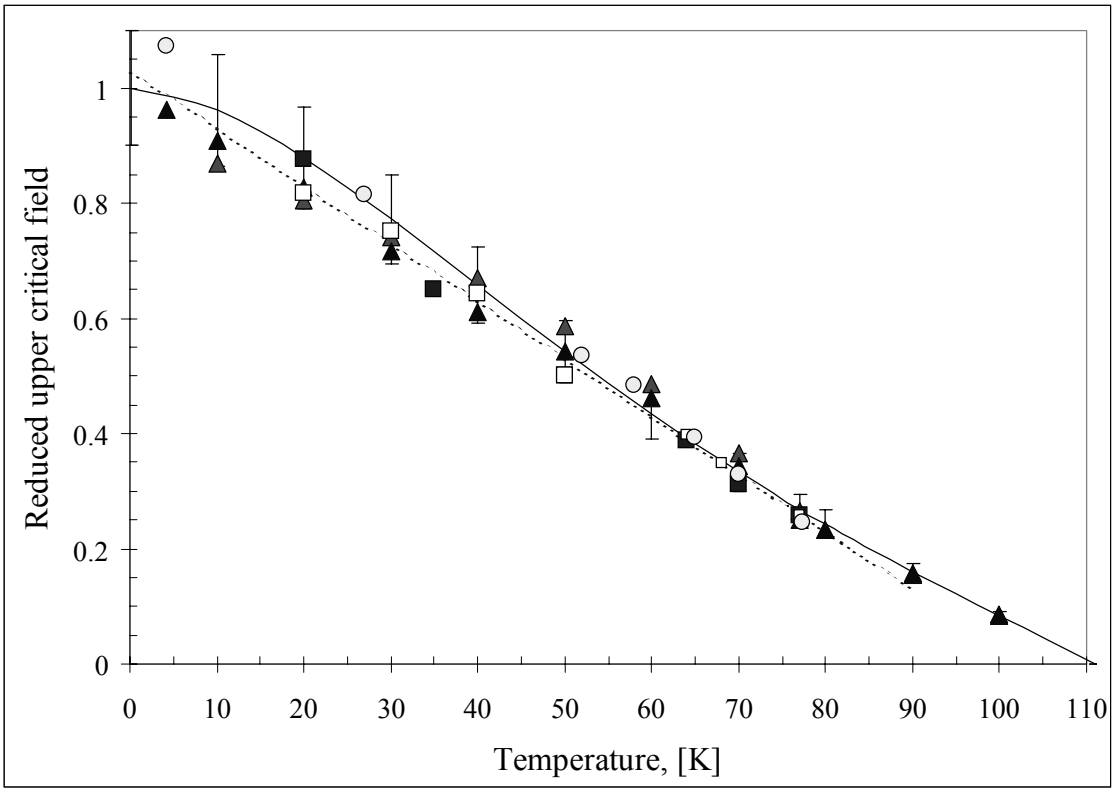

Figure A1.6 Temperature dependence of the upper critical magnetic field for Bi-2223/Ag tapes.

A.7.4 The critical current

Figure A1.7 illustrates temperature dependence of the scaled critical current derived from Equation A1.11. The solid line is calculated using Equation A1.15, the actual values of the GL-parameter and of the upper critical filed as shown in Figures A1.5 and A1.6 respectively are used for the data. Again, the scaling of the critical current for different tapes is allowed with a reasonable error (±10 % error bars are shown in the Figure).

A.7.5 Discussion

Equations A1.10 to A1.15 permit a scaling of relevant temperature-dependent properties for Bi-2223 tapes from different manufacturers with reasonable accuracy. This means the method developed for Nb_3Sn in principle can be extended to Bi-2223 tapes. So far the method uses the experimental data obtained under conditions when both the magnetic field of the transport current through a tape and the remaining strain affect the critical current not in a controlled way (the self –field is not suppressed, exact details of interface between a sample and a holder, material of the holder are not reported) see Figure A1.4. Using the method described in this chapter, more accurate values of the involved parameters can be obtained once the critical current of a tape will be measured as function of temperature and remaining strain with the self-field effect suppressed.

For applications the temperature range from 4 to 80 K is most important, Figure A1.4. Within this range the curvature of the line in Figure A1.6 is less pronounced and the relation between the variables is almost linear. For this reason the solid line in Figure A1.6 (Equation A1.12) is replaced by the straight piece shown as the dashed line in the figure. To allow even better fit to the experimental data, the critical temperature is made a free parameter as it is shown in the Figure A1.5. Example fits are shown as dashed lines in Figures A1.5 –A1.7. Resulting fit to the source experimental data is shown in Figure A1.4. It is seen that the obtained fits to the experiment data in the temperature range from 4 to 80 K are linear in agreement with [Kane99].

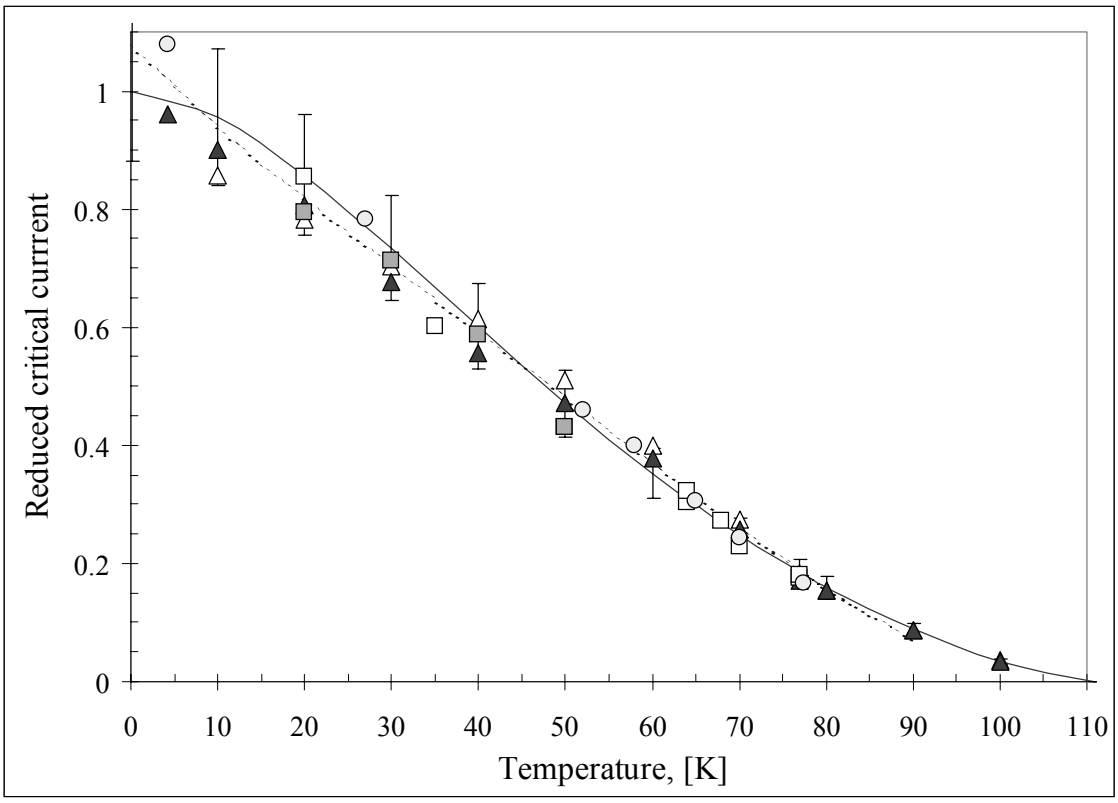

Figure A1.7 Temperature dependence of the critical current for Bi-2223 tapes.

A.8 Conclusions

The scaling method previously developed for Nb_3Sn is extended to describe the temperature dependence of the critical current for Bi-2223 tapes. At present, the experimental data for Bi-2223 tapes are affected by the magnetic field of the transport current through a tape and possibly by the remaining strain. Nevertheless, a scaling relation of the critical current in absence of external magnetic field and strain is established for Bi-2223 tapes. The relation describes the temperature dependence of the critical current, upper magnetic field and Ginzburg-Landau parameter with reasonable accuracy. Even a better accuracy is obtained within the temperature range 4-80 K.

Appendix B

B.1 Mutual and self-inductance

Mutual and self-inductances of cells with final dimensions, such as displayed in Figure 3.3 can be defined in a way that shows explicitly required mathematical operations:

$$M_{ik} = \frac{1}{i_i i_k} \int_{i_i} di' \int_{i_k} \overline{M} di'' , \qquad \textit{Eq. B3.1}$$

$$L = M_{kk} = \frac{1}{i_k^2} \int_{i_k} di' \int_{i_k} \overline{M} di'' . \qquad \textit{Eq. B3.2}$$

Here the Neumann formula [Grov46] is used for the mutual inductance $\overline{M}$ of two parallel line cells with currents di' and di'' that are assumed to be in phase with each other:

$$\overline{M} = \frac{\mu}{4\pi} \oint_{z'} \oint_{z''} \frac{dz' dz''}{\eta_1} , \qquad \textit{Eq. B3.3}$$

where dz' and dz'' are length elements of the two lines z' and z'', η_1 is the distance between the elements and the integration is to be taken over the contours of the two circuit elements. The lines z' and z'' belong to the same cell (k) or to two different cells (i, k) when calculating L or M respectively.

B.2 Inductances of long and straight cells with finite dimensions

For two long, straight and parallel cells of equal length ℓ_v and of arbitrary cross-section constant along the length, placed next to each other and spaced by the distance η from each other, see Figure 3.3: $\eta_1^2 = (z'' - z')^2 + \eta^2$, the integration of Equation B3.1 returns the exact formula for a mutual inductance (per unit length, at low frequency and $i \neq k$) of two such cells:

$$M = \frac{\mu}{2\pi} \left[\ln\left(\frac{\ell_v}{g_{ik}} + \sqrt{\frac{\ell_v^2}{g_{ik}^2} + 1} \right) - \sqrt{1 + \frac{g_{ik}^2}{\ell_v^2}} + \frac{g_{ik}}{\ell_v} \right] . \qquad \textit{Eq. B3.4}$$

Here g_{ik} is the (mutual) geometrical mean distance of the cell's cross-section areas from each other [Grov46] and μ is the constant magnetic permeability inside and outside the cells. Accurate formulas for calculating mutual and self-inductances as a rule use mean geometric, arithmetic and quadratic distances. When to assume $\left(\frac{g_{ik}}{\ell_v};\frac{g_{ik}^2}{\ell_v^2}\right)<<1$ in Equation B3.4, a simple though less accurate equation can be obtained:

$$M_{ik}=\frac{\mu}{2\pi}\left(\ln\frac{2\ell_v}{g_{ik}}-1\right). \qquad \textit{Eq. B3.5}$$

Similar considerations lead to the following formula for self-inductance (per unit length, at low-frequency and $i=k$) of a long and straight cell of finite length ℓ_v and arbitrary cross-section constant along the cell length [Grov46]:

$$L=M_{kk}=\frac{\mu}{2\pi}\left(\ln\frac{2\ell_v}{g_k}-1\right), \qquad \textit{Eq. B3.6}$$

where g_k is a geometric mean distance of the cell cross-section area from itself. For a cell with a round cross-section of radius r_w: $g_k=r_w\cdot e^{-1/4}$ (for a line cell with point cross-section $r_w\to 0$). For a cell with finite rectangular cross-section $\Delta x\times\Delta y$, see Figure 3.2 $g_k=k_s\cdot(\Delta x+\Delta y)$, where for the range $1<\Delta x/\Delta y<40$ k_s changes only slightly: $0.22333<k_s<0.22369$ and hence the average over the range value $k_s=0.2236$ can be used in most of the cases.

B.3 Mean geometric distances

The mutual mean geometric distance g_{ik} of two cross-section areas s_i and s_k by definition is:

$$\ln g_{ik}=\frac{1}{s_i s_k}\int_{s_i}\int_{s_k}\ln\eta_1 ds_i ds_k, \qquad \textit{Eq. B3.7}$$

where η is distance between elements ds_i and ds_i of the areas s_i and s_k respectively [Grov46]. The mean geometric distance g_k of cross-section area s_k from itself by definition is:

$$\ln g_k=\frac{1}{s_k^2}\int_{s_k}\int_{s_k}\ln\eta_1 ds_k' ds_k'', \qquad \textit{Eq. B3.8}$$

where η_1 is distance between elements ds_k' and ds_k'' of the area s_k respectively [Grov46]. For two line cells g_{ik} is simply the distance between the cells: $g_{ik}=r=|r_i-r_k|$.

For two cells the cross-sections of which are rectangles of equal size ($\Delta x\times\Delta y$ and $\Delta x>\Delta y$) with corresponding sides parallel to each other and the distance between centres of the rectangles $\eta_1=|r_i-r_k|>\Delta x$, see Figure 3.2:

$$\ln\frac{g_{ik}}{\eta_1}=\frac{1}{12}(\beta^2-v^2)(1-2\cos^2\xi)-\frac{1}{60}(\beta^4+v^4-\frac{5}{2}\beta^2v^2)(1-8\cos^2\xi+8\cos^4\xi)+\ldots, \qquad \textit{Eq. B3.9}$$

where $\beta = \Delta x/\eta_1$, $v = \Delta y/\eta_1$, and ξ is the angle between the vector $\boldsymbol{r_{ik}} = \boldsymbol{r_i} - \boldsymbol{r_k}$ and the positive direction of *x*-axis. For two cells the cross-sections of which are rectangles of equal size ($\Delta x \times \Delta y$) with corresponding sides parallel to each other and situated in the same column, that is for $\eta = |r_i - r_k| < \Delta x$ see Figure 3.2:

$$\ln\frac{g_{ik}}{k_s} = \frac{1}{2}\left(\frac{\eta_1}{\Delta y}+1\right)^2 \ln(\eta_1 + \Delta x + \Delta y) + \frac{1}{2}\left(\frac{\eta_1}{\Delta y}-1\right)^2 \ln(\eta_1 + \Delta x - \Delta y) - \left(\frac{\eta_1}{\Delta y}\right)^2 \ln(\eta_1 + \Delta x). \quad \textit{Eq. B3.10}$$

Here $k_s = 0.2236$ (see previous section). When the cells are in the same row, the corresponding equation is obtained from Equation B3.10 by replacing Δx with Δy and vice versa.

Obviously, Equation 3.13 cannot be used for calculating the diagonal terms of the matrix $\overline{\mathbf{M}}_{\mathbf{G}}$ as it diverges and instead it was suggested [Rabb01], pp. 37 to use the following formula for square cells $\Delta x \approx \Delta y$; $r_i = r_j$ and $r_0 = 1$ m:

$$\overline{M}_{G,kk} = \frac{\mu_0}{4\pi}\ln\left[\frac{(r_i - r_j)^2 + 1.5\cdot 10^{-2}\Delta y^2}{r_0}\right]. \quad \textit{Eq. B3.11}$$

Comparing Equations B3.6 and B3.11 one may conclude that Equation B3.11 is a source of error in the numerical model and Equations B3.6 and B3.8 should be used instead.

B.4 Magnetic field constants of rectangular cells

Magnetic field constants of *m* - 1 straight and long rectangular "source" cells (each with the finite dimensions $\Delta x \times \Delta y$, see Figure 3.2; the remaining "field" cell is the one in which magnetic field is obtained) are calculated using superposition of magnetic fields and formulas from [Seeb98], p. 494, while the formulas for cells of arbitrary cross-section are given in [Wils83], ch. 3:

$$X_{ik}^{\Diamond} = \frac{\mu}{2\pi}\cdot\left\{\begin{array}{l} \dfrac{x+\Delta x/2}{2}\ln\dfrac{(x+\Delta x/2)^2+(y-\Delta y/2)^2}{(x+\Delta x/2)^2+(y+\Delta y/2)^2} + \\ \dfrac{x-\Delta x/2}{2}\ln\dfrac{(x-\Delta x/2)^2+(y+\Delta y/2)^2}{(x-\Delta x/2)^2+(y-\Delta y/2)^2} + \\ (y+\Delta y/2)\cdot\left[\operatorname{atan}\left(\dfrac{y+\Delta y/2}{x+\Delta x/2}\right) - \operatorname{atan}\left(\dfrac{y+\Delta y/2}{x-\Delta x/2}\right)\right] + \\ (y-\Delta y/2)\cdot\left[\operatorname{atan}\left(\dfrac{y-\Delta y/2}{x-\Delta x/2}\right) - \operatorname{atan}\left(\dfrac{y-\Delta y/2}{x+\Delta x/2}\right)\right] \end{array}\right\} \text{ and } \quad \textit{Eq. B3.12}$$

$$Y_{ik}^{\Diamond} = \frac{\mu}{2\pi} \cdot \left\{ \begin{array}{l} \dfrac{y+\Delta y/2}{2} \ln \dfrac{(x+\Delta x/2)^2 + (y+\Delta y/2)^2}{(x-\Delta x/2)^2 + (y+\Delta y/2)^2} + \\ \dfrac{y-\Delta y/2}{2} \ln \dfrac{(x-\Delta x/2)^2 + (y-\Delta y/2)^2}{(x+\Delta x/2)^2 + (y-\Delta y/2)^2} + \\ (x+\Delta x/2) \cdot \left[\operatorname{atan}\left(\dfrac{x+\Delta x/2}{y-\Delta y/2} \right) - \operatorname{atan}\left(\dfrac{x+\Delta x/2}{y+\Delta y/2} \right) \right] + \\ (x-\Delta x/2) \cdot \left[\operatorname{atan}\left(\dfrac{x-\Delta x/2}{y+\Delta y/2} \right) - \operatorname{atan}\left(\dfrac{x-\Delta x/2}{y-\Delta y/2} \right) \right] \end{array} \right\}, \qquad \textit{Eq. B3.13}$$

where $x \pm \Delta x/2 = x_i - x_k \pm \Delta x$; $y \pm \Delta y/2 = y_i - y_k \pm \Delta y$ and $i \neq k$.

Summary

In this study, the electro-magnetic properties of high-T_c tapes and coils are investigated. The focus is on Bi-2223/Ag tapes with non-twisted superconducting filaments as these are the only high-T_c superconductors at present available in sufficient length for practical applications. The study is confined to high-temperature superconductors and power coils operated in liquid nitrogen and intended for large-scale applications.

The aim of the study is three-fold: to explore the options and the potential of increasing the critical currents and reducing the alternating current losses of practical superconductors in power coils hence aiming at improved performance; to build a model that is sufficient to describe behaviour and to calculate voltage-current characteristics of advanced Bi-2223 superconductors and coils carrying alternating current and exposed to alternating magnetic field; the application target is to develop fundamentals of high-T_c superconducting power coils and as an example to make and to study a prototype 1-MVA resonator coil both experimentally and numerically and hence to demonstrate the feasibility and predictable behaviour of high-T_c superconducting power devices. The final objective is, using the knowledge and the experience gained in the study, to evaluate the viability of a power transformer with high-T_c superconducting coils.

An overview of practical high-T_c superconductors such as Bi-2223/Ag tapes is given. The accent is on the direct voltage-current characteristics of superconductors carrying transport current and exposed to a uniform transversal magnetic field. The influence of magnetic field direction and magnitude on the critical current is analysed. The scaling relation between the critical current, magnetic field and temperature is derived for Bi-2223/Ag tapes. A compact way to accurately describe direct voltage-current characteristics of the superconductors is found and used to create input data files for the numerical model. An advanced method of electrical insulation of Bi-2223/Ag tapes is presented together with the test results gathered for insulated tapes.

The basics of an electro-magnetic numerical model for calculating voltage-current curves of high-T_c superconductors and coils carrying alternating current and exposed to alternating magnetic field are laid down. Existing formulations of the classical eddy current problem are compared and a new *E-J* formulation leading to a more elegant and precise procedure of solving the governing equations is derived. It is shown that in the two-dimensional case under the same assumptions, a simple numerical network model (employing Kirchhoff's instead of Maxwell's equations) can be used with equally good result. Using the network model the total, magnetisation and transport currents and the losses are calculated and the corresponding loss electric fields are derived hence resulting in the voltage-current curves. The model is verified with the experimental data available for relevant Bi-2223 tapes. Using the network model an error (due to so-called self-field effect on the critical current) is eliminated from the measured direct voltage-current curves.

The essentials of superconducting power coils are presented using a 1-MVA-resonator coil operated in liquid nitrogen as an example. Arrangement, techniques and manufacturing of the prototype coil (with a considerable effort from Dutch industry) are portrayed. Optimisation of the coil design has led to a circular coil that consists of four long and thin concentric solenoids with a large diameter. The radial component of the magnetic field (to which Bi-2223 tapes are most sensitive) is suppressed by small iron pieces applied around the coil edges. The effect is studied both analytically and numerically; the results contributed to the coil design and are validated experimentally. For several magnetic configurations of the coil the direct and alternating voltage-current curves are calculated numerically and measured. Finally numerical estimates, their experimental verification and the results for the 1-MVA coil operated at 77 and 65 K are presented and discussed.

Conventional and high-T_c superconducting power transformers are compared and the viability of a superconducting transformer is dealt with from the economical and technical points of view. For a power transformer, the technical and economical parameters are linked tightly due to the fact that copper transformers have been produced for almost a century and have reached physical and technological limits in many aspects. The crucial question for future applications: “at which cost-effective conditions can the overall efficiency of a high-T_c transformer be made higher than that of the conventional one?” is discussed and answered in the chapter. Total, energy and capital costs of a model superconducting and a copper transformer rated at 30-MVA are compared. The energy costs of a high-T_c transformer are lower than those of a conventional transformer. The other costs are driven mostly by the superconductor specific cost (usually expressed in US $/kA/m). For a 30-MVA high-T_c transformer competitive total and capital costs are expected to be at 50 and 25 US $/kA/m respectively. With the present price approaching the 50 US $/kA/m benchmark, the chances to apply high-T_c superconductors in power transformers and coils are improving.

Samenvatting (Summary in Dutch)

Het onderzoek beschreven in dit proefschrift betreft de elektromagnetische eigenschappen van supergeleidende tapes en spoelen met een hoge kritieke temperatuur T_c. Met name gaat het om tapegeleiders van het materiaal $Bi_2Sr_2Ca_2Cu_2O_x$/Ag (Bi-2223/Ag) met niet-getwiste supergeleidende filamenten. Dit is de enige hoge T_c supergeleider die op dit moment beschikbaar is in voldoende lengte voor praktische toepassingen. Het onderzoek is beperkt tot supergeleiders en vermogensspoelen die werken bij 77 K in vloeibaar stikstof en bedoeld zijn voor grootschalige toepassingen.

Het onderzoek kent drie doelen. Het eerste punt van aandacht is het onderzoeken van de opties en de mogelijkheden voor het opvoeren van de kritieke stroom en het reduceren van wisselstroomverliezen in praktische supergeleiders voor vermogensspoelen en het daarmee verbeteren van de prestaties ervan. Het tweede deel betreft het opzetten van een theoretisch model die een goede beschrijving geeft van het gedrag van hoge T_c supergeleiders en een voldoende nauwkeurige spanning-stroom karakteristiek kan berekenen voor de geavanceerde supergeleiders op basis van Bi-2223, geleiders die geïmplementeerd zijn in wisselstroomspoelen en die bloot staan aan wisselende magnetische velden. Het derde onderdeel betreft de toepassing: het leggen van het fundament voor hoge T_c supergeleidende vermogensspoelen.

Het onderhavige demonstratieproject betreft het bouwen en bestuderen, zowel experimenteel als numeriek, van een prototype van een resonatorspoel voor 1 MVA en 50 Hz. Aan de hand van dit instrument is de haalbaarheid en de voorspelbaarheid van het gedrag van hoge T_c supergeleidende vermogensapparaten bestudeerd en aangetoond. Met de kennis en ervaring die in de studie zijn opgedaan, is, als uiteindelijk doelstelling, de levensvatbaarheid van een vermogenstransformator met hoge T_c supergeleidende spoelen geëvalueerd.

Er is een overzicht opgesteld van praktische hoge T_c supergeleiders zoals tapes op basis van Bi-2223 /Ag. De nadruk ligt daarbij op de karakteristieken voor wisselspanning en –stroom voor supergeleiders die stroom transporteren en blootgesteld worden aan een uniform transversaal magnetische veld. Een analyse is uitgevoerd van de invloed van de grootte en richting van het magnetisch veld op de kritieke stroom. De schaalrelatie tussen kritieke stroom, magnetisch veld en temperatuur is afgeleid voor tapes van Bi-2223/Ag. Verder is een compacte manier gevonden om de karakteristieken van gelijkspanning en stroom voor de supergeleiders nauwkeurig te beschrijven. Daarmee zijn de invoer gegevensbestanden opgezet voor het numerieke model. Een geavanceerde methode om tapes van Bi-2223/Ag elektrisch te isoleren is gepresenteerd tezamen met de testresultaten die voor geïsoleerde tapes zijn verkregen.

De grondbeginselen zijn opgesteld voor het numeriek en elektromagnetisch model om de spanning-stroom krommen te berekenen voor hoge T_c supergeleiders en supergeleidende spoelen die wisselstroom voeren en bloot gesteld zijn aan wisselende magnetische velden. Bestaande formuleringen voor het klassieke probleem van wervelstromen zijn met elkaar vergeleken en een nieuwe *EJ*-formulering is afgeleid die leidt tot een elegantere en

nauwkeuriger procedure om de basisvergelijkingen op te lossen. Aangetoond wordt dat voor het tweedimensionale geval onder dezelfde aannamen een eenvoudig numeriek netwerkmodel, waarin de wetten van Kirchhoff worden gebruikt in plaats van die van Maxwell, is te gebruiken waarvan de resultaten net zo goed zijn. Met het netwerkmodel zijn de totale stroom, de magnetisatiestroom en de transportstroom berekend als ook de verliezen. Eveneens zijn de elektrische velden afgeleid die behoren bij de verliezen en daarmee ook de spanning-stroom karakteristieken. De experimentele gegevens voor de betreffende Bi-2223 tape geleiders bevestigen de juistheid van het model. Door toepassing van het netwerkmodel is de fout die ontstaat ten gevolge van het zogenaamde eigenveld (self-field) effect op de kritieke stroom geëlimineerd.

Aan de hand van het voorbeeld van een resonatorspoel voor 1 MVA die wordt bedreven in vloeibare stikstof, zijn de beginselen van supergeleidende vermogensspoelen aangegeven. De configuratie, de technieken en de fabricage van het prototype van de spoel – met een aanzienlijke inspanning van de Nederlandse industrie – zijn geschetst. Optimalisering van het ontwerp van de spoel heeft geleid tot een cilindrische spoelset die bestaat uit vier lange en dunne concentrische solenoïdes met grote diameter. De radiale component van het magnetisch veld waarvoor de tapes van Bi-2223 het meest gevoelig zijn, is onderdrukt door kleine stukken ijzer op de juiste wijze te plaatsen rond de uiteinden van de spoelen. Zowel langs analytische als numerieke weg is het effect bestudeerd en de resultaten hebben essentieel bijgedragen tot het optimale ontwerp van de spoel en zijn experimenteel gevalideerd. Voor verschillende magnetische configuraties van de spoel zijn de spanning-stroom krommen zowel voor gelijkstroom als wisselstroom numeriek berekend en gemeten. Tenslotte worden numerieke schattingen en hun experimentele verificatie als ook de resultaten voor de 1 MVA spoel gepresenteerd en besproken.

Een vergelijking is gemaakt tussen conventionele en hoge T_c supergeleidende vermogenstransformatoren. De levensvatbaarheid van een supergeleidende transformator is behandeld vanuit economische en technische gezichtspunten. De technische en economische parameters voor vermogenstransformatoren zijn nauw met elkaar verbonden vanwege het feit dat transformatoren met koper al bijna een eeuw worden geproduceerd en op veel punten fysische en technologische grenzen hebben bereikt. De cruciale vraag voor toekomstige toepassingen is: “Onder welke kosteneffectieve condities kan de algehele efficiëntie van een hoge T_c supergeleidende transformator hoger worden gemaakt dan die van een conventionele transformator?” Deze vraag wordt besproken en beantwoord.

Voor een 30 MVA model van een supergeleidende transformator en een conventionele transformator zijn de totale kosten, de energiekosten en kapitaalkosten met elkaar vergeleken. De energiekosten van een hoge T_c supergeleidende transformator zijn verwacht lager dan die van een conventionele transformator. De andere kosten worden vooral bepaald door de specifieke kosten van de supergeleider, gewoonlijk uitgedrukt in US$/kA/m. Voor een hoge T_c supergeleidende en een conventionele transformatoren verwacht men vergelijkbare totale en kapitaalkosten met de specifieke bedragen van respectievelijk 50 en 25 US$/kA/m. Bij de huidige prijzen die het referentiepunt van 50 US$/kA/m benaderen, worden de kansen zich voor grootschalige toepassingen van hoge T_c supergeleiders in vermogenstransformatoren en spoelen beter.

Acknowledgement

When the proposal for this project was conceived and written in 1996, the knowledge of and experience in the design and making of high-T_c power devices was very limited in the Netherlands.

I would like to thank Herman ten Kate (currently at CERN most of the time) for taking a major risk in setting up this ambitious project in 1996-1997 and leading it all the way, for trusting me with this study, for guiding the writing process and stimulating its quality as well as for many useful discussions.

Many thanks to Geert Damstra (TU Eindhoven), who has initiated participation of KEMA in the project, has given a lot of support and fruitful advices on various aspects of coil design, related especially to high voltage and who helped with the relevant measurements.

I am grateful to Horst Rogalla for creating an inspiring scientific atmosphere of the low temperature department.

Periodic discussions with Peter Vaessen (KEMA), Gert Mulder (Philips Medical Systems) and other members of the project utilization committee have provided an important feedback and broadened the view on potential applications of superconducting coils.

Brief, but useful discussions with Johan Smit (TU Delft) about the future of applied superconductivity in large electrical systems are appreciated.

Essential and valuable discussions on the possible future of superconducting tapes and power transformers with Alexis Malozemoff and Jürgen Kellers (American Superconductor Corporation USA and Europe) have improved my view and are gratefully acknowledged.

Concepts of a Bi-2223 power coil and of the 1-MVA resonator coil system described in this book where proposed by the author. However, a step to the detailed technical design and realisation of the system and setting up relevant technological base would not be the same without friendly advice of Andries den Ouden, Arend Nijhuis and Hennie Knoopers as well as skilful help of Arno Godeke, Erik Krooshoop and Sander Wessel. Contributions of Jan Jaap Rabbers and Bennie ten Haken are also appreciated. Many other UT-colleagues not mentioned yet, thank you very much!

Assistance of Cees Spoorenberg, Gerard Rutten, Oğur Karahan and Bart Broeren from Smit Transformatoren B. V. in manufacturing the sub-coils and of Paul Klein Schiphorst and Andre Scholten from Smit Draad Nijmegen B. V. in careful insulating kilometres of fragile superconductor tape (used for coil manufacturing) is greatly acknowledged.

I would like to express thanks to my colleagues at Van Swinden Laboratory of the Netherlands Institute of Metrology and Technology in Delft (Cor van der Ploeg, Helko van den Brom and Gert Rietveld in particular) for their interest, attention and support during the writing of the final chapters of the book.

Countless thanks to Harold Blaauw, without your friendly support and advice this book would probably have never been written.

Last, but not least I would like to thank my wife Olga and our daughter Elena for their help, understanding and serenity, to my parents Lillian and Alexander for giving me life and to my brother Alex for many stimulating discussions.

Oleg Chevtchenko,

Rotterdam,
The Netherlands,

5 September 2002.